



HAL
open science

Multi-physics modeling of startup and shutdown of a PEM fuel cell and study of the carbon support degradation: mitigation strategies and design optimization

Bolahaga Randrianarizafy

► **To cite this version:**

Bolahaga Randrianarizafy. Multi-physics modeling of startup and shutdown of a PEM fuel cell and study of the carbon support degradation: mitigation strategies and design optimization. Chemical and Process Engineering. Université Grenoble Alpes, 2018. English. NNT: 2018GREAI101 . tel-02140284

HAL Id: tel-02140284

<https://theses.hal.science/tel-02140284>

Submitted on 27 May 2019

HAL is a multi-disciplinary open access archive for the deposit and dissemination of scientific research documents, whether they are published or not. The documents may come from teaching and research institutions in France or abroad, or from public or private research centers.

L'archive ouverte pluridisciplinaire **HAL**, est destinée au dépôt et à la diffusion de documents scientifiques de niveau recherche, publiés ou non, émanant des établissements d'enseignement et de recherche français ou étrangers, des laboratoires publics ou privés.

THÈSE

Pour obtenir le grade de

**DOCTEUR DE LA COMMUNAUTE UNIVERSITE
GRENOBLE ALPES**

Spécialité : **MEP : Mécanique des fluides, Energétique, Procédés**

Arrêté ministériel : 25 mai 2016

Présentée par

Bolahaga RANDRIANARIZAFY

Thèse dirigée par **Yann BULTEL**, Professeur Grenoble INP
et encadrée par **Mathias GERARD** et **Pascal SCHOTT**

préparée au sein du **CEA Grenoble / LITEN**
dans l'**Ecole Doctorale I-MEP2 – Ingénierie - Matériaux,
Mécanique, Environnement, Energétique, Procédés, Production**

**Modélisation multi-physiques des arrêts-
démarrages de PEMFC et étude sur la
dégradation du support carbone : stratégies
de mitigation et optimisation de design**

**Multi-physics modeling of startup and
shutdown of a PEM fuel cell and study of the
carbon support degradation: mitigation
strategies and design optimization**

Thèse soutenue publiquement le **13 décembre 2018**,
devant le jury composé de :

Monsieur Christophe TURPIN

Directeur de Recherche, Institut National Polytechnique de Toulouse,
Président

Monsieur Gaël MARANZANA

Professeur, Université de Lorraine, Rapporteur

athalie JOB

Associate Professor, Université de Liège, Rapporteur

Monsieur Yann BULTEL

Professeur, Université Grenoble Alpes, Directeur

Monsieur Pierrick BALESTRIERE

Ingénieur de Recherche, Faurecia, Invité

Monsieur Mathias GERARD Ingénieur de Recherche, CEA LITEN,
Invité

Monsieur Pascal SCHOTT

Ingénieur de Recherche, CEA LITEN, Invité



L'important dans une citation, ce n'est pas forcément qui est l'auteur mais surtout pourquoi.

Confucius Ranpiffour

Acknowledgements

Je souhaite au travers de ces quelques phrases remercier toutes les personnes qui ont permis de réaliser et réussir ces travaux de thèse.

Tout d'abord merci aux membres du jury d'avoir pris le temps de lire et d'apporter une discussion constructive et enrichissante sur ces travaux. Tout d'abord Natalie Job et Christophe Turpin qui grâce à leur expertise dans des domaines connexes m'ont permis de mieux évaluer les enjeux globaux de ces travaux. Christophe Maranzana qui par sa connaissance approfondie du domaine nous a permis un dialogue enrichissant sur les points forts mais aussi les points faibles de cette thèse. Et enfin Pierrick Ballestriere qui a posé des questions permettant de réaliser l'importance du transfert de technologie de la recherche à l'industrie.

Que serait une thèse sans ses encadrants et surtout son directeur de thèse. Grâce à ton côté humain et investi dans les travaux de tes doctorants, je pense que j'ai trouvé un modèle en relation humaines en ta personne Yann Bultel. Au-delà de ça, tu as su ne pas me lâcher et me pousser afin de donner le maximum jusqu'au bout (ce chapitre 3 te hantera longtemps j'ai l'impression) et je te remercie grandement pour tout ce que tu as fait.

Un grand merci à Mathias Gerard de m'avoir fait confiance pour la thèse. Malgré tes nouvelles responsabilités de chef, tu as su m'accorder du temps et du soutien tout au long de la thèse. A Pascal Schott qui m'a encadré depuis le stage de fin d'études, je n'aurais pas de mot pour te remercier suffisamment. Ton humilité et ta bonne humeur sont des qualités auxquelles j'aspire. Toutes les discussions scientifiques (ou non-scientifiques) ont été une mine d'informations sans fin durant tout mon passage au CEA.

Je souhaite remercier aussi toute l'équipe modélisation: Guillaume Serre, Marion Chandesris, Didier Buzon. Au travers de la thèse de nombreuses discussions tournant autour de la pile mais

aussi d'autres domaines tels que les batteries ont toujours été enrichissantes. De même avec les différents échanges avec différents laboratoires du CEA comprenant Sylvie Escribano, Fabrice Micoud (sacrées nuits à l'ESRF), Sebastien Rosini et plein d'autres que j'oublie de citer. Une pensée particulière pour Ramon qui fut un soutien significatif et une grande aide morale qui nous guidât dans nos moments sombres.

Je ne peux parler de cette thèse sans parler des autres stagiaires, doctorants et post-doc. Merci à Max, Nico, Gauthier, Youcef, Pierre, Miguel qui ont permis de supporter les moments durs de la thèse grâce à des discussions "constructives" allant de la considération métaphysique à des sujets plus légers. Mention spéciale aux "chinois" (comme dirait Maxime) qui ont été le coeur de ma (on pourrait même dire notre j'espère) motivation tout au long de la thèse. Que ce soit Plazo ou la Rage, les moments de la 324 sont des moments que je vais chérir pendant un long moment :-).

Enfin la famille qui m'a soutenu de bout en bout jusqu'à la soutenance. Mon frère qui m'a toujours encouragé à faire des études longues. Mon père le "vrai" docteur qui même s'il a un "faux" docteur de fils m'a toujours soutenu sans faille et restera un exemple à suivre. "yo yo yo" Ma sister (spéciale casse-dédi sisi), Seb et Tara "tabou tabou tabou" m'ont toujours montré qu'aussi forte soit l'adversité, je peux toujours compter sur eux et surtout faire leur vaisselle :-). Et finalement Zbouby ou plutôt Julie la plus belle qui sans elle je serais juste qu'une personne qui se plaint au lieu de faire ! Merci de m'avoir supporté et encouragé jusqu'au bout spécialement les derniers mois. Sans toi je ne sais pas si j'aurais atteint le but. Merci pour toutes les attentions et messages d'amour quotidiens afin de me remonter le moral qui m'ont permis d'avancer sans trop trébucher. Merci tout simplement d'être là pour moi et je te rendrais la pareille sache-le !

Contents

General Introduction	1
1 Fuel cell background	5
1.1 Hydrogen carrier and fuel cell technologies for automotive application	6
1.1.1 Production	7
1.1.2 Storage	7
1.1.3 Refuelling	8
1.2 PEMFC context and limitations within transport	9
1.3 PEMFC description	11
1.3.1 Fuel cell operation	11
1.3.2 Fuel cell components	13
1.4 Degradations	16
1.4.1 Membrane degradations	17
1.4.2 Degradation of Pt nanoparticles	19
1.4.3 Carbon support degradation	20
1.5 Conclusion	23
2 Modeling and simulation framework	25
2.1 Description of the performance model of PEMFC	26
2.1.1 MUSES platform and EuROPIUM code	26
2.1.2 Geometry and domains	27
2.1.3 Species transport modeling	28

2.1.4	Electrochemistry	35
2.1.5	Electronic transport	37
2.1.6	Ionic transport	37
2.1.7	Thermal	38
2.2	Local conditions distributions	41
2.2.1	Electrochemical model fitting	41
2.2.2	Oxygen depletion in the cathode channel	43
2.2.3	Relative humidity along the channel	46
2.3	Practical case : Design sensitivity	46
2.3.1	Design optimization of bipolar plates	46
2.3.2	Impact of operating conditions	54
3	Modeling of carbon support corrosion during transient phases	57
3.1	Introduction to the reverse-current decay mechanism	58
3.2	Modeling in EuROPIUM of transient startup and shutdown	61
3.3	Carbon corrosion and reverse-current decay mechanism simulation	64
3.3.1	Simulation of mechanism during a startup	64
3.3.2	Simulation of mechanism during a shutdown	76
3.3.3	Rib-channel	84
3.4	Carbon corrosion validation	93
3.4.1	SAXS/WAXS experiment	93
3.4.2	CO ₂ at cathode outlet	96
3.4.3	In-situ and ex-situ analyses	99
3.5	Conclusion	103
4	Optimization and mitigation strategies	105
4.1	Optimization of materials and design	106
4.1.1	Anodic specific surface	107
4.1.2	Impact of rib-channel design	107
4.2	Operating strategies	118
4.2.1	Gas flow velocity	118
4.2.2	Startup with a resistor	121
4.2.3	Front dilution	124
4.3	Conclusion	126
	Conclusions and prospects	129
	Bibliography	133

A SAXS/WAXS Description

147

List of Figures

1.1	Hydrogen refuelling station (courtesy of Toyota.eu)	8
1.2	Schematics of a fuel cell	11
1.3	Polarization curve PEMFC (reprinted from [1])	12
1.4	Description of a single cell (reprinted from [2])	13
1.5	Scanning electron microscopy-FEG image of a GDL (reprinted from [3])	15
1.6	Structure of PFSA ionomer	15
1.7	Scanning electron microscopy of a MEA (reprinted from [4])	17
1.8	Total average fluorine and sulfur emission rates for a Nafion 112 membrane during OCV decay as a function of temperature (reprinted from [5])	18
1.9	Infrared images of some aged MEA (reprinted from [2])	18
1.10	Schematics of Pt nanoparticles degradation mechanism reprinted from [6]	20
1.11	SEM image with an example of the formation of a Pt-band in the membrane	20
1.12	SEM image of corroded MEA after several startups	22
1.13	SEM images of top view aged MEA and cross sections under a channel and under a land (reprinted from [7])	23
2.1	MUSES platform	27
2.2	2D models of a single PEMFC (BP: Bipolar Plate, CH: Gas Channel, GDL: Gas Diffusion Layer, MPL: Microporous Layer, CL: Catalyst Layer, MB: Membrane)	28
2.3	Simplified agglomerate source terms model	33
2.4	Schematics of activation free enthalpies and free enthalpy of reaction	37
2.5	Experimental and fitted polarization curves	42

2.6	Oxygen and hydrogen concentrations @0.8 A/cm ²	44
2.7	Oxygen concentration through the channel and MEA for the three cut lines at a medium 0.8 A/cm ² (a) and an high 1.2 A/cm ² (b) current density	45
2.8	Current density distributions along the cathodic catalyst layer	45
2.9	Relative humidity at 0.8 A/cm ² (the dashed lines represent the cut lines)	46
2.10	Electronic cathode potential profile (a) and oxygen concentration profile (b) for a large channel (left) and a thin channel (right) at the inlet	48
2.11	Electronic cathode potential distribution from rib to catalyst layer and current density along the catalyst layer @0.675V at the inlet	49
2.12	Performance of the fuel cell @0.675V as function of position in the channel and the ratio cathode channel width/total width	50
2.13	Oxygen concentrations @0.8 A/cm ² for the optimal design in AutoStack operating conditions	51
2.14	Electronic cathode potential distribution from rib to catalyst layer and current density along the catalyst layer @0.675V at the inlet	52
2.15	Electronic cathode potential distribution from rib to catalyst layer and current density along the catalyst layer @0.675V at the outlet	53
2.16	Performance of the fuel cell @0.675V as function of position in the channel and the ratio cathode channel width/total width and for special operating conditions	55
2.17	Oxygen concentrations @0.8 A/cm ² for the optimal design for stoichiometry O ₂ : 2	56
3.1	Relative impact of operating conditions on PEMFC degradations (reprinted from [8])	58
3.2	Potentials along the channel (a) and through plane (b) before the startup of a PEMFC	59
3.3	Potentials along the channel (a) and through plane at each side of the H ₂ /O ₂ front: O ₂ side (b) and H ₂ side (c) during the startup of a PEMFC	60
3.4	Geometry of the models: along the channel (a) and Rib-channel (b)	62
3.5	Molar fractions imposed at the anode inlet during the startup	65
3.6	Concentration of gases along the anodic channel during different phases of startup: (a) 1.1 s, (b) 2s and (c) 3s	66
3.7	Oxygen (top) and hydrogen (bottom) concentrations distributions during different phases of a startup: (a) 1.1 s, (b) 2s and (c) 3s	67
3.8	Electrode potentials along the cathode (a) and anode (b) catalyst layer during a startup.	69

3.9 Cathode (a) and anode (b) potential in the catalyst layer at the cathode inlet and outlet during a startup	70
3.10 Cell potential during a startup	71
3.11 Phase 1 current distribution	72
3.12 Dissolved oxygen and hydrogen in the anode catalyst layer at the anode inlet (a) and outlet (b) as function of time during a startup	73
3.13 Current distribution during a startup (phase 2)	74
3.14 OER and ORR (a) and COR (b) current density along the cathode catalyst layer during a startup	75
3.15 Oxygen (top) and hydrogen (bottom) concentrations distributions during different phases of a shutdown: (a) 10.1 s, (b) 11.3 s and (c) 13 s	77
3.16 Electrode potentials along the cathode (a) and anode (b) catalyst layer during a shutdown	78
3.17 Cell potential during a shutdown	79
3.18 Cathode (a) and anode (b) potential in the catalyst layer at the cathode inlet and outlet during a shutdown	79
3.19 Current distribution during a shutdown during phase 2	80
3.20 Dissolved oxygen and hydrogen in the anode catalyst layer at the anode inlet (a) and outlet (b) as function of time	81
3.21 Dissolved oxygen and hydrogen in the cathode catalyst layer at the cathode outlet (a) and inlet (b) as function of time	82
3.22 Predicted cumulated carbon loss distribution along the cathode flow-field for a startup and a shutdown for a counter-flow and a co-flow	83
3.23 Hydrogen concentration during startup before the hydrogen front (a), during (b) and after (c) at the anode inlet	85
3.24 Schematics of expected potentials during a startup at the rib/channel scale	86
3.25 Dissolved hydrogen (a) and oxygen (b) concentrations in plane of the middle of the anode catalyst layer during a startup at the anode inlet	87
3.26 Cathodic (a) and anodic (b) electrode potentials along the catalyst layers during a startup at the anode inlet (rib-channel model)	88
3.27 Current distribution in plane at the anode (a) and cathode (b) catalyst layer during a startup at the anode inlet	89
3.28 Hydrogen and oxygen fractions profile at the anode channel/GDL interfaces at the middle (a) and the outlet (b)	90
3.29 Cathode electrode potential along the cathode catalyst layer during a startup at the middle of the cell (rib-channel model)	91

3.30	Current distribution in plane at the anode (a) and cathode (b) catalyst layer during a startup at the middle of the cell	92
3.31	Amount of oxidized carbon (in $\mu g_C/cm^2$) in-plane in the middle of the cathode catalyst layer for different positions: anode inlet, middle and outlet	93
3.32	WAXS spectra at two different potentials along the thickness	94
3.33	WAXS spectra at two different potentials at the cathode (a) and the anode (b)	95
3.34	Spectra in the middle of the cathodic catalyst layer at OCV (spectre 6) and during potentiostatic study @1.2 V at 90 s (spectre 7), 145 s (spectre 8) and 220 s (spectre 9)	96
3.35	Carbon corrosion current of the cathode catalyst layer as function of time	97
3.36	Predicted quantity of CO ₂ in ppm at the cathode outlet during a startup in Gu et al. conditions	98
3.37	Quantity of CO ₂ measured at the exit of the cathode during startup-shutdown events (reprinted from [9])	98
3.38	Predicted quantity of CO ₂ in ppm at the cathode outlet during a startup and a shutdown in reference conditions	99
3.39	Fuel cell used and simplified schematic of the flow field	99
3.40	Startup/shutdown protocol (reprinted from [4])	100
3.41	Difference in current distribution between end and beginning of test @0.5 A/cm ²	100
3.42	Quantity of hydrogen desorbed as function of location at the anode (a) and cathode (b) (the higher the quantity of hydrogen desorbed the higher the ECSA)	101
3.43	SEM images of the fresh sample (a) and after 69 startup/shutdown at H ₂ inlet (b), air outlet (c) and middle of the cell (d)	102
4.1	ORR current (a) and cathode potential (b) during a startup with two different anodic specific surface	108
4.2	Amount of oxidized carbon (in $\mu g_C/cm^2$) along the middle of the cathode catalyst layer for different anode platinum loading	109
4.3	Cathode potential during phase 2. The vertical dashed line is the middle of the cell	110
4.4	Cathodic electrode potential (a) and dissolved hydrogen concentration in the anode catalyst layer (b) at the middle of the flow field for 30 % rib/total length ratio	111
4.5	Cathodic electrode potential (a) and dissolved hydrogen concentration in the anode catalyst layer (b) at the outlet of the flow field for 90 % rib/total length ratio	112

4.6	Cathodic electrode potential at the anode outlet two design of rib/channel: 30 % (a) and 90 % (b) rib/total length ratio	113
4.7	Cathode potential under the middle of the channel and the rib at the anode outlet and middle for two rib/total length ratio: 30 % (a) and 90 % (b)	114
4.8	Amount of oxidized carbon (in $\mu g_C/cm^2$) in the middle (a) and anode outlet (b) cathode catalyst layer for different anodic rib/total length ratio during a startup	115
4.9	Amount of oxidized carbon (in $\mu g_C/cm^2$) in the middle (a) and anode inlet (b) cathode catalyst layer for different anodic rib/total length ratio during a shut-down	117
4.10	Cell potential during a startup as function of the flow velocity	119
4.11	Dissolved concentration at the anode outlet during a startup for different flow velocities	119
4.12	Cathodic electrode potential at the cathode inlet during a startup for different flow velocities	120
4.14	Total amount of carbon corroded as function of the anode flow velocity	121
4.13	Amount of oxidized carbon predicted along the cathode flow-field for different flow velocities	121
4.15	Resulting current leak during startup	122
4.16	Cell potential during a startup with and without a resistor	122
4.17	Cathodic electrode potential at the cathode inlet during a startup with and without a resistor	123
4.18	Amount of oxidized carbon predicted along the cathode flow-field with and without a resistor	124
4.19	Molar fractions at the anode inlet as function of time	124
4.20	Cell potential (a) during a startup for different switch times and zoom on the overshoot (b)	125
4.21	Cathode potential at the cathode inlet during a startup for different switch times	126
4.22	Quantity of CO_2 at the cathode outlet for several cases during a startup	127
A.1	Scale of different scattering methods	147
A.2	Scheme of beamline experiment	148
A.3	Design of the cell and MEA used	149
A.4	Movement description of the sample	149
A.5	Example of a full scan in the thickness (z-axis) in N_2/N_2 at 65% RH	150
A.6	Examples of isolated spectra expected to be in the membrane and in a catalyst layer	150
A.7	Intensity of the graphite, Pt 111 and Nafion peak along the thickness	151

List of Tables

1.1	Some types of fuel cells	6
2.1	Physics and domain affectations	39
2.2	Correlations and values used in the model	40
2.3	Geometric parameters	40
2.3	Geometric parameters	41
2.4	Operating conditions for fuel cells simulated in this work	42
2.5	Electrochemical parameters (bold are fitted)	43
2.6	Geometry values for the initial design in AutoStack-CORE	47
3.1	Parameters for the models	64
3.2	Geometry values used in the simulations	65
4.1	Relative corrosion as function of rib-channel design and location in the flow field during a startup	116
4.2	Relative corrosion as function of rib-channel design and location in the flow field during a shutdown	118
4.3	Elapsed time in phase 2 for the different velocities	120
4.4	Summary of mitigation	127

Nomenclature

Abbreviation

BP Bipolar plates

CH Channel

CL Catalyst layer

COR Carbon Oxidation Reaction

ECSA Electrochemical Catalyst Specific Area

FEG Field Emission Gun

GDL Gas diffusion layer

HER Hydrogen Evolution Reaction

HOR Hydrogen Oxidation Reaction

MB Membrane

MEA Membrane electrode assembly

MPL Micro-porous layer

OER Oxygen Evolution Reaction

ORR Oxygen Reduction Reaction

PEM Proton Exchange Membrane

PEMFC Proton Exchange Membrane Fuel Cell

SAXS Small Angle X-ray Scattering

SEM Scanning electron microscopy

SOFC Solide Oxide Fuel Cell

WAXS Wide Angle X-ray Scattering

Greek

α	Charge transfer coefficient	[–]
ΔG	Gibbs free energy	[J]
$\Delta H_{c/a}^{\circ}$	Standard molar enthalpy	[J · mol ⁻¹]
$\Delta H_{c/a}^{\circ}$	Standard molar enthalpy	[J · mol ⁻¹]
ΔH_{ox}^{\ddagger}	Enthalpy of formation of the activated complex (in the way of oxidation)	[J · mol ⁻¹]
ΔH_{ox}^{\ddagger}	Enthalpy of formation of the activated complex (in the way of oxidation)	[J · mol ⁻¹]
$\Delta S_{c/a}^{\circ}$	Standard molar entropy	[J · mol ⁻¹ · K ⁻¹]
$\Delta S_{c/a}^{\circ}$	Standard molar entropy	[J · mol ⁻¹ · K ⁻¹]
ΔS_{ox}^{\ddagger}	Entropy of formation of the activated complex (in the way of oxidation)	[J · mol ⁻¹ · K ⁻¹]
ΔS_{ox}^{\ddagger}	Entropy of formation of the activated complex (in the way of oxidation)	[J · mol ⁻¹ · K ⁻¹]
ϵ	Porosity	[–]
$\epsilon_{ionomer}$	Ionomer proportion in the membrane and catalyst layers	[–]
η	Overpotential	[V]
Γ	Rib to total length ratio	[%]
κ	Permeability	[m ²]
λ	Thermal conductivity	[W · m ⁻¹ · K ⁻¹]
λ	Water content	[–]

μ	Dynamic viscosity	[Pa · s]
ν_j	Stoichiometry coefficient of the specie j	[–]
Φ	Ionic potential	[V]
Ψ	Electronic potential	[V]
ρ	Density	[kg · m ⁻³]
σ_e	Electronic conductivity	[S · m ⁻¹]
σ_i	Ionic conductivity	[S · m ⁻¹]
τ	Tortuosity	[–]

Roman

\vec{N}_i	Molar flow of specie i	[mol · m ³ · s ⁻¹]
\vec{U}	Volume velocity tensor	[m · s ⁻¹]
\vec{u}	Mass-based velocity tensor	[m · s ⁻¹]
a_C	Carbon Specific surface	[m ² · m ⁻³]
a_i	Activity of specie i	[–]
a_v	Platinum Specific surface	[m ² · m ⁻³]
c_i	Concentration of specie i in gas phase	[mol · m ⁻³]
c_g	Total concentration of gases	[mol · m ⁻³]
C_i	Dissolved concentration of specie i	[mol · m ⁻³]
C_p	Heat capacity	[J · kg ⁻¹ · K ⁻¹]
$C_{SO_3^-}$	Nafion's sulphonated sites concentration	[mol · m ⁻³]
D_i^a	Diffusion coefficient in electrolyte phase of specie i	[–]
D_i^k	Knudsen diffusion coefficient of i	[m ² · s ⁻¹]
D_{ij}	Binary diffusion coefficient	[m ² · s ⁻¹]
F	Faraday constant	[C · mol ⁻¹]

h	Planck constant	[J · s]
H_i	Constant of Henry of specie i	[Pa·m ³ ·mol ⁻¹]
i_e	Electronic current	[A]
i_i	Ionic current	[A]
j_0	Exchange current density	[A · m ⁻²]
J_p	Current density of permeation	[A · m ⁻³]
J_r	Current density of the reaction	[A · m ⁻³]
$k_{ox/red}^0$	Constant reaction rate	[mol · m ⁻² · s ⁻¹]
k_b	Boltzmann constant	[J · K ⁻¹]
l	Width	[m]
M_i	Molar mass of specie i	[kg · mol ⁻¹]
n	Number of electrons or number of moles	[–] or [mol]
N_A	Avogadro constant	[mol ⁻¹]
p	Relative pressure	[Pa]
P_g	Total pressure of gases	[Pa]
P_i	Partial pressure of specie i	[Pa]
Q_i	Local heat source	[W · m ⁻³]
R	Universal gas constant	[J·K ⁻¹ ·mol ⁻¹]
R_p	Pore radius	[m]
s_0	Average Pt surface per reaction site	[m ²]
S_i	Source terms	[–]
t	Time	[s]
W_{e-}	Local electric energy	[W · m ⁻³]
X_i	Molar fraction of specie i	[–]

z_i	Charge of the specie j	[–]
e	Thickness	[m]
T	Temperature	[K]

General Introduction

As global warming is a concern around the world, numerous questions about energy rise. Where the debate for industry and housing is oriented towards green electricity and nuclear energy, transport applications lean towards electrochemical solution. The two leading fields are lithium-ions batteries and fuel cells. The first chapter of this thesis presents the hydrogen as an energy carrier in the context of transport and the constraints that it implies. Fuel cell technologies and especially proton exchange membrane fuel cell (PEMFC) are described. A more thorough description of PEMFC is done showing its perks and disadvantages in an automotive application. The degradation mechanisms which the fuel cell (in particular the electrodes and membrane) undergoes are introduced.

The second chapter details the different multi-physics models developed and used in this work as a base for implementation of carbon corrosion. The objective is to model the performance of a PEMFC at the MEA and cell scales and implement a simulation framework into a CEA multi-physics modelling platform (called MUSES). Two modelling scales are described: an along the channel model and a rib-channel models. Both of them, model the layers that constitutes the cell from the bipolar plates to the membrane. The physics taken into account, including the different transports equations, electrochemical reaction and thermal balance equations are detailed. Thanks to the CFD approach, impact of local conditions onto global performance can be analysed and a couple of case studies are shown. An original use of the models consists of coupling the along the channel and rib/channel model together to perform an optimization on the design of the cathode rib/channel pattern. Indeed, an optimum flowfield design has to be found between the supply of oxygen under the rib and the current collection. Using the along the channel model to obtain the local conditions in the channels, they are implemented in the rib/channel to perform the optimization. Several designs are tested at different location in the channel leading to an optimal design, and a varying width channel is proposed to improve global performance. Impact of several operating conditions is also studied showing the scope of the optimization.

The third chapter focuses on the modeling of carbon catalyst support corrosion during startup and shutdown of the fuel cell. Indeed, during these transient phases, the fuel cell suffers severe degradation especially the acceleration of carbon support corrosion. This degradation leads to an important active surface loss and structural damage provoked by the active layer collapsing. While the potential of the fuel cell remains under 1 V during operation, literature shows that the cathode reaches value up to 1.6 V . These incursions on high electrode potential are explained by a phenomenon called reverse-current decay mechanism. The models presented in chapter 2 were improved to be able to simulate those startup and shutdown during transient phases. A thorough description is carried out with the along the channel model. Establishment of the reverse-current mechanism is depicted and impact of the local conditions is detailed.

Carbon corrosion during these transient phases is estimated and impact of the flow configuration is shown. Another part of the chapter portrays what happens during these startup-shutdown at the rib/channel scale. As done before, local conditions are extracted from the along channel model to be reused in the rib/channel model. As literature highlights carbon support corrosion heterogeneities between rib/channel, the models presented confirms and exhibits the different behaviours. The latter includes rib/channel disparities but also disparities between locations along the channel. Finally, validations are performed: first by comparison to CO_2 measurements at the cathode outlet issued from the literature and qualitatively with SEM images. Innovative experiments using SAXS/WAXS technologies were initiated.

In order to limit the carbon corrosion during startup/shutdown, several mitigation strategies have been proposed and simulated. The fourth chapter investigates how the models are used to study these strategies and to propose new ones. First, the impact of anode catalyst loading is studied. The relation between the loading and the resulting corrosion is estimated. Then sensitivity analysis of the local conditions on the corrosion amount was performed. The impact of anode rib/channel design onto corrosion during startup and shutdown has finally been investigated. Distinct results are obtained between startup and shutdown. Simulations results show that the design has a significant impact on corrosion and is present either at the cathode outlet during startup or at the cathode inlet during shutdown. As for performance presented in chapter 2, an anodic varying width channel should be considered in order to mitigate the carbon degradation. The second section of the chapter analyses some system strategies. Several anodic flow velocities for the startup are tested. Thanks to the multiphysics model, gas transport effects are showcased. The last strategy studied is the use of an auxiliary load to limit the cathode potential.

Finally, the study is concluded opening up prospects about coupling the corrosion of the carbon with other degradations like platinum dissolution and improvements for validation of kinetics.

Fuel cell background

Contents

1.1	Hydrogen carrier and fuel cell technologies for automotive application	6
1.1.1	Production	7
1.1.2	Storage	7
1.1.3	Refuelling	8
1.2	PEMFC context and limitations within transport	9
1.3	PEMFC description	11
1.3.1	Fuel cell operation	11
1.3.2	Fuel cell components	13
1.4	Degradations	16
1.4.1	Membrane degradations	17
1.4.2	Degradation of Pt nanoparticles	19
1.4.3	Carbon support degradation	20
1.5	Conclusion	23

1.1 Hydrogen carrier and fuel cell technologies for automotive application

In order to address answer the challenge of the always growing energy demand, new technologies are developed especially in transport application. Indeed, the limited fossil resources and its impact on greenhouses gases emission create the need of new energy producing means. As thermal motors produce several toxic wastes (like NO_x), electric motors are considered to replace them. Several clean intermittent solutions are currently promoted like solar or wind turbines to produce electricity. However one of the main hindrance is their intermittent nature inducing production of energy when it is not needed (for example during the day for solar). New storage solutions have to be developed and hydrogen is a promising one. In this context, fuel cells are an innovative and a pertinent way to generate electricity and heat. Indeed, fuel cell operation consumes fuel (like hydrogen) and oxygen from the air to generate energy producing water as the only waste in general. Thus, this technology have great potential to have a limited impact on global warming and pollution. This is one of the reason why this technology is promising for complementing or even replacing current technology with heavy CO_2 emitting field area like electric and heat generator or transport. Several fuel cell technologies are currently investigated and are still in development.

Table 1.1: Some types of fuel cells

	SOFC	MCFC	PAFC	HT-PEMFC	DMFC	AFC	PEMFC
Operating temperatures	1273 K	923 K	423 – 493 K	393 – 473 K	333 – 403 K	343 – 373 K	323 – 353 K
Typical electrical efficiency	< 200 kW	> 200 kW	> 50 kW	< 100 kW	< 1 kW	> 20 kW	< 250 kW
Electrical efficiency	50 – 65 %	45 – 60 %	35 – 40 %	60 %	40 %	45 – 60 %	40 – 60 %
Electrolyte	Ceramic	Immobilised liquid molten carbonate	Immobilised liquid phosphoric acid	Mineral acid-based	Polymer membrane	Potassium hydroxide	Polymer membrane
Applications	Stationary	Stationary	Stationary	Small stationary	Portable	Submarines, spacecraft	Vehicles, small stationary

A list of these different technologies is presented in Table 1.1 [10]. For stationary applica-

tions (like electricity and heat generator for a building), high temperature fuel cells like SOFC (Solid Oxide Fuel Cells) are a promising technology thanks to the possibility to use different fuels (dihydrogen, methane, methanol or ethanol). However, the high temperature ($> 1000\text{ }^\circ\text{K}$) hinders its use in a non-stationary application like transport. For this latter use, Proton Exchange Membrane Fuel Cell (PEMFC) is one of the most prominent candidates. Thanks to its low temperature of operation ($< 100\text{ }^\circ\text{C}$) and the possible small bulk of the system, PEMFC has a great profile answering the automotive challenge. They are also used for example as an emergency electricity generator, micro-production for electronic devices. While this technology shows great promise, many hurdles have still to be overcome.

1.1.1 Production

Nowadays, hydrogen production is mainly done by reforming petroleum product at very low costs ($< 3\text{ €/kg}$) using steam reformers which is not ideal. They typically have capacities of up to $10,000\text{ kg/h}$ hydrogen production and emit $8 - 11\text{ kg}$ of CO_2 per 1 kg of hydrogen. Large-scale and efficient electrolysis technologies to produce hydrogen from renewable electricity like wind turbines or solar could significantly reduce those emissions. But costs are still a major hindrance. Furthermore, the alternative nature of these sources leads to another major issue which is the storage.

An option to decrease green hydrogen costs to a level close to fossil hydrogen is high temperature steam electrolysis (SOEC). Low-cost waste heat or steam at low temperatures ($< 200\text{ }^\circ\text{C}$) may be reused from industrial process to reduce the electrical energy requirement. The electricity consumption can be reduced to $< 40\text{ kWh/kg}$ thanks to the availability of steam. When targeting large scale applications, a scale-up to the ‘megawatt’ is an important milestone in the development of electrolyser.

1.1.2 Storage

Hydrogen storage is still heavy, bulky and expensive. Its low density makes it necessary to compress at very high pressure (several hundreds bars). However, even highly compressed its volumetric energy density is still pretty low (for example at 700 bar it is only 30% of the standard gasoline one).

Currently available mechanical hydrogen compressors are too costly for large-scale applications and lack the desired durability, efficiency and reliability. This results in high operational and maintenance costs. The low reliability of mechanical compressors is due to the large number of moving parts. Guaranteeing the tightness of high-pressure moving parts remains also a challenging part as well as the lifetime of membranes ($\sim 2000\text{ h}$).

Breakthrough disruptive technologies exist (including electrochemical and metal hydride



Figure 1.1: Hydrogen refuelling station (courtesy of Toyota.eu)

compressors) and promise significant reduction of total cost of ownership of hydrogen refuelling stations because of the elimination of mechanical compressor disadvantages. However, the maturity of these technologies has to be increased with respect to capacity, durability, lifetime and reliability. Until now, none of these technologies has demonstrated the ability of providing sufficient flow rates for large-scale applications at reasonable costs. However, no large-scale system has been developed to date, as the focus was set on 200 kg/day stations, corresponding to the needs of the market introduction of passenger cars.

1.1.3 Refuelling

Costs associated to the hydrogen refuelling station represent a large share of the overall hydrogen costs in transport applications, with a strong impact on the business models of hydrogen mobility. Large scale refuelling (e.g. hydrogen passenger cars, buses and trucks fleets, rail transport as well as maritime applications) expected in the next years will require hydrogen refuelling stations with capacities of 1 t/day or more, at pressure levels of 350 bar or 700 bar (i.e. 450 bar or 900 bar at the station). 50% of the costs are related to the compression, making this component a significant bottleneck for fuel cell vehicle deployments. In particular, operational expenditures are critical in the context of large-scale stations. These costs include energy, maintenance, as well as the indirect costs induced when a station is out of order.

Therefore, there is a need for major improvements to meet the criteria of large refuelling stations, both at the scale of the core technology (focus on kinetics and scale effects in selec-

ted materials, impact of improved kinetics on lifetime and performances, architecture of core components) as well as for the system integration (design of entire system, innovative concepts adapted to larger scale, choice of adapted auxiliaries). In addition, the new technologies currently require the use of critical raw materials (such as platinum or rare-earths) in most of the developed concepts.

In this chapter, a brief summary of the PEMFC technology is done within its context. Then, a description of the system and its components is carried out. Finally the degradations that occurs inside the core of the fuel cell are explained.

1.2 PEMFC context and limitations within transport

For transport related activities, PEMFC is the key technology for tackling these applications. Mid and heavy-duty truck fleets are a strategic application because it benefits plenty of the advantages of fuel cell systems over other solutions: fast refuel and long range. In the same field of application, the PEM technology can fit some maritime ones as used in Energy Observer¹. Nevertheless, the automotive field is the most discussed in public. Since 2015, several hydrogen cars were distributed the first one being the Toyota Mirai². Even though many advantages have to be raised (the range going beyond 500 kilometres or the fast refuelling), the car is expensive at 80 000€ and no information is given on the fuel cell durability. The the Fuel Cell and Hydrogen 2 Joint Undertaking (FCH2JU) describes what should be a competitive fuel cell system for a car application [11]:

- Power density $> 2 \text{ W/cm}^2$ at 0.66 V;
- Volumetric power density $> 5 \text{ kW/l}$ at nominal power;
- Specific power density $> 4 \text{ kW/kg}$ at nominal power;
- Durability: $> 6,000$ hours;
- Stack production cost $< 20 \text{ €/kW}$ (for $> 100\,000$ units/year);
- Stack max operating temperature of 105 °C ;

Cost-wise, even though important progresses are made, PEMFC are currently an expensive technology. The stack represents ca. 50% of the total fuel cell system cost and the MEA components around 60% of the stack cost. This latter high cost comes from the use of noble catalyst namely platinum. The current cost for the production of 20.000 cars is around 250 €/kW which is far from the FCH2JU goal.

¹<http://www.energy-observer.org/>

²<https://www.toyota.fr/new-cars/new-mirai/landing.json>

The other main hurdle is the life expectancy of the fuel cell. Its lifespan depend strongly on the way the fuel cell is used. In a stationary usage for a building for example, the expected lifespan is around 9.000 h [12]. However in non-stationary application like personal vehicle, current life expectancy of PEMFC is around 3.000h [13] while currently, thermal motors lifespan is around 5.000h. Furthermore, during its service, the health of the fuel cell degrades decreasing the yield until a critical failure ends abruptly its life. The annual work plan of the FCH2JU describes the expected targets for the fuel cell which are defined in order to obtained a competitive system [11]:

- Lower the MEA cost to a target price of 6.0 €/kW on a production of 1 million m^2 per year;
- Enhanced durability: maximum power loss of 10 % after 6000 hours of operation for the MEA
- Enable higher operating temperature: MEA operating at $1.5 A/cm^2 @ 0.67 V$ with coolant outlet temperature of $105 ^\circ C$ for 5% of the lifetime (around 300 hours).
- Increase the power density to $1.80 W/cm^2 @ 0.6 V$ at a specific range of operating conditions:
 - Inlet pressure: $P_{Cath,An} < 2.5 bar$;
 - Stoichiometry: $1.3 < \lambda_{Cath,An} < 1.5$
 - Humidity: 30 % % (relative to coolant inlet temperature);
 - Inlet temperature: $60^\circ C < T_{inlet} < 70^\circ C$;
 - $10^\circ C < dT_{Coolant} < 15^\circ C$;
 - 100% H_2 concentration at anode inlet;

1.3 PEMFC description

1.3.1 Fuel cell operation

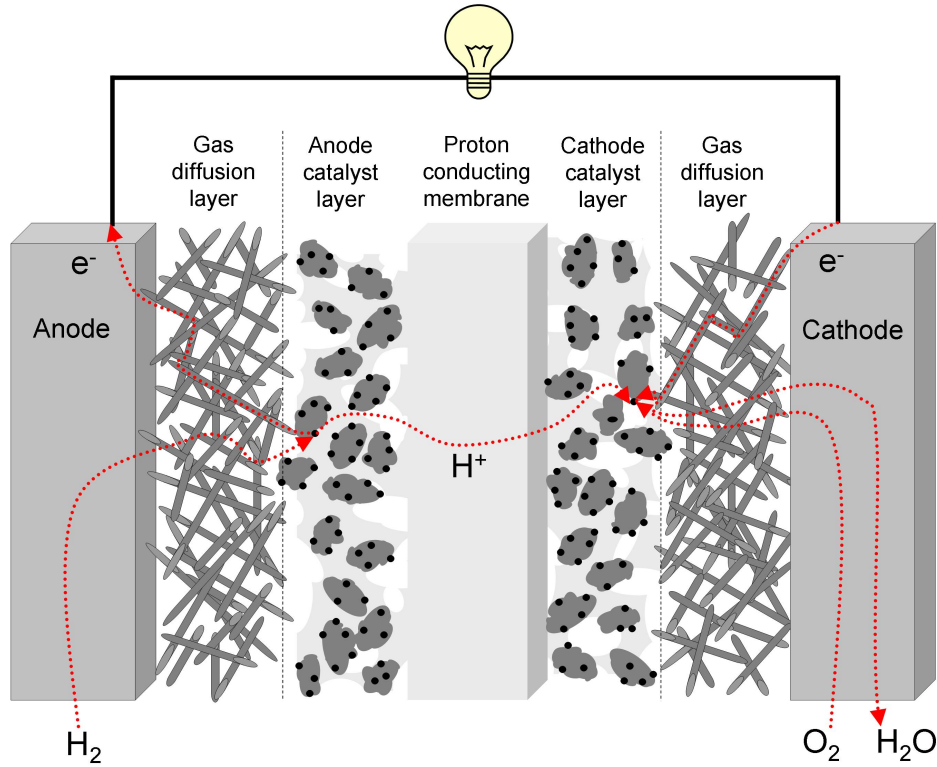


Figure 1.2: Schematics of a fuel cell

A fuel cell is an electrochemical conversion device transforming hydrogen and oxygen into electricity and heat as seen in Figure 1.2. The global balance reaction in a PEMFC is:



This global reaction are separated into two oxidation and reduction reactions (Equation 1.2 and Equation 1.3) which happen respectively in the anode and cathode. These two electrochemical reactions are:



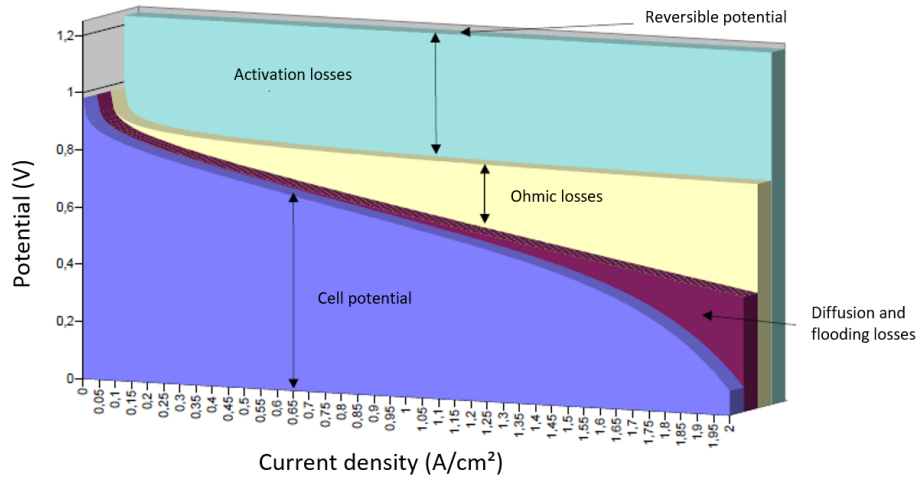
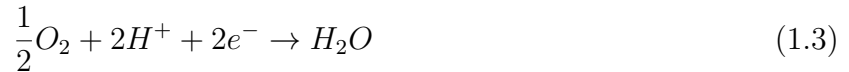


Figure 1.3: Polarization curve PEMFC (reprinted from [1])



In standard operation, the electrode where occurs the oxidation of hydrogen is the anode and the other where there is the reduction of oxygen is the cathode.

The power delivered by the cell depends on the current flowing through the stack and the potential difference between the end plates of the fuel cell. The higher the current the lower the potential is. Figure 1.3 shows a common polarization curve of a fuel cell which describes the relation between the cell potential as function of the current delivered by the cell.

The thermodynamic potential is evaluated with the Nernst equation:

$$E_{rev} = E^0 + \frac{RT}{2F} \ln \left(\frac{a_{H_2} \sqrt{a_{O_2}}}{a_{H_2O}} \right) \quad (1.4)$$

where E^0 is the standard potential around $1.23 V$, a_{H_2} , a_{O_2} and a_{H_2O} the activity of hydrogen, oxygen and water, R the universal gas constant, T the temperature and F the Faraday constant. The OCV or Open Circuit Voltage is the potential when no current is drawn from the cell. The OCV is actually lower than the thermodynamic potential because of the hydrogen crossover from the anode to the cathode.

Activation losses are the main losses at low current value. Indeed a certain amount of energy named activation energy (see Equation 2.36 in subsection 2.1.4) is required to activate the electrochemical reaction. These losses are mainly dependant on the operating conditions

and of the materials used in the MEA.

Ohmic losses are linear due to the internal electronic resistor of the different components of the fuel cells (like the bipolar plates and the GDL) and the protonic resistance of the membrane. As described later in chapter 2, the higher the water content in the electrolyte, the better the protonic conduction in the membrane is (see Table 2.2).

Concentration or diffusion losses increase at higher current. At those values, the diffusion of the reactants in the gas diffusion medium is too slow to offset the consumption at the electrodes. This lack of reactant at the catalyst layers leads to a severe drop in performance.

1.3.2 Fuel cell components

As presented in Figure 1.4, a cell is made of several layers: a bipolar plate (BP) that isolate the gases of each cell; a gas diffusion medium consisting of a GDL or Gas Diffusion Layer and sometimes MPL or Micro Porous Layer and at the centre of the cell, there is the MEA or the Membrane Electrode Assembly. This assembly regroupes the anode and cathode electrodes (CL) where electrochemical reactions occur and the membrane (MB) that isolates the two electrodes. A stack is a series assembly of several cells. Each components will be described below with the expected work to tend towards the desired targets accordingly to the FCH2JU.

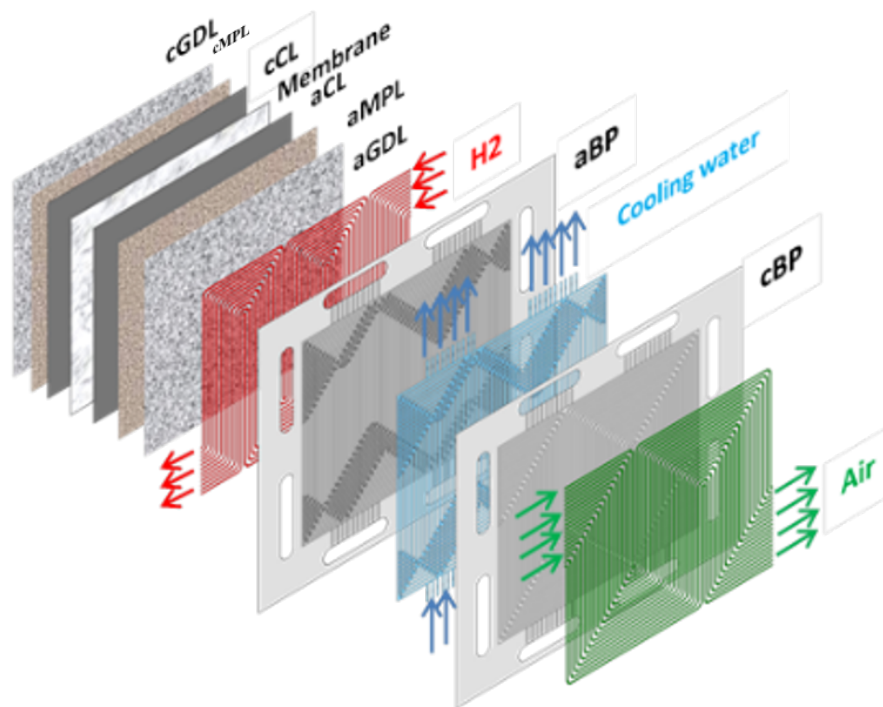


Figure 1.4: Description of a single cell (reprinted from [2])

Bipolar plates

As explained before, the role of the bipolar plates is to separate the reactant gases preventing them to react with each other and collect the current from the GDL. At the same time it allows the cooling water to flow between each cell and to refrigerate the stack. They are in general constituted of two metallic (stainless steel) plates that are stamped. In a stack, each plate at the extremity is a monopolar plate. The required specifications of a bipolar plates are fluids (gases and liquids) impermeability and high electronic conductivity. Furthermore, they have the role to mechanically strengthen the assembly by staying as light as possible. The pattern of rib and channel is defined by the design of the bipolar plate. The rib represents the area where the bipolar plates directly makes contact with the GDL allowing the electron conduction. The channel is the area under the bipolar plates where the reactant gases flow to access the cell.

Gas diffusion media

Containing the GDL (and sometimes MPL), its role is to diffuse the gases all over the cell and also to assure a thermal and electronic conduction (see Figure 1.2). Thus they are made of carbon as a woven cloth or fibres to assure electronic conduction [14]. Thanks to these layer, gases are expected to go under the rib to homogenize their concentration. As water is produced at the cathode, these layers have to be hydrophobic to evacuate the water (liquid or vapour). In order to upgrade this component, development of high through-plane thermal conductivity GDLs to enable low local temperatures at the catalyst layers is desirable. Higher in-plane diffusivity GDLs are also desired to reduce the effect of wide ribs on bipolar plates. A combination of GDL properties are desired, including reduced thickness, to achieve optimum contact resistance, gas flows under the landings, water management and thermal conduction.

Proton Exchange Membrane (PEM)

As its name implies, the membrane in a PEMFC is commonly a polymer called perfluorosulfonic acid (PFSA). This polymer is often called Nafion[®] and is distributed by Du Pont de Nemours but other companies propose the same type of membrane like Aciplex[®], Flemion[®] and Gore-Select[®]. Figure 1.6 shows the chemical structure of the PFSA polymer. It is composed of a backbone of $-(CF_2)_n-$ groups for the mechanical stability where hydrophilic sulfonic acid groups $-SO_3H-$ are attached.

The polymer is an electrolyte allowing the protons produced at the anode to flow at the cathode and to feed the reduction of oxygen. However to avoid a short circuit, the membrane has to electronically isolate the anode from the cathode. Durable membranes are expected to reduce gas crossover and to support viable operation at higher temperature (to 110 °C). They

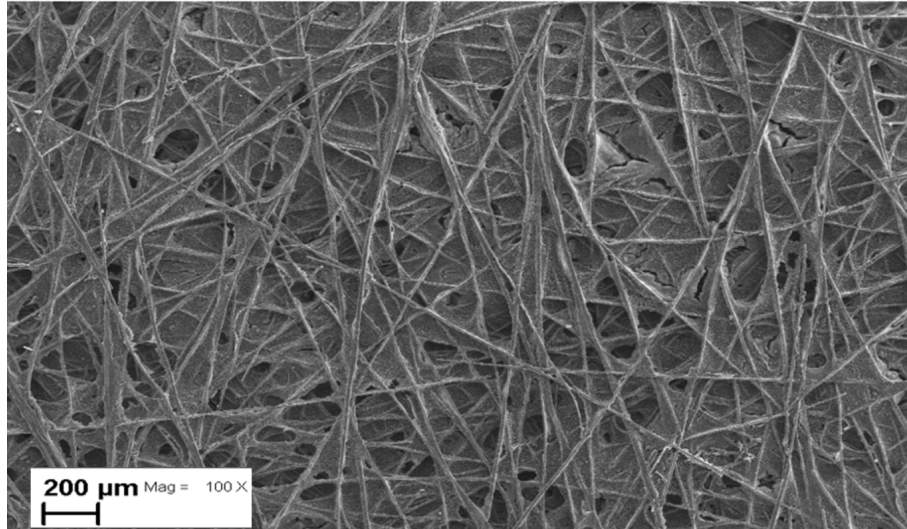


Figure 1.5: Scanning electron microscopy-FEG image of a GDL (reprinted from [3])

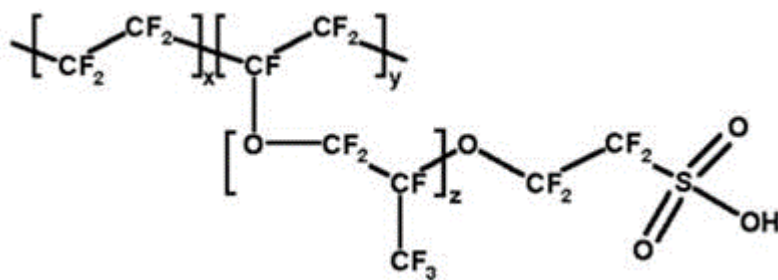


Figure 1.6: Structure of PFSA ionomer

also have to display the proton conductivity of currently available ionomers, or better, and to be mechanically and chemically stable under RH cycling and OCV conditions.

Electrodes

Electrodes or catalyst layers (CL) are a complex tri-phase structure between the gas diffusion medium and the membrane. It is a porous media composed of carbon support with a catalyst nanoparticles deposited on it, meshed with electrolyte. The electrochemical reactions occur at this location. Catalyst layer allows the gases to diffuse from the gas diffusion medium to the reactive site. The electrochemical reactions, taking place on the catalyst nanoparticle surface, consume or produce protons and electrons. The carbon support acts as the electronic conduction medium while the electrolyte ensures the ionic conduction. Current state of the art MEAs have a loading in the range of 0.25 to 0.35 mg/cm^2 . In order to lower the cost of the MEA, the reduction of the total platinum loading is expected without losing performance. Here are the several areas of development for the electrodes suggested by the FCH2JU [11]:

- *Catalyst*: Development of new catalysts with higher mass-specific activity, durability and active surface area. The catalyst has to be capable of being integrated in a layer that allows operation at higher current densities;
- *Catalyst Support*: Development of corrosion resistant supports which promote optimal layer ionomer distribution and operation at high current densities. These supports have also to meet the durability requirements during dynamic operating conditions, such as start-stop;
- *Catalyst layer Design*: New electrode designs, structured layers and additives to improve performance at high current density and increase durability. Focus has to be placed on minimization of mass transport losses while ensuring manufacturability of the layer;
- *Catalyst Layer ionomer*: Ionomers with higher protonic conductivity, higher permeability to O_2 and stable behaviour at low RH (<50% RH) and high temperatures (80 - 110 °C);

1.4 Degradations

Over the last decade, despite considerable progress in performance, durability and platinum loadings decrease, research and development activities are still required to provide materials and designs that can address the durability issue whilst reaching other important targets like cost and operating temperature. Furthermore, a number of new materials were developed that meet performance at the beginning of life of the fuel cell but suffered with high degradation and

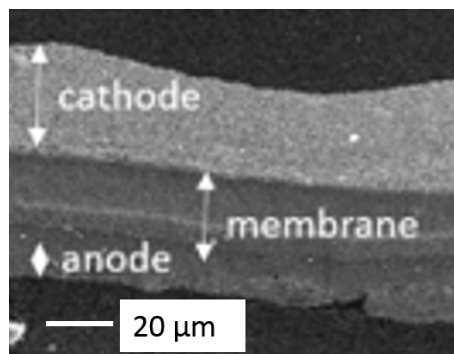


Figure 1.7: Scanning electron microscopy of a MEA (reprinted from [4])

other issues during their operating time. In order to improve the lifespan of the fuel cell, it is important to understand the several degradations it is subjected to.

1.4.1 Membrane degradations

As described before, the PEM separates the anode and the cathode of the fuel cell. At the same time, it allows the proton to flow from the anode to fuel the cathode. During operation especially in non-stationary applications, the PEM and the electrodes have to deal with variations of temperature, chemical environment and humidity. These local conditions changes, seen by membrane go through, affect the polymer. Chemical degradation also occurred by damaging the polymer backbone or the sulfonic acid groups by the formation of radicals. Two groups of radicals are at the origin of that degradation: peroxides and hydroperoxides. Both of them come from the two-electron pathway of the oxygen reduction reaction (ORR) [15, 16, 17]. These radicals attack the ionomer of the membrane diminishing its thickness locally even leading to its piercing [18]. The degradation may be quantified with the fluorine release rate (FRR) or the sulfur emission rate [19] (Figure 1.8).

Finally, the last failure and degradation of PEM is the mechanical one. When the PEMFC goes under temperature and humidity cycling, the membrane also cycles through phase of swelling and shrinking leading to expansion and contraction [20, 21, 22, 23, 24, 25, 26]. The stress results in apparition on several physical defects as cracks, tears, pinholes and punctures [27, 28, 29]. These defects leads to an increase of gases crossover favouring the formation of radical species in the case of oxygen crossover. These radicals are responsible of the chemical degradation and also the apparition of hot spots [30]. Figure 1.9 presents IR images obtained from cells in aged stacks. Preferential paths for hydrogen crossover are in red and represent the location of the degradations.

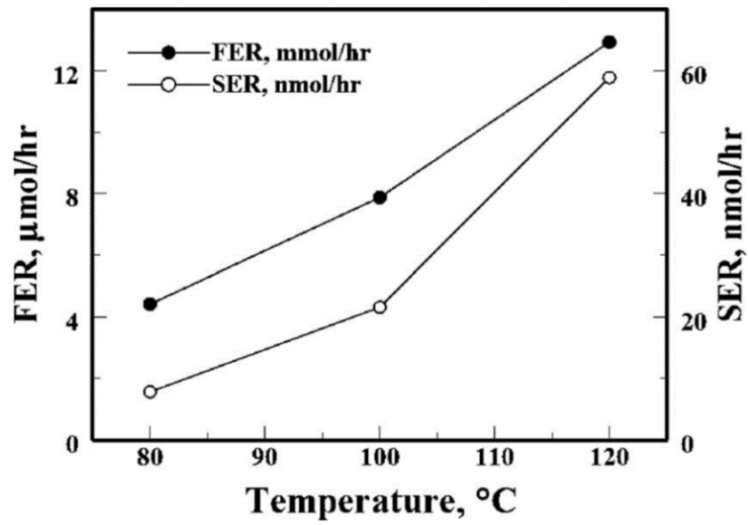


Figure 1.8: Total average fluorine and sulfur emission rates for a Nafion 112 membrane during OCV decay as a function of temperature (reprinted from [5])

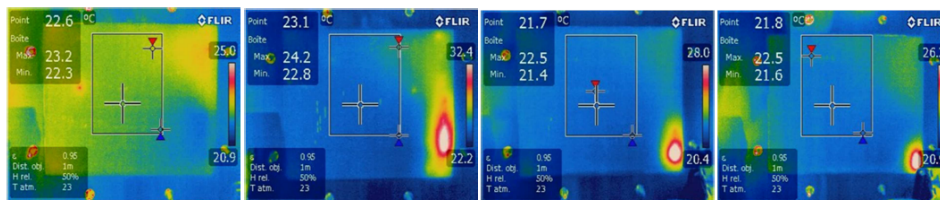


Figure 1.9: Infrared images of some aged MEA (reprinted from [2])

1.4.2 Degradation of Pt nanoparticles

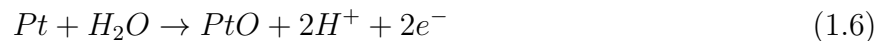
As electrochemical reactions take place on platinum catalyst nanoparticles in the fuel cell, degradation of the platinum has a significant impact on performance. Three major degradation mechanisms are identified:

- Dissolution of Pt and chemical reduction of Pt^{2+} inside the membrane through H_2 crossing from the anode to the cathode,
- Ostwald ripening, consisting in the dissolution of the smallest Pt particles redepositing onto larger ones,
- Pt nanoparticle detachment from the carbon support or the concurrent agglomeration and coalescence [31, 32].

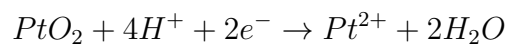
Numerous parameters affect the dissolution of the small Pt particles such as their size, the gaseous atmosphere, the temperature and the potential range and/or sweep rate defined by the PEMFC operating conditions [33, 34, 35, 36]. The first way is by a simple electrochemical oxidation step:



Another way is through a surface oxide of Pt which is dissolved in a 2nd reduction step:



or the surface oxide is electrochemically reduced [37]:



When PtO is electrochemically reduced, the dissolution of Pt is aggravated [38, 39, 40]. Ostwald ripening consists of a electrochemical redeposition of the Pt^{z+} ions onto larger Pt crystallites [33, 31, 34]. This mechanism reduces the surface Gibbs energy of the whole particles.

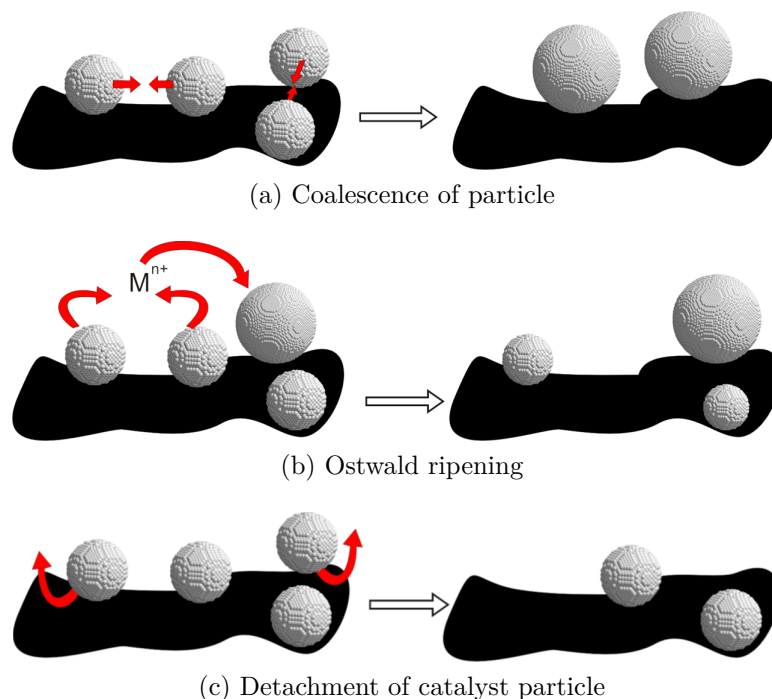


Figure 1.10: Schematics of Pt nanoparticles degradation mechanism reprinted from [6]

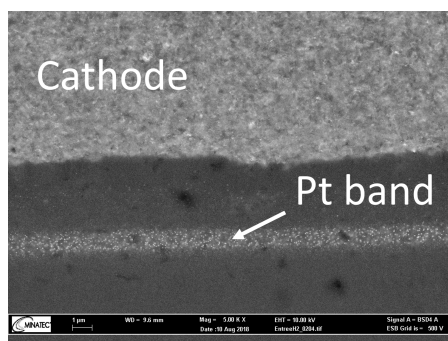


Figure 1.11: SEM image with an example of the formation of a Pt-band in the membrane

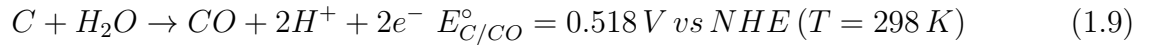
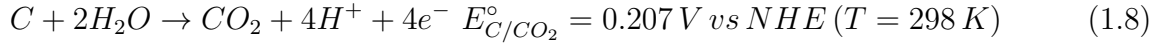
The particles under a critical radius disappear in favour of the largest one [41][42]. It is concomitant with the diffusion of these ions throughout the membrane which are reduced by the crossover gases forming a Pt band (as shown in Figure 1.11). Migration of nanocrystallites induces an agglomeration of catalyst particles on the carbon support. Mass fraction of Pt, pore size distribution and the specific surface of the carbon support affect the electrochemical catalyst specific area (ECSA) loss due to platinum agglomeration and coalescence [43].

1.4.3 Carbon support degradation

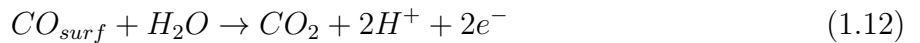
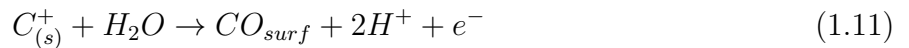
Binder [44], Kinoshita and Bett [45, 46, 47, 48] did the first studies during the 70s and the 80s on the degradation of carbon supports in fuel cells. Their researches were focused on PAFCs

that work at higher temperatures than PEMFC ($T > 423 K$). At the time, carbon corrosion was expected non significant in PEMFCs which later was proven wrong [49, 50].

Kinoshita et al [51] described the carbon oxidation reaction (COR) with a dual pathway mechanism. The first pathway is the direct one where carbon is oxidized into carbon monoxide and carbon dioxide. Carbon dioxide is mostly produced over carbon monoxide at $E > 0.9 V$ vs RHE [52]. This direct pathway is described by the two following reactions:



The second pathway happens by the formation of defects due to the oxidation of the carbon lattice (Equation 1.10). These defects designed as $C_{(s)}^+$ enable the formation of carbon surface oxides (Equation 1.11) that are ultimately oxidized into CO_2 (Equation 1.12):



Several works show that the kinetic of the COR are strongly dependent on the temperature, the potential, the structure, the surface properties and the morphology of the carbon materials [53, 54, 55, 56, 57, 10]. COR is also proven catalysed by the platinum deposited onto the carbon support. Wilsau et al. [52] use differential electrochemical mass spectroscopy to first described the phenomena. Carbon surface oxides which are close to the Pt nanoparticles may be adsorbed to surface of these particles (Equation 1.13). When the electrode potential rises sufficiently, these adsorbed CO are oxidized into CO_2 at around $0.8 V$ vs RHE (Equation 1.14) [50, 58, 57, 59, 60, 61, 62]:

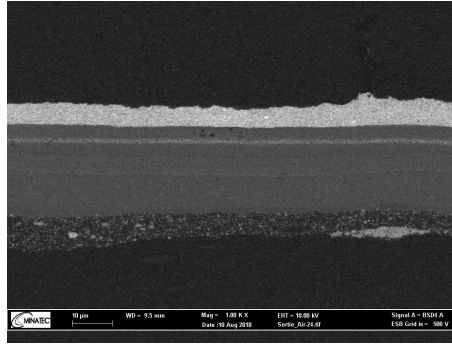
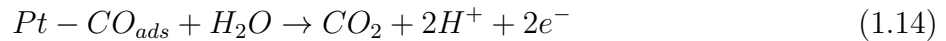


Figure 1.12: SEM image of corroded MEA after several startups



Accelerated stress tests demonstrated that this catalyse by the Pt nanoparticles is connected with the electrode potential [58, 61]. Linse and Ball showed that during voltage cycles, Pt nanoparticles and/or carbon surface groups are repeatedly oxidized and reduced [55, 61]. These constant reactions speed up the COR kinetics through the reactions described in Equation 1.13 and Equation 1.14. Furthermore, COR kinetics are strongly dependent on the structure of the carbon support. The more graphitized the carbon is, the less it is prone to COR [63, 53]. However, the correlation between COR kinetics and the structure of the carbon support involves a lot of parameters like, for example, hydrophilicity/phobicity or electrochemical activity for the ORR [56].

During the lifetime of a car, several thousands of starts and stops are expected. These startup and shutdown that are imposed on the fuel cell provoke heavy transient phases that cause severe degradation. The main degradation phenomena during these phases is the carbon support corrosion which count for 30% of the total degradation during the fuel cell lifetime (see section 3.1). The mechanism provoking the damage is the “reverse-current” mechanism and is described in chapter 3. First observable impact is a increase of electronic resistance and mass-transport losses at the cathode at a macro-scale [64, 65, 66, 67, 68, 69]. Furthermore, catalyst nanoparticles suffers from detachment, agglomeration and coalescence as described in previous sub-section which are observable at a nano-scale. These degradations implies an heterogeneous loss of ECSA (see Figure 3.42 b) [31, 33, 64].

Durst et al. [7] present an example of heterogeneity in corrosion between channel and rib.

The difference in thickness of the aged cathode between under a land and under a channel is 48% showing a significant impact which is shown in Figure 1.13. These heterogeneities highlights that the corrosion is more severe under the land than the channel.

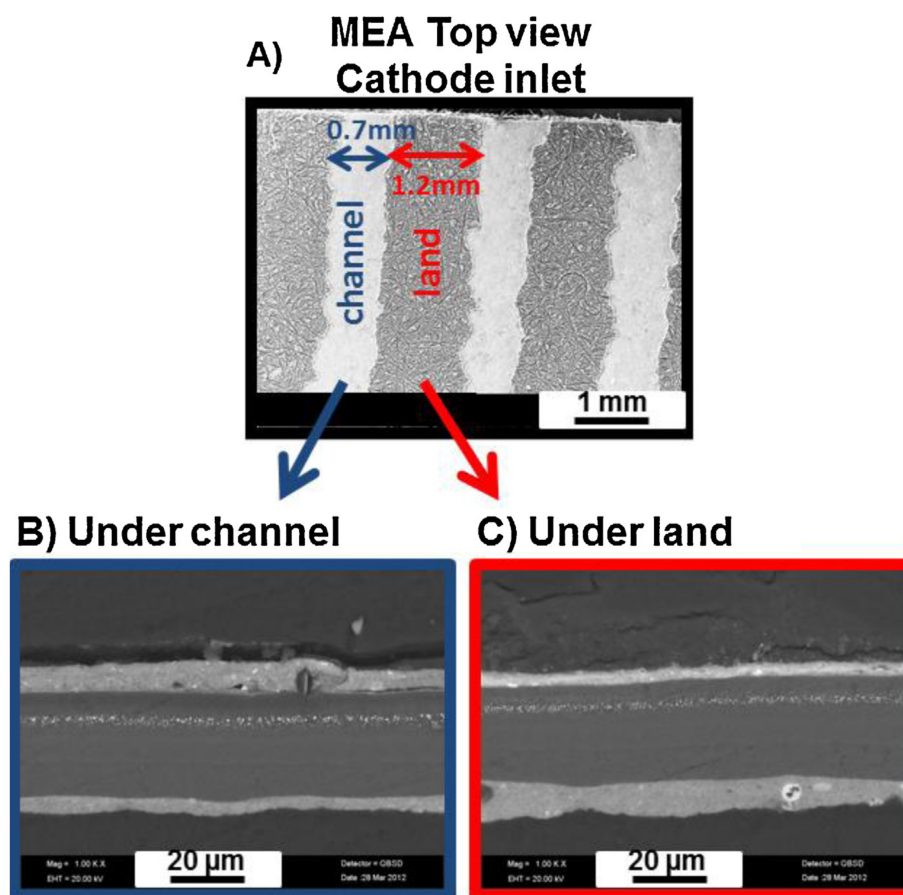


Figure 1.13: SEM images of top view aged MEA and cross sections under a channel and under a land (reprinted from [7])

1.5 Conclusion

PEMFC are considered as a serious alternative for transport application with several commercialised cars and also a functional train done by Alstom³. However this technology faces several obstructions to become a serious contender. At the scale of the cell, the two main axes of improvement are the cost and reliability. Despite substantial progress in durability, MEA has still a long way to go before reaching the expected goals for a global industrialization. In order to mitigate the degradations, numerous studies have been done to understand the mechanisms. As they are progressively grasped, an important optimization work has to be done to reach the targets. This is where numerical modelling shines by its ability to perform high number

³<https://www.alstom.com/fr/coradia-ilint-le-premier-train-hydrogene-au-monde>

of scenarios within a reasonable time and cost frame. Models have a high cost at first to be developed and implemented. Nevertheless, they allow to accomplish extensive studies. This work presents the development and implementation of degradation models especially carbon corrosion and the beginning of the optimization studies.

Modeling and simulation framework

Contents

2.1	Description of the performance model of PEMFC	26
2.1.1	MUSES platform and EuROPIUM code	26
2.1.2	Geometry and domains	27
2.1.3	Species transport modeling	28
2.1.4	Electrochemistry	35
2.1.5	Electronic transport	37
2.1.6	Ionic transport	37
2.1.7	Thermal	38
2.2	Local conditions distributions	41
2.2.1	Electrochemical model fitting	41
2.2.2	Oxygen depletion in the cathode channel	43
2.2.3	Relative humidity along the channel	46
2.3	Practical case : Design sensitivity	46
2.3.1	Design optimization of bipolar plates	46
2.3.2	Impact of operating conditions	54

Numerous models are currently developed and presented in the literature. OpenFCST is an open-source modelling software developed in C++ by M. Secanell [70]. OpenFCST propose a multi-dimensional analysis and design tool for PEMFC using finite element method. FC-Apollo which is a fork of the FAST Project¹ is developed within the foam-extend framework. Honda also performs multi-scale modelling for water content distribution [71] using a modified version of a simulation tool called “P-Stack” [72]. “openFuelCell” [73] is a project from multiple institutes. JRC is also developing its own 3D model. DLR developed a 2D transient multi-physics model inside their framework “NEOPARD-FC” [74]. Despite progress in HPC, the drawback of 3D models is computing times remain usually huge, which makes difficult to run an optimisation process. Furthermore, these means are not always available for fuel cell designers.

The different models described in this work are build within the CEA multi-physics simulation platform called MUSES. The goal is to create a simulation framework suited for modeling PEMFC at the MEA and cell scale in the first place. Furthermore, a fine discretisation is used to have a better understanding between local conditions and global performance. Finally, the simulation framework is also improved to do optimization allowing extensive parameter studies in a short amount of time.

2.1 Description of the performance model of PEMFC

2.1.1 MUSES platform and EuROPIUM code

MUSES is an acronym for Multi-Scale Simulation of Electrochemical Systems which is a platform dedicated to the multi-physics and multi-scale modeling and simulation of PEMFC, PEMWE and Li-ions Batteries. It focuses both on performance and durability aspects. The different models of the platform, from material to the system, are developed with a common material and physical database and a multi-scale methodology [1, 75, 76, 77, 3, 78, 79, 80, 81, 82].

At the smallest scale, EDMOND is a 0D double layer model. Based on a dynamic coupling between the kinetics of the various reaction steps and the local operating conditions, the local surface potential at the surface of the catalyst as well as the coverage of the various reaction intermediates is calculated [77].

At the largest scale, MePHYSTO (MultiPHYsical Simulation TOol) is a dynamic multi-physics model taking into account two phases flow and heat transport equations [81]. Knowing all the inputs: the current, temperature, and for both the inlet gases their relative humidity, stoichiometry, and pressure, the model gives the voltage. It is a 2D+0D fuel cell model, based on lumped bond graph approach taking into account gas diffusion, two phases flow, heat transfer and electrochemistry.

¹<https://www.fastsimulations.com/>

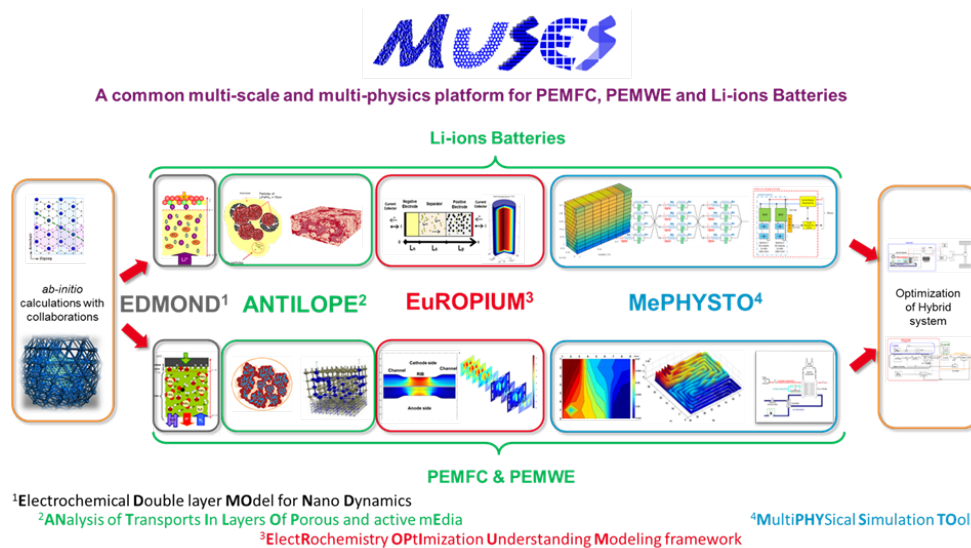


Figure 2.1: MUSES platform

The models used in this thesis have been developed within EuROPIUM (ElectRochemistry OPTimization Understanding Modeling), the modelling framework developed at CEA for solving coupled processes at the MEA and cell level which are relevant for PEMFC performance [82]:

- Proton transport, water transport and gas permeation in the membrane,
- Electrochemical reactions, transports in porous media in the catalyst layers,
- Multi-component gases transport in porous media for the GDL/MPL and active layers,
- Coupling of free flow with porous media flow in the channels.

The models are developed to be solved within the COMSOL® Multiphysics software. Two 2D-models are developed, along the channel and through-plane direction (see Figure 2.2). The model is used to monitor these local conditions, which are not reachable by experiments.

2.1.2 Geometry and domains

In this section, the 2D-models of a single PEM fuel cell are presented. Figure 2.2 shows the two entire geometries of the 2D-models. The Figure 2.2.a on the left represents the fuel cell along the channel while the Figure 2.2.b shows a cross section of the channel and rib design. Figure 2.2 reveals the details of the different domains of the MEA modelled. Domain's names are in bold and boundary's names are in *italic*. In each domain, the physics that are solved as well as the different governing equations will be described in the subsequent section (Table 2.1).

Seven to nine layers are taken into account as function of the model : membrane, catalyst layers, microporous layers, gas diffusion layers and gas channels or bipolar plates. The gases are composed of O_2 , N_2 , vapour at the cathode and H_2 , N_2 and vapour at the anode.

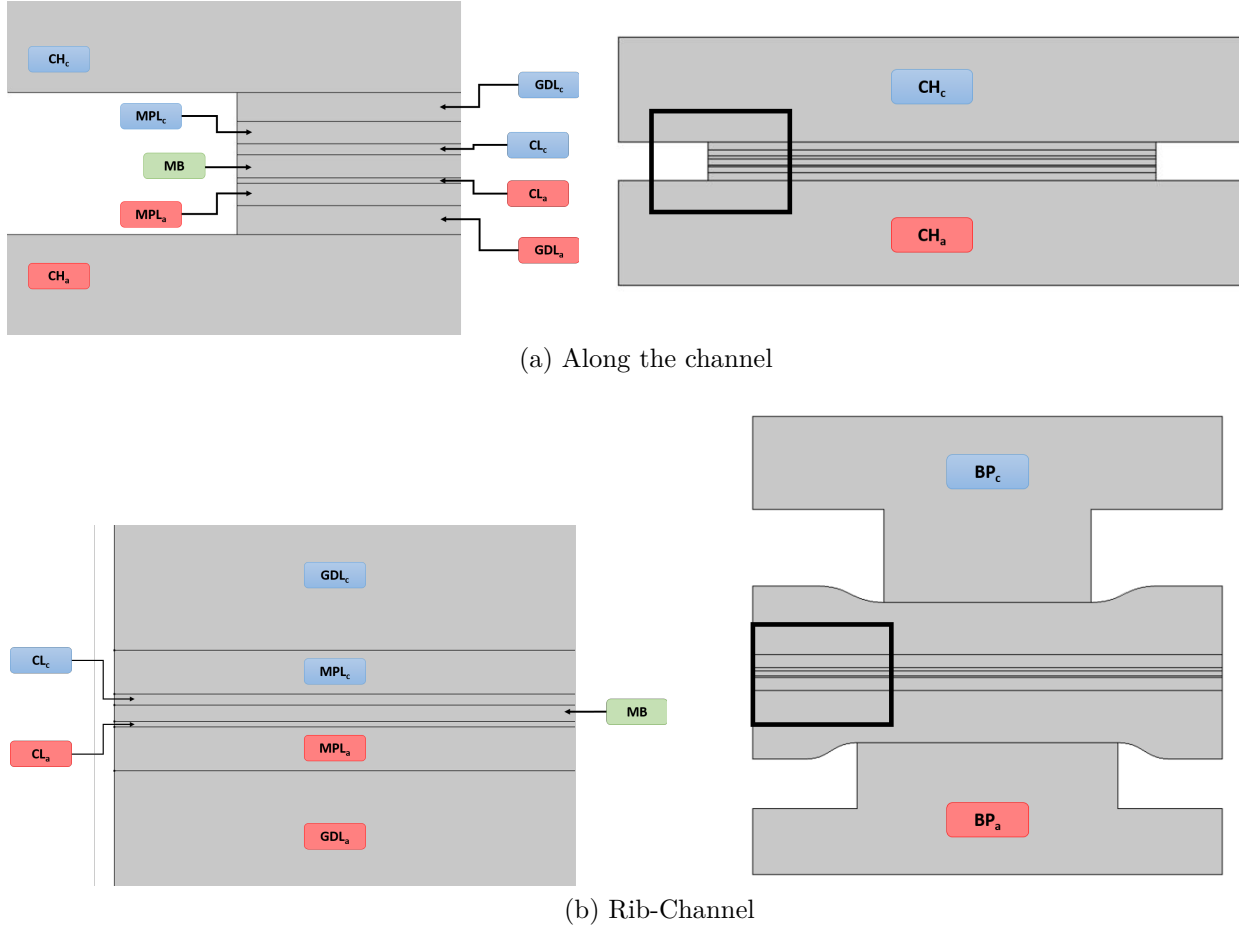


Figure 2.2: 2D models of a single PEMFC (BP: Bipolar Plate, CH: Gas Channel, GDL: Gas Diffusion Layer, MPL: Microporous Layer, CL: Catalyst Layer, MB: Membrane)

2.1.3 Species transport modeling

2.1.3.1 In the channels

In the channels, gas convection is described by the Navier-Stokes equation. As multi component diffusion occurs, two different velocities have to be distinguished as proposed by Brenner [83]: \vec{u} is the mass-based average velocity vector and \vec{U} the volume (or molar) average velocity vector. Indeed, because the diffusion implies the movement of species with different molar masses, the two velocities are different. They are linked by the diffusive fluxes:

$$\vec{U} = \vec{u} - \frac{\sum_i M_i \vec{N}_i^d}{\rho_g} \quad (2.1)$$

Where ρ_g is the density of the gas, M_i the molar mass of the specie and \vec{N}_i^d the diffusive flux of the specie (see Equation 2.5 and Equation 2.6). So Navier-Stokes with Newtonian fluid

hypothesis is written as a momentum balance:

$$\rho_g \left(\frac{\partial \vec{u}}{\partial t} + (\vec{u} \cdot \vec{\nabla}) \vec{u} + M_v S_{cond} \vec{u} \right) = -\vec{\nabla} p + \nabla \cdot \left(\mu_g \left(\nabla \vec{U} + (\nabla \vec{U})^T \right) - \frac{2}{3} \mu_g (\nabla \cdot \vec{U}) I \right) \quad (2.2)$$

Where S_{cond} is the condensation source term of the vapour, p the relative pressure, μ_g the dynamic viscosity of the gas mixture, I is identity matrix. The left side of the equation is the continuum part based on the Cauchy momentum equation that describes acceleration as function of a sum of body forces for a molecule thus the mass-based average velocity \vec{u} . The right side of the equation contains the stress tensor part which represents deformation on a continuum body thus the non-molecular volume average velocity vector \vec{U} [83]. The overall molar balance for the gas phase is written:

$$\frac{\partial c_g}{\partial t} + \nabla \cdot (c_g \vec{U}) = \sum_i S_i$$

$$\text{where in the channels } S_i = S_{cond} \text{ for the vapor,} \quad (2.3)$$

$$S_i = 0 \text{ for the other gases}$$

c_g is the total concentration of gases. At the channel GDL interface, the porous media is considered as a continuous media. Continuity of flux is written with $\vec{U} = \frac{\sum N_i^{GDL}}{c_g}$ where $\overline{N_i^{GDL}}$ is the total molar flux in the GDL of specie i . Moreover, inlet velocity is calculated as function of the stoichiometry and the current expected by the fuel cell to be delivered. Liquid water is taken into account considering condensation in the vapour mass balance as a term source. The mass balance for each component minus one (as the total is already computed in Equation 2.3) is computed:

$$\frac{\partial c_i}{\partial t} + \nabla \cdot (\overline{N_i^d} + c_i \vec{U}) = S_i \quad (2.4)$$

Where c_i is the concentration of specie i . Note that diffusion fluxes $\overline{N_i^d}$ are evaluated by the resolution of the Stefan-Maxwell equations [84, 85]:

$$c_g \vec{\nabla} X_i = \sum_{j \neq i} \frac{X_i \overline{N_j^d} - X_j \overline{N_i^d}}{D_{i,j}} \quad (2.5)$$

coupled with the definition of diffusion defined in [86]:

$$\sum_i \vec{N}_i^d = 0 \quad (2.6)$$

Binary diffusion coefficient $D_{i,j}$ can be found in Table 2.2. At the inlets, the molar fractions are imposed:

$$X_i = X_i^0 \quad (2.7)$$

Finally, at the channel/GDL interface, the continuity of flux is assumed for each species:

$$\left(\vec{N}_i^d + c_i \vec{U} \right) - \vec{N}_i^{GDL} = 0 \quad (2.8)$$

$\vec{N}_i^d + c_i \vec{U}$ is the sum of the diffusive flux and the convection flux on the channel side and \vec{N}_i^{GDL} is total flux on GDL side (see subsection 2.1.3.2).

2.1.3.2 In the porous media

A continuous approach is used for the porous media and physics are modified for each layer through parameters like porosity and tortuosity to account for their specifications. Each layer is considered as a continuous medium and its specificities are described by its effective transport parameters taking into account the porosity (ϵ) and tortuosity (τ). The porosity in the GDL is modified as function of the GDL thickness to model the crushing effect by the rib on the GDL:

$$\epsilon_{GDL} = 1 - \frac{(e_{GDL}^{max} \cdot (1 - \epsilon_{GDL}^{ns}))}{e_{GDL}} \quad (2.9)$$

where e_{GDL}^{max} is the maximum thickness of the GDL (under the channel), ϵ_{GDL}^{ns} is the porosity of the GDL non squished and e_{GDL} the thickness of the GDL. The conductivities (electronic and thermal) in the GDL are also modified by the crushing effect interpolating the values between the non squished value and the squished one:

$$x_{GDL} = \frac{(x_{GDL}^{max} - x_{GDL}^{min}) \cdot (e_{GDL}^{max} - e_{GDL})}{(e_{GDL}^{max} - e_{GDL}^{min})} + x_{GDL}^{min} \quad (2.10)$$

Where x_{GDL} is the thermal or electronic conductivity (in plane or through plane) in the

GDL and e_{GDL}^{min} the minimum thickness of the GDL. By this mean, the complex geometry of the porous diffusion layers is accounted and the governing equations are modified accordingly. Correlations and values used in the simulations can be found in Table 2.2.

The situation in the porous media is more complex because Darcy [87] and Knudsen [88] effects have to be taken into account. The approach proposed by Young and Todd has been implemented [86]. The constitutive equations of the model are similar to Stefan-Maxwell, but include also convection and Knudsen diffusion [88]. For (n-1) species:

$$\frac{c_g \cdot \epsilon}{\tau^2} \cdot \vec{\nabla} X_i = \sum_j \left[\frac{X_i \cdot \vec{N}_j}{(D_A)_{ji}} - \frac{X_j \cdot \vec{N}_i}{(D_A)_{ij}} \right] \quad (2.11)$$

where ϵ is the porosity, τ the tortuosity and \vec{N}_i the total molar flux of specie i . The model allows to mathematically interpolate what happen between two limit cases of pure gaseous diffusion and Knudsen diffusion by defining mean transport properties using the Bosanquet equation [89]:

$$\frac{1}{(D_A)_{ij}} = \frac{1}{D_{ij}} + \frac{1}{D_i^k} \quad (2.12)$$

where Knudsen diffusion coefficients are calculated according to:

$$D_i^k = \left(\frac{2}{3} \cdot R_p \cdot \sqrt{\left(\frac{8 \cdot R \cdot T}{\pi \cdot M_i} \right)} \right) \quad (2.13)$$

R_p being the pore radius. The overall convection component in the MEA is given by:

$$\frac{\epsilon}{\tau^2} \cdot \vec{\nabla} P_g = -A_C \sum_i \sqrt{M_i} \cdot \vec{N}_i \quad (2.14)$$

where P_g is the total pressure of gases. Compared to the original formulation proposed by Young and Todd [86], the expression of the convection coefficient A_C has been modified to depend on permeability (κ) instead of pore radius:

$$A_C = \frac{\mu}{c_g \cdot \kappa \cdot \sum_i x_i \sqrt{M_i}} \quad (2.15)$$

Where μ is the dynamic viscosity and x_i is the mass fraction of specie i . Whilst, A_K stands for the convection due to Knudsen diffusion and is defined as:

$$A_K = \frac{3}{4 \cdot R_p} \cdot \sqrt{\left(\frac{\pi \cdot R \cdot T}{2} \right)} \quad (2.16)$$

Finally from Equation 2.15 and Equation 2.16, the coefficient A_A is defined as follows:

$$\frac{1}{A_A} = \frac{1}{A_C} + \frac{1}{A_K} \quad (2.17)$$

The mass balance is computed for each species:

$$\begin{aligned} \epsilon \frac{\partial c_i}{\partial t} &= \nabla \cdot \vec{N}_i + S_i \\ S_i &= S_{vap}^d + S_{cond} \text{ for the vapour} \\ S_i &= S_i^a \text{ for the other gases} \end{aligned} \quad (2.18)$$

Where S_{vap}^d is the water adsorbed by the ionomer in the CL and S_i^a the gas dissolution rate and diffusion in the ionomer of the CL (see Equation 2.23 and Figure 2.3). At the Channel/GDL interface, continuity of concentrations is considered:

$$c_i^{CH} = c_i^{GDL} \quad (2.19)$$

where c_i^{CH} and c_i^{GDL} is the value of c_i respectively in the channels and in the GDL. Otherwise no flux is assumed, either because of symmetry or because of insulation:

$$\vec{N}_i \cdot \vec{n} = 0 \quad (2.20)$$

2.1.3.3 In the electrolyte phase

The membrane is the separator as well as the electrolyte which also appears in the two catalyst layers. Hydrogen diffusion takes place through the anodic catalyst layer and through the membrane (see Figure 2.3). Hydrogen crossover is included in the model (see Equation 2.30) (for example to evaluate the OCV). Transport of dissolved oxygen is solved only in the cathodic catalyst layer, as its effect on the crossover current can be assumed to be negligible.

Each species balance equation follows these relation:

$$(1 - \epsilon) \epsilon_{ionomer} \frac{\partial C_i}{\partial t} = -\nabla \cdot (\vec{N}_i^a) + S_i^a + S_i \quad (2.21)$$

where S_i^a is the diffusion flux through the ionomer's film and S_i the source terms coming from the electrochemical reactions at the Pt surface. For diffusion of dissolved gases, flux \vec{N}_i^a is calculated by considering a Fick's law (D_i^a values can be found in Table 2.2) while the water

flux has two components, an electro-osmosis flux and a diffusion flux:

$$\begin{aligned} \vec{N}_i^a &= -D_i^a \vec{\nabla}(C_i) \\ \vec{N}_{H_2O}^a &= n_d \frac{\vec{i}_i}{F} - D_w \vec{\nabla}(C_{H_2O}) \end{aligned} \quad (2.22)$$

where \vec{i}_i is the ionic current density and n_d the electro-osmotic drag coefficient [90] (see Table 2.2).

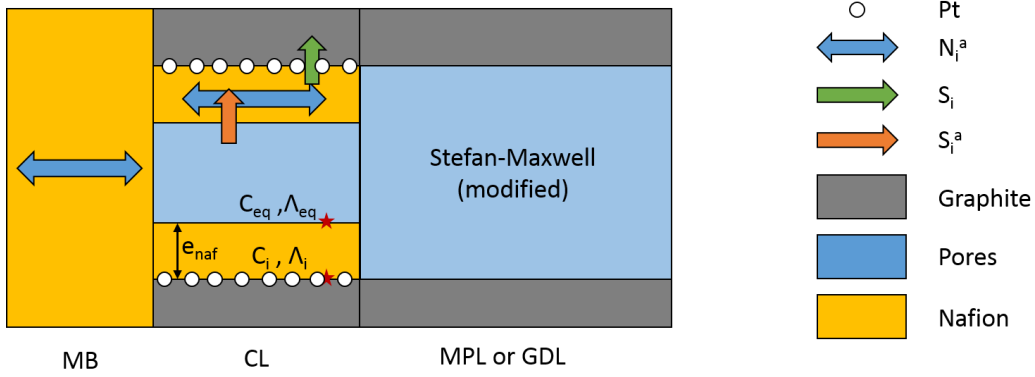


Figure 2.3: Simplified agglomerate source terms model

The agglomerate thickness (e_{naf}) is not discretized so diffusion through the ionomer layer is modelled as a source terms as described in Figure 2.3. The source term S_i^a (S_{vap}^d for the water) estimates the diffusion flux through the Nafion's film:

$$\begin{aligned} S_i^a &= \frac{D_i^a \cdot a_v}{e_{ionomer}} (C_i^{eq} - C_i) \text{ in CL} \\ S_i^a &= 0 \text{ in MB} \end{aligned} \quad (2.23)$$

where a_v is the specific surface. An equilibrium is assumed at the electrolyte/porous media interface between the gases in the porous phase and the gases dissolved in the electrolyte (C_i^{eq}). This equilibrium is formulated as [91, 92]:

$$C_i^{eq} = P_i H_i \quad (2.24)$$

where H_i is the Henry's constant and P_i is the partial pressure of the specie i . For the equality of chemical potential at the equilibrium between gas and dissolved specie, dissolved species activity in ionomer is written taking into account the previously defined H_i constant:

$$a_i = \frac{H_i \cdot c_i}{P^\circ}$$

$$a_{H_2O} = \frac{P_{vap}}{P_{sat}(T)} \quad (2.25)$$

where $P_{vap} = c_{vap}RT$ and P° is the standard pressure. The water concentration in the ionomer is defined by:

$$C_{H_2O} = \lambda \cdot C_{SO_3^-} \quad (2.26)$$

at the interface between the pore and the agglomerate, the equilibrium concentration is estimated at the ionomer/pore by [93]:

$$\lambda_{eq}(a_{H_2O}) = 0.043 + 17.81a_{H_2O} - 39.85a_{H_2O}^2 + 36a_{H_2O}^3 \quad (2.27)$$

The thickness of the ionomer can be evaluated from the specific surface and the Nafion content:

$$e_{ionomer} = \frac{(1 - \epsilon) \epsilon_{ionomer}}{a_v} \quad (2.28)$$

The source terms S_i are:

$$S_{H_2} = -\frac{J_r}{2F} \text{ for the anode CL}$$

$$S_{H_2O} = 0 \text{ for the anode CL}$$

$$S_{O_2} = \frac{J_r + J_p}{4F} \text{ for the cathode CL}$$

$$S_{H_2O} = -\frac{J_r + J_p}{2F} \text{ for the cathode CL}$$

where a_{H_2O} is the activity of water at interface defined in Equation 2.25. The crossover of hydrogen to the cathodic catalyst layer give us a permeation current which is spread uniformly over the catalyst layer thickness. The permeation current density at the cathode is estimated from the H_2 flux $\overrightarrow{N_{H_2}^a}$ reaching the cathode interface:

$$\begin{aligned}
 J_p &= 0 \text{ for the anode CL} \\
 J_p &= \frac{\overrightarrow{N_{H_2}^a} \cdot 2 \cdot F}{e_{CL_c}} \cdot \overrightarrow{n} \text{ for the cathode CL}
 \end{aligned}
 \tag{2.29}$$

where e_{CL_c} is the thickness of the cathodic catalyst layer. Otherwise, dissolved species stays in the electrolyte phase so no flux is assumed:

$$\overrightarrow{N}_i^a \cdot \overrightarrow{n} = 0
 \tag{2.30}$$

2.1.4 Electrochemistry

The local electrochemical response is computed by the oxygen reduction reaction at the cathode electrode and the hydrogen oxidation reaction at the anode electrode. For the general electrode's reaction $\sum_j \nu_j \cdot M_j^{z_j} \xrightleftharpoons[\text{red}]{\text{ox}} n \cdot e^-$ (z_j and ν_j are the charge and the stoichiometry coefficient of the specie M_j respectively), the Butler-Volmer's relation is written [94, 1] in order to estimate the current density:

$$j_r = j_0 \cdot \left[\exp\left(\frac{\alpha \cdot n \cdot F}{R \cdot T} \cdot \eta\right) - \exp\left(\frac{-(1 - \alpha) \cdot n \cdot F}{R \cdot T} \cdot \eta\right) \right]
 \tag{2.31}$$

$$J_r = a_v \cdot j_r
 \tag{2.32}$$

where η is the overpotential, α and $1 - \alpha$ are the symmetry factors of the reaction and a_v is the specific surface area of platinum. j_0 is the exchange current density that depends on the reaction kinetics and local species activities:

$$j_0 = n \cdot F \cdot (k_{ox}^0)^{1-\alpha} \cdot (k_{red}^0)^\alpha \cdot \left(\prod_{\nu_j > 0} (a_j^{\nu_j}) \right)^{1-\alpha} \left(\prod_{\nu_j < 0} (a_j^{-\nu_j}) \right)^\alpha
 \tag{2.33}$$

where a_j is the activity of the specie (see Equation 2.25) and $k_{ox/red}^0$ are the reaction rate coefficients, which depend on activation free enthalpies (which are not the same as the reaction free enthalpies ΔG°):

$$k_{ox}^0 = k^0 \exp\left(\frac{\Delta G_{ox}^\ddagger}{RT}\right) \quad (2.34)$$

$$k_{red}^0 = k^0 \exp\left(\frac{\Delta G_{red}^\ddagger}{RT}\right)$$

the constant k^0 is given by the Eyring equation :

$$k^0 = \frac{k_b T}{s_0 N_A h} \quad (2.35)$$

where k_b is the Boltzmann constant, h the Planck constant, s_0 the average Pt surface per reaction site and N_A the Avogadro constant . As k_{ox}^0 and k_{red}^0 describe the reaction rate on the Pt surface, the Eyring equation is adapted from the reaction rate from one site to the Pt surface using s_0 and the Avogadro constant. As shown in Figure 2.4, the activation free enthalpies can be defined from the activation enthalpies and activation entropies:

$$\Delta G_{ox}^\ddagger = \Delta H_{ox}^\ddagger - T \cdot \Delta S_{ox}^\ddagger$$

$$\Delta G_{red}^\ddagger = \Delta G_{ox}^\ddagger + \Delta G^\circ \quad (2.36)$$

The overpotential η is the difference between the electrode and ionic potentials ($\Psi - \Phi$):

$$\eta = (\Psi - \Phi) - E \quad (2.37)$$

and E being the standard potential that depends on temperature, pressure and concentrations according to the Nernst's law:

$$E = -\frac{\Delta G^\circ}{n \cdot F} + \frac{R \cdot T}{n \cdot F} \cdot \log\left(\prod_{v_j} a_j^{v_j}\right) \quad (2.38)$$

where ΔG° is the reaction free enthalpy:

$$\Delta G^\circ = \Delta H^\circ - T \Delta S^\circ \quad (2.39)$$

To determine ΔG° , values derived from Lampinen and Formino [95] are used and described in Table 2.2.

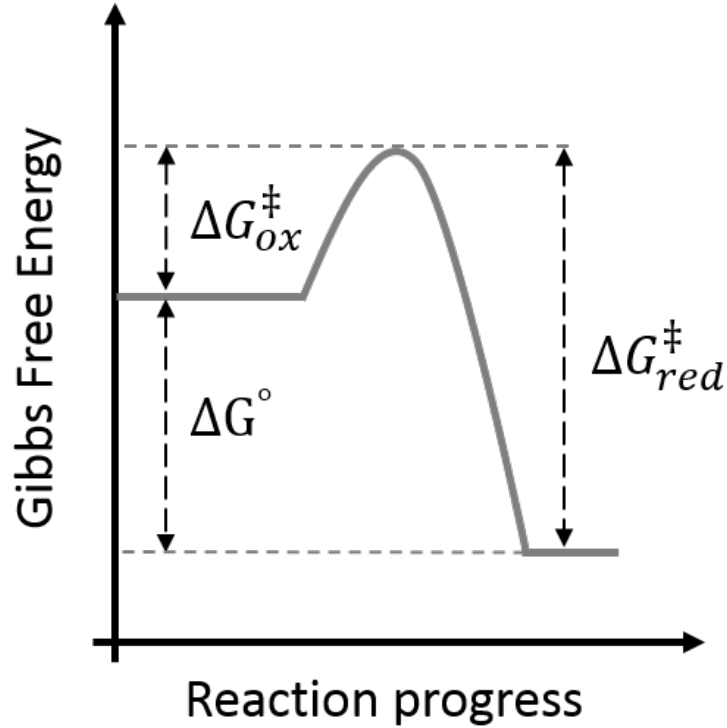


Figure 2.4: Schematics of activation free enthalpies and free enthalpy of reaction

2.1.5 Electronic transport

The electronic potential distribution is computed in the GDL, MPL and CL and BP.

Charge conservation equation in each domain is written by using the Ohm's law as the following:

$$\nabla \cdot \vec{i}_e = -\nabla \cdot (\sigma_e \cdot \vec{\nabla} \Psi) = S_e \quad (2.40)$$

where i_e is the electronic current, σ_e the electronic conductivity and S_e the source term. In the GDL and the MPL there is no production/consumption of electronic current whereas in the catalyst layers, there are the current from the reaction but also the permeation current which gives these source terms:

$$\begin{aligned} S_e &= 0 \text{ in the GDL and MPL} \\ S_e &= J_r - J_p \text{ in the CL} \end{aligned} \quad (2.41)$$

2.1.6 Ionic transport

The ionic potential distribution is computed in the CL and membrane. Only protons flow in the membrane as well as the Nafion phase of the catalyst layer.

The ionic potential is given by the following equation :

$$\nabla \cdot \vec{i}_i = -\nabla \cdot (\sigma_i \cdot \vec{\nabla} \Phi) = S_i \quad (2.42)$$

where i_i is the ionic current and σ_i the ionic conductivity. In the membrane there is no production/consumption of ionic current while in the catalyst layers, the source term is the opposite of the electronic current:

$$\begin{aligned} S_i &= 0 \text{ in the MB} \\ S_i &= -J_r + J_p \text{ in the CL} \end{aligned} \quad (2.43)$$

Ionic conductivity of the membrane depends of its water content [96] and in the catalyst layer, an effective conductivity can be defined as a function of the porosity and the tortuosity:

$$\sigma_i = \frac{(1 - \epsilon) \cdot \epsilon_{ionomer}}{\tau^2} \cdot \sigma_{i,m} \quad (2.44)$$

where $\sigma_{i,m}$ is the ionic conductivity of the Nafion (see Table 2.2). At any location in the catalyst layer, the total current i is defined as the sum of electron current flowing in the carbon (electronic current) and of current flowing in the Nafion (ionic current).

2.1.7 Thermal

The heat balance equation in solid media is taken into account in the current implementation:

$$\rho C_p \frac{\partial T}{\partial t} + \nabla \cdot (-k \vec{\nabla} T) = \sum Q \quad (2.45)$$

Where C_p is the heat capacity, k the thermal conductivity and Q a source term. The source term depends on the domain. For now the heat convected by the gases is neglected in the model. The sum of electrical energy (W_{e-}) and heat (Q_{reac}) powers produced by the reactions at each catalyst layer is given by:

$$\frac{\Delta H_{a/c}^\circ}{nF} J_r = W_{e-} + Q_{reac} \quad (2.46)$$

where ΔH_a° is the enthalpy of the hydrogen oxidation reaction, ΔH_c° the enthalpy of the oxygen (water) oxidation reaction and $W_{e-} = (\Phi - \Psi) \cdot J_r$ the local electric energy produced in the catalyst layer. The local heat source terms for the reactions in the catalyst layers are then

expressed as:

$$Q_{reac} = ((\Psi - \Phi) + \frac{\Delta H_{a/c}^\circ}{nF}) \cdot J_r \quad (2.47)$$

Permeation current also produce heat at the cathode side only:

$$Q_{perm} = -\frac{\Delta H_a^\circ + \Delta H_c^\circ}{nF} \cdot J_p \quad (2.48)$$

The other local heat source terms are Joule heating source terms in each domain:

$$Q_j = \frac{i^2}{\sigma_j} \quad (2.49)$$

At the BP/GDL interface, the temperature is fixed to:

$$T = T_0 \quad (2.50)$$

Otherwise, the cell is supposed thermally insulated and no thermal flux is assumed:

$$-k \vec{\nabla} T = \vec{0} \quad (2.51)$$

Table 2.1: Physics and domain affectations

	CH	GDL	MPL	CL	MB	BP
Navier-Stokes	X					
Diffusion	X	X	X	X	X	
Ionic Transport				X	X	
Electric Transport		X	X	X		X
Electrochemistry				X		
Thermal		X	X	X	X	

a : anode
c : cathode

Table 2.2: Correlations and values used in the model

Symbol	Expression	References
H_{O_2} [Pa·m ³ /K]	$\frac{c_0}{P_0} \cdot \exp\left(\frac{5.88 \cdot 10^3}{R \cdot T}\right)$	[92]
H_{H_2} [Pa·m ³ /K]	$\frac{c_0}{P_0} \cdot \exp\left(\frac{9.05 \cdot 10^3}{R \cdot T}\right)$	[92]
$D_{H_2}^a$	$4.1 \cdot 10^{-7} \exp\left(-\frac{2602}{T}\right)$	[97]
$D_{O_2}^a$	$3.1 \cdot 10^{-7} \exp\left(-\frac{2768}{T}\right)$	[97]
$D_{N_2}^a$	$4.24 \cdot 10^{-6} \exp\left(-\frac{2246}{T}\right)$	[97]
D_w	$(6.707 \cdot 10^{-8} \Lambda + 6.387 \cdot 10^{-7}) \cdot \exp\left(-\frac{2416}{T}\right)$	[1][98]
n_d	$1.0 + 0.0028\Lambda + 0.0026\Lambda^2$	[90]
$\sigma_{i,m}$ [S/m]	$\epsilon^{3/2}(0.5139 \cdot \Lambda_{eq} - 0.326) \cdot \exp\left(1268 \cdot \left(\frac{1}{303} - \frac{1}{T}\right)\right)$	[96]
$D_{O_2-H_2O}$ [m ² /s]	$(4.27 \cdot 10^{-6}) \frac{T^{2.334}}{P}$	[99]
$D_{N_2-O_2}$ [m ² /s]	$(6.34 \cdot 10^{-5}) \frac{T^{1.823}}{P}$	[99]
$D_{N_2-H_2O}$ [m ² /s]	$(4.46 \cdot 10^{-6}) \frac{T^{2.334}}{P}$	[99]
$D_{H_2-H_2O}$ [m ² /s]	$(2.16 \cdot 10^{-6}) \frac{T^{2.334}}{P}$	[99]
$D_{H_2-N_2}$ [m ² /s]	$(2.46 \cdot 10^{-4}) \frac{T^{1.823}}{P}$	[99]
$D_{H_2-O_2}$ [m ² /s]	$(2.53 \cdot 10^{-4}) \frac{T^{1.823}}{P}$	[99]
ΔH_c° [kJ/mol]	-285.8	[95]
ΔH_a° [kJ/mol]	0	[95]
ΔS_c° [J/mol/K]	-163.18	[95]
ΔS_a° [J/mol/K]	-0.104	[95]

Table 2.3: Geometric parameters

Geometric parameters	Anode			Cathode		
σ^{BP} [S/m]	1.20 · 10 ⁶ [100]			1.20 · 10 ⁶ [100]		
	GDL	MPL	CL	GDL	MPL	CL
ϵ^{ns} (non squished)	0.72	1	0.47	0.72	1	0.47
ϵ^s (squished)	0.63	1	0.47	0.63	1	0.47
$\tau_{in-plane}$	1.1442	1	1.5	1.1442	1	1.3
$\tau_{through-plane}$	3	1	1.5	3	1	1.3
R_p [m]	1 · 10 ⁻⁵	1 · 10 ⁻⁶	1 · 10 ⁻⁸	1 · 10 ⁻⁵	1 · 10 ⁻⁶	1 · 10 ⁻⁸
$\kappa_{in-plane}$ [m ²]	5.8 · 10 ⁻¹²	1 · 10 ⁻¹²	1 · 10 ⁻¹²	5.8 · 10 ⁻¹²	1 · 10 ⁻¹²	1 · 10 ⁻¹²
$\kappa_{through-plane}$ [m ²]	4.2 · 10 ⁻¹²	1 · 10 ⁻¹²	1 · 10 ⁻¹²	4.2 · 10 ⁻¹²	1 · 10 ⁻¹²	1 · 10 ⁻¹²
$\sigma_{in-plane}$ (non squished) [S/m]	5660	1000	20	5660	1000	20
$\sigma_{in-plane}$ (squished) [S/m]	9230	1000	20	9230	1000	20
$\sigma_{through-plane}$ (non squished) [S/m]	23	200	20	23	200	20

Table 2.3: Geometric parameters

$\sigma_{through-plane}(\text{squished})$ [S/m]	107	200	20	107	200	20
$\lambda_{in-plane}(\text{non squished})$ [W/m/K]	86.87	10	3	86.87	10	3
$\lambda_{in-plane}(\text{squished})$ [W/m/K]	51.4	10	3	51.4	10	3
$\lambda_{through-plane}(\text{non squished})$ [W/m/K]	0.35	10	3	0.35	10	3
$\lambda_{through-plane}(\text{squished})$ [W/m/K]	0.60	10	3	0.60	10	3
Contact angle [deg]	115	105	95	115	105	95
C_p [J/kg/K]	708	708	708	708	708	708
a_v [m ² /m ³]			$1.67 \cdot 10^7$			$1.67 \cdot 10^7$
ρ_{sol} [kg/m ³]	2250	2250	2250	2250	2250	2250
τ^{Nafion}			1			1
C_p^{Nafion} [J/kg/K]			1046			1046
$\epsilon_{ionomer}$			0.2			0.2
	MB					
λ^{MB} [W/m/K]	0.186					

2.2 Local conditions distributions

2.2.1 Electrochemical model fitting

In order to use the model to study local conditions distributions, it is necessary to validate the model. Four parameters are used to fit the electrochemical response. The first one is the enthalpy of formation of the activated complex of the cathode ΔH_{ox-c}^\ddagger . The reduction activation enthalpy is then defined through Equation 2.36. It is the reason that only the oxidation has to be fitted. At the anode, the activation enthalpy is set to limit the overpotential under 50 mV. The second parameter which is fitted is the factor of symmetry α involved in the reaction kinetics in Equation 2.31. The last two are the ionic conductivity of the membrane $\sigma_{i,m}$ and the diffusion coefficient of the hydrogen in the Nafion $D_{H_2}^a$ (which impacts the H_2 permeation and so the OCV). These two are fitted by a correction factor respectively called σ_{corr} and D_{corr}^a . Each fitted parameters can not deviate too extremely for its initial value in order to avoid spurious values. For the enthalpy of formation the limit is 5%. For the factor of symmetry it is an absolute deviation of 0.1 and for the other parameters it is a factor of two. The fitting is obtained by minimizing the area between the experimental polarization curve and the computed one using

trapezoidal method.

The fitting procedure was implemented in two cases (Figure 2.5). The first case is a CEA fuel cell and the second one is the fuel cell used in AutoStack-CORE where the operating conditions are described in Table 2.4.

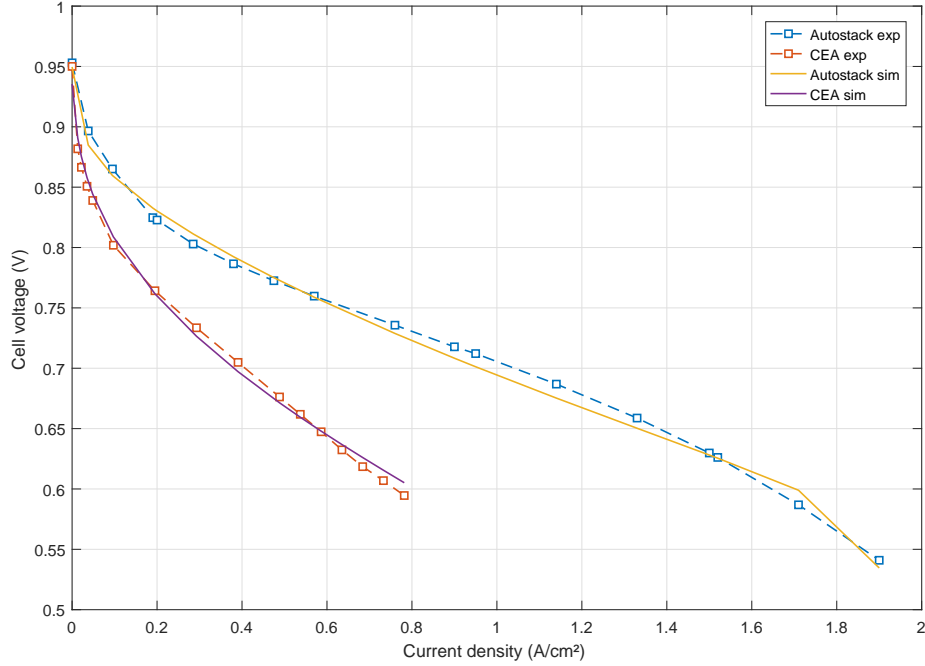


Figure 2.5: Experimental and fitted polarization curves

Operating conditions	CEA reference conditions [80]	AutoStack-CORE
Anode channel inlet pressure [Pa]	$1.5 \cdot 10^5$	$2.35 \cdot 10^5$
Cathode channel inlet pressure [Pa]	$1.5 \cdot 10^5$	$2.35 \cdot 10^5$
Anode rib/channel temperature [K]	351	341
Cathode rib/channel temperature [K]	351	341
Anode channel relative humidity [%]	50	40
Cathode channel relative humidity [%]	50	50
Anode inlet channel hydrogen molar fraction	1	0.7
Cathode inlet channel oxygen molar fraction	0.21	0.21
Hydrogen stoichiometry ratio	1.5	1.4
Oxygen stoichiometry ratio	2	1.6

Table 2.4: Operating conditions for fuel cells simulated in this work

Figure 2.5 shows the results of the fitting for each polarization curves. Although the two cases are extremely different, a very good agreement is obtained. A large drop is observed at

the end of the simulated curve for the Autostack-CORE case. The four parameters obtained by the fitting are given in Table 2.5 as well as the electrochemical parameters used for the study.

Table 2.5: Electrochemical parameters (bold are fitted)

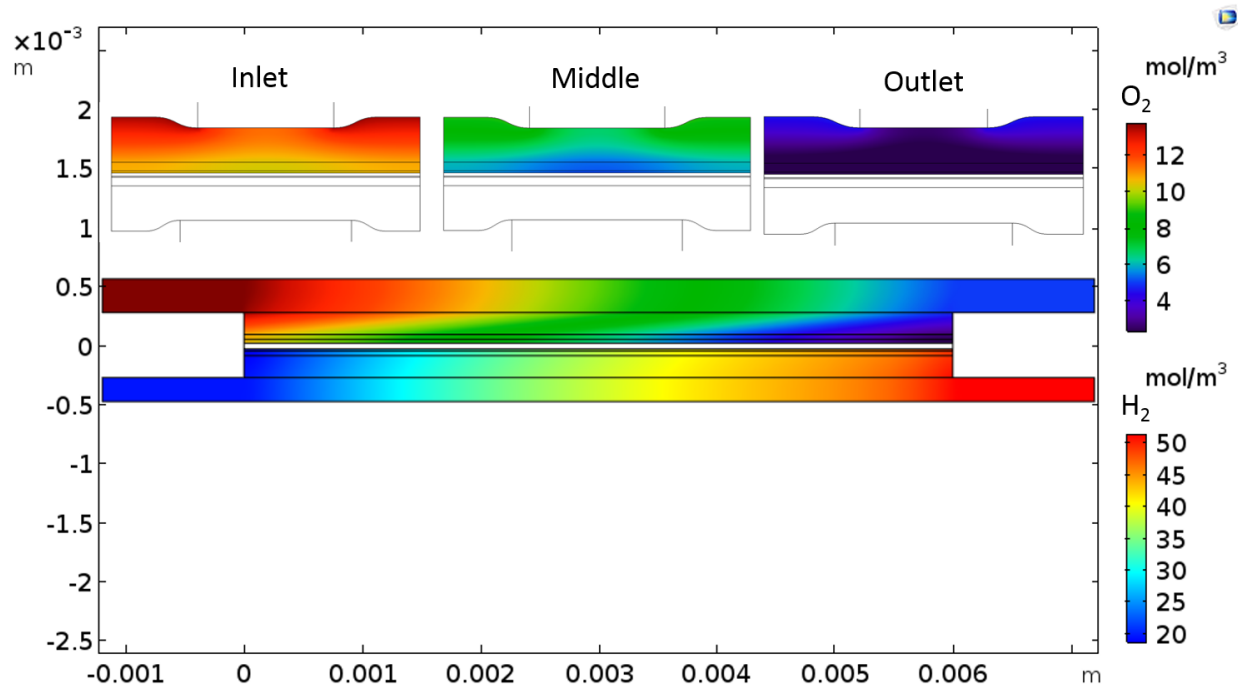
$C_{SO_3^-}$ [mol/m ³]	2036
s_0 [m ²]	$6.41 \cdot 10^{-20}$
ΔH_{ox-a}^\ddagger [kJ/mol]	24.4
ΔS_{ox-a}^\ddagger [J/mol/K]	-172
ΔH_{ox-c}^\ddagger [kJ/mol]	81.5
ΔS_{ox-c}^\ddagger [J/mol/K]	-285
α_a	0.5
α_c	0.216
σ_{corr}	1.202
D_{corr}^a	0.941

2.2.2 Oxygen depletion in the cathode channel

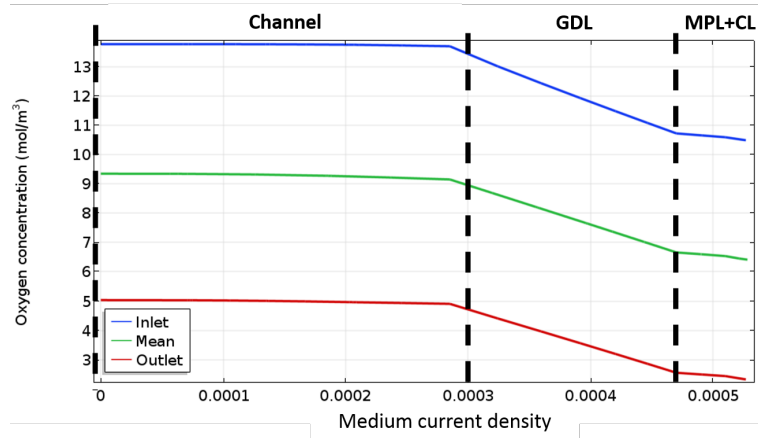
The hydrogen and oxygen stoichiometry (see Table 2.4) is defined as the ratio of the reactant inlet flow to the reactant consumption. That is to say, if the stoichiometry is two, two times more reactant is supplied at the inlet than necessary. However, this parameter does not provide any direct information about the local gas concentration along the gas channel or at the interface with the GDL. Using the along channel model, the oxygen depletion by convection/diffusion and consumption along (with the geometry Figure 2.2.a) and across the channel (Figure 2.2.b) can be estimated. Figure 2.6 shows the oxygen and hydrogen concentration profiles along the channel and in the porous media as well as the oxygen concentration for a cross section of the channel and rib. Nine cut lines are used to extract local conditions in the gas channel to be implemented as a boundary conditions for the through plane model (see Figure 2.9). These cut lines represent nine positions that are used in the design optimization in the further section. For the oxygen concentration, rib-channel profiles at the inlet, middle and outlet are also shown.

Reactants are supplied in a counterflow scheme. Therefore, in Figure 2.6, air enters in top left while hydrogen enters in bottom right. For the reactants, concentrations decrease along the channel as they are consumed in the catalyst layers. Moreover, there is a stronger through plane gradient in the porous media (GDL and CL) than in the channel, which reflects the more difficult path for the gas in the porous media than in the channel. The two types of profile for the oxygen show the combination of the concentration drop along the channel but also oxygen starvation under the rib due to the difficult diffusion of the oxygen even at medium average current density.

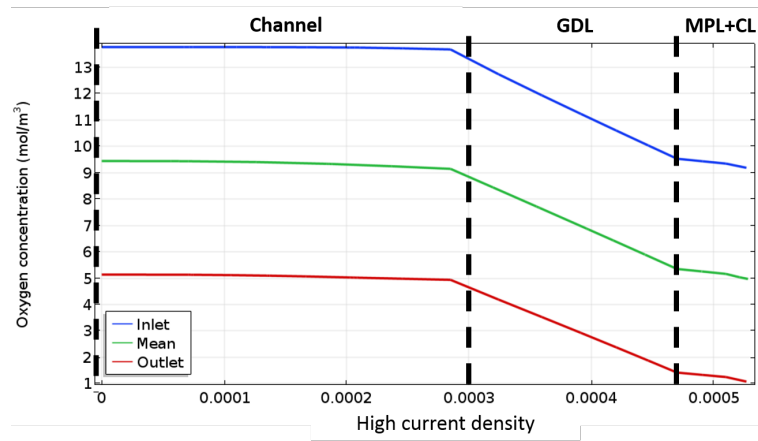
To investigate further in the influence of diffusion, Figure 2.7 shows the oxygen concentration for a fixed current density along three of the cut lines showed in Figure 2.6 (inlet, middle and

Figure 2.6: Oxygen and hydrogen concentrations @0.8 A/cm²

outlet). The top one shows the concentration profile at a medium average current density (0.8 A/cm²) whereas the second one is at higher average current density (1.2 A/cm²). The concentration at the left is at the top of the cathodic channel and the concentration at the right is the concentration at the cathodic catalyst layer near the membrane. For the inlet at the medium average current density, the oxygen depletion between the CL and GDL/Channel interface is around 15% but for the outlet that difference goes up to 40%. The oxygen concentration drop along the channel combined with the diffusion through the porous media can lead to oxygen starvation and a severe loss of performance especially at high current density. For example, for a average current density of 1.2 A/cm², there is almost no more oxygen at the catalyst layer close to the outlet. Thus, heterogeneities increases between inlet and outlet and it can be showcased by the current density distribution in Figure 2.8. At high mean current density, there is a 30% difference between outlet and inlet current density whereas at a medium one, it is around 10%. Moreover, the oxygen concentration under the rib is even lower because of the hindered diffusion (as shown as in Figure 2.6) leading to an even more important disparity. This latter phenomena is investigated in the next section.



(a) Medium current density



(b) High current density

Figure 2.7: Oxygen concentration through the channel and MEA for the three cut lines at a medium 0.8 A/cm^2 (a) and an high 1.2 A/cm^2 (b) current density

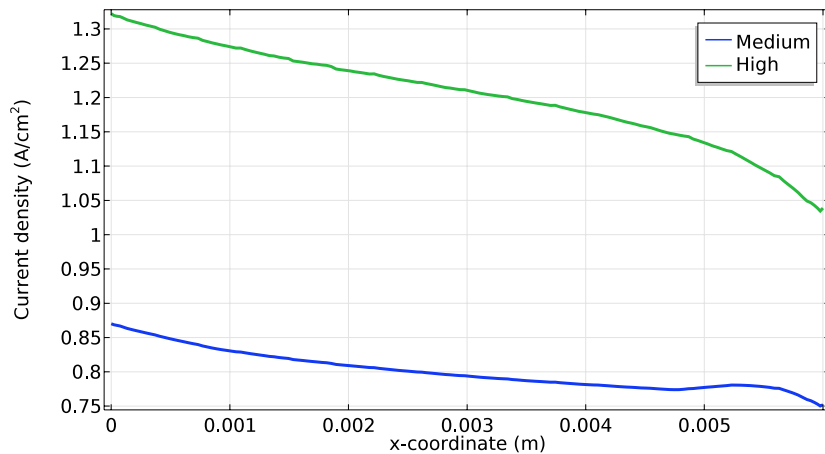


Figure 2.8: Current density distributions along the cathodic catalyst layer

2.2.3 Relative humidity along the channel

Figure 2.9 shows the relative humidity along the channel and in the porous media. There are also strong heterogeneities for the relative humidity along the channel. A swift increase of the RH alongside the channel is observed from the gas inlet to the outlet combined to a little decrease inside the GDL and catalyst layer at the outlet for the both anode and cathode side. The water concentration increase at the anode side is related to the water transport through the membrane.

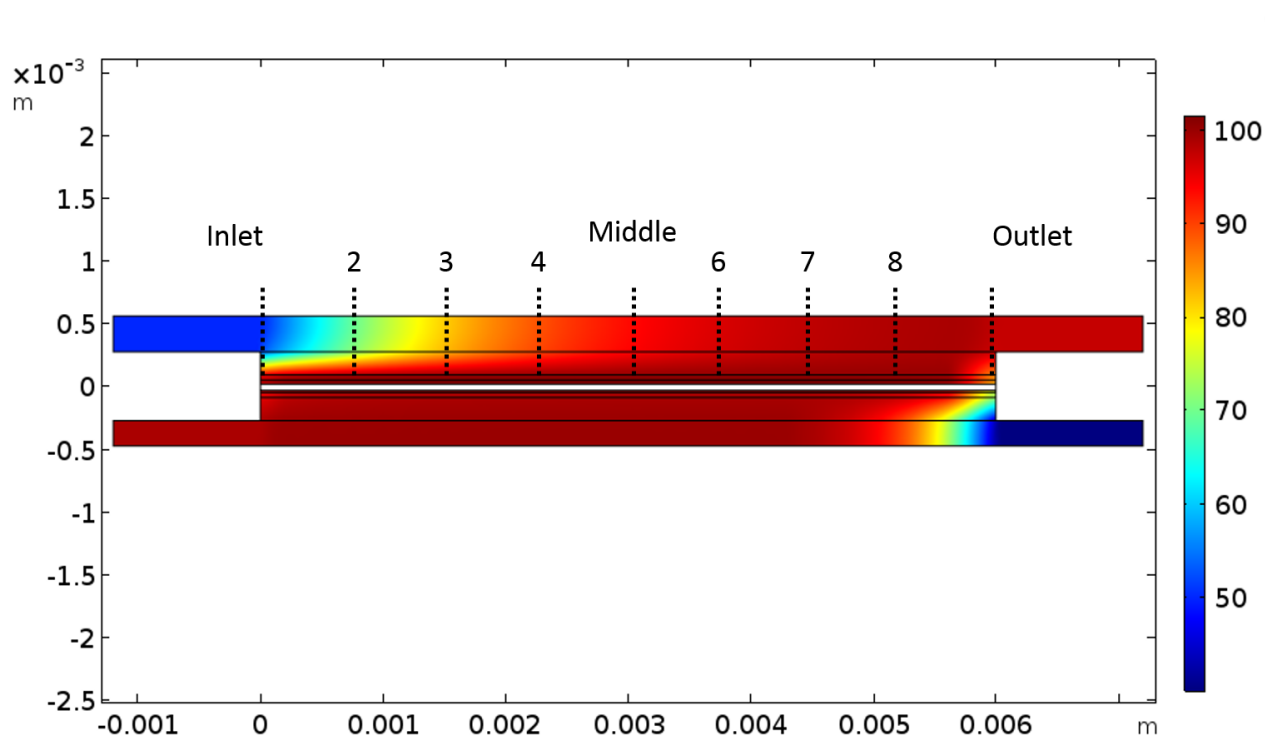


Figure 2.9: Relative humidity at 0.8 A/cm^2 (the dashed lines represent the cut lines)

2.3 Practical case : Design sensitivity

2.3.1 Design optimization of bipolar plates

An optimization of the bipolar plate design is performed and compared to the reference design of AutoStack-CORE described in Table 2.6. Because of the competition between the current collection by the ribs and the gas supply by the gas channels, the 2D-model with the rib-channel geometry is used to perform the optimization of the bipolar plate design. A parameter of interest is defined as the ratio between the channel width and the total width of the pattern:

$$\Gamma = \frac{l_{CH}}{(l_{CH} + l_{Rib})} \cdot 100 \quad (2.52)$$

Where l_{CH} is the width of the channel and l_{Rib} the width of the rib. The range of Γ in that study varies from 10% to 90% by steps of 5% (for a total pattern length of $1.44 \cdot 10^{-3}$ m). In order to model different locations in the channel, the along channel model is simulated to provide necessary information on the local conditions along the channel at the interface with the GDL. These parameters (RH, oxygen and hydrogen concentration, pressure) are inputs to provide an accurate analysis at different locations. In this study, nine locations from inlet to outlet are analysed (see Figure 2.6 for the cut lines used).

Table 2.6: Geometry values for the initial design in AutoStack-CORE

	Anode	Cathode
Channel depth [m]	$2.02 \cdot 10^{-4}$	$2.85 \cdot 10^{-4}$
l_{CH} Channel width [m]	$0.64 \cdot 10^{-3}$	$0.805 \cdot 10^{-3}$
l_{Rib} Rib width [m]	$0.8 \cdot 10^{-3}$	$0.635 \cdot 10^{-3}$
e_{GDL} GDL thickness [m]	$2.1 \cdot 10^{-4}$	$2.1 \cdot 10^{-4}$
e_{GDL}^{1MPa} GDL thickness at 1MPa [m]	$1.61 \cdot 10^{-4}$	$1.61 \cdot 10^{-4}$
MPL thickness [m]	$4 \cdot 10^{-5}$	$4 \cdot 10^{-5}$
CL thickness [m]	$6 \cdot 10^{-6}$	$1.2 \cdot 10^{-5}$
MB thickness [m]	$2.5 \cdot 10^{-5}$	

The model is able to provide some rules in order to optimize the cathode channel. Indeed, the thinner the channel, the larger the rib and thus a better electronic conduction. Conversely, the thinner the rib, the larger the channel and thus a better oxygen supply. On one hand, the model is used to track the ohmic losses and oxygen depletion in through plane direction by evaluating the electronic cathode potential changes and oxygen concentration. Figure 2.10 shows the full electronic potential profile and the oxygen concentration profile at the cathode for the two extreme cases : a very thin channel ($\Gamma = 10\%$) and a very large channel ($\Gamma = 90\%$).

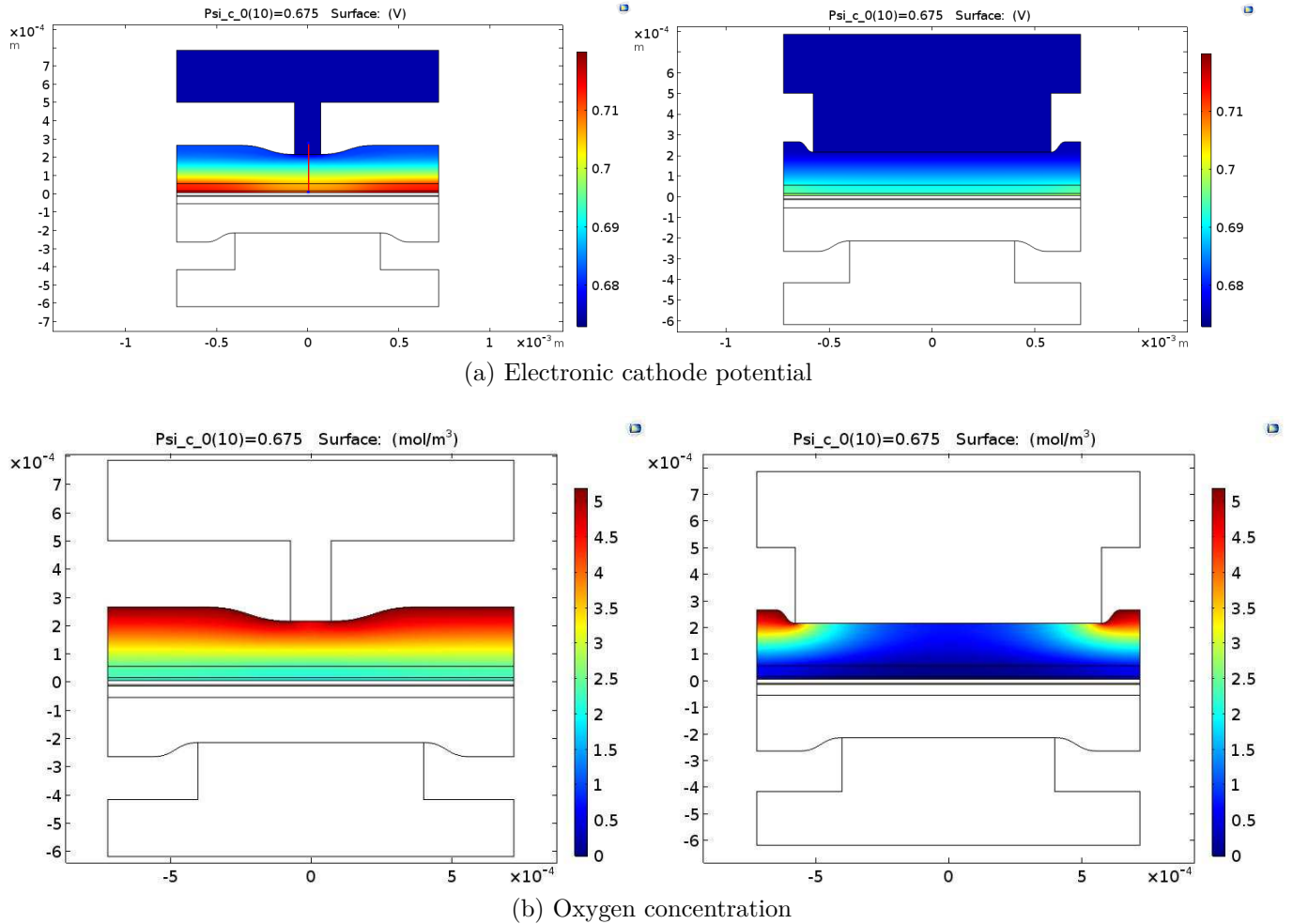


Figure 2.10: Electronic cathode potential profile (a) and oxygen concentration profile (b) for a large channel (left) and a thin channel (right) at the inlet

For the large channel, the potential gradient inside the MEA is more than 35 mV whereas for a large rib it is only 20 mV which is more than a 50% difference. On the other hand, the full potential profile exhibits also a stronger gradient in-plane for a large channel showcasing the in-plane electronic current collection. There is a better current collection under the rib because of a higher electronic conductivity thanks to the crushing effect of the rib. On the contrary for a thin channel, oxygen starvation under the rib is observed.

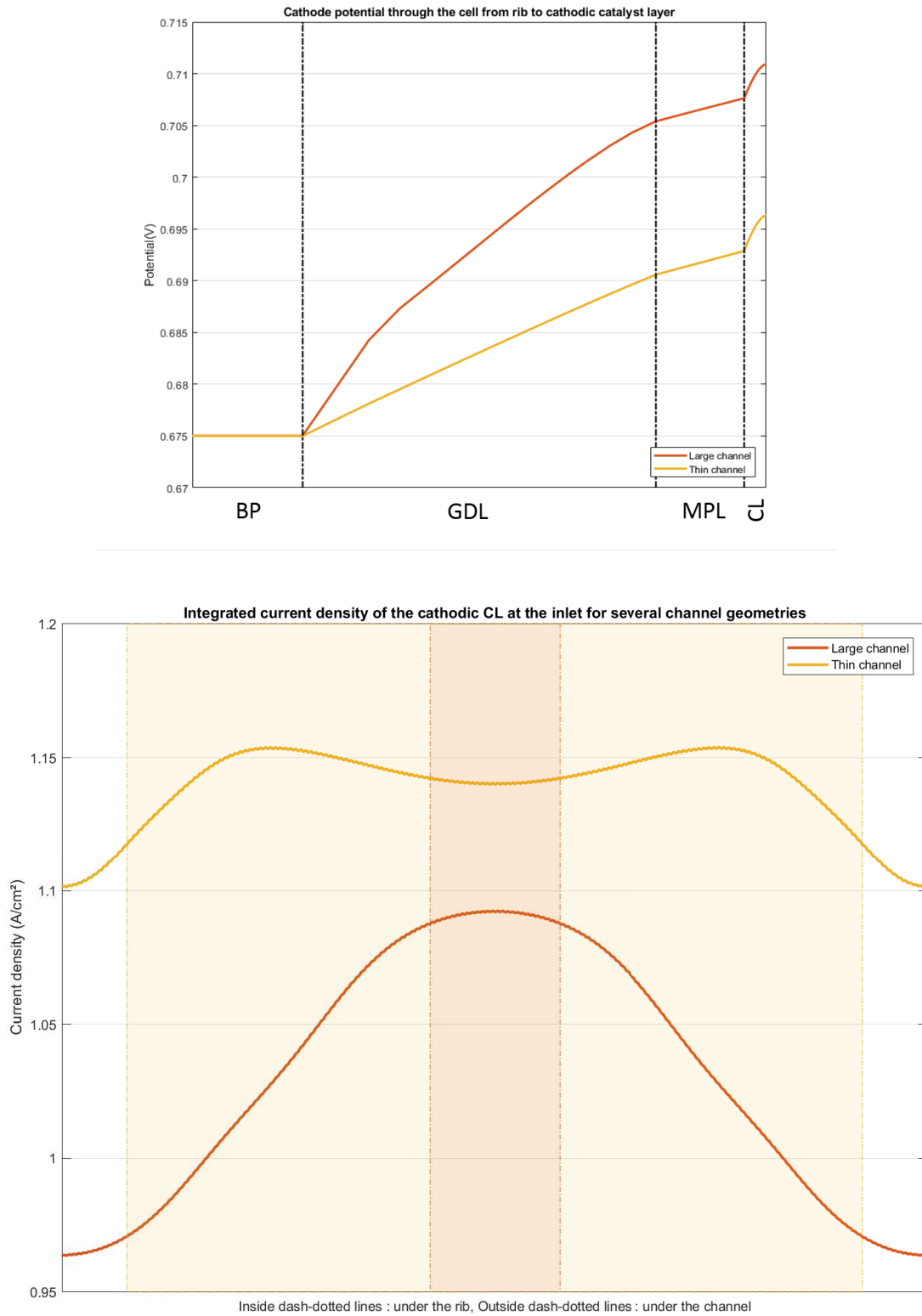


Figure 2.11: Electronic cathode potential distribution from rib to catalyst layer and current density along the catalyst layer @0.675V at the inlet

Figure 2.11 shows the potential profile from the middle of the rib to the cathodic catalyst layer and the current density distribution under the channel and the rib for the two latter cases. An higher through plane gradient of potential for a large channel is also observed. According to the current density distribution, the performance at the inlet worsens with a large channel than a thin channel. A difference of 10% between the current density under the channel and under the rib is observed for a large channel, whereas for large rib it is only 5%. However for the latter, a dip in the current density is found under the middle of the rib. The oxygen gas depletion highlights that oxygen is hindered to go under the rib at which explains the need of a larger channel for a better oxygen supply.

The optimization is performed to maximize the performance at a fixed voltage. The parametric study on the channels width is used to evaluate its impact on a set of operating conditions described in Table 2.4. In that case, the competition between the diffusion through plane and in-plane is observed and the impact of the rib width can be estimated.

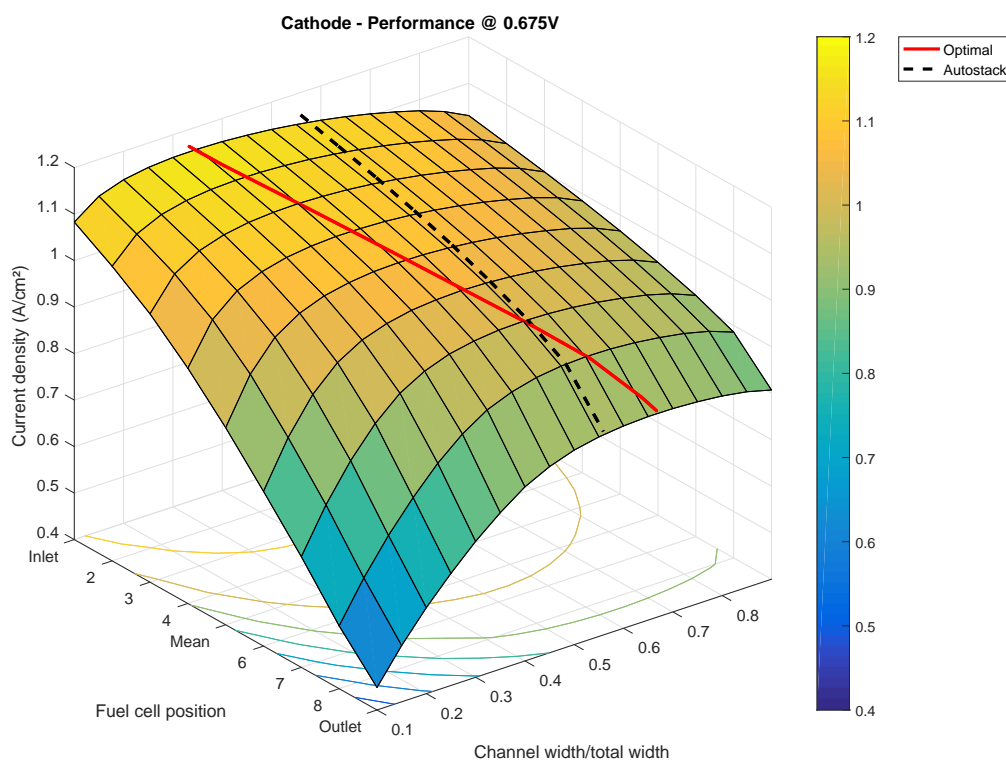


Figure 2.12: Performance of the fuel cell @0.675V as function of position in the channel and the ratio cathode channel width/total width

Figure 2.12 shows the current density as function of the channel length for nine positions in the channel at the cathode. The dotted line represents the reference case (AutoStack-CORE) used for the geometry. For the cathode, different optima are observed as function of the position

in the channel whose are highlighted by the red line. Close to inlet, the best performance is observed with a smaller channel. On the contrary, at the outlet, the maximum is found with a larger channel.

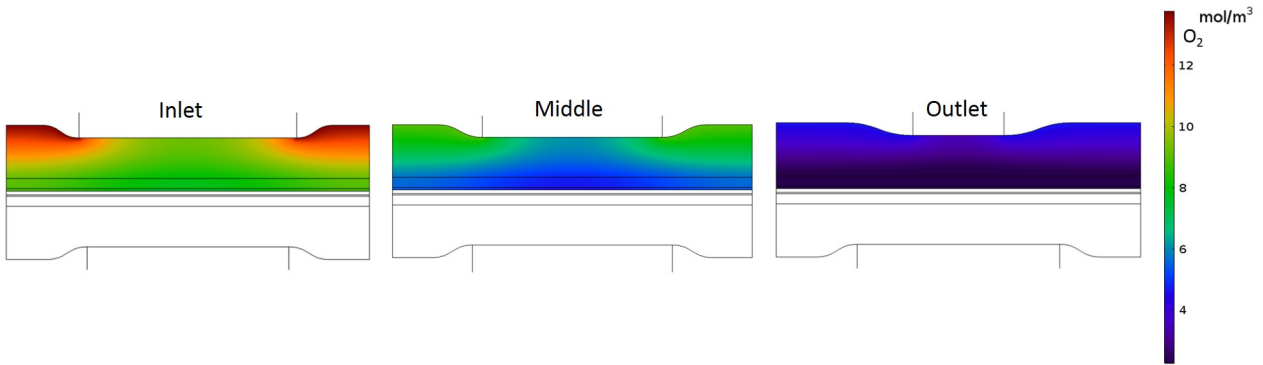


Figure 2.13: Oxygen concentrations @0.8 A/cm² for the optimal design in AutoStack operating conditions

Figure 2.13 shows the through plane oxygen concentration under the ribs. Figure 2.14 shows the potential profile from the middle of the rib to the cathodic catalyst layer and the current density distribution at the inlet along the total pattern length for the AutoStack design and for the optimal channel design. At the inlet, there is clearly less oxygen under the rib than on the standard design (see Figure 2.6.b) because of the larger rib of the optimal design. However it exhibits a better current density with the optimal design than the AutoStack one. This can be explained by a better current collection which is shown by a lower potential gradient in the bottom part of Figure 2.14. At the outlet, thanks to the larger channel, an higher concentration of oxygen is observed hence a better oxygen supply to the catalyst layer. Figure 2.15 shows the potential profile and the current density distribution but at the outlet. The optimal design gives better performance than the AutoStack one through an higher current density. It shows also that the current collection worsens with the optimal design because of a higher potential gradient but oxygen concentration is higher by using a thinner rib. In this case, it illustrates that the oxygen supply is the key factor for the performance at the outlet. The larger channel of the optimal design at the outlet favours more oxygen under the rib which leads to an increased current density even though the current collection is worse. AutoStack-CORE promotes a better use of the outlet with quite a large channel, so it is mainly the inlet channel design that could be improved.

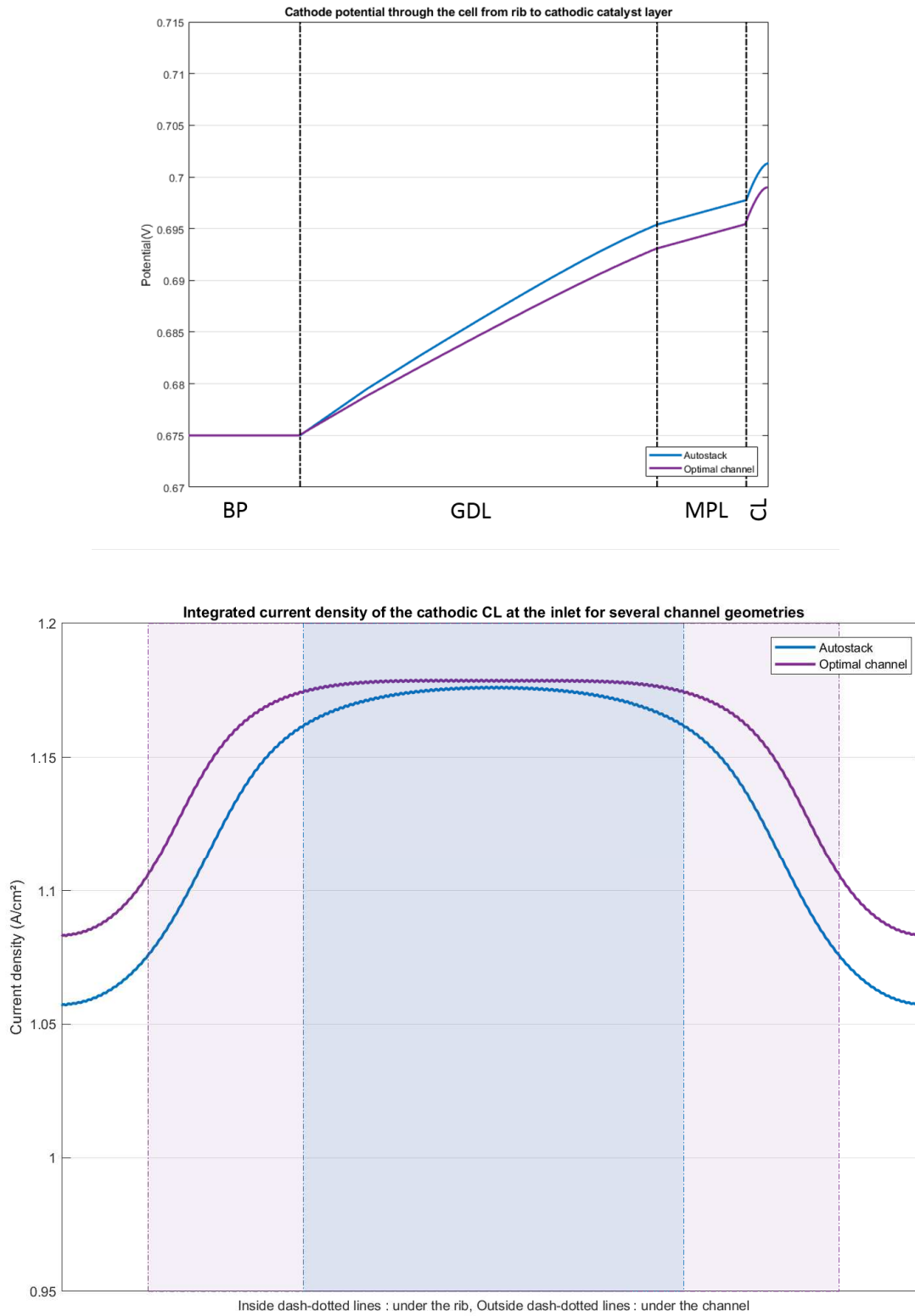


Figure 2.14: Electronic cathode potential distribution from rib to catalyst layer and current density along the catalyst layer @0.675V at the inlet

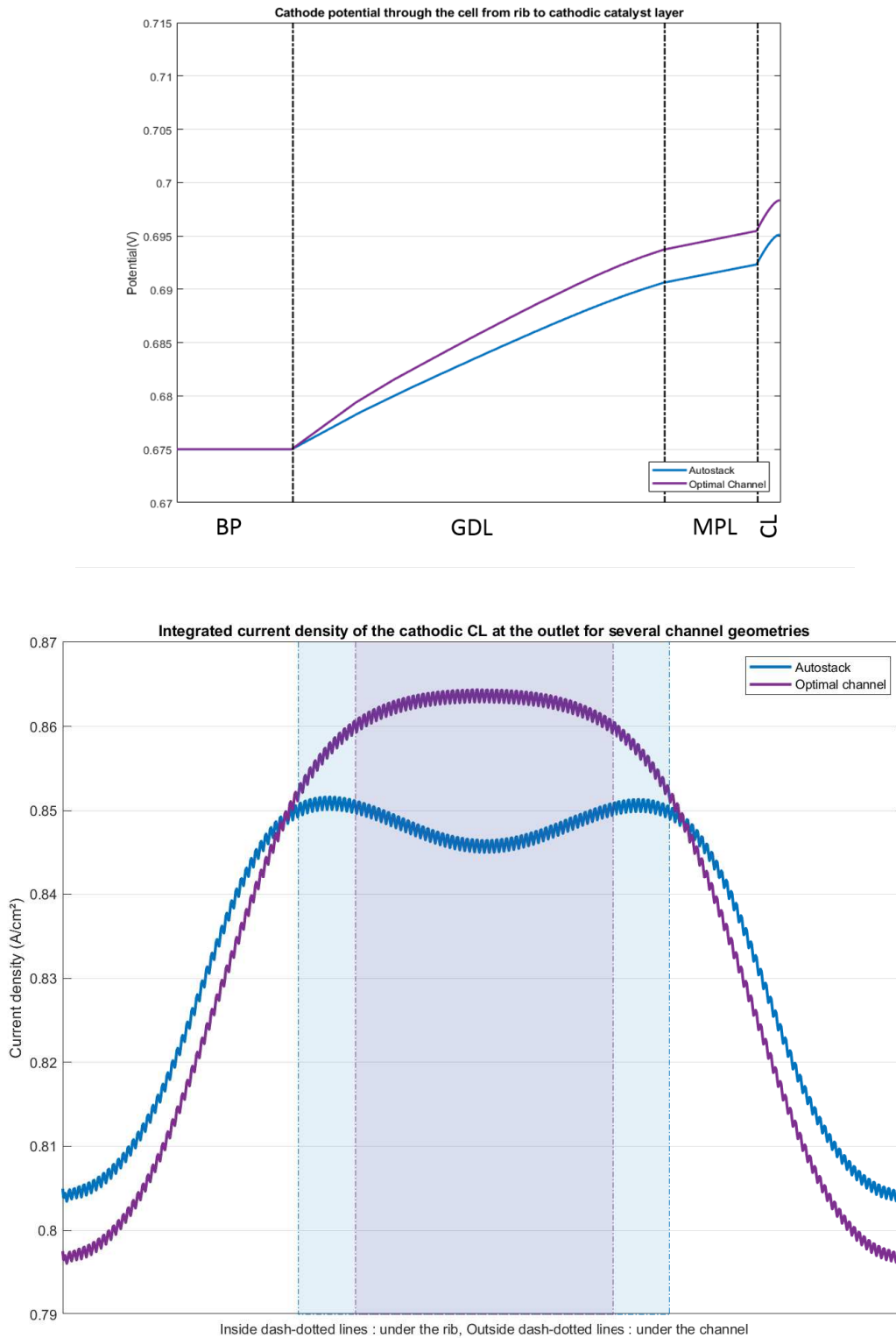


Figure 2.15: Electronic cathode potential distribution from rib to catalyst layer and current density along the catalyst layer @0.675V at the outlet

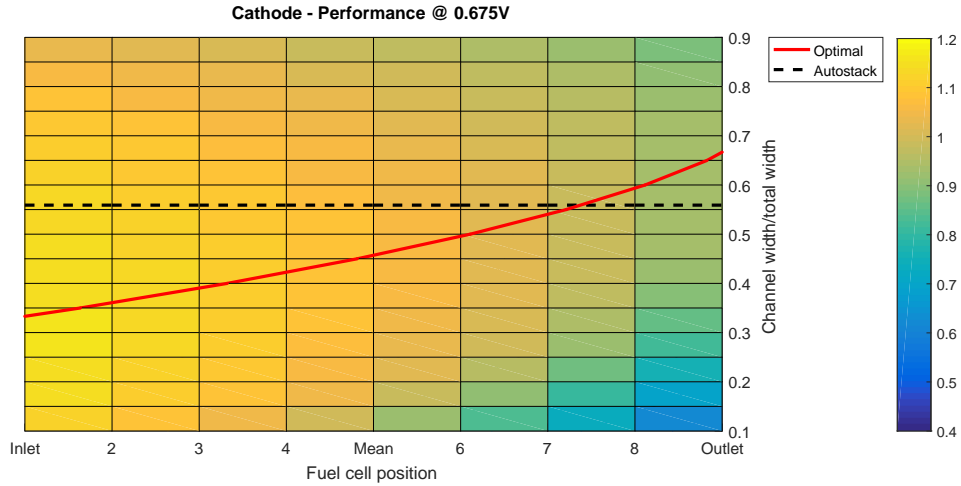
2.3.2 Impact of operating conditions

To extend this parametric study, variations on the operating conditions were done: lower relative humidity (35% at the cathode, 25% at the anode), lower pressure (1.5 bar at both inlets) and higher stoichiometry (2 for the air). Results are shown in Figure 2.16. Lowering the humidity has no significant impact on the global performance. The fuel cell is well hydrated whatever the location thanks to the high inlet pressure which is confirmed when the along the channel model is used to determined the local conditions. Only the inlet and the outlet of the fuel cell are slightly influenced by the modification of relative humidity. This result suggests that the optimal design weakly depends on the relative humidity.

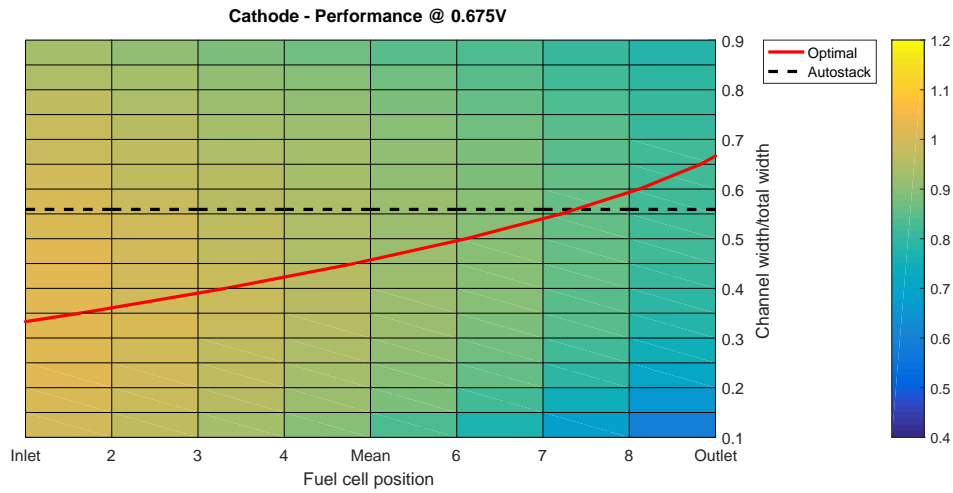
With a lower pressure at both inlets, a global decrease of performance is observed because of a worse humidification of the MEA. However, the optimal design suggested is the same as before. It implies that both RH or the pressure have no significant impact on the optimal channel design and thus the same design can be used to optimize the performance. In both operation conditions, the through plane oxygen concentration and electronic potential distribution remains very close to the one observed with the optimal design (see Figure 2.13).

Nonetheless, if the air stoichiometry is increased (2 instead of 1.6), the optimal design changes from the reference operating conditions. Figure 2.17 shows the oxygen concentrations with the optimal design for the increased stoichiometry. At the inlet, there are no modifications compared to the AutoStack operating conditions (see Figure 2.13) because there is not an actual better oxygen supply. But at the outlet, an higher oxygen concentration is seen which can explain why a thinner channel at that position leads to better performance. With an higher stoichiometry, it is expected that the gas inlet will provide a better oxygen supply hence the possibility to enlarge the rib for a better electronic conduction without being oxygen starved at the catalyst layer.

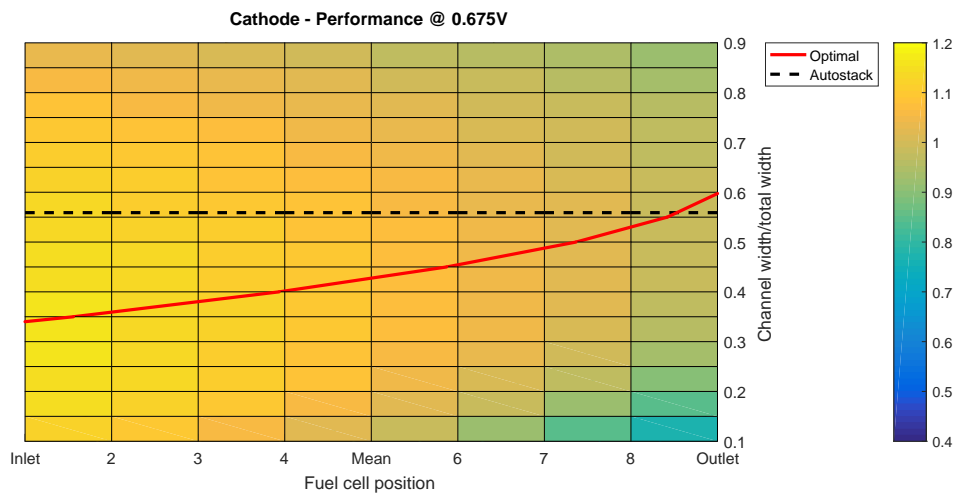
The competition between the oxygen supply and the electronic conduction along the channel is here showed as the main lever to optimize bipolar plate design. A larger rib is needed at the inlet to optimize the electronic current collecting, a larger channel is required at the outlet for oxygen gas supply under the rib. In the reference case, the choice is to optimize the outlet performance because of the severe loss when the channel is too small. The model suggests an optimal design (red) as an interesting option to maximize current density (of the order of a few percent) considering a variable width along the channel for the nominal operating point. Moreover in that case, this optimal design is shown poorly dependent of some operating conditions such as a lower relative humidity at the gas inlet or a lower inlet pressure.



(a) Relative humidity : 35 cathode/25 anode



(b) Low Pressure : 1.5 bar



(c) Stoichiometry O_2 : 2

Figure 2.16: Performance of the fuel cell @0.675V as function of position in the channel and the ratio cathode channel width/total width and for special operating conditions

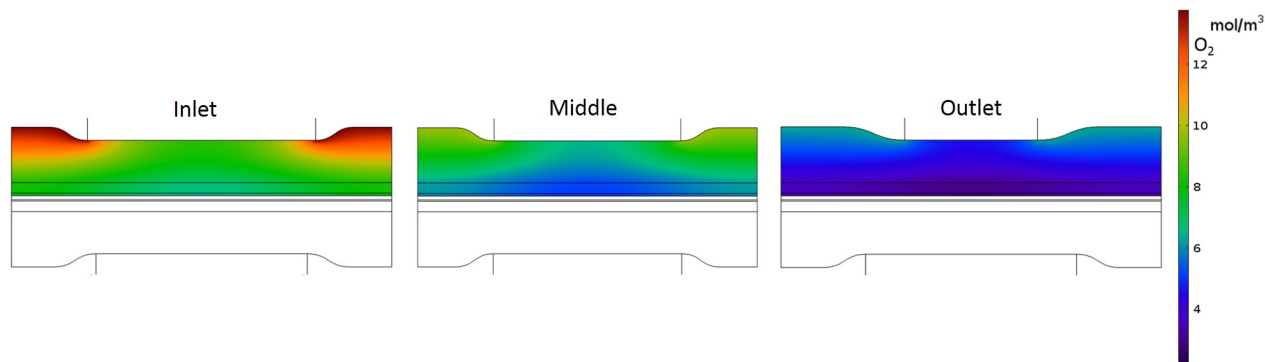


Figure 2.17: Oxygen concentrations @0.8 A/cm² for the optimal design for stoichiometry O₂ : 2

Conclusion

In this chapter, two 2D multiphysics models have been developed and used in order to investigate heterogeneities at different locations and scales. These models developed in EuROPIUM framework with COMSOL Multiphysics have been validated globally using polarization curves. Already at a medium current density, important disparities appear such as the current density between the inlet and the outlet of the cell. A section is dedicated to the study of the oxygen depletion at the cathode channel. Indeed, oxygen starvation leads to dramatic loss of performance and should be avoided performance wise. The hindered transport by the porous media especially under the rib because of the crushing effect lowering the access to the catalyst layer for the gases. In order to use this study in a practical case, an optimization of bipolar plate design is performed by modifying the ratio between the channel width and the total width. The along the channel model is first used to give the conditions at different location along the flow. These conditions are then used in the rib/channel model. This case exhibits the competition between the oxygen supply and the current collection by the ribs. By quantitatively evaluating each contribution, the model suggests an optimal design by finding the best compromise. Furthermore this trade-off can be overall along the channel however an varying width along the channel is also evaluated as long as the mechanical constraints for the bipolar plates are met. Simulations show that the good oxygen supply at the cathode inlet induces a larger rib whereas a larger channel is better at the outlet because of the oxygen starvation. Moreover, by increasing the air stoichiometry, the optimal design changes especially at the outlet because of the better oxygen supply.

Modeling of carbon support corrosion during transient phases

Contents

3.1	Introduction to the reverse-current decay mechanism	58
3.2	Modeling in EuROPIUM of transient startup and shutdown . . .	61
3.3	Carbon corrosion and reverse-current decay mechanism simulation	64
3.3.1	Simulation of mechanism during a startup	64
3.3.2	Simulation of mechanism during a shutdown	76
3.3.3	Rib-channel	84
3.4	Carbon corrosion validation	93
3.4.1	SAXS/WAXS experiment	93
3.4.2	CO ₂ at cathode outlet	96
3.4.3	In-situ and ex-situ analyses	99
3.5	Conclusion	103

3.1 Introduction to the reverse-current decay mechanism

Various factors such as transient operation, dynamic operating conditions or even auxiliaries perturbations affect the life expectancy of the fuel cells [101, 33, 27, 102]. One of the main known issues is related to the system startup or shutdown. In the working condition for automotive fuel cell, Pei et al. [8] divided the operating conditions into four modes: load changing, start-stop, high power and idling. Several works suggest that, compared to the idling and high power conditions, degradations of the fuel cell components is more likely due to the start-stop and load changing conditions [19, 103, 104]. Figure 3.1 shows that start-stop induces could 33 % of the total degradation of a PEMFC.

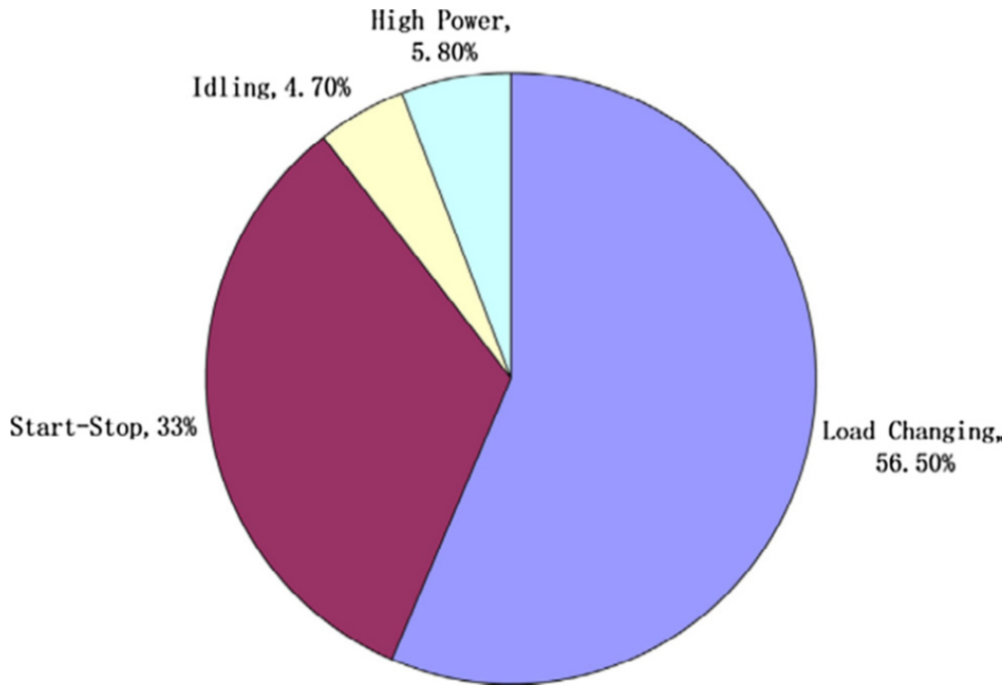


Figure 3.1: Relative impact of operating conditions on PEMFC degradations (reprinted from [8])

During startup, the filling of the anode side by the hydrogen creates two zones along the channel until the remaining oxygen being chased off. One zone is simply a standard fuel. The other zone has water oxidation mechanism and oxygen reduction. This phenomenon is called reverse-current decay mechanism which is described by Reiser et al. [105]. High cathode potential are thus reached, up to 1.6 V leading to unwanted side reactions [106]. Among these side reactions, oxidation of the carbon support leads to important catalyst layer degradations especially at the cathode. Figure 3.2 shows a sketch of a PEMFC full of air before a startup and the different potentials: electronic (Ψ), ionic (Φ) and electrode ($\Psi - \Phi$). Note that in this work,

by convention, when the cell operates under counter-flow configuration: cathode and anode channels are fed from the left and the right respectively. Figure 3.2a shows the potentials along the channel and Figure 3.2b presents the through plane potential distribution in the different layers. Because it is considered to be the ground, the anode electronic potential (Ψ_a) is fixed to 0V. As no current is drawn from the fuel cell the cathode electronic potential (Ψ_c) is also 0V and the ionic potential of the membrane is around $-1.2V$ because of the equilibrium potential of the couple O_2/H_2O .

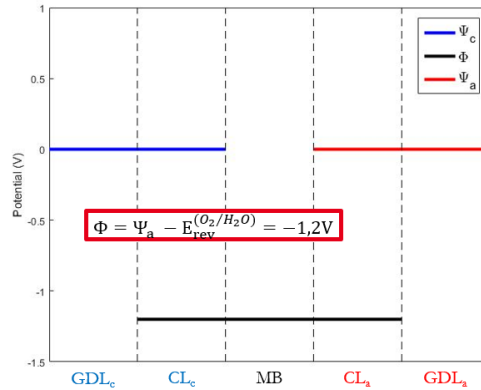
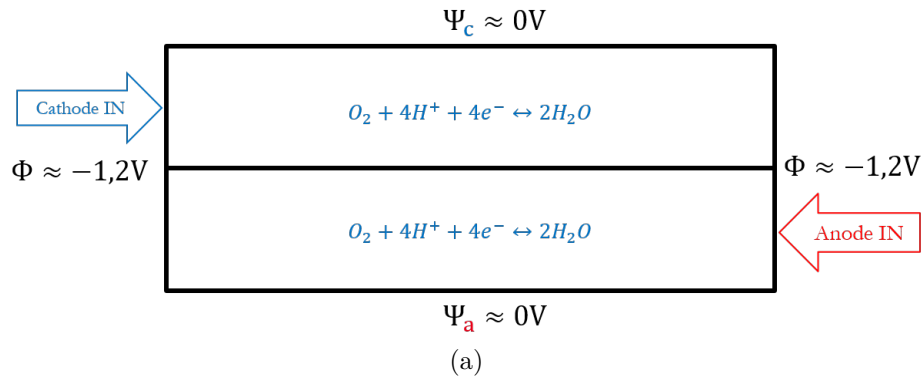


Figure 3.2: Potentials along the channel (a) and through plane (b) before the startup of a PEMFC

Figure 3.3a is a sketch of a PEMFC during startup when hydrogen is filling the anode compartment. The fuel cell is now divided into four parts because of the H_2/O_2 gas front in the anode. In this configuration, the reverse-current decay mechanism proposed by Reiser et al. [105] assumes that hydrogen oxidation and oxygen reduction occurs in the right side of the PEMFC while oxygen reduction and water oxidation take place on the left. Based on the reverse-current decay mechanism, Figure 3.3b and Figure 3.3c show a scheme of the potentials at each side of the H_2/O_2 front from the cathode GDL to the anode GDL.

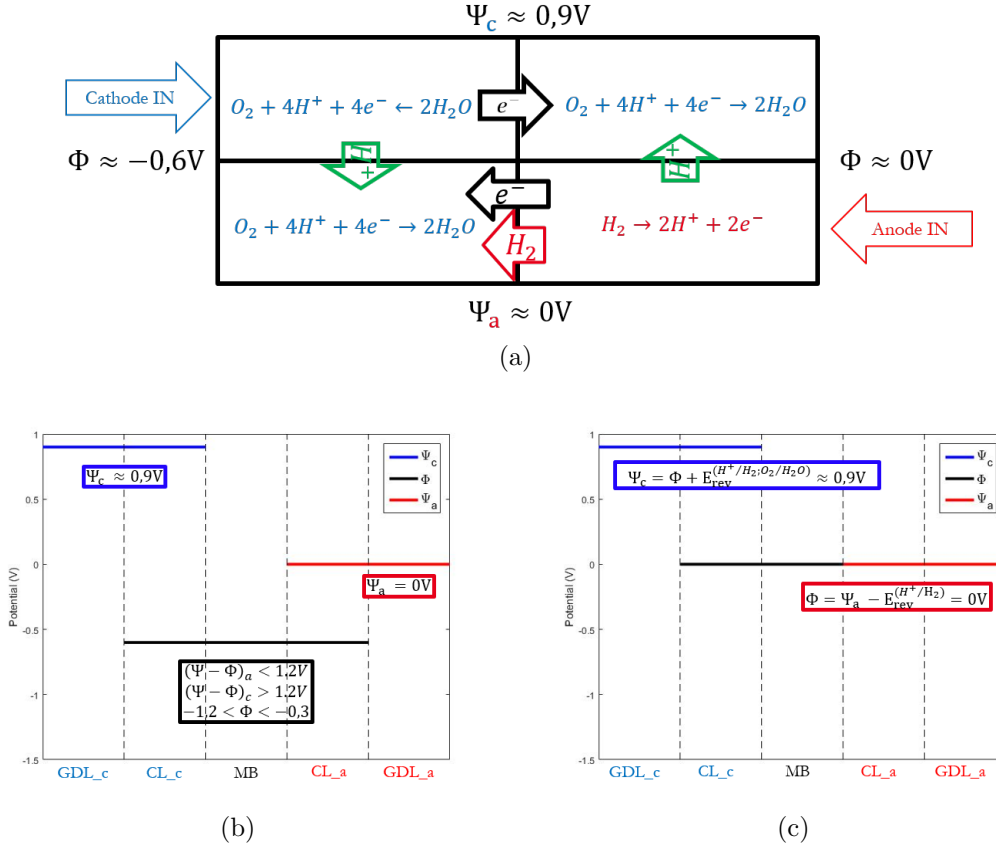


Figure 3.3: Potentials along the channel (a) and through plane at each side of the H_2/O_2 front: O_2 side (b) and H_2 side (c) during the startup of a PEMFC

The right image describes how the hydrogen supplied into the cell enforces the ionic potential to be equal to zero in the left part of the cell because of the fast hydrogen oxidation reaction. For the cathodic side, the electrode potential is defined by a mixed potential between the O_2/H_2O couple and the H^+/H_2 couple because of the hydrogen permeation through the membrane. That is why the cathode electronic potential is lower than the 1.2V observed precedently and close to 0.9V during startup. Figure 3.3.b describes how the section with the remaining air behaves during the startup. Because of the high conductivities of the bipolar plates, cathode potential goes to 0.9V considering a reference potential of 0V for the anode. As no current is delivered from the cell during startup, it appears that electrons released by the hydrogen oxidation have to be consumed with the reduction of the remaining oxygen at the left side of the hydrogen front. Nevertheless, this latter reduction reaction needs protons coming from the cathodic side. These protons are produced by the oxidation of water at the cathode side which also supply electrons to the reduction of the oxygen at the other side of the hydrogen front at the cathode. In the literature, ionic potential coming from the equilibrium is around -0.6V which gives a local cathode potential over 1.5V [105, 107, 106, 108, 109]. Because of this high potential during these transient steps, side reactions like carbon oxidation become non-negligible.

Experimentally, these degradations have shown strong heterogeneities between cathode inlet and outlet for a startup and a shutdown [110]. Heterogeneities have also been observed between the region under the channel and under the rib [111, 7]. To characterize the carbon oxidation, several experimental techniques are used like carbon dioxide measurements [112, 69] that can be combined with segmented cells with local reference electrodes [113, 114, 115, 109].

Several models have been developed to have a better understanding of this mechanism and to suggest mitigation strategies [105, 107, 116, 117, 118, 119, 120, 113, 114, 109]. As reviewed by Gu et al. [9], several groups of models may be used to define the studies as function of the physical phenomena taken into account: from kinetic models using the electrochemical reactions in place [105] to a more coupled way with also transport models inside porous media and/or membrane [107, 116]. Maranzana et al. [109] used a “pseudo2D” model to simulate a transient startup with the injection of hydrogen to study spatial and temporal variations and comparing them to their segmented cell. Cell is discretized into twenty sections which are modeled with a 1D generic electrode model. This 1D model includes kinetics of the several electrochemical reactions including surface platinum oxidation/reduction, HOR/HER, ORR/OER and two carbon oxidation reactions. Mass transfer is solved in GDL and membrane. Electrode is associated with GDL and are assumed only diffusive. Gases crossover through the membrane is taken into account as a resistive mass transfer for the dissolved species. Concentrations of gases in the channels are boundary conditions. Simulation results are validated with the experiment results from the segmented cell using local currents and total amount of carbon oxidized. Pseudo-capacitive impact of platinum oxides is highlighted.

3.2 Modeling in EuROPIUM of transient startup and shutdown

Figure 3.4 shows the geometry of the 2D-models developed used for the carbon corrosion modeling. The first model is an along the channel model to study especially the inlet-outlet heterogeneities while the second one focuses on the rib-channel induced local heterogeneities. The fuel cell is in a counter flow configuration for the along the channel model. Channels and catalyst layers are not discretized in the thickness for the along the channel model. The model and physics are based on the one described in chapter A.

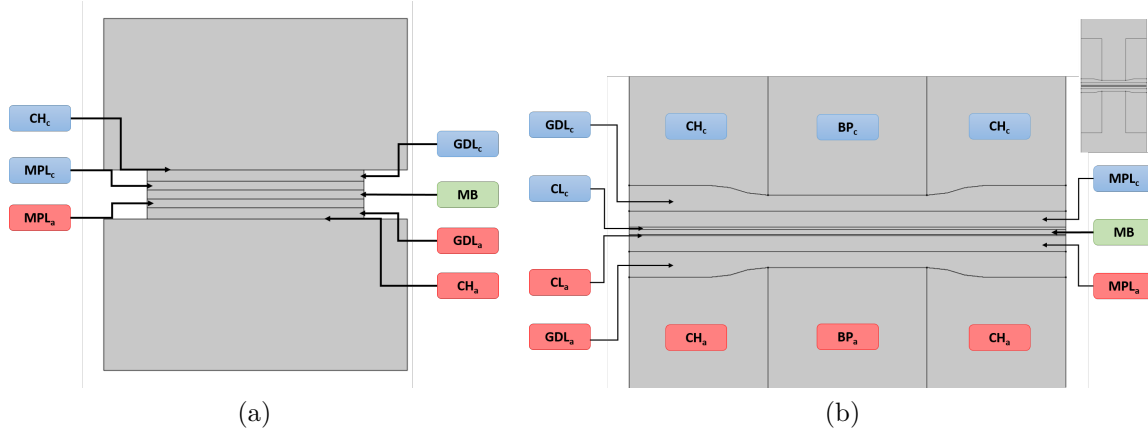
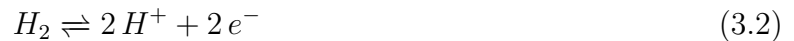


Figure 3.4: Geometry of the models: along the channel (a) and Rib-channel (b)

For the electrochemical model, the same reactions are implemented both at the cathode and anode catalyst layers. The potential and reaction rates depend only on local conditions which leads to a mixed equilibrium potential. First, the oxygen reduction reaction (ORR) and the oxygen evolution reaction (OER) are considered :



These reactions are in competition with the hydrogen oxidation reaction (HOR) and the hydrogen evolution reaction (HER) :



Reactions are written in the general form (see subsection 2.1.4):

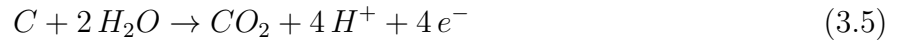


where z_i and ν_i are the charge and the stoichiometry coefficient of the specie M_i respectively and n the number of electron involved in the reaction. The oxidation and reduction currents are written as function of the local electrode potential defined as $e = \Psi - \Phi$:

$$\begin{aligned}
 i_{ox} &= nFk_{ox}^0 \prod_{\nu_i > 0} a_i^{\nu_i} \cdot \exp\left(\frac{\alpha nF}{RT} e\right) \\
 i_{red} &= -nFk_{red}^0 \prod_{\nu_i < 0} a_i^{-\nu_i} \cdot \exp\left(-\frac{(1-\alpha)nF}{RT} e\right)
 \end{aligned} \tag{3.4}$$

Where R is the universal gas constant, T the temperature, F the Faraday constant, α and $1 - \alpha$ are the symmetry factors of the reaction, a_i being the activity of specie i . Both kinetic factors are expressed the same way as in Equation 2.34 in chapter A.

Finally oxidation of the carbon support (COR) is added:



Several mechanisms are suggested in the literature to explain the corrosion of the carbon support. Literature shows that the carbon corrosion mechanism is tightly linked with platinum oxides. As our model is focused on the transport strategies simulation and coupling with fluidics, a global kinetic law for the carbon corrosion support is implemented:

$$J_{COR} = a_C \cdot j_{0,COR} \cdot a_{H_2O}^2 \cdot \left[\exp\left(\frac{\alpha_{COR} F}{RT} \cdot (e - E_{COR})\right) \right] \tag{3.6}$$

where a_C is the specific surface of carbon and E_{cor} the apparent potential for corrosion which depends on the water activity (a_{H_2O}):

$$E_{COR} = E_{C/CO_2}^0 - \frac{RT}{nF} \cdot \log\left((a_{H_2O})^2\right)$$

Table 3.1 lists the electrochemical parameters used.

Table 3.1: Parameters for the models

Symbol		
ΔH_{WOR}° [kJ/mol]	-282.9	[95]
ΔH_{HOR}° [kJ/mol]	0	[95]
ΔS_{WOR}° [J/mol/K]	-163.18	[95]
ΔS_{HOR}° [J/mol/K]	-0.104	[95]
$\Delta H_{HOR}^{\ddagger}$ [kJ/mol]	24.4	
$\Delta S_{HOR}^{\ddagger}$ [J/mol/K]	-172	
$\Delta H_{WOR}^{\ddagger}$ [kJ/mol]	81.5	
$\Delta S_{WOR}^{\ddagger}$ [J/mol/K]	-285	
E_{C/CO_2}^0 [V]	0.207	
E_{O_2/H_2O}^0 [V]	1.23	
E_{H^+/H_2}^0 [V]	0	
j_{COR}^0 [A/cm ²]	$1.03 \cdot 10^{-18}$	[9]
α_{COR}	0.67	[9]
$a_v^{cathode}$ [m ² /m ³]	$2.5 \cdot 10^7$	
a_v^{anode} [m ² /m ³]	$1.67 \cdot 10^7$	
$a_C^{cathode}$ [m ² /m ³]	$6.67 \cdot 10^7$	
a_C^{anode} [m ² /m ³]	$4.4 \cdot 10^7$	

The channels are in 1D for the modeling of startup and shutdown. Species transport in the channels considers an overall molar balance for the gas phase and Stefan-Maxwell equations are solved with a mass balance for each component except one (see subsection 2.1.3.2). The hydrogen is supplied at 1s and ramp up to its nominal value in 0.1s. At the same time the supply of oxygen is stopped. Species transport in porous media are modeled as described in chapter A with the approach proposed by Young and Todd. Electronic and ionic transports are governed by ohmic conduction. As specified in chapter A, only the conduction and the heat balance in solid media are taken into account thermally wise.

3.3 Carbon corrosion and reverse-current decay mechanism simulation

3.3.1 Simulation of mechanism during a startup

This section presents the simulation results of the reverse-current decay mechanism during the PEMFC startup in the model along the channel. The parameters used for the design are described in Table 3.2 and the operating conditions are the CEA reference given in Table 2.4. Before the startup, air is fuelled in the anode. Hydrogen is supplied at the anode from 1s onwards. Figure 3.5 shows the molar fraction of gases imposed at the anode inlet as boundary

condition. The fuel cell is in a counter flow scheme.

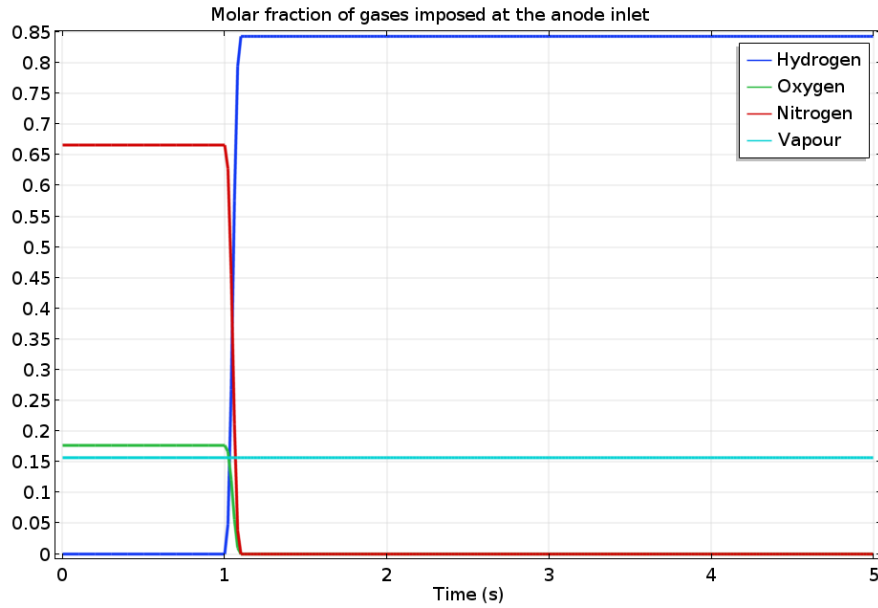
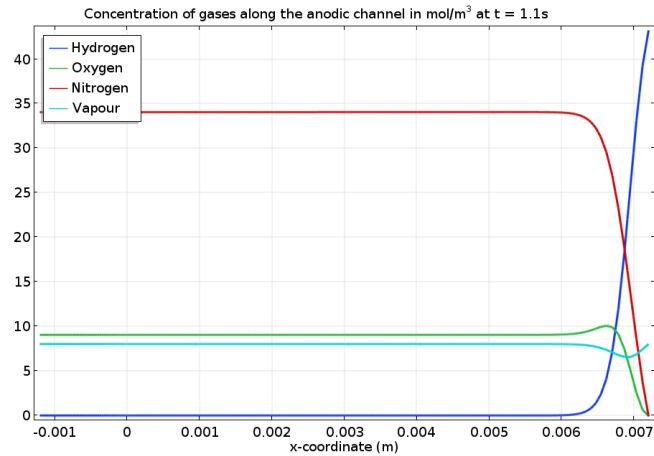


Figure 3.5: Molar fractions imposed at the anode inlet during the startup

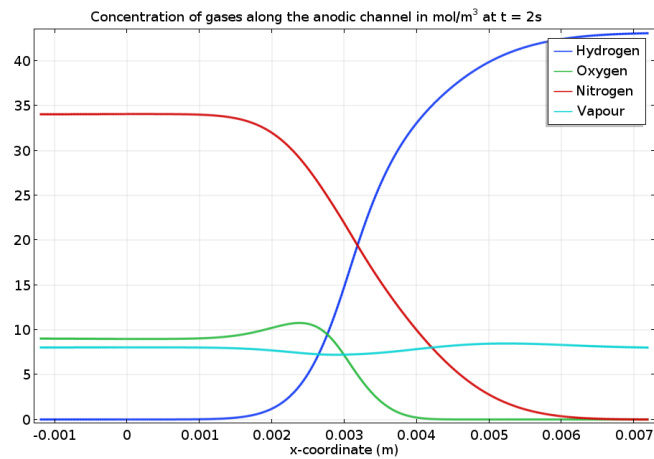
Table 3.2: Geometry values used in the simulations

	Anode	Cathode
Channel depth [m]	$1.4 \cdot 10^{-3}$	$1.4 \cdot 10^{-3}$
Channel length [m]	$5 \cdot 10^{-2}$	$5 \cdot 10^{-2}$
l_{CH} Channel width [m]	$1.4 \cdot 10^{-3}$	$1.4 \cdot 10^{-3}$
l_{Rib} Rib width [m]	$7.92 \cdot 10^{-4}$	$7.92 \cdot 10^{-4}$
e_{GDL} GDL thickness [m]	$2.1 \cdot 10^{-4}$	$2.1 \cdot 10^{-4}$
e_{GDL}^{1MPa} GDL thickness at 1MPa [m]	$1.61 \cdot 10^{-4}$	$1.61 \cdot 10^{-4}$
MPL thickness [m]	$4 \cdot 10^{-5}$	$4 \cdot 10^{-5}$
CL thickness [m]	$6 \cdot 10^{-6}$	$1.2 \cdot 10^{-5}$
MB thickness [m]	$2.5 \cdot 10^{-5}$	

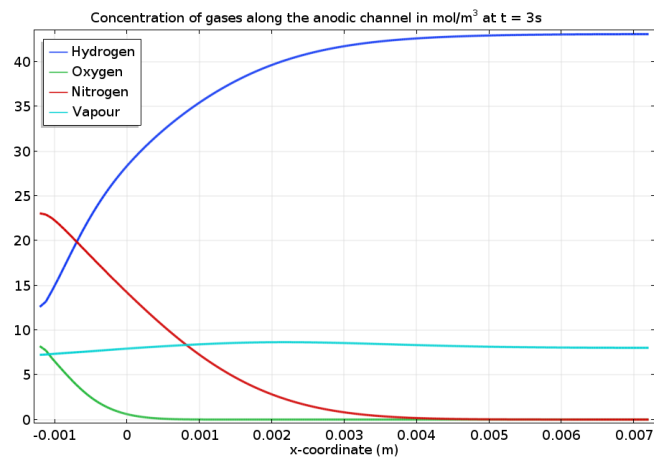
Figure 3.6 shows the concentration of the gases in the anodic channel during different times of a startup. Figure 3.6a shows just after the injection of hydrogen (which is at 1s). The fronts of each concentration are very sharp and effect of gas transport are observed onto the oxygen and vapour profile. Over the duration of startup, the profiles of concentration for each gases are more and more shallow as time passes. For example at 2s, Figure 3.6b shows that the hydrogen front is largely more spread out than at the beginning.



(a) t = 1.1s



(b) t = 2s



(c) t = 3s

Figure 3.6: Concentration of gases along the anodic channel during different phases of startup: (a) 1.1 s, (b) 2s and (c) 3s

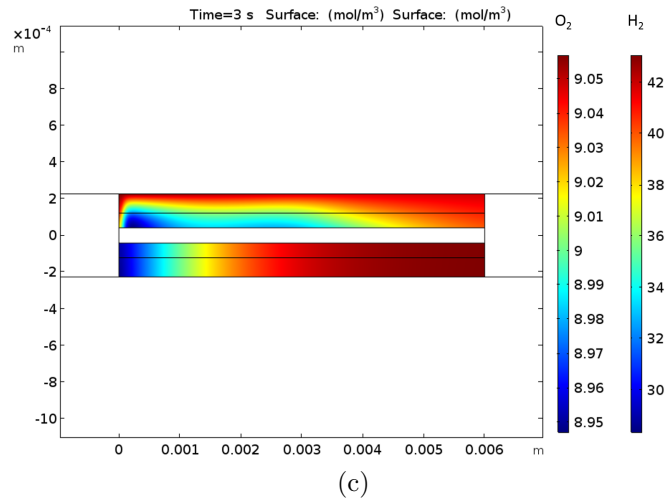
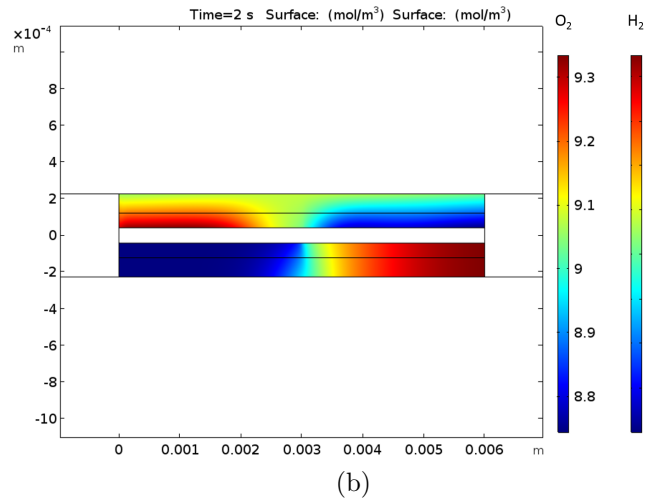
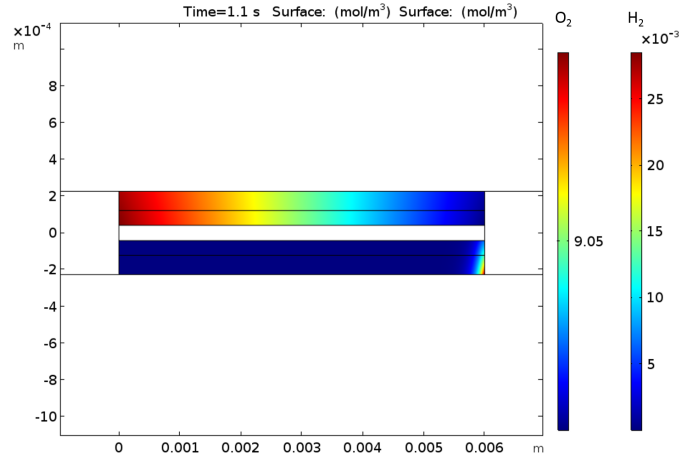


Figure 3.7: Oxygen (top) and hydrogen (bottom) concentrations distributions during different phases of a startup: (a) 1.1 s, (b) 2s and (c) 3s

Figure 3.7 shows the oxygen (cathode) and hydrogen (anode) concentration at different

moments of a startup in the porous media. Figure 3.7a is just during the start of the hydrogen feeding in the anode catalyst layer at 1.1s. Small amount of hydrogen is observed in the porous media especially in the GDL as it arrives in the channel (see Figure 3.6a). Figure 3.7b shows the hydrogen front located in the middle of the anode side at 2s. At the cathode side, oxygen production on the left side (increased concentration) and consumption on the right side (decreased concentration) are observed. Finally, Figure 3.7c shows the end of the startup at 3 s when gas concentrations start to homogenize. Using these concentrations in the equations of section 3.2, the model allows to simulate the local electrode potentials.

Simulation results

Figure 3.8 shows the cathode and anode electrode potentials along the cathode catalyst layer at different times during a startup. A sharp electrode potential front, moving from the right to the left, is observed during the startup with the profiles at 1.6, 1.9, 2.2 and 2.5 second. The two zones at the cathode and anode side described in the Figure 3.3 are defined by an important difference in electrode cathode potential (see Figure 3.8a). The OER takes place where the cathodic electrode potential goes from 1.45 V to 1.62 V in the left side, from the cathode inlet to the location of the H_2/O_2 front while the ORR occurs in the zone where the electrode cathode potential goes from 0.83 V to 0.9 V in the right side, from the H_2/O_2 front to the cathode outlet (Figure 3.8 a). At the anode (Figure 3.8 b), the ORR happens at the left side where the anodic electrode potential goes from 0.75 V to 0.85 V while HOR occurs at the right side at the front with a potential around 0.05 V.

To go further, Figure 3.9 and Figure 3.10 show respectively the electrode potentials close to the inlets and outlets and the cell potential and as function of time during a startup. The start-up can be separated into four phases. Phase 0, is the initial condition before the injection of H_2 . Each electrode potential is around the potential of the couple H_2O/O_2 near 1.23 V. The cell potential is lower than the Nernst potential because it results from a mixed potential between the H_2O/O_2 couple and the H_2/H^+ couple due to the permeation of hydrogen across the membrane. To describe the phase 1 and 2, a closer look on the different reactions happening is necessary.

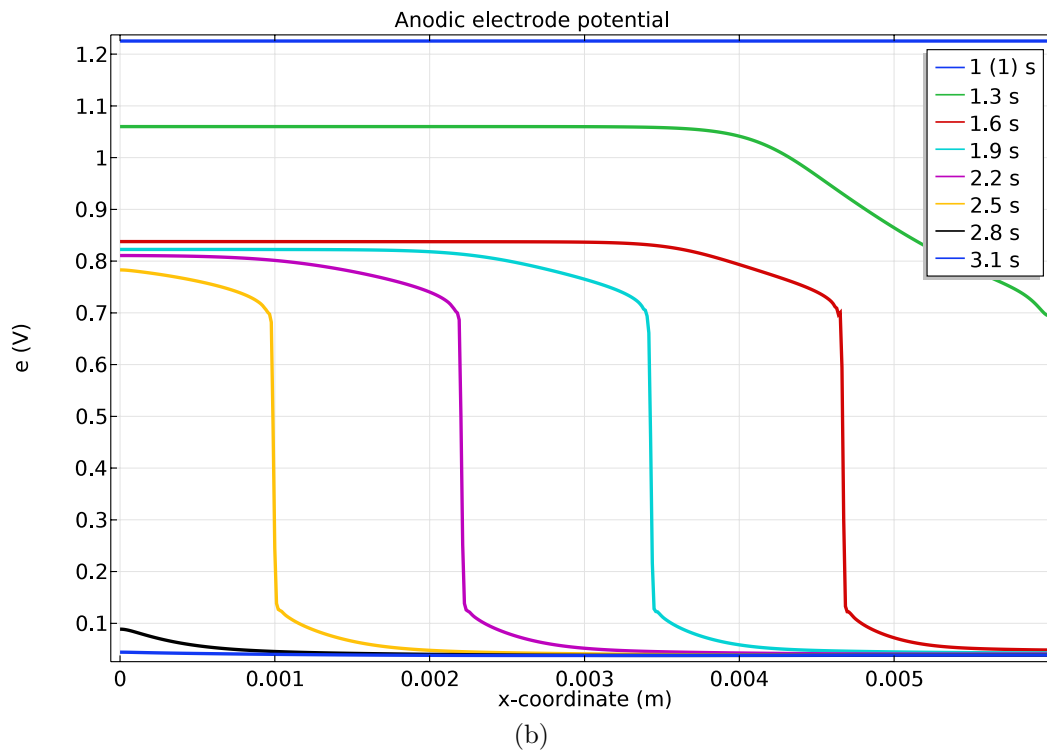
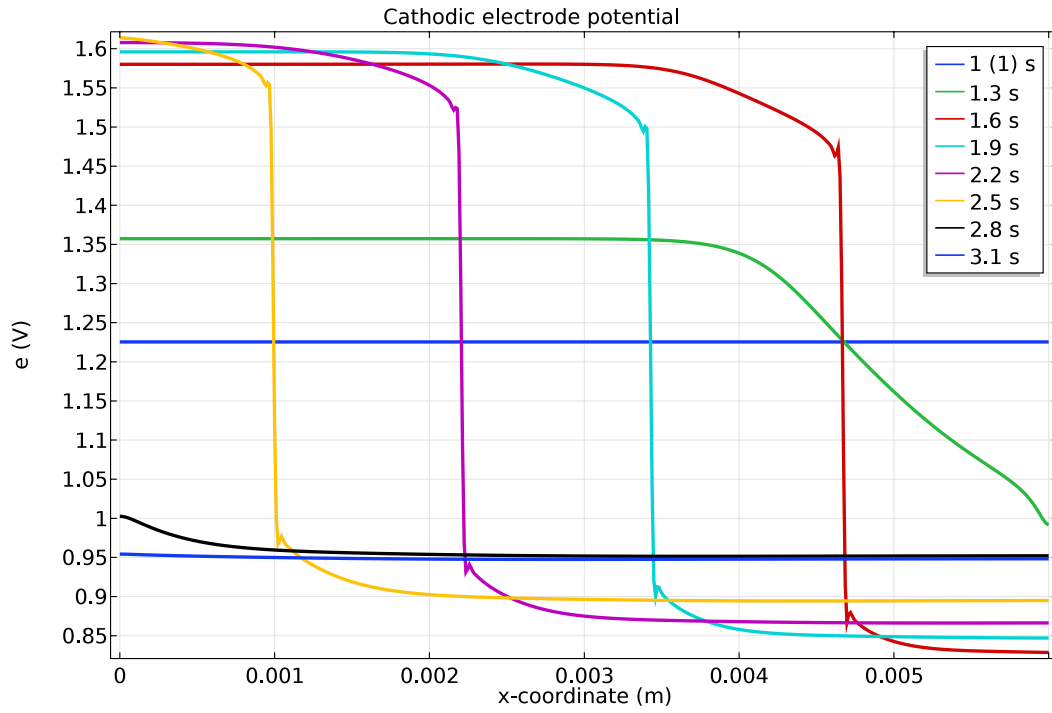


Figure 3.8: Electrode potentials along the cathode (a) and anode (b) catalyst layer during a startup.

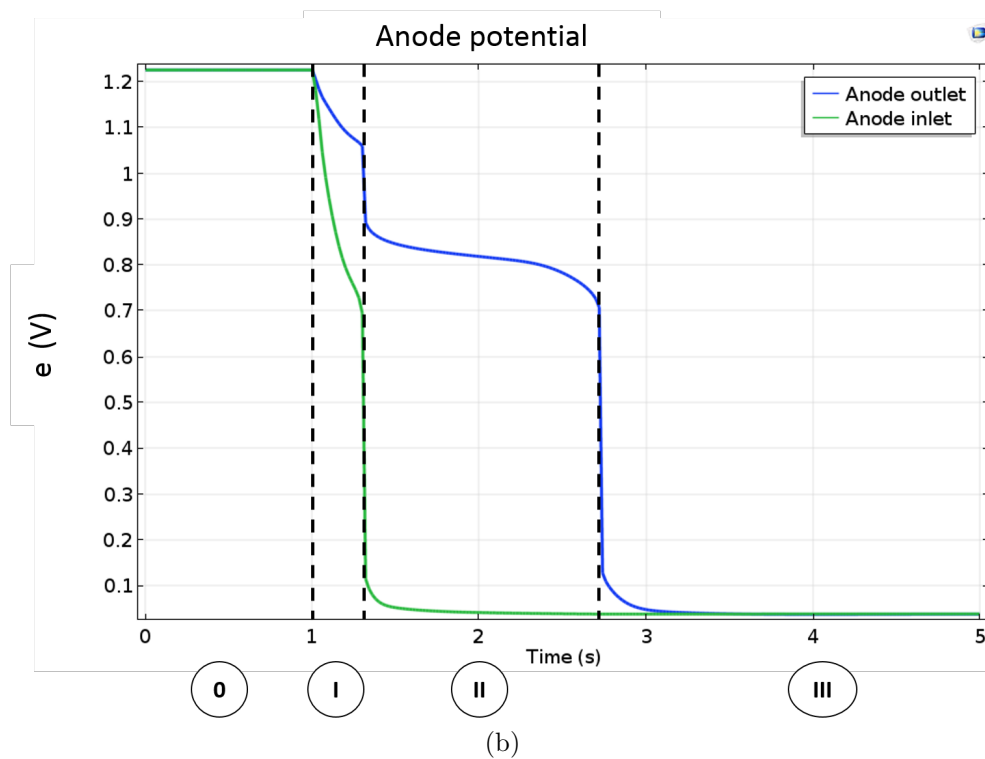
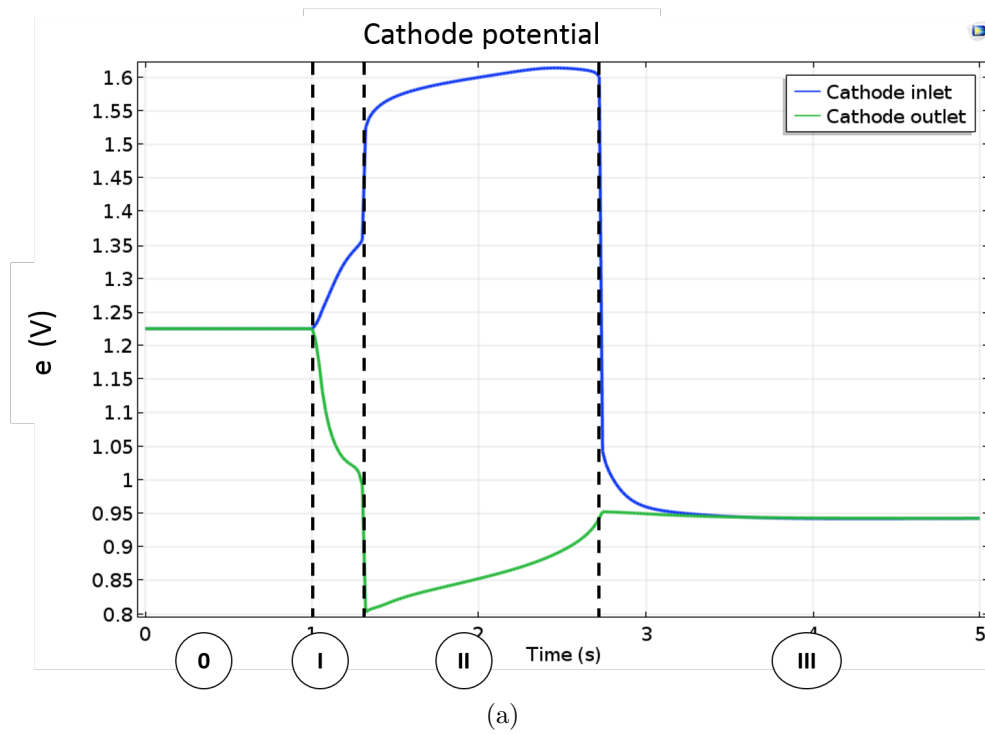


Figure 3.9: Cathode (a) and anode (b) potential in the catalyst layer at the cathode inlet and outlet during a startup

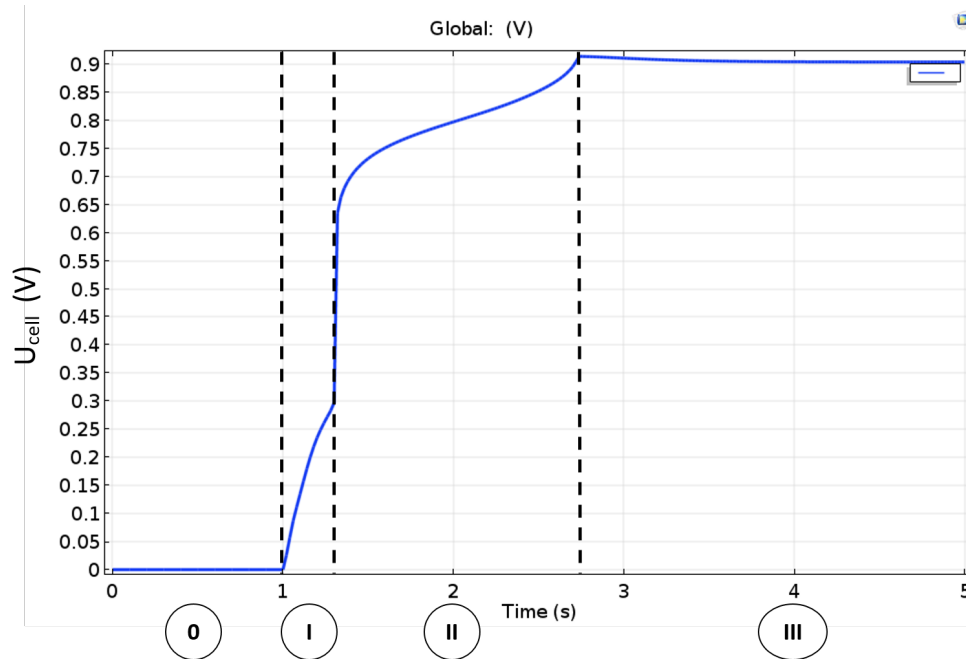
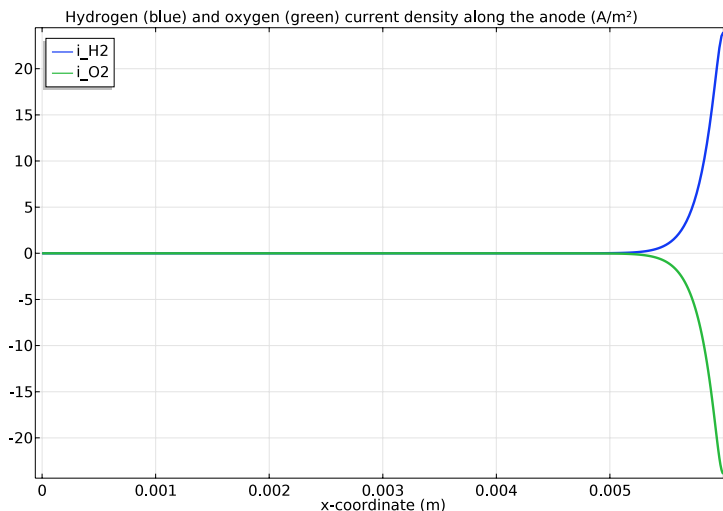
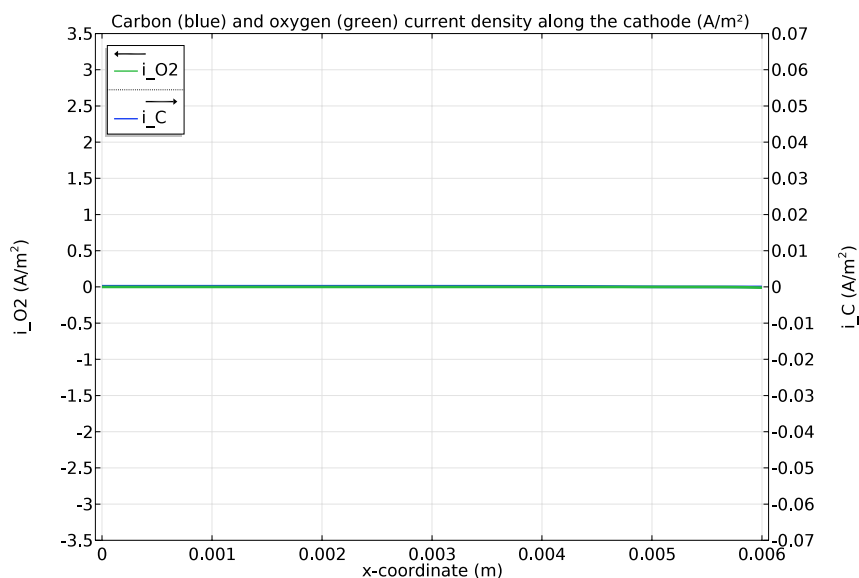


Figure 3.10: Cell potential during a startup

Phase 1 During the phase 1, the cell voltage increases drastically from 0 V to 0.3 V because the anode potential (Figure 3.9b) drops when hydrogen is supplied at the anode inlet (Figure 3.7a) while the cathode outlet potential decreases more slowly (Figure 3.9a). Figure 3.11 presents the currents along the anode and cathode catalyst layers at a moment during phase 1. At the anode, oxidation of hydrogen (blue curve) and reduction of oxygen (green curve) are observed at the same location (i.e. inlet). As no current is observed at the cathode (Figure 3.11b), the remaining oxygen at the anode inlet is reduced thanks to the anode potential drop to consume the protons and the electrons produced by the HOR (Figure 3.11b). At the cathode inlet, the electrode rises to 1.35 V while the one at the anode outlet decreases to 1.05 V (Figure 3.9).



(a) Hydrogen and oxygen current at the anode catalyst layer

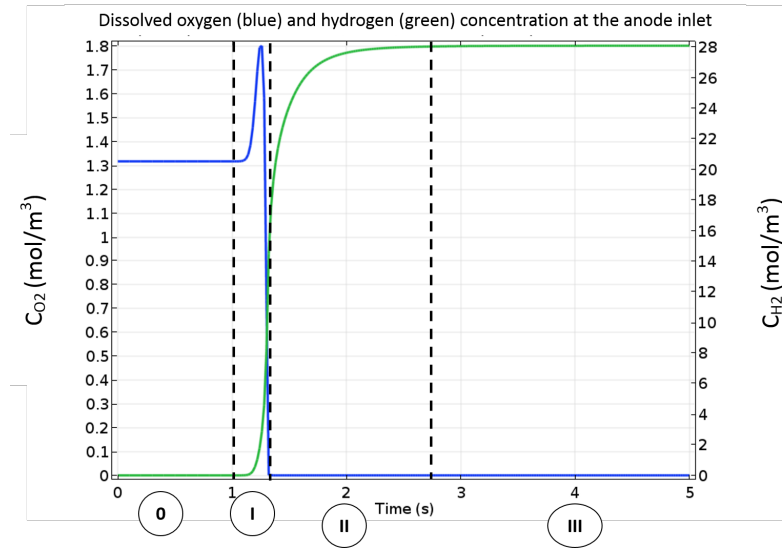


(b) Oxygen and carbon current at the cathode catalyst layer

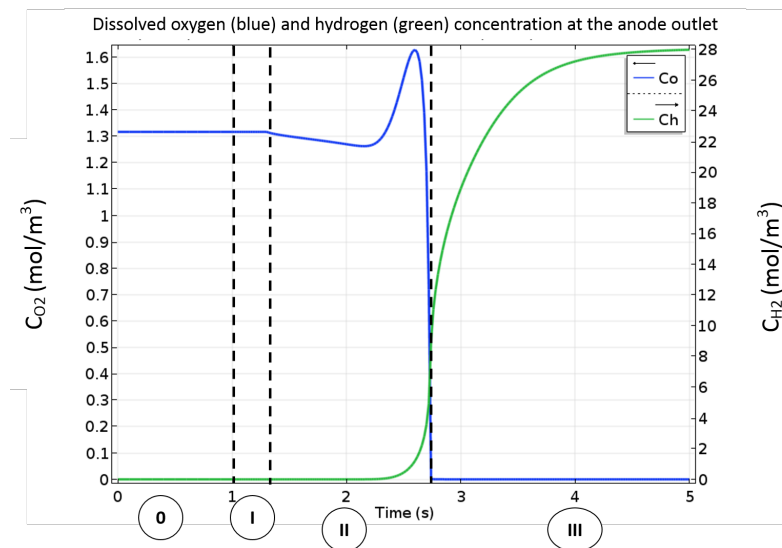
Figure 3.11: Phase 1 current distribution

These discrepancies come from spatial gradient of ionic potential between inlet and outlet where cathode electronic potential is almost the same everywhere. The cathode overpotential is then too low for the OER and too high for the ORR to take place and the cathode current remains equal to zero (Figure 3.11b). During the phase 1, OER as well as ORR currents at the cathode is negligible because the local potential at the cathode is too close to the potential of the H_2O/O_2 couple. Figure 3.8 shows that at 1.3 second when phase 1 ends, there is no front in terms of potentials.

Phase 2 Phase 2 is when the reverse-current decay mechanism occurs from 1.3 to around 2.72 second. At the beginning of the phase 2, the cell voltage leaps from 0.3 V to 0.65 V because the anode potential (Figure 3.9b) drops to zero since there is no dissolved oxygen left in catalyst layer at the anode inlet.



(a)

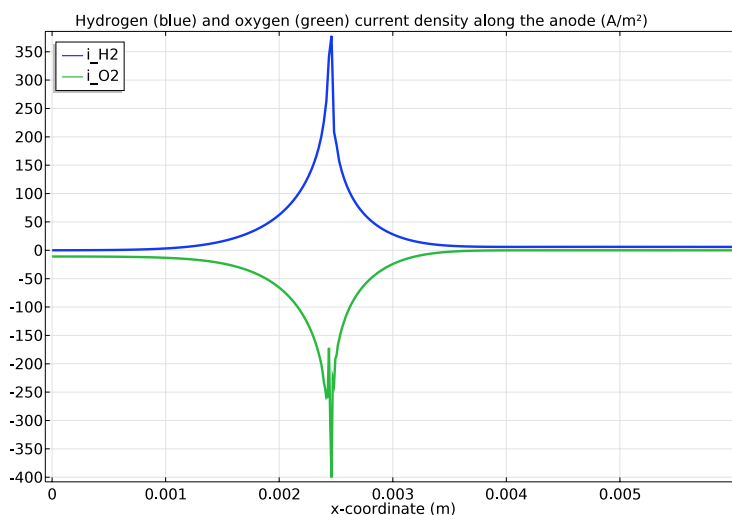


(b)

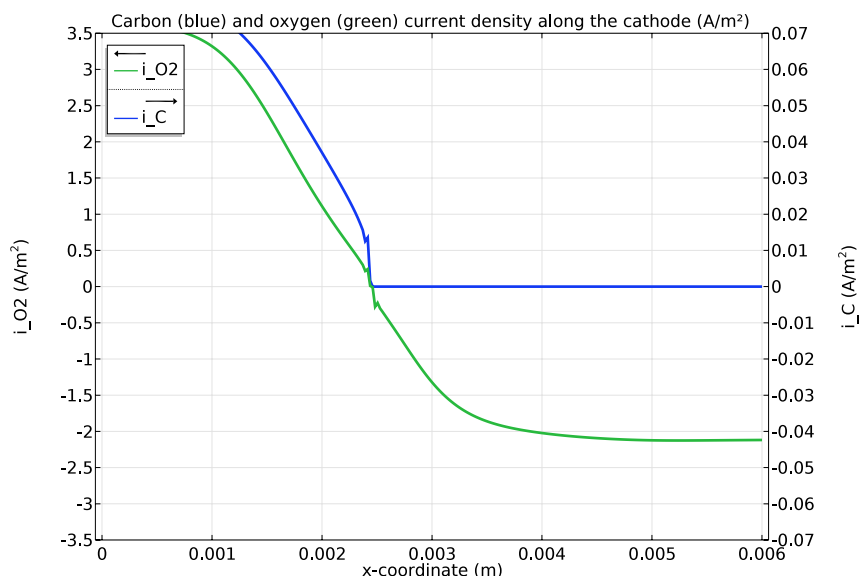
Figure 3.12: Dissolved oxygen and hydrogen in the anode catalyst layer at the anode inlet (a) and outlet (b) as function of time during a startup

Figure 3.12 shows the concentration of dissolved oxygen (blue) and hydrogen (green) at the anodic catalyst layer at the anode inlet and outlet. Figure 3.12a highlights the depletion of dissolved oxygen leading to the phase 2 by showing the evolution of the concentration of dissolved oxygen in the catalyst layer at the anode inlet. The accumulation before the beginning of the

phase 2 comes from the multi-components transport. Dissolved hydrogen concentration starts to ramp up before the beginning this phase at the anode inlet.



(a) HOR and ORR current at the anode catalyst layer



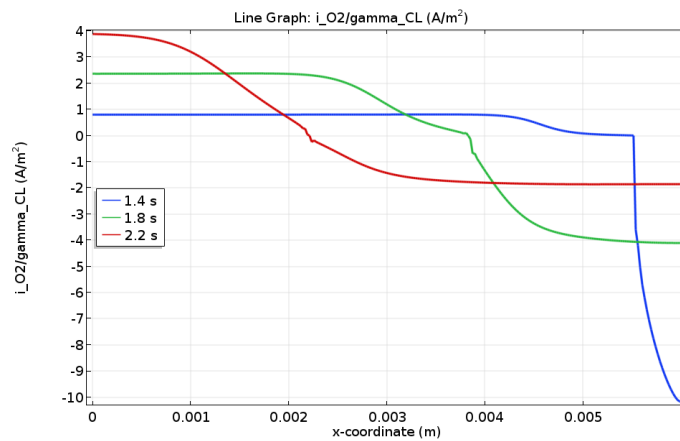
(b) OER, ORR and COR current at the cathode catalyst layer

Figure 3.13: Current distribution during a startup (phase 2)

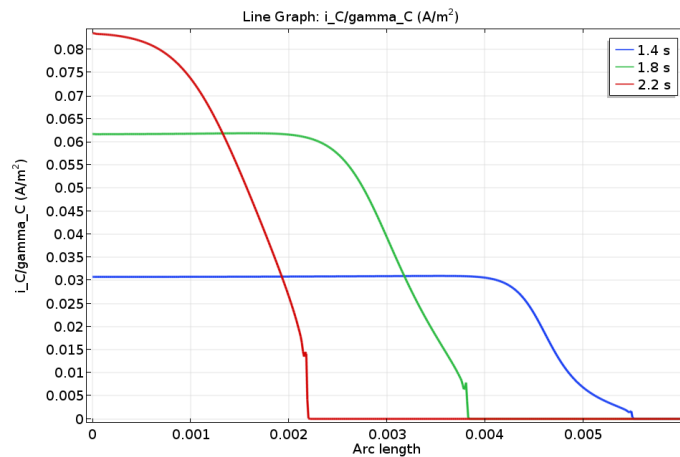
Figure 3.13 presents the currents along the anode and cathode catalyst layers during phase 2. At the anode (Figure 3.13a), HOR and ORR currents peak at the front for the same reasons as during phase 1. At the left side of the front, oxygen reduction current still occurring but at slower rate. Same at the right side of the front where hydrogen oxidation happens. At the cathode (Figure 3.13b), oxygen is reduced at the right side of the front and water is oxidized at the left side (green curve). The potential front (Figure 3.8) is located where the current sign changes. Carbon corrosion occurs at the left side of the front (blue curve) because this is the

area where the potential is close to 1.6 V (see Figure 3.8a).

Figure 3.14 shows the current of either oxygen reduction or water oxidation and carbon corrosion along the cathode catalyst layer during several moments of phase 2. At the left of the front, the current associated to the OER is distributed from the cathode inlet to the front. At the right of the front, the current associated to the ORR is distributed from the front to the cathode outlet. After the front appears (blue line at 1.4s), the current density for the oxygen reduction is higher than the OER one because of the smaller surface available for the reaction. When the front is moving from the anode inlet to the outlet, the ORR current density decreases while OER one is increasing. The current distributions at the cathode catalyst layer for the ORR and the OER is totally different than those at the anode for the HOR and the ORR. Figure 3.14 b shows how the front impacts the COR current density. The closer of the cathode inlet is the front, the higher the current density leading to an high degradation near the cathode inlet as shown by the curve at 2.2 s.



(a)



(b)

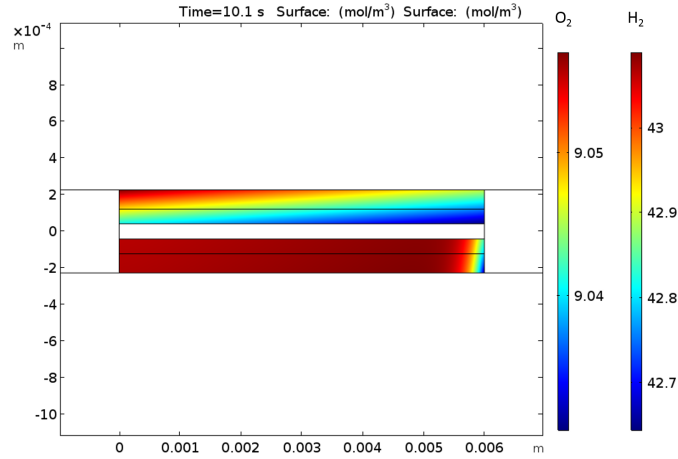
Figure 3.14: OER and ORR (a) and COR (b) current density along the cathode catalyst layer during a startup

Phase 3 At the end of phase 2, the potential overshoots and slightly decrease to attain the OCV during phase 3. At the cathode inlet, the cathode potential collapses from around 1.6 V to 0.95 V (see Figure 3.9b) marking the end of the corrosion of the carbon support. The fuel cell is then ready to operate.

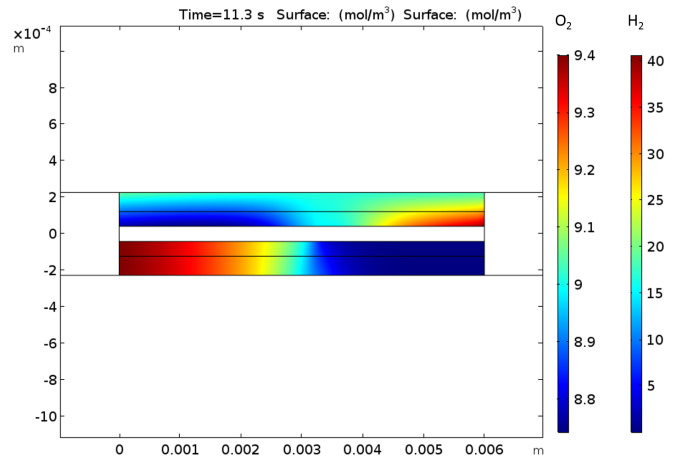
A startup is divided in four phases. Phase 0 is when the anode is full of air. Phase 1 is the creation of the hydrogen air front. During this phase, hydrogen starts to arrive at the anode catalyst layer and is oxidized. At the same location, the protons and electrons produced by this oxidation are consumed by the remaining oxygen. When at the anode inlet there is no more oxygen, phase 1 ends. Phase 2 is the moment when the reverse-current decay mechanism occurs. The hydrogen/air front moves from the anode inlet to the outlet and creates an ionic potential front. This ionic potential front divides the cell in two parts: a standard operating fuel cell and a air/air configuration. In this air/air configuration, the cathode potential reaches 1.6 V causing the corrosion of the carbon support. When the hydrogen/air front attains the anode outlet and all the remaining oxygen is consumed at the anode, phase 2 ends.

3.3.2 Simulation of mechanism during a shutdown

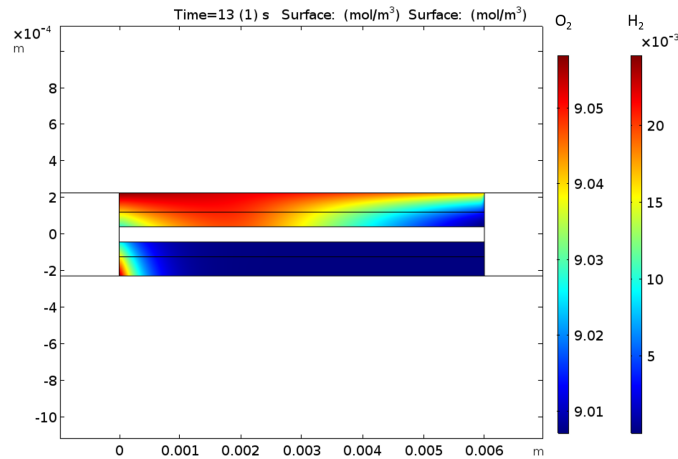
This section gives another view of the simulation of the reverse-current decay mechanism during the PEMFC shutdown. Figure 3.15 presents the concentrations of the reactants at different moment of a shutdown from 10 s. Figure 3.15a shows the arrival of air inside the anode porous media at 10.1 s. Figure 3.15b simulates the air front in the middle of the anode side at 11.3 s provoking oxygen production on the right and consumption on the left because of the reverse-current mechanism. Figure 3.15c shows the end of the shutdown when air almost filled up the anode compartment at 13s. Figure 3.16 shows the cathode and anode electrode potential along the cathode catalyst layer during a shutdown. Same profiles are observed as the startup at the cathode but the high potential zone ($e > 1.45\text{ V}$) is switched at the right side of the front and the lower potential zone ($e < 0.95\text{ V}$) is at the left side (Figure 3.16a). At the anode (Figure 3.16b), the HOR occurs at the left side of the front ($e < 0.1\text{ V}$) and the ORR at the right side of the front ($e > 0.75\text{ V}$).



(a)



(b)



(c)

Figure 3.15: Oxygen (top) and hydrogen (bottom) concentrations distributions during different phases of a shutdown: (a) 10.1 s, (b) 11.3 s and (c) 13 s

Figure 3.17 and Figure 3.18 show respectively the cell and the electrodes potentials at the

inlets and outlets as function of time during a shutdown. The same four phases as described during startup are observed.

Phase 3 Phase 3 is here the initial condition before the air is supplied to the anode.

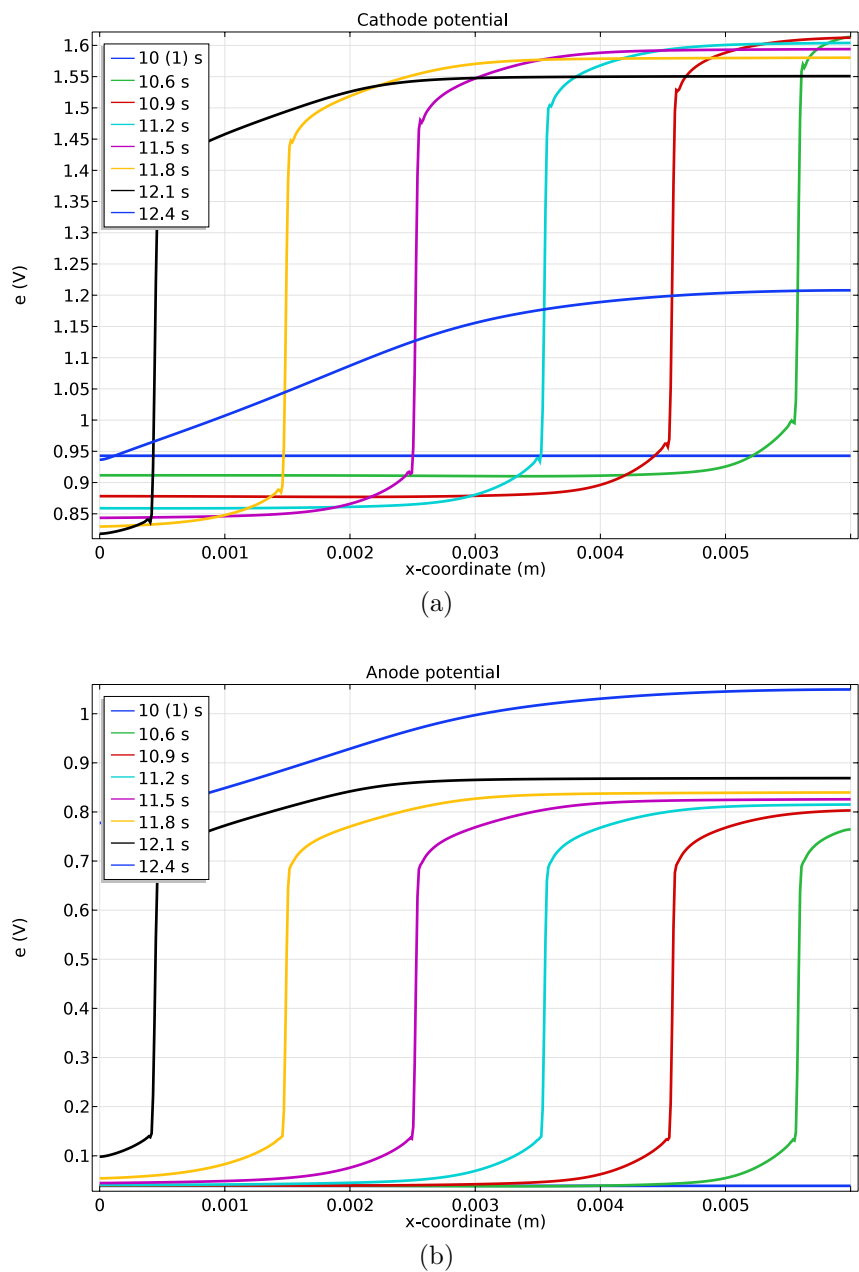


Figure 3.16: Electrode potentials along the cathode (a) and anode (b) catalyst layer during a shutdown

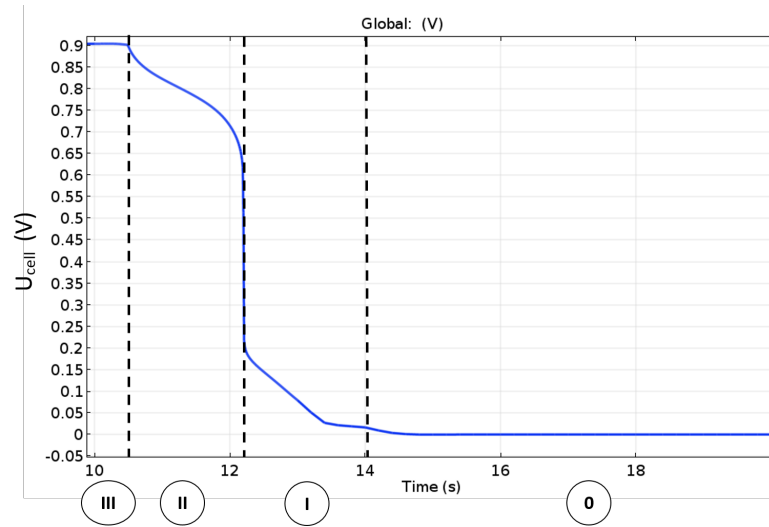


Figure 3.17: Cell potential during a shutdown

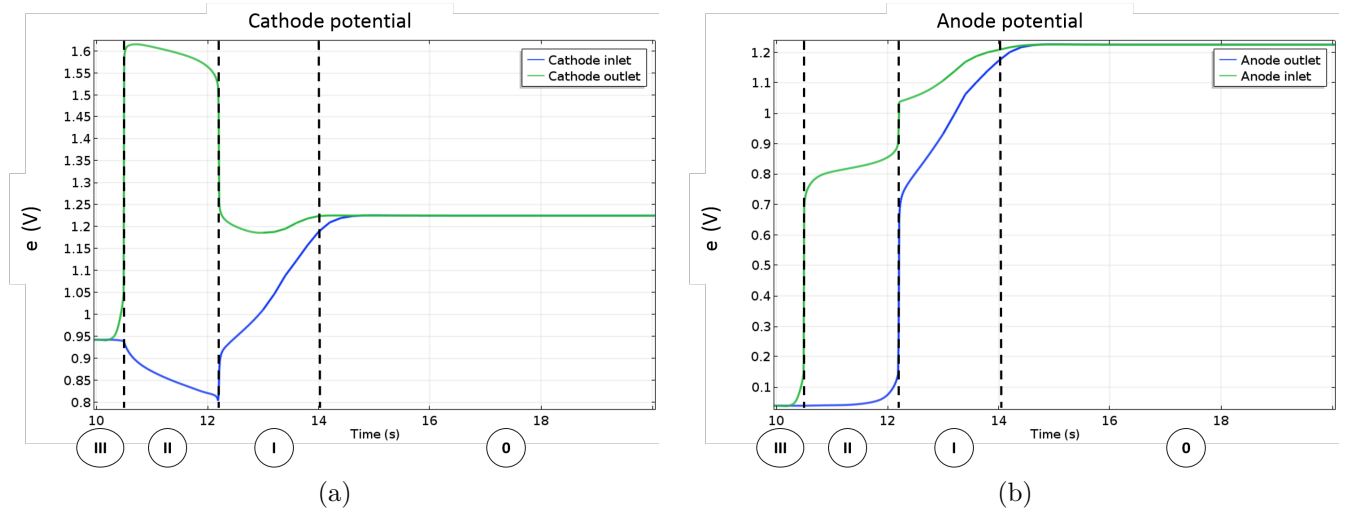


Figure 3.18: Cathode (a) and anode (b) potential in the catalyst layer at the cathode inlet and outlet during a shutdown

Phase 2 Phase 2 is shorter during a shutdown than a startup lasting around 30% less time. During this phase the cell potential decreases from 0.9 V to 0.65 V (same value as startup). Figure 3.19 shows the currents along the anode and cathode catalyst layer at a moment during phase 2. The same profiles are observed as during the startup: hydrogen oxidation and oxygen reduction peaks at the anode (Figure 3.19a). At the cathode, oxygen reduction and water oxidation occurs respectively at the left side and at the right side of the front. The corrosion happens only at the right side of the front where water is oxidized (Figure 3.19b).

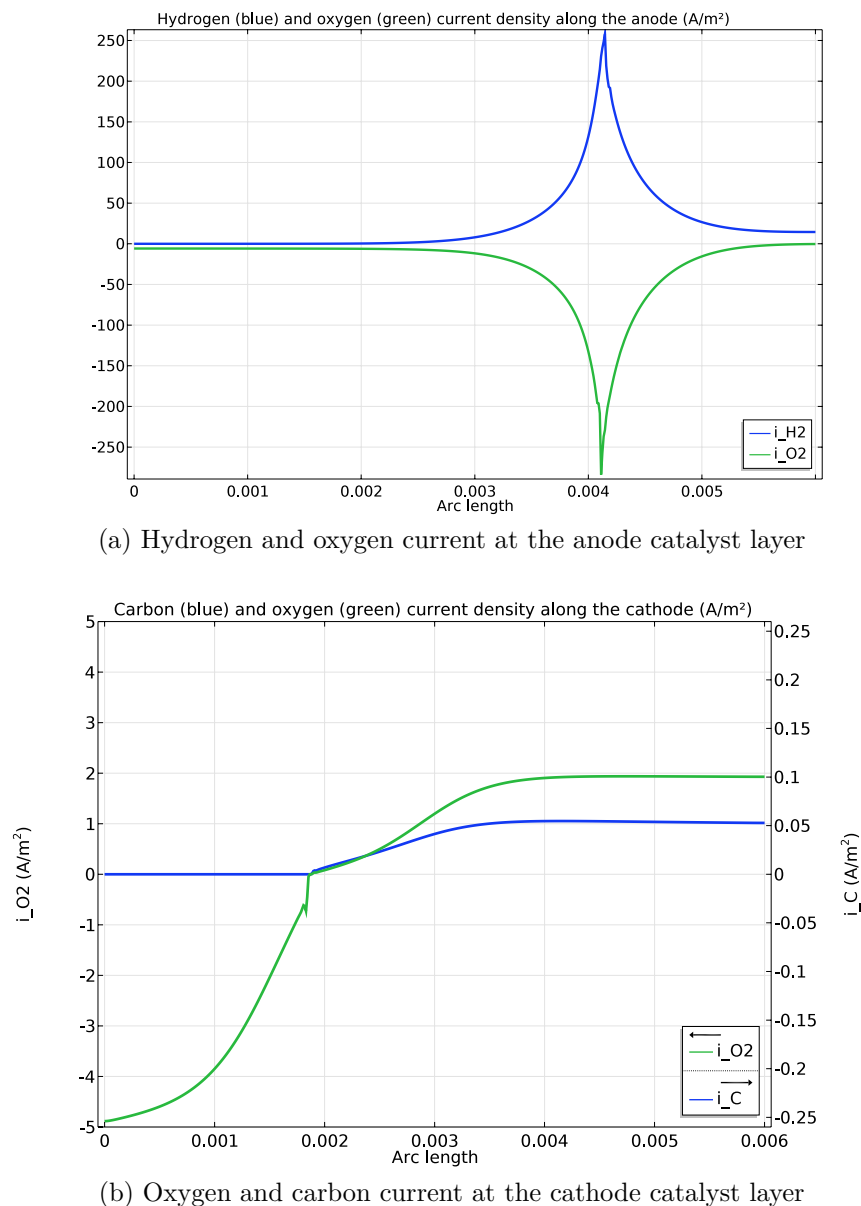


Figure 3.19: Current distribution during a shutdown during phase 2

Figure 3.20 presents the concentration of dissolved oxygen (blue) and hydrogen (green) at the anode inlet and outlet. The beginning of the phase 2 is marked by the apparition of dissolved oxygen at the anode inlet and its end when it reaches at the anode outlet. In both cases, it depends on the velocity of oxygen supply and its consumption by the remaining hydrogen. In the case of a startup, the limitation is the supply of hydrogen and the consumption of oxygen. For a shutdown it is the supply of oxygen and then the consumption of hydrogen. However when the hydrogen supply is stopped, the remaining hydrogen is also consumed by its permeation to the cathode and the permeation of oxygen to the anode. It could explain the shortest time of the phase 2 during shutdown than startup.

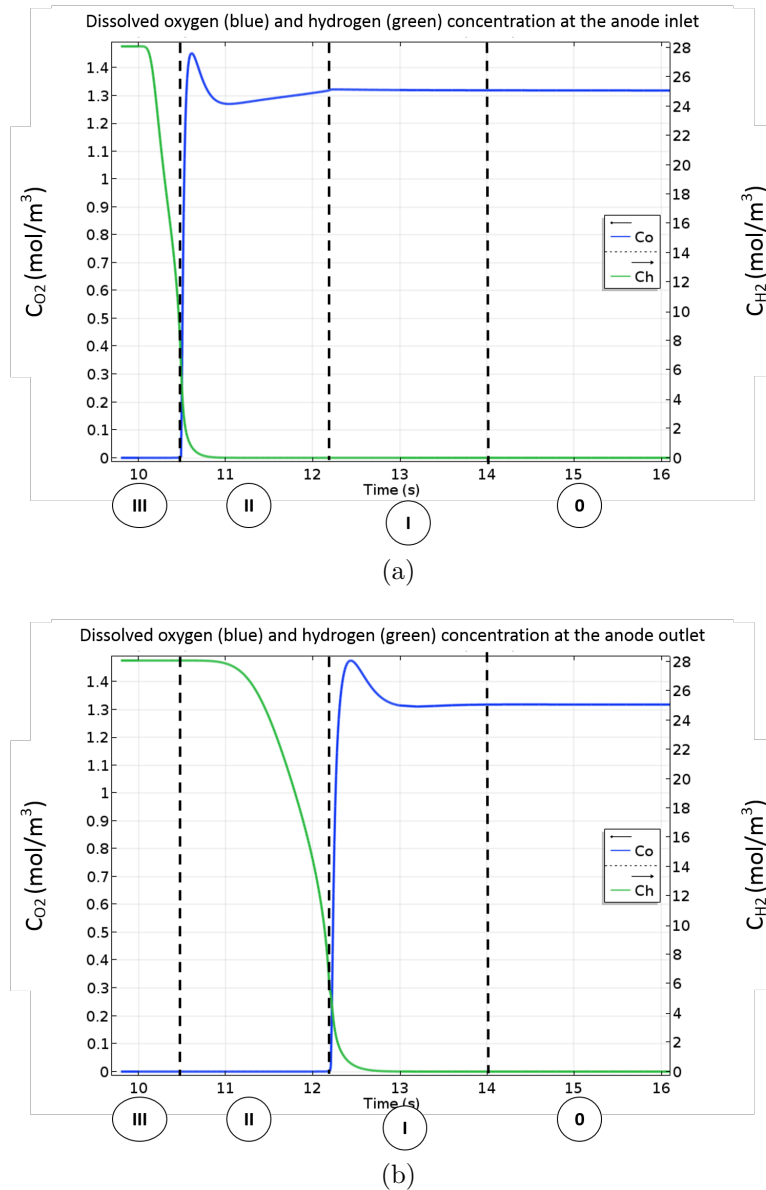


Figure 3.20: Dissolved oxygen and hydrogen in the anode catalyst layer at the anode inlet (a) and outlet (b) as function of time

Phase 1

Phase 1 is considerably longer in a shutdown than in a startup lasting around 2.6 s. Furthermore, the cell potential presents different events that will be called phase 1A and 1B. Phase 1A is the first slope between 12.2 s and 13.4 s that corresponds to the depletion of all the dissolved hydrogen in the anode catalyst layer at the outlet (see Figure 3.20b). Indeed, when the hydrogen is fully consumed at the anode there is no more mixed potential here (Figure 3.18b). The phase 1B corresponds to the concentration of dissolved hydrogen at the cathode inlet in the cathode catalyst layer reaching zero at 14s (Figure 3.21a). Figure 3.21 presents the dissolved

concentration during a shutdown in the cathode catalyst layer at the outlet and inlet. The green curve in Figure 3.21b depicts that the concentration of dissolved hydrogen reaches zero at 14s marking the end of the shutdown.

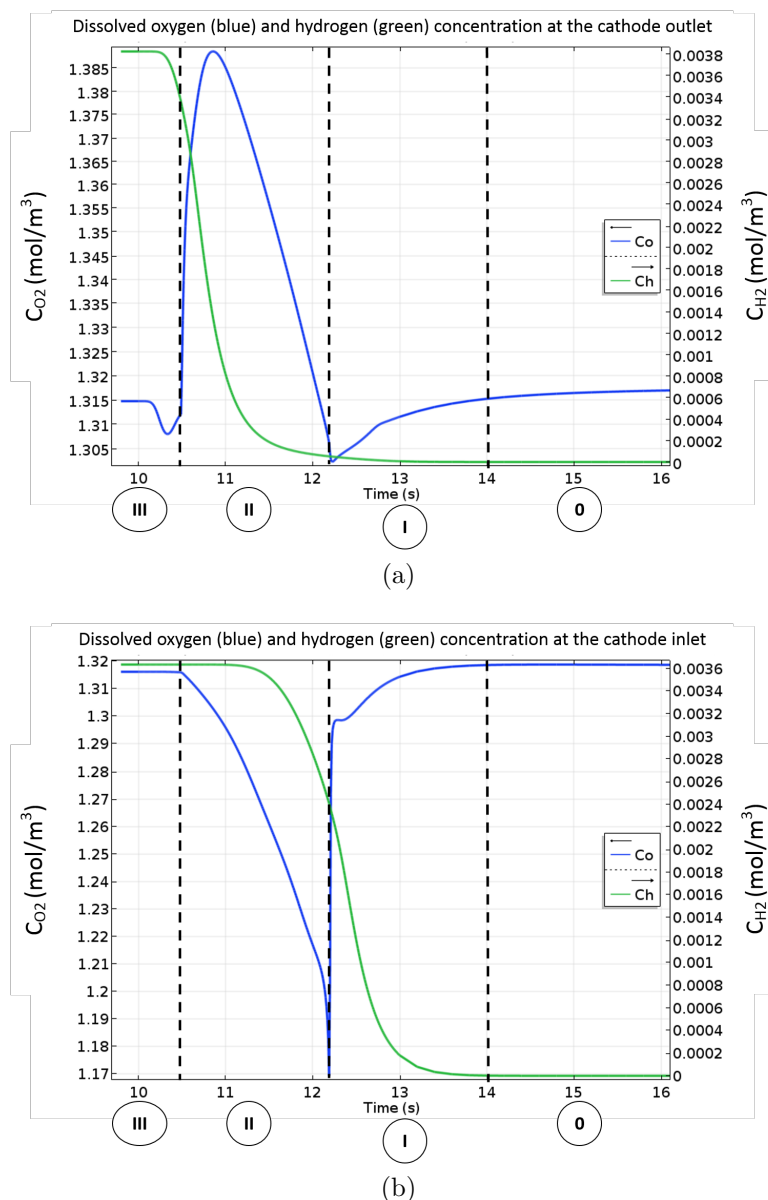
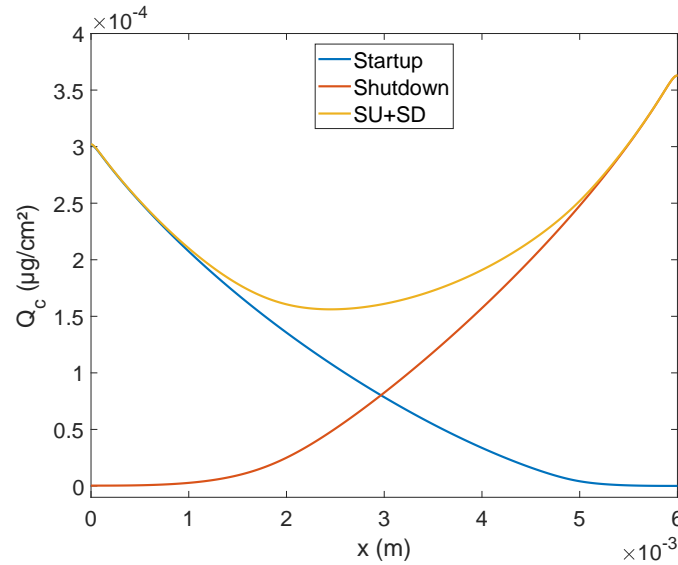


Figure 3.21: Dissolved oxygen and hydrogen in the cathode catalyst layer at the cathode outlet (a) and inlet (b) as function of time

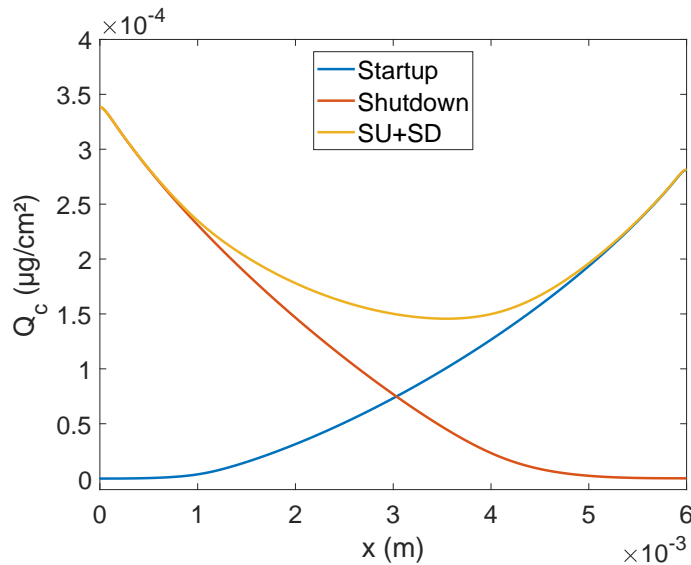
During a shutdown, same phases described for the startup are used but in reverse order. Whereas phase 2 during a startup is the consumption of the remaining oxygen in the anode, it is its apparition in the anode for a shutdown. Furthermore, phase 2 is shorter during a shutdown because the consumption of hydrogen is sped up by the crossover of oxygen from the cathode. Some slight differences are also observed during phase 1 because of the slow consumption of the

remaining hydrogen at the anode.

Figure 3.22 shows the predicted cumulated carbon loss distribution along the cathode flow-field for a startup and a shutdown and combining the both in counter flow and co flow. The results shows an asymmetrical loss distribution.



(a) Counter-flow



(b) Co-flow

Figure 3.22: Predicted cumulated carbon loss distribution along the cathode flow-field for a startup and a shutdown for a counter-flow and a co-flow

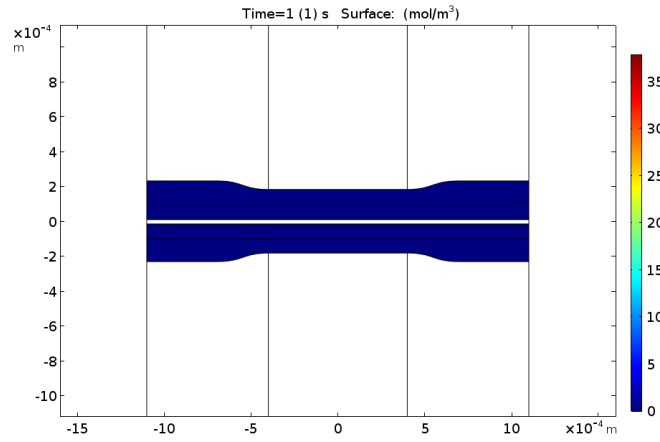
The model predicts the shutdown corrodes more than the startup when the flow fields are in counter-flow or in co-flow. Even though phase 2 during shutdown is shorter in counter flow, the corrosion current is higher at the cathode outlet during the shutdown than the one at the

cathode inlet during the startup, leading to an higher corrosion for the shutdown. Nevertheless the difference is very small. In co-flow, the corrosion is a little lower for example during a startup, the highest corroded location (cathode outlet) shows around $2.7 \mu g_c/cm^2$ whereas in counter flow it shows around $3 \mu g_c/cm^2$ (at the cathode inlet) which is a difference of 10 %. Same differences are observed during shutdown.

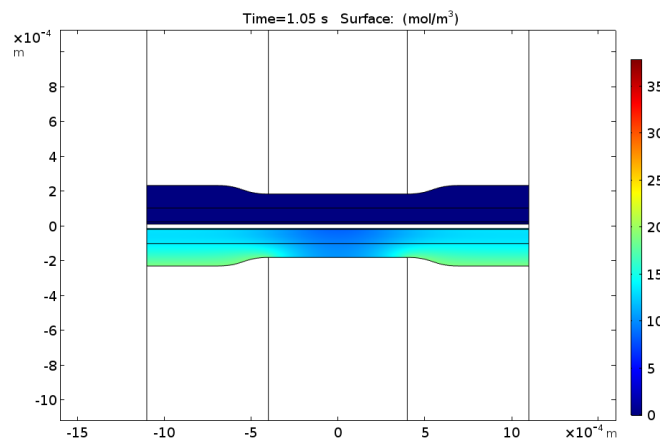
3.3.3 Rib-channel

Heterogeneities in carbon corrosion between rib-channel have been proven possibly significant in certain conditions [111][7]. Figure 3.23 shows the simulated concentration of hydrogen in porous media under the channel and rib during a start-up at the anode inlet. The results are obtained by rib-channel model (Figure 3.4b) which allows to simulate the gas transport in both the GDL and catalyst layer. Channels are supposed parallel and supplied at the same time which means that hydrogen arrives simultaneously at each side of the rib. For the anode inlet, same concentrations profile as the along the channel model are applied at the channel/GDL boundary (Figure 3.7). Figure 3.23a and Figure 3.23c show respectively before the arrival of the hydrogen at 1 s and when the compartment is full of hydrogen at 1.1 s. Figure 3.23b presents the concentrations when hydrogen is supplied at 1.05 s. A gradient is clearly observed in the porous media between the region under the channel and the other under the rib exhibiting the slower transport in the later domain.

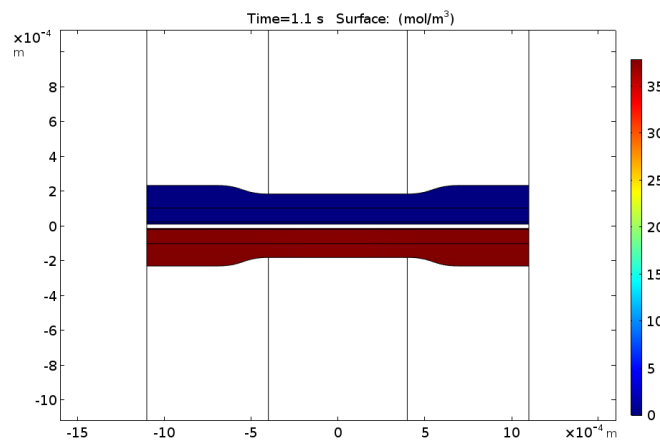
Figure 3.24 presents a schematics of a PEMFC during startup at the rib/channel scale when hydrogen arrives from the channel and diffuses through the porous media. When hydrogen starts to arrive at the anodic catalyst layer under the channel, same mechanisms as the along the channel is expected (see Figure 3.3a). Hydrogen oxidation and oxygen reduction occurs under the anodic channel while oxygen reduction and water oxidation takes place under the anodic rib. Indeed, because of the necessity for the hydrogen to diffuse under the anodic rib, local fuel starvation occurs creating an hydrogen front perpendicular to the one coming along the channel. Potentials are thus expected to follow the same variations as along the channel mechanism.



(a) 1 s



(b) 1.05 s



(c) 1.1 s

Figure 3.23: Hydrogen concentration during startup before the hydrogen front (a), during (b) and after (c) at the anode inlet

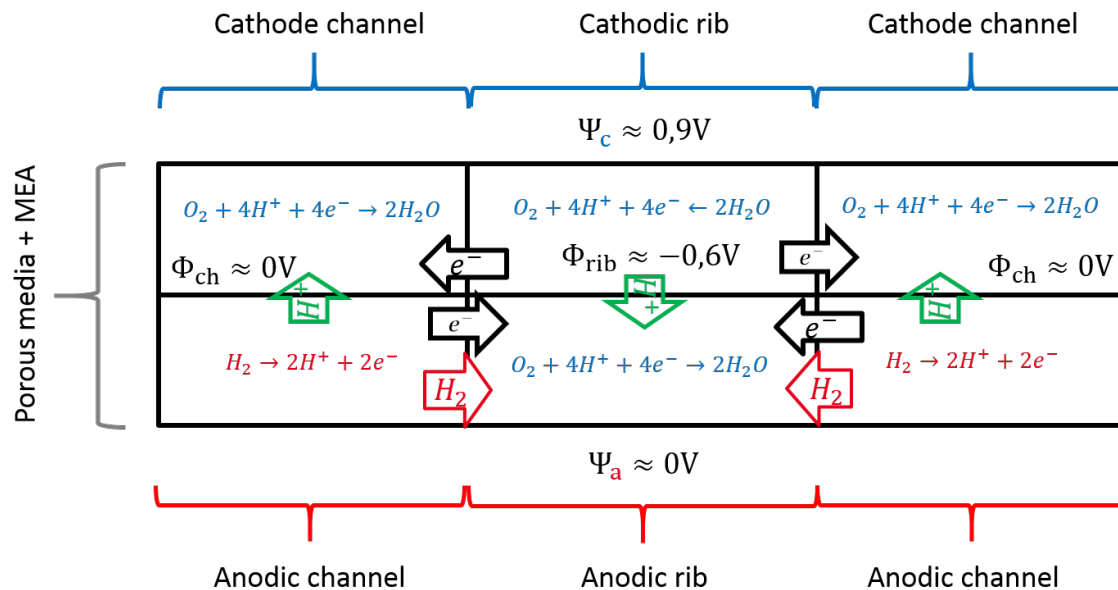


Figure 3.24: Schematics of expected potentials during a startup at the rib/channel scale

Figure 3.25 shows the dissolved hydrogen and oxygen concentration in plane at the middle of the anode catalyst layer during a startup at the inlet. After 1.048 s, the dissolved oxygen concentration under the channel decreases rapidly to reach zero whereas at the middle of the rib, there is still some dissolved oxygen. Its consumption is linked to the arrival hydrogen that is oxidized supplying protons and electrons for the reduction of oxygen. This phenomena is similar to the one observed during the phase 1 with the along channel model. The temporal evolution of the electrode potentials is linked with the evolution of dissolved gas concentrations. The cathode electrode potential is influenced through the ionic potential by the anode electrode potential. As explained in subsection 3.3.1, the anode electrode potential is enforced to be close to zero by the arrival of hydrogen at the anode catalyst layer. Figure 3.26 presents the electrode potentials in-plane in the middle of the catalyst layer during a startup at the anode inlet.

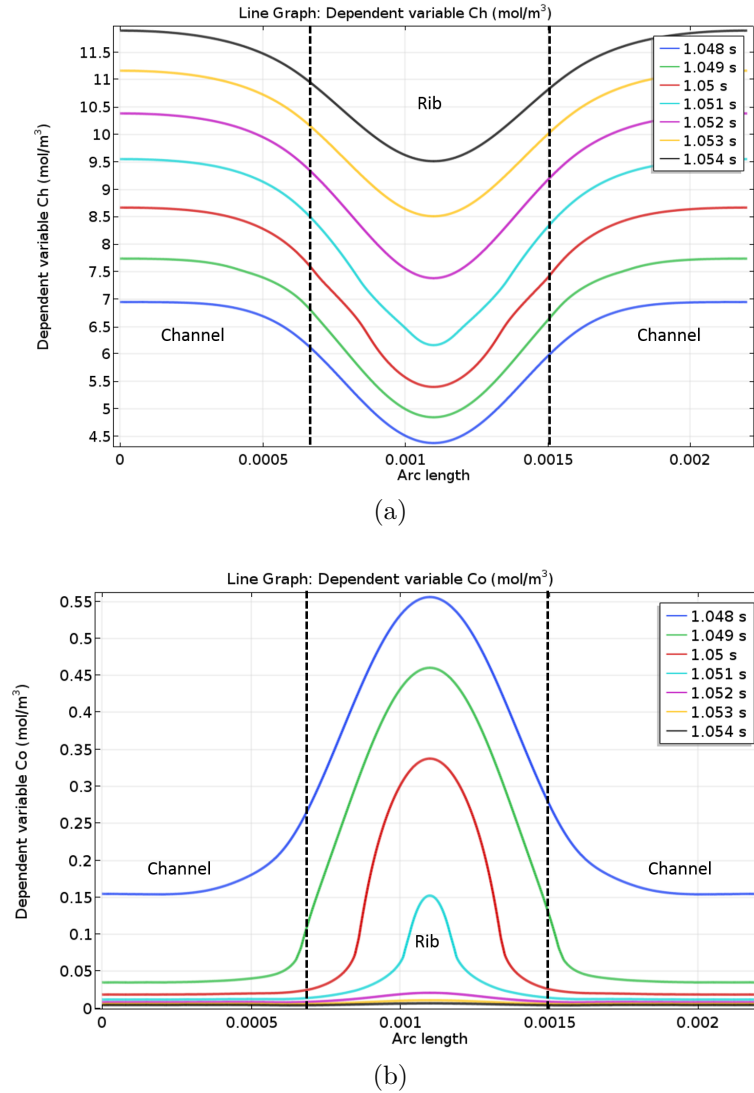
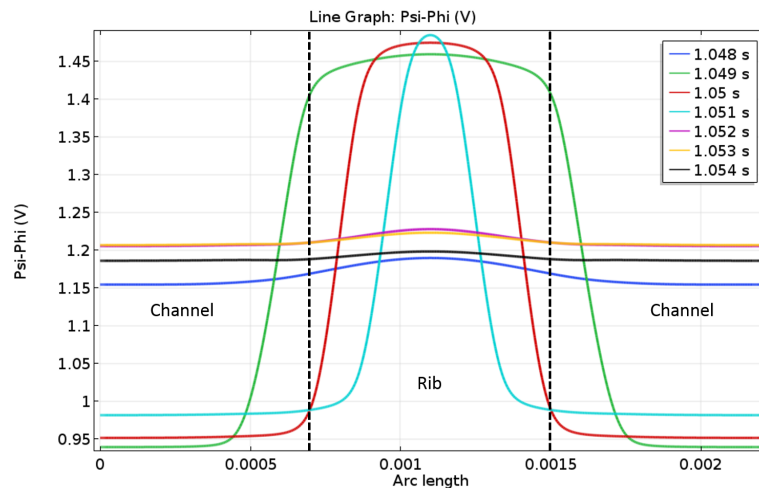
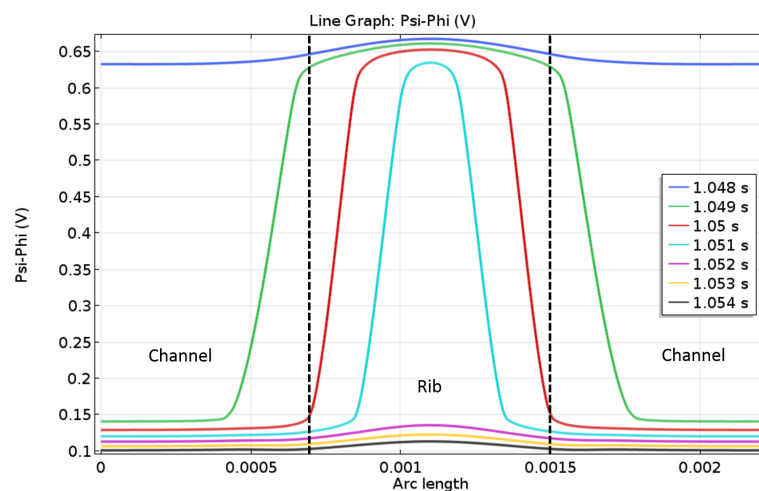


Figure 3.25: Dissolved hydrogen (a) and oxygen (b) concentrations in plane of the middle of the anode catalyst layer during a startup at the anode inlet

The blue curve at 1.048 s shows the electrode potential before the establishment of the reverse current mechanism (around 1.15 V). Later, two potential leaps are observed from each side of the ribs (1.049 s). Because of the hydrogen arriving to the anode catalyst layer, anode potential under the channel drops close to 0 V (Figure 3.26b). However, the slower transport under the rib avoid the hydrogen to arrives simultaneously leading to a potential still over 0.5 V in the middle of the rib. Therefore, the cathode potential goes over 1.4 V in this area whereas under the channel it collapses under 1 V. Both of them converging into the middle of the rib to finally disappear at 1.052 s. Thus, the middle of the rib sees the highest potentials close to 1.5 V for the longest time.



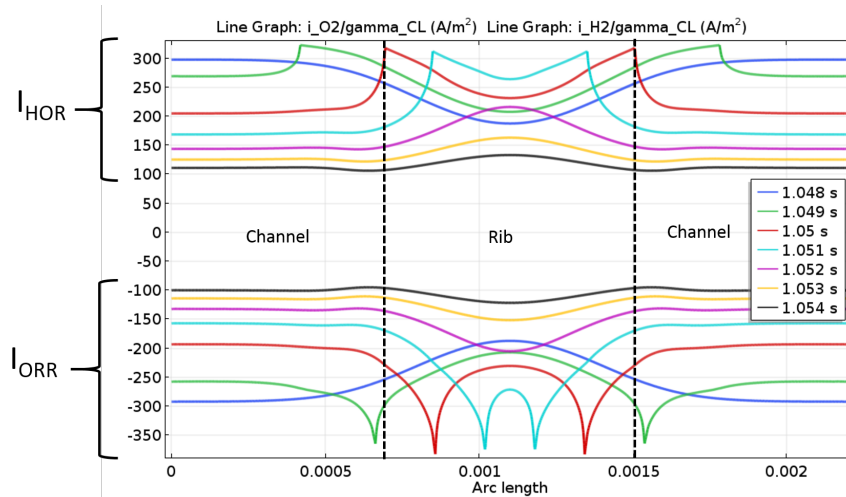
(a) Cathode



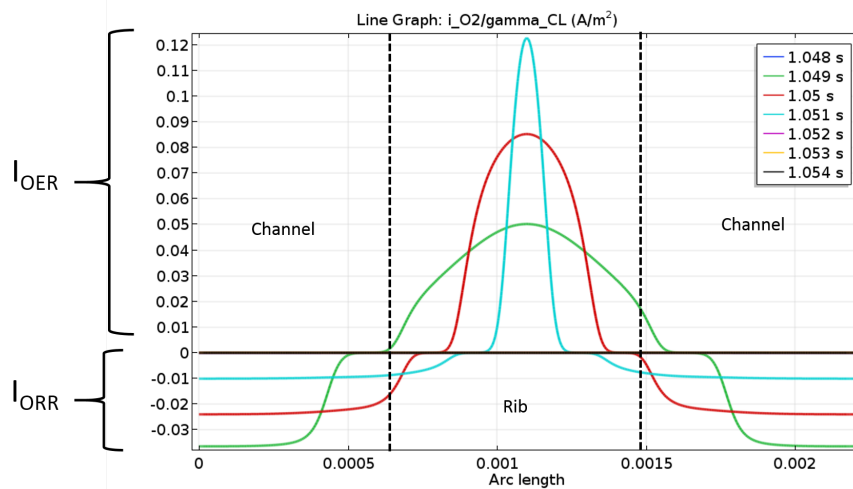
(b) Anode

Figure 3.26: Cathodic (a) and anodic (b) electrode potentials along the catalyst layers during a startup at the anode inlet (rib-channel model)

Figure 3.27 presents the currents in plane along the middle of the anode and cathode catalyst layers during a startup at the anode inlet. At the anode, Figure 3.27a shows the HOR with the positive currents and the ORR with the negative currents at different times of the startup. At the same time of presence of potential leaps in Figure 3.26 (1.049 to 1.051 s), both current distributions present two symmetrical spikes where the oxygen ones are more pronounced. It seems a of reverse current mechanism occurs where at the front, the hydrogen oxidized at one side is a supply of protons and electrons for the oxygen reduced at the other side. This hypothesis is strengthened by Figure 3.27b when during these potential leaps, OER occurs at the middle of the rib and ORR at the middle of the channel however with very low current values. Because of the cathode potential distribution, carbon corrosion can occur only under the rib.



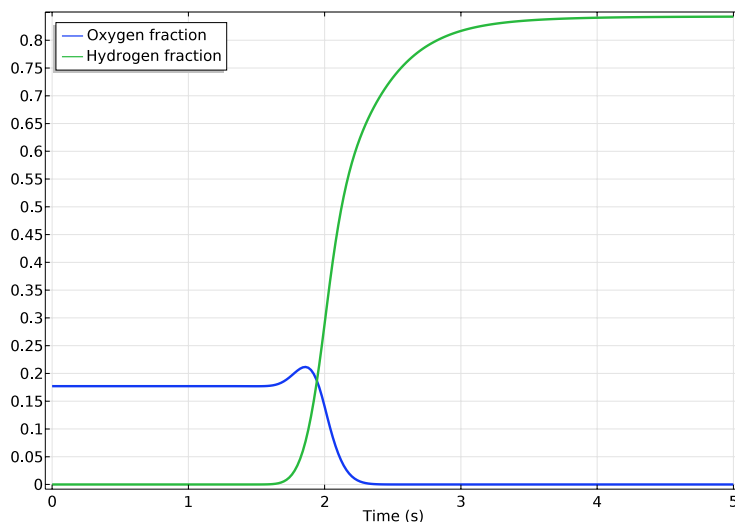
(a) Hydrogen (top) and oxygen (bottom) current distribution at the anode



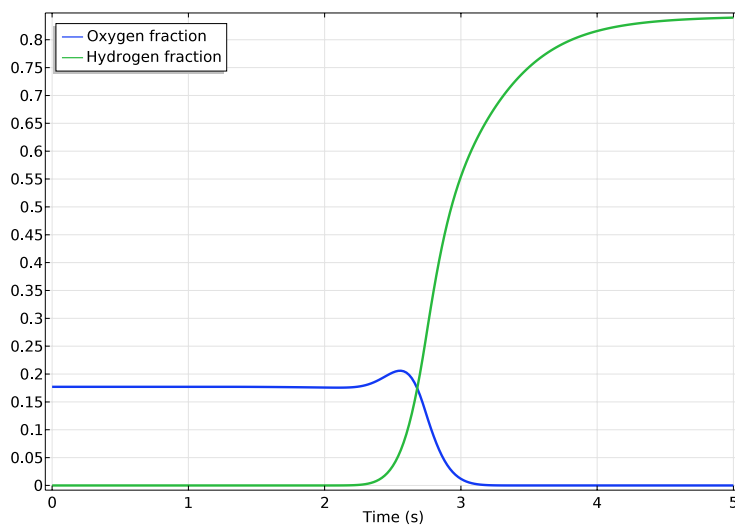
(b) Oxygen current distribution at the cathode

Figure 3.27: Current distribution in plane at the anode (a) and cathode (b) catalyst layer during a startup at the anode inlet

Farther from the anode inlet, the cathode electronic potential profile for the BP boundary condition is obtained from the along the channel model. This electronic potential is equal the cell potential as the anode electronic potential is set to 0 V (see Figure 3.10). Assuming that the hydrogen flows faster in the channel than in the porous media, the boundary condition at the channel/GDL interfaces at the anode middle and outlet for the gas fractions are extracted from the along the channel model and is shown in Figure 3.28.



(a)

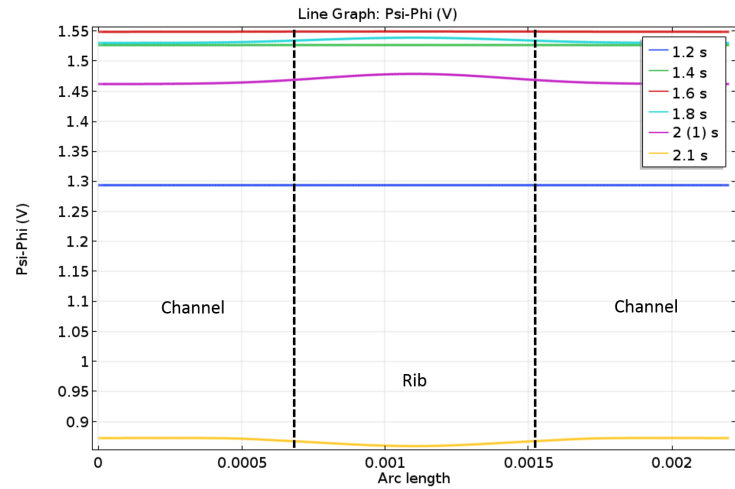


(b)

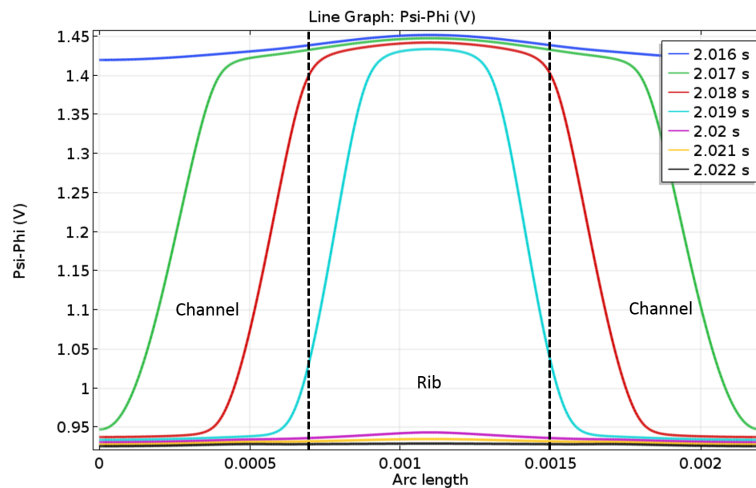
Figure 3.28: Hydrogen and oxygen fractions profile at the anode channel/GDL interfaces at the middle (a) and the outlet (b)

Figure 3.29 shows the cathode electrode potential in-plane in the middle of the catalyst layer during a startup at the middle of the cell. Figure 3.29a shows that before arrival of hydrogen, no heterogeneity appears between channel and rib (1.2 s, 1.4 s, 1.6 s). However when hydrogen starts to arrive around 1.7 s (Figure 3.28), difference in electrode potential between rib and channel also starts to appear. For example at 2 s (purple curve in Figure 3.29a), there is an increase of 200 mV in the electrode potential between the middle of the rib and the channel. This higher potential causes higher carbon corrosion under the rib. Figure 3.29b presents the cathodic electrode potential when the reverse current decay mechanism is established at the scale of the rib/channel. The blue curve at 2.016 s is at the beginning of the mechanism when the cathodic electronic potential is set by the cell voltage (Figure 3.10) at 0.8 V. As hydrogen

diffusion is faster under the channel, the cathode potential drops first in this zone until hydrogen arrives under the rib homogenizing the potential at 0.95 V.



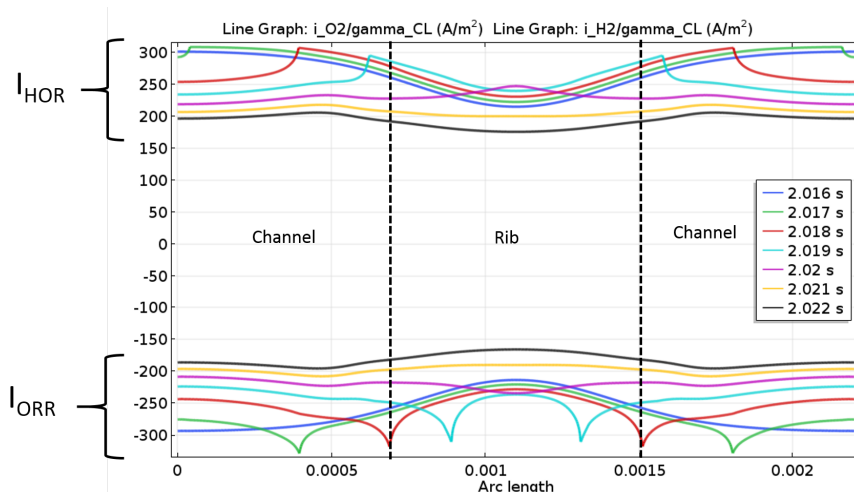
(a)



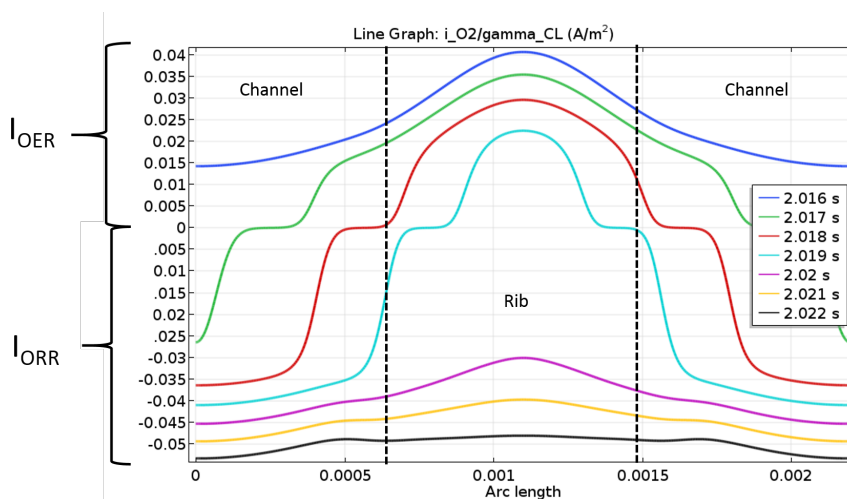
(b)

Figure 3.29: Cathode electrode potential along the cathode catalyst layer during a startup at the middle of the cell (rib-channel model)

Figure 3.30 shows the currents in plane along the middle of the anode and cathode catalyst layers during a startup at middle of the cell. Looking at Figure 3.30a, same profiles as the anode inlet is observed (Figure 3.27a). For the cathode side, Figure 3.30b shows that before this local reverse current mechanism, OER is happening because of the high cathodic electrode potential (blue curve at 2.016 s in Figure 3.29b). Then, oxygen reduction appears under the channel following the cathodic potential variations (red curve at 2.018 s in Figure 3.29b). And finally only ORR occurs when anode compartment has enough hydrogen (yellow curve at 2.021 s in Figure 3.29b).



(a) Hydrogen (top) and oxygen (bottom) current distribution at the anode



(b) Oxygen current distribution at the cathode

Figure 3.30: Current distribution in plane at the anode (a) and cathode (b) catalyst layer during a startup at the middle of the cell

Figure 3.31 presents the amount of oxidized carbon in-plane in the middle of the cathode catalyst layer for different positions: anode inlet, middle and outlet. The predicted values under the channel agree to those simulated with the along the channel as shown in Figure 3.22. The corrosion at the outlet is three times more important than in the middle. The strongest heterogeneities are observed at the anode inlet with more than two times under the centre of the rib than in the centre of the channel. However, the total corrosion is so small at the anode inlet that it is not significant. For the middle part, the corrosion under the rib is 8% more important and for the outlet is 5% more. As this reverse current decay mechanism at the rib/channel scale only lasts 0.003 s, another mechanism(s) probably explains the heterogeneities of corrosion observed experimentally under the rib.

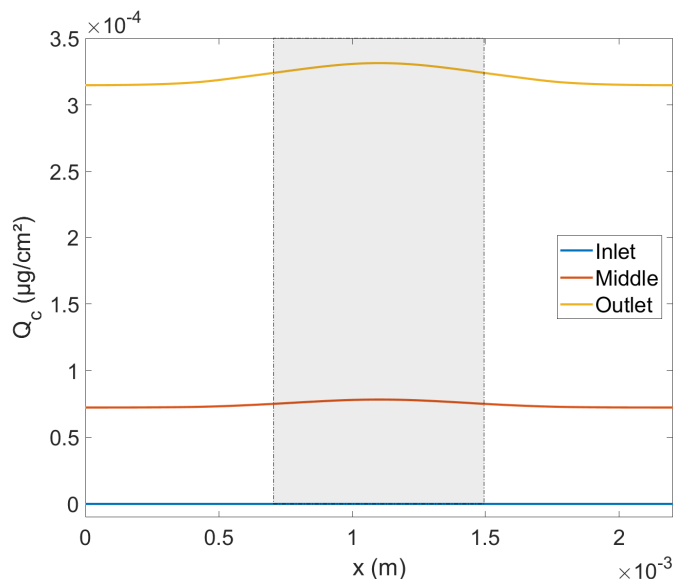


Figure 3.31: Amount of oxidized carbon (in $\mu g_C/cm^2$) in-plane in the middle of the cathode catalyst layer for different positions: anode inlet, middle and outlet

3.4 Carbon corrosion validation

3.4.1 SAXS/WAXS experiment

Scattering is a general physical process where some forms of radiation, such as light, sound, or moving particles, are forced to deviate from a straight trajectory by one or more paths due to localized non-uniformities in the medium through which they pass. It allows to probe the structure of matter at different scales. For the Wide Angle X-ray Scattering or WAXS, the scale of the matter observed is under 1 nm and the Small Angle X-ray Scattering or SAXS is between the nanometre and the micrometre.

In order to observe the platinum oxides, scans of the catalyst layers are done in O_2/H_2 at 0.9 V and 0.4 V. Figure 3.32 shows the spectra obtained along the total thickness with the circles correspond to the 0.4 V case and the crosses to the 0.9 V. Slight differences are already observable. For example the second spectrum from the top see a smaller peak around the Pt peak at 0.9 V than at 0.4 V. Furthermore, its shape seems to have changed indicating a change of environment. These type of difference highlights the difficulty of identifying the causes of modification. As these are two different conditions, it may be linked to a displacement of the MEA by a few micrometers because of the change of water content in the PEM making it shrink or swell. There is also the problem that some peak of Nafion, graphite and platinum (111) are really close of each other making hard to discriminate one another. To try to observe the oxidation of Pt, spectrum has to be in the centre of the catalyst layer.

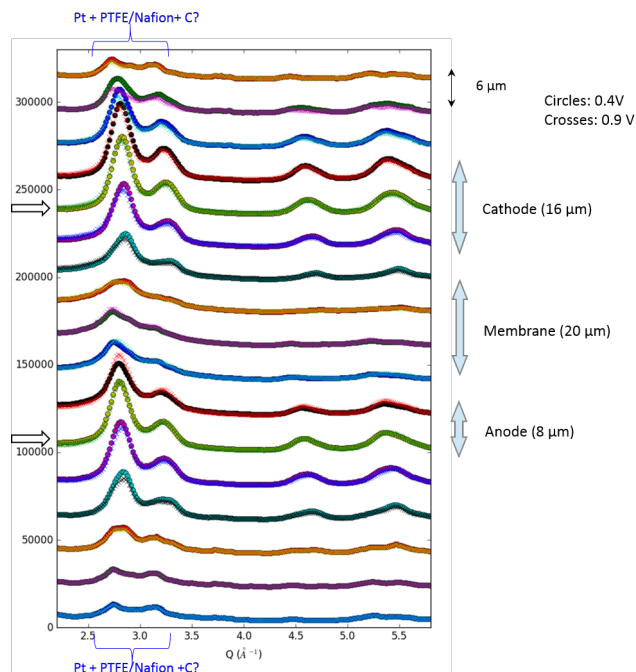


Figure 3.32: WAXS spectra at two different potentials along the thickness

Figure 3.33 presents the WAXS spectra at the cathode and the anode for the two potentials 0.4V and 0.9V. Literature shows that when platinum surface is oxidized, the Pt (111) peak at 2.8 \AA^{-1} tends to lower its intensity and moves slightly to a lower angle because of the longer Pt – Pt bonding distance for the oxide [121, 122]. This phenomena is slightly observed in Figure 3.33a where the crosses moves slight left and down compared to the circles, signs that there is a possible Pt oxidation. However at the anode, Figure 3.33b no such shift is observed suggesting there is no Pt oxidation.

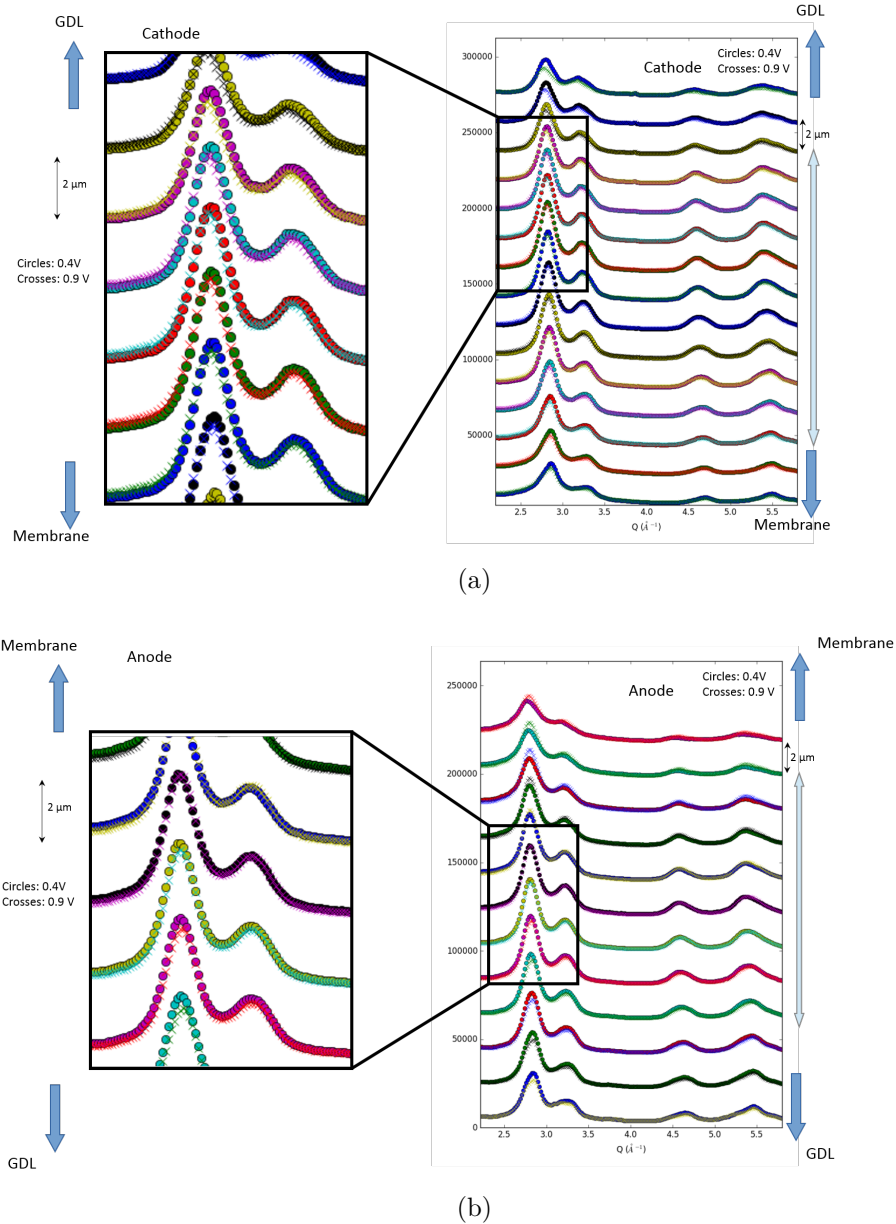


Figure 3.33: WAXS spectra at two different potentials at the cathode (a) and the anode (b)

A potentiostatic study is then done to try to follow the evolution of the graphite peak. The fuel cell is maintained at 1.2 V with H_2/N_2 at 75° C and 65% HR. Spectres are made before the application of potential and after in the middle of the cathode catalyst layer. Figure 3.34 shows the spectra obtained during the study. Spectre 6 is before the potential is applied when the fuel cell is at the OCV. Spectre 7 is 90 s after 1.2 V is applied to the fuel cell. The graphite peak does not vary whereas the intensity of the Pt (111) peak increases. This counter-intuitive results may be due to the liquid water. Spectre 8 and 9 are respectively 145 and 220 s after the start of the potentiostatic study. The graphite peak still does not change. The Pt (111) peak intensity decreases and moves to a lower angle which is characteristic of the platinum oxides.

Unfortunately, the rest of the study was not able to be done because of the lack of beam time. Higher potentials would have been tested to study its impact on the graphite expecting to see a change of shape of the peak showing an evolution of the structure because of the corrosion.

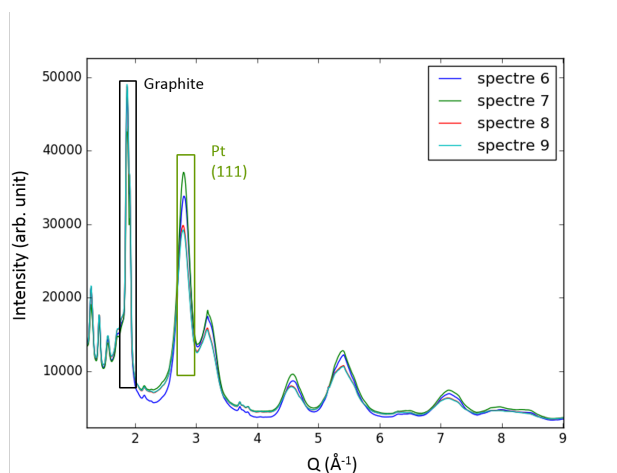


Figure 3.34: Spectra in the middle of the cathodic catalyst layer at OCV (spectre 6) and during potentiostatic study @1.2 V at 90 s (spectre 7), 145 s (spectre 8) and 220 s (spectre 9)

3.4.2 CO₂ at cathode outlet

Figure 3.35 shows the currents associated with carbon corrosion at the cathode during a startup. It is worth mentioning that the carbon corrosion peak is higher at the cathode inlet than at the outlet. The carbon corrosion begins at the same time as phase 2 and happens everywhere in the cathode catalyst layer except at the cathode outlet. Indeed the cathode outlet electrode potential drops instantly at 0.8 V even at the beginning of the phase 2 as explained before (Figure 3.9a). As a consequence, the part near the cathode inlet is more corroded than the cathode outlet because its electrode potential stays over 1.5 V, growing during the whole phase 2 (Figure 3.9a). The increase of the electrode potential explains also the steady increase of carbon corrosion until the end of the phase 2.

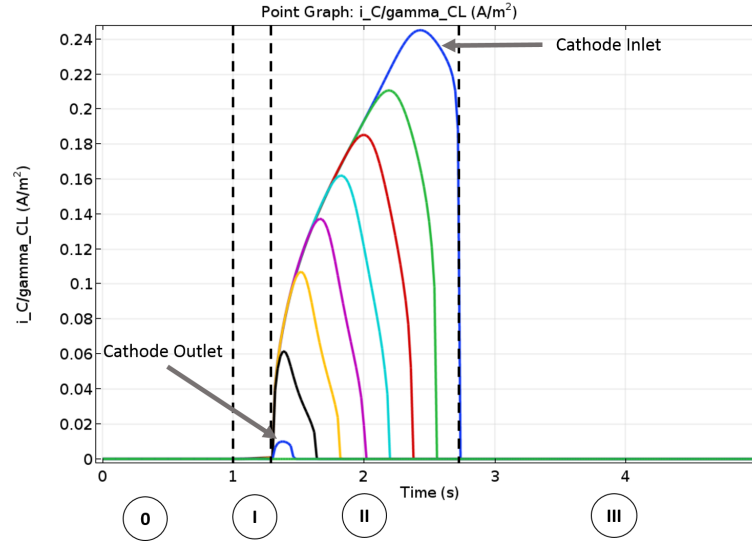


Figure 3.35: Carbon corrosion current of the cathode catalyst layer as function of time

In order to validate the carbon corrosion kinetic, the CO_2 concentration at the cathode outlet is simulated. Figure 3.36 shows the quantity of CO_2 at the cathode outlet during a startup. There is a slight delay between the start of Phase 2 and the arrival of CO_2 at the cathode outlet which is related to the transport time from the catalyst layer to the cathode outlet. The simulation predicts a peak value of 75 ppm very close to the 100 ppm found by Gu et al. [9] in similar conditions. Figure 3.37 shows the results obtained by Gu et al. with the measurement of CO_2 at the cathode outlet during startup and shutdown. The peak value for the shutdown (around 60 ppm) is clearly lower than the one for the startup. However, the quantity of CO_2 observed during a shutdown takes more time to reach zero than during a startup. Figure 3.38 presents the predicted quantity of CO_2 for the startup and shutdown in the reference condition used in subsection 3.3.1 and subsection 3.3.2. The peak value for the shutdown is actually lower even though the difference is not as important as in Gu et al. As observed in Figure 3.37, the predicted quantity of CO_2 at the cathode outlet during a shutdown takes longer to reach zero than during a startup (more than two times).

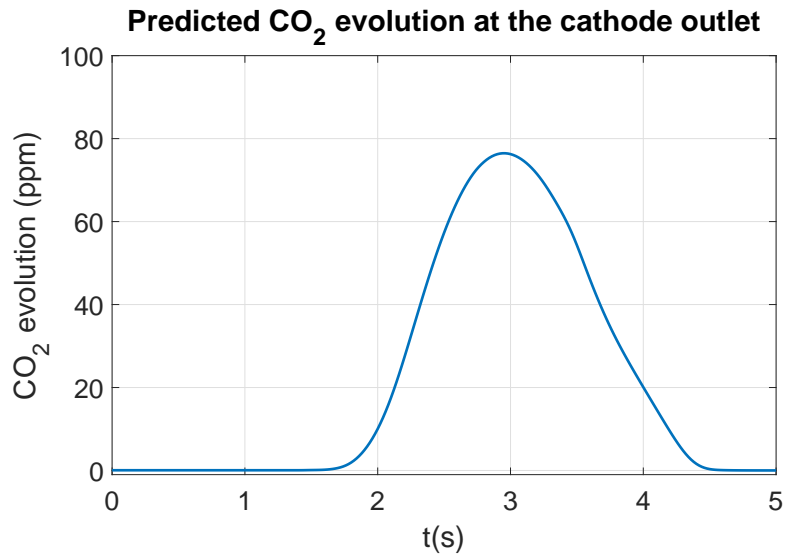


Figure 3.36: Predicted quantity of CO₂ in ppm at the cathode outlet during a startup in Gu et al. conditions

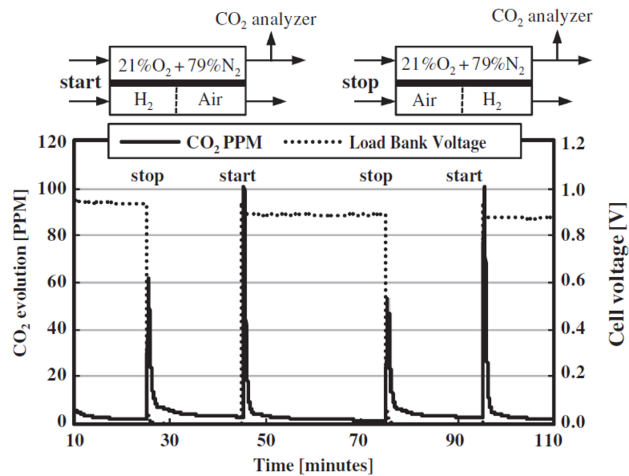


Figure 3.37: Quantity of CO₂ measured at the exit of the cathode during startup-shutdown events (reprinted from [9])

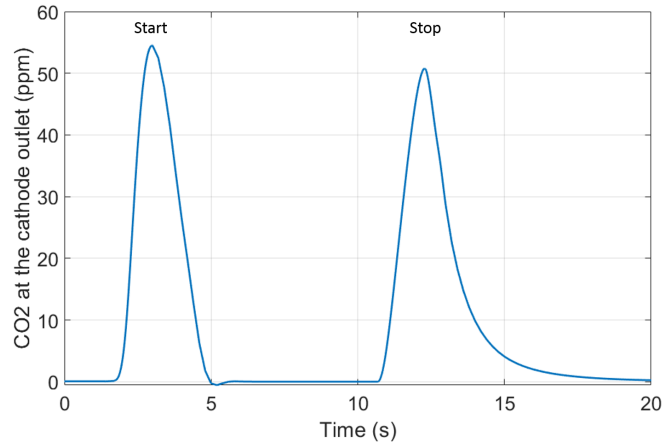


Figure 3.38: Predicted quantity of CO_2 in ppm at the cathode outlet during a startup and a shutdown in reference conditions

3.4.3 In-situ and ex-situ analyses

Experiments on startup/shutdown on PEMFC stacks has been performed at CEA in order to observe the reverse current phenomena in a complex geometry which is a serpentine flow-field described in Figure 3.39 [4]. In-situ investigations are done inside the stack with electrochemical diagnostics (polarization curves, cyclic voltammetry) and current density distribution measurements with an S++[®] segmented cell. The total active surface area is 220 cm^2 . Ex-situ post-mortem investigations are also performed including electron microscopy and electrochemical diagnostics. These ex-situ characterizations are done on small area of 2 cm^2 extracted from the cell. Figure 3.40 presents the protocol used to age the stack. The startup consists of an H_2 supply at the anode to create the hydrogen/air front. Then current is drawn from 0 to 110 A and back to 0 A by steps without cooling. The shutdown consists of closing the anode while maintaining the air supply at the cathode in order to consume the remaining hydrogen. Whenever the cell potential drops to 0.2 V , another startup is done.

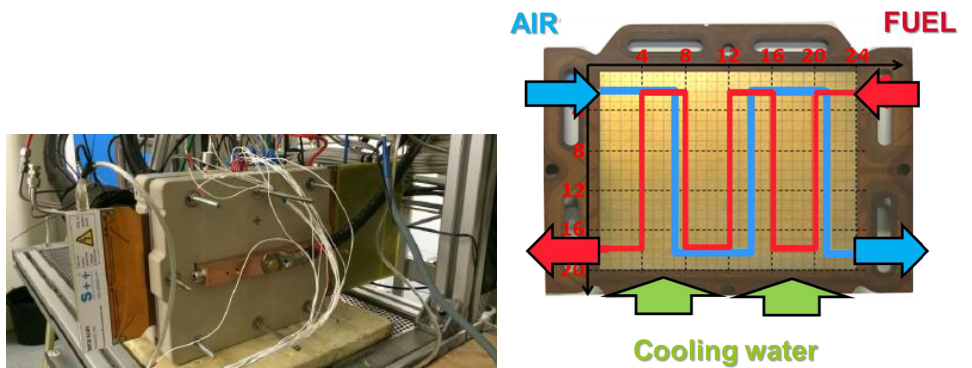


Figure 3.39: Fuel cell used and simplified schematic of the flow field

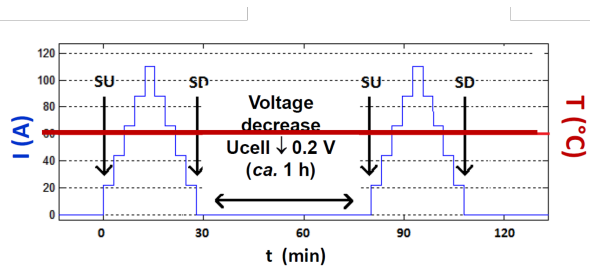
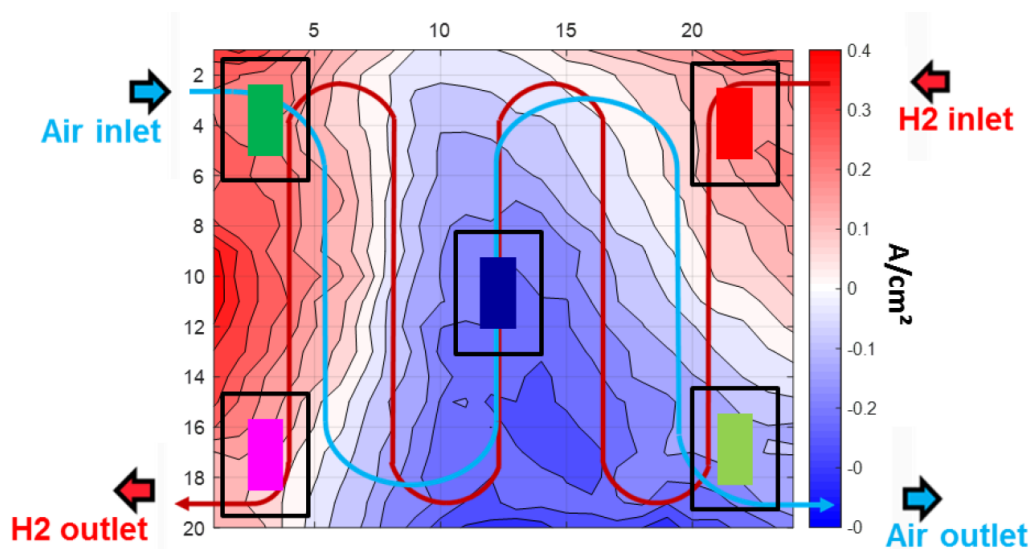


Figure 3.40: Startup/shutdown protocol (reprinted from [4])

Figure 3.41 shows the difference in the current distribution inside a cell between the end of test (which corresponds to 69 startup/shutdown) and the initial measurements. At the middle of the cell and air outlet (bottom right), severe decrease of current density is observed whereas, near the air inlet (top left) and hydrogen outlet (bottom left) there is an increase. The increase at the hydrogen outlet is not expected by the reverse-current mechanism. However, there are some residual hydrogen at the outlet that probably leaks back into the cell protecting this area.

Figure 3.41: Difference in current distribution between end and beginning of test @ 0.5 A/cm^2

First characterization is on the evolution of the ECSA both at the anode and cathode by hydrogen stripping through a cyclic voltammetry. Figure 3.42 presents the quantity of hydrogen desorbed for the different locations and the initial sample. At the anode (Figure 3.42 a), around 10 to 20 % of ECSA is lost in each of the analysed parts. However this loss is almost homogeneous in these areas. This confirms that there is no specific degradation heterogeneity at the anode which agrees with the reverse current decay mechanism. At the cathode (Figure 3.42 b), the global ECSA loss is around 65 %. Even though all areas suffers from these losses (even the hydrogen inlet), strong heterogeneities appears, mainly between the middle and the hydrogen outlet. Degradation is significantly harsher at the cathode than the anode however

ECSA cannot explain solely the performance heterogeneities observed. Thus, micro-structure is observed through SEM.

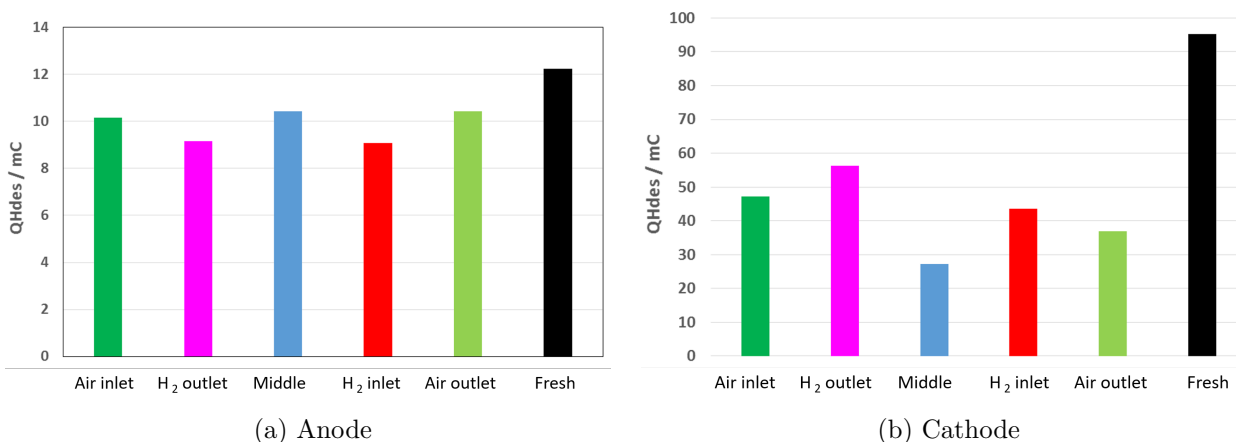


Figure 3.42: Quantity of hydrogen desorbed as function of location at the anode (a) and cathode (b) (the higher the quantity of hydrogen desorbed the higher the ECSA)

Figure 3.43 shows SEM images of the MEA before the test and after at different locations. Figure 3.43a presents the fresh sample with the cathode brighter than the anode, showing the higher catalyst loading. Looking at the H_2 inlet after the test, Figure 3.43b shows that the contrast of the cathode did not change and a Pt band appeared in the membrane. However at the air outlet, Figure 3.43c highlights that the cathode is brighter than the fresh sample and the Pt band is closer to this catalyst layer. The displacement of the Pt band can be explained by a lower porosity of the CL hindering the diffusion. The change of contrast highlights that the platinum is more dense at the air outlet suggesting carbon corrosion even if some catalyst has been degraded. This phenomenon is emphasized at the middle of the cell with an even brighter cathode and Pt redeposited next to the cathode.

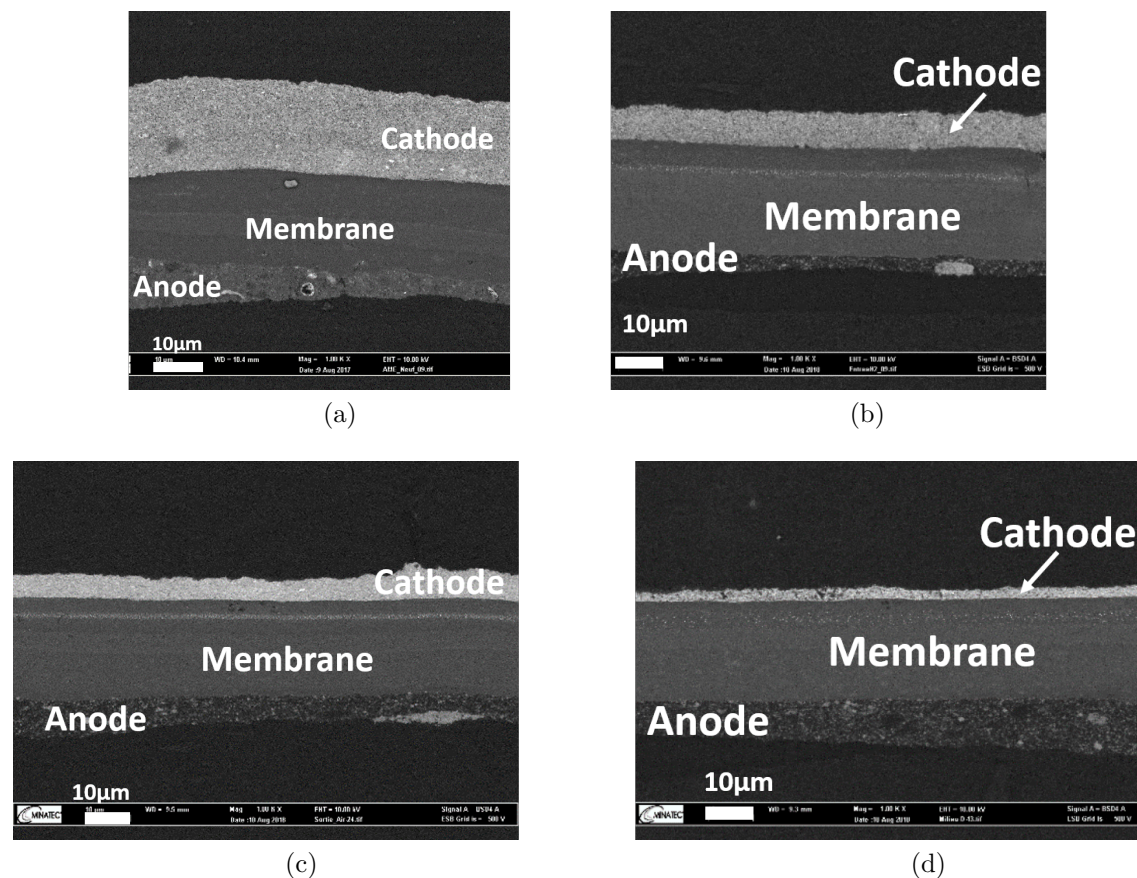


Figure 3.43: SEM images of the fresh sample (a) and after 69 startup/shutdown at H_2 inlet (b), air outlet (c) and middle of the cell (d)

Because of the complexity of the flow field, gas transport is more complex than a straight channel. However, looking at the part between the hydrogen inlet (top right) and air outlet (bottom right), hydrogen and oxygen are in a co-flow configuration which can be compared with the model. As predicted by the model during a startup, hydrogen inlet is protected and progressive degradation is observed until the air outlet (see Figure 3.41). Also during shutdown, because of the protocol with the anode shut, there is probably some remaining hydrogen near the hydrogen inlet protecting this part while it is consumed at the air outlet.

As shutdown takes longer than startup with this protocol, the cell may suffer more degradation during the shutdown. If there is some remaining hydrogen near hydrogen inlet and outlet, the middle may consume faster the remaining hydrogen than the other parts and become the first part of the cell in fuel starvation. As showed before, the corrosion current decrease as the surface corroded increases (see Figure 3.14b). The most degraded part may be thus the first part in fuel starvation during a shutdown when there is no flow at the anode. However this does not explain why the air inlet is more protected than the air outlet and especially the part between the air outlet and hydrogen inlet. A simulation of this shutdown with an anode shut

may help understand the impact of the protocol.

3.5 Conclusion

In this chapter, transient phases are modeled and simulated especially startup and shutdown. The startup can be divided into 4 phases which are characterized by the cell potential. The first one is the arrival of hydrogen at the anode catalyst layer at the anode inlet that start to react. It supplied protons and electrons to the reduction of oxygen at the anode and modify the ionic potential. Phase 2 begins when there is no more oxygen at the anode close to the anode inlet. An hydrogen/air front is moving from the anode inlet to the anode outlet creating a ionic potential front. This ionic potential front defines the four zones described by the reverse-current mechanism. In the compartment close to the anode outlet, carbon corrosion occurs at the cathode and intensifies as the potential front arrives to the anode outlet. Phase 3 is when the anode compartment is full of hydrogen making the fuel cell ready to operate. Same phenomena are observed during a shutdown but in the other way beginning from phase 3 to phase 0. However, even though the same velocity is used at the anode, phases and especially phase 2 do not last the same amount of time. During a shutdown, phase 2 is shorter than during a startup. Even though it is shorter our models shows that corrosion is more important during a shutdown. However, literature shows that corrosion is lessened in a shutdown which may be due to a pseudo-capacitive effect of the platinum that is not taken into account in the model.

The model predicts that during a startup the cathode part facing the anode outlet is more corroded than the one facing the anode inlet which is validated by the literature. Rib-channel models are also used to investigate heterogeneities between the rib and channel. Higher degradation is observed under the anodic rib especially close to the anode outlet during startup. Model shows that the diffusion of hydrogen under the rib is responsible of the heterogeneity inciting to look at the impact of the width of the rib.

Optimization and mitigation strategies

Contents

4.1	Optimization of materials and design	106
4.1.1	Anodic specific surface	107
4.1.2	Impact of rib-channel design	107
4.2	Operating strategies	118
4.2.1	Gas flow velocity	118
4.2.2	Startup with a resistor	121
4.2.3	Front dilution	124
4.3	Conclusion	126

According to literature, numerous strategies are used and suggested for the startup or shutdown to limit the carbon corrosion at the cathode. A review of these is done by Zhang et al. [123]. Several approaches have been investigated in this chapter which are focus on the materials of the catalyst layer and system strategies.

As the carbon support is the main casualty under frequent startup-shutdown cycles, modifications on the support to make it more stable is a first way of mitigation. A more graphitized carbonaceous material has been proven effective to limit the degradation by 80 % compared with the standard carbon support[124]. Highly resistant graphitized carbon has also shown to significantly reduce the degradation during startup while improving the performance thanks to a more homogeneous distribution of Pt nanoparticles [125].

The other way to limit degradations during startup and shutdown is the development of mitigation strategies through system controls. A lot of research has been done worldwide by researchers but also companies (UTC, General Motors, Honda, etc...) that has patented several mitigation strategies. Gas purge is one of the main element in feasible strategies such as hydrogen purge at the cathode [126], air purge at the anode [127] and nitrogen purge at the anode [8].

Auxiliary loads also help to eliminate the remaining excess of reactants. Several works pointed out that an auxiliary load is mitigating the degradation by delaying the decrease of ECSA [128, 129]. Indeed, this method limits the high potential reached by the cathode and thus reduce the degradation rate during a startup [111].

Study on the design of the rib-channel has been done. Schneider et al. shows with current distribution measurements that significant in-plane currents appears perpendicular to the fuel channel at the rib/channel scale [111]. As gas transport in the GDL is mostly diffusion, this study suggest to focus the mitigation strategies on the flow field design especially rib and channel design and the GDL properties. Furthermore, Durst et al. [7] highlights that fuel starvation events are emphasized in the cathode facing an anodic rib showcasing heterogeneities at this scale as shown in Figure 1.13. To the best of our knowledge, so little studies have been done on the design of the ribs to limit the corrosion during startup/shutdown.

4.1 Optimization of materials and design

In this section, the models are used to simulate the impact of the materials and design onto the corrosion of the carbon support. Two cases are here studied:

- Optimization of the anodic catalyst loading. At the anode, the platinum loading should be the lowest possible to limit the oxygen reduction kinetic [130][114].
- Optimization the anodic rib/channel design to minimize the degradation in the cathode

facing the rib.

4.1.1 Anodic specific surface

To understand how the reduction of oxygen at the anode modified the ionic potential and thus the cathode electrode potential, the anode specific surface impact has been studied. By lowering its value, the cathode electrode potential is expected to be lowered because of the difficulty for the oxygen to be reduced at the anode [130, 114]. So, Figure 4.1a shows the oxygen reduction current in the anodic catalyst layer during the startup. The integrated current density of ORR over the anodic catalyst layer is compared here. The reference case is the startup simulation described in chapter 3. By dividing the anodic specific surface by 2, the oxygen reduction current is significantly less important by around 20 %.

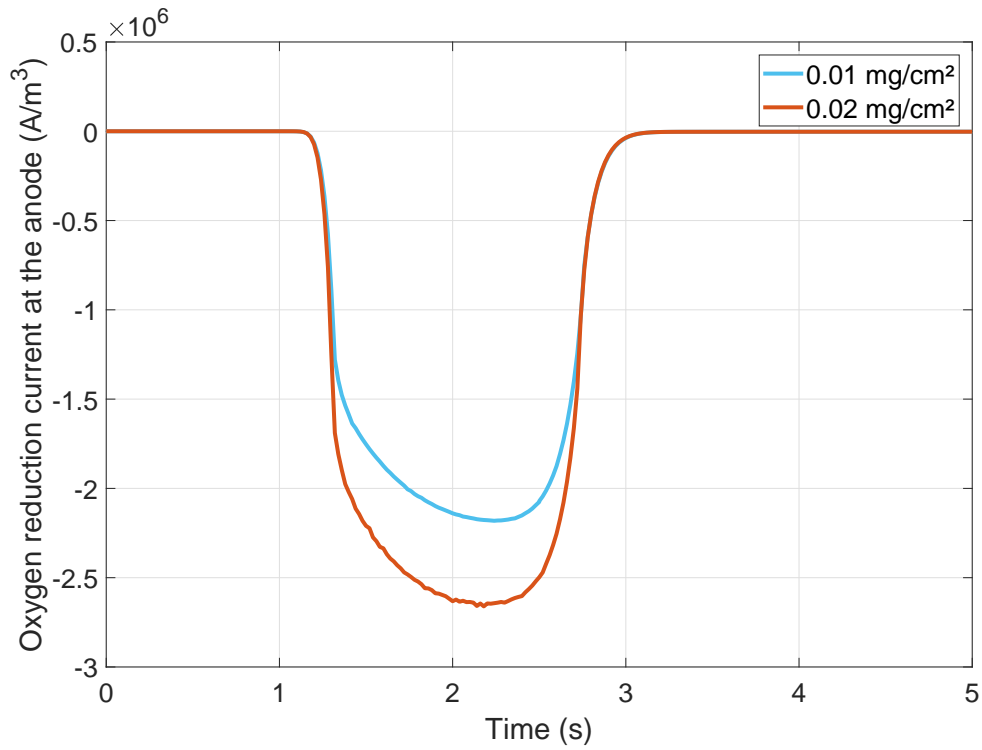
Figure 4.1b shows the local cathode inlet potential for the reference case (red curve) and a lower anodic catalyst loading (turquoise curve). Even though they spend the same time in each phase, small differences between them can be noticed. While there is no difference in potential during phase 1 for the two cases, a small gap is observed during all phase 2. The small gap is due to the lower ORR current at the anode seen in Figure 4.1a leading to a slightly higher ionic potential and thus a slightly lower cathode potential.

Figure 4.2 shows the amount of oxidized carbon in the middle of the cathode layer. The corrosion is mitigated all along the cathode thanks to the lower cathode potential. The effect is maximal at the cathode inlet (left of the figure) where the corrosion is the most prominent as seen in chapter 3. Comparing the lower anodic catalyst loading (0.1 mg/cm^2) with the reference case (0.2 mg/cm^2), the simulation shows that the amount of corroded carbon decreases by more than 18 % going from $40 \mu\text{g}_C/\text{cm}^2$ to $35 \mu\text{g}_C/\text{cm}^2$ (see Table 4.4) even though the variation of the potential is small. It confirms the results obtained by Eom et al. and Dillet et al. about the significant impact of the anode specific surface on the quantity of carbon corroded.

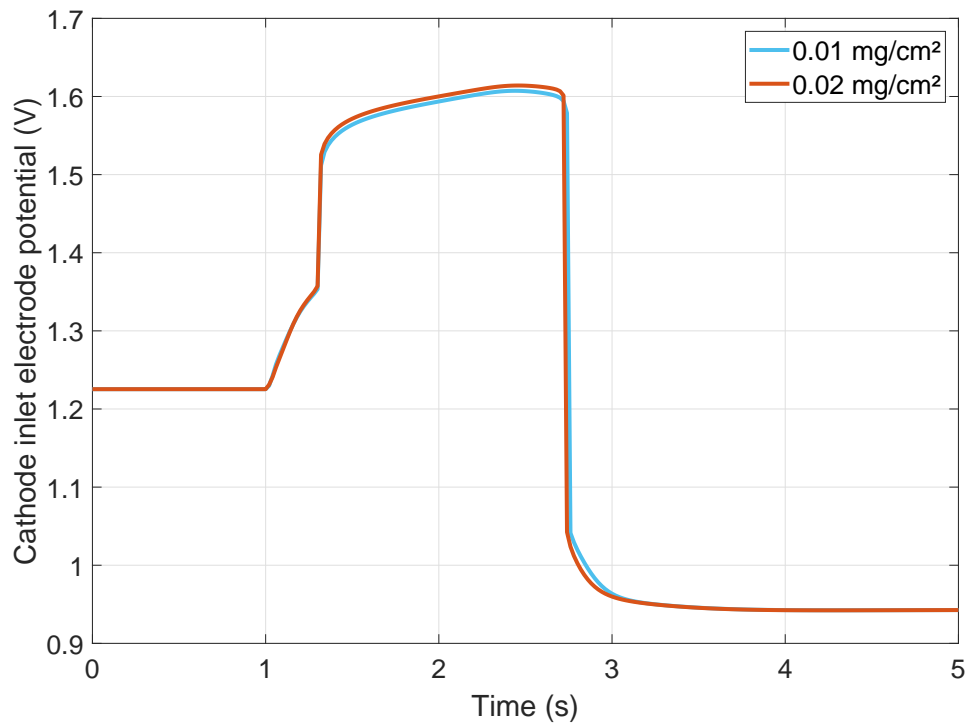
4.1.2 Impact of rib-channel design

As shown in subsection 3.3.3, reverse current mechanism occurs when hydrogen/air front appears under the anodic ribs during startup. The model actually gives an outlook of the impact of the rib-channel design of the anode on the diffusion of the gases under the rib and the heterogeneities in carbon corrosion between the rib and the channel. According to the simulation results, these heterogeneities occurs mostly at the cathode inlet (facing the anode outlet) considering a counter-flow configuration.

The influence of the anode rib to total length ratio Γ (see subsection 2.3.1) is studied with the use of 4 values in addition to the reference case (36%): 30%, 50%, 70% and finally 90%. This ratio is defined the same way as the one in Equation 2.52 in chapter 2:



(a) ORR current integrated along the anodic catalyst layer



(b) Cathode inlet electrode potential

Figure 4.1: ORR current (a) and cathode potential (b) during a startup with two different anodic specific surface

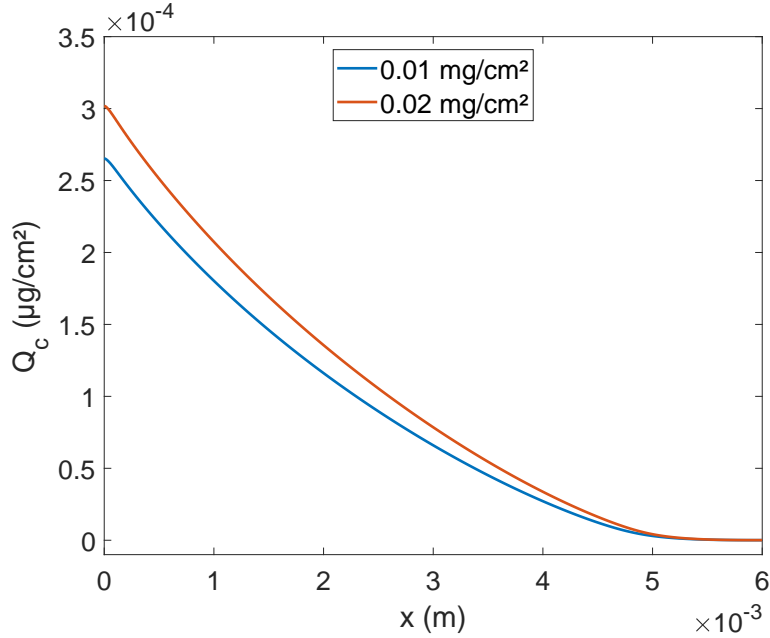


Figure 4.2: Amount of oxidized carbon (in $\mu\text{g}/\text{cm}^2$) along the middle of the cathode catalyst layer for different anode platinum loading

$$\Gamma = \frac{l_{CH}}{(l_{CH} + l_{Rib})} \cdot 100 \quad (4.1)$$

In the section, the rib width is modified without changing the total pitch.

4.1.2.1 Startup

The study focuses on the cathode middle and inlet where the corrosion is the most important during startup. Simulated electronic potential profile and concentration profiles obtained with the along the channel are used as boundary conditions in the rib-channel model as explained in chapter 3.

Figure 4.3 shows the cathode potential along the catalyst layer during phase 2. At the middle of the flow field, two periods of time are distinguished: when the potential is over 1.45 V and when it is under 0.95 V. The first period until 2s happens before the arrival of hydrogen at the middle of the flow field (see Figure 3.28a in subsection 3.3.3).

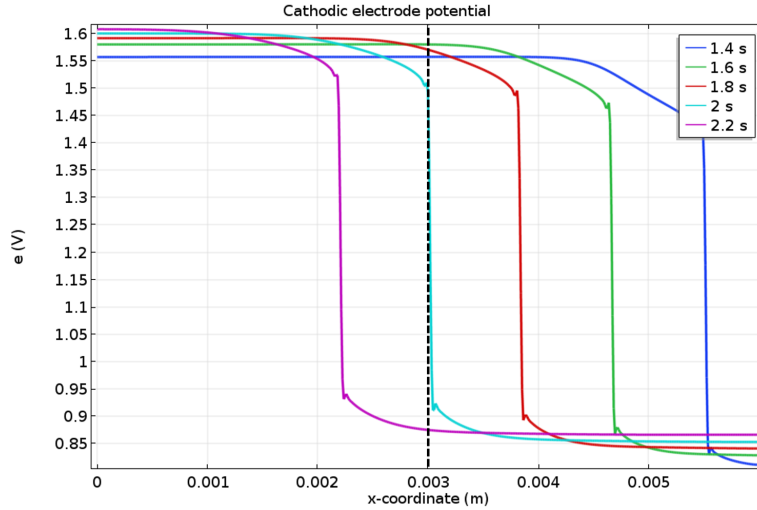
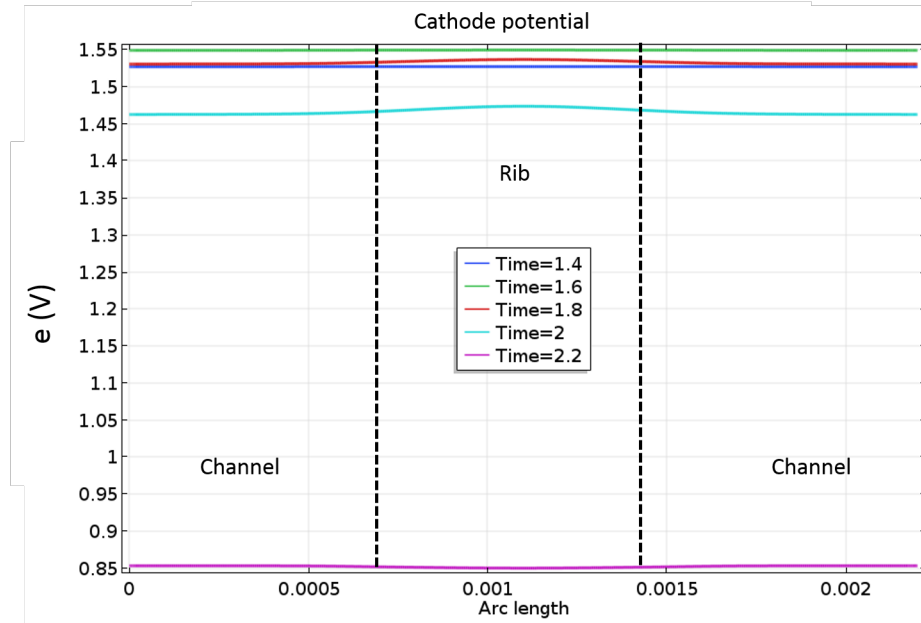
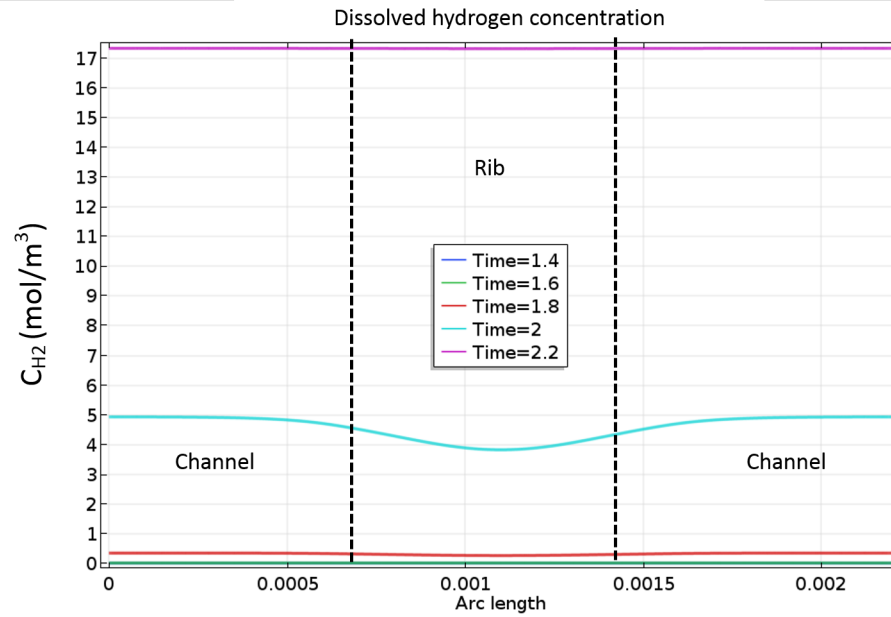


Figure 4.3: Cathode potential during phase 2. The vertical dashed line is the middle of the cell

Figure 4.4 and Figure 4.5 present the simulated cathodic electrode potential and the concentration of dissolved hydrogen (C_{H_2} see subsection 2.1.3.3) in the anode catalyst layer respectively for two designs: 30 % and 90 % rib/total length ratio at the middle of the flow field as function of time during phase 2. No heterogeneities are observed at 1.4 and 1.6 s whereas they appear at the same time independently of the design at 1.8 s. The heterogeneities are exacerbated with a larger rib/total length ratio design (Figure 4.5a). Furthermore, the potential is the same for the two designs before the hydrogen front arrival but higher cathodic potentials are observed for a larger rib during the front passage. This higher potential is related to the stronger heterogeneity in dissolved reactants in the catalyst layer. Indeed Figure 4.4b and Figure 4.5b show the concentration of dissolved hydrogen for the two designs. At 1.4 and 1.6 s, there are no trace of dissolved hydrogen in the anode catalyst layer in both cases. However at 1.8 s, hydrogen starts to accumulate in the anode catalyst layer under the channel creating electrode potentials heterogeneities. Figure 4.4a and Figure 4.5a shows the cathode potential respectively for $\Gamma = 30\%$ and $\Gamma = 90\%$ at the different times. These heterogeneities appear at the same time for both cases because the length of the rib weakly interferes on the diffusion of the hydrogen through plane from the channel to the catalyst layer. Nevertheless, the dissolved concentration of hydrogen under the rib in the 30 % rib/total length ratio (Figure 4.4b) is more homogeneous at 2s (turquoise curve) than for the 90 % rib/total length ratio (Figure 4.5b). Thus, the potential is also more homogeneous with a small rib than with a large rib. Even if cathode potential is heterogeneous, its maximal value does not exceed 1.55 V (green curve) which leads to a moderate corrosion of the carbon support. However at the cathode inlet, the situation is more contrasted.

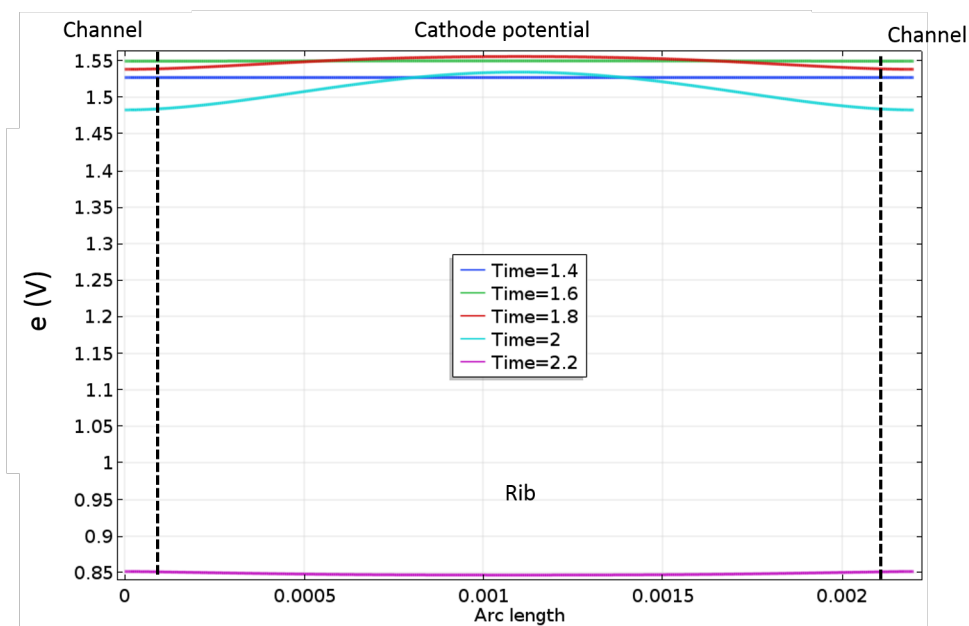


(a) Cathode electrode potential

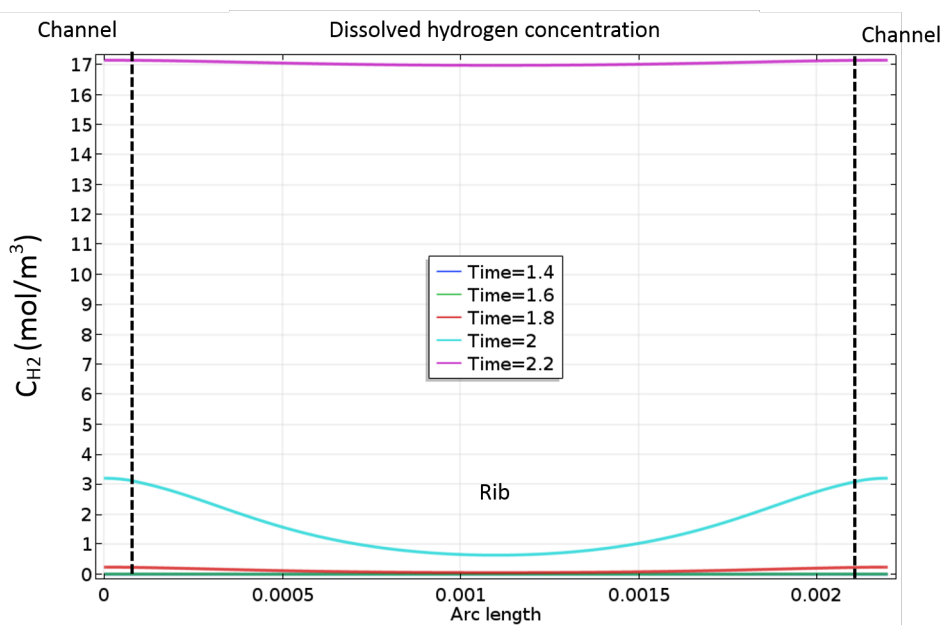


(b) Dissolved H_2 concentration in the anode catalyst layer

Figure 4.4: Cathodic electrode potential (a) and dissolved hydrogen concentration in the anode catalyst layer (b) at the middle of the flow field for 30 % rib/total length ratio



(a) Cathode electrode potential

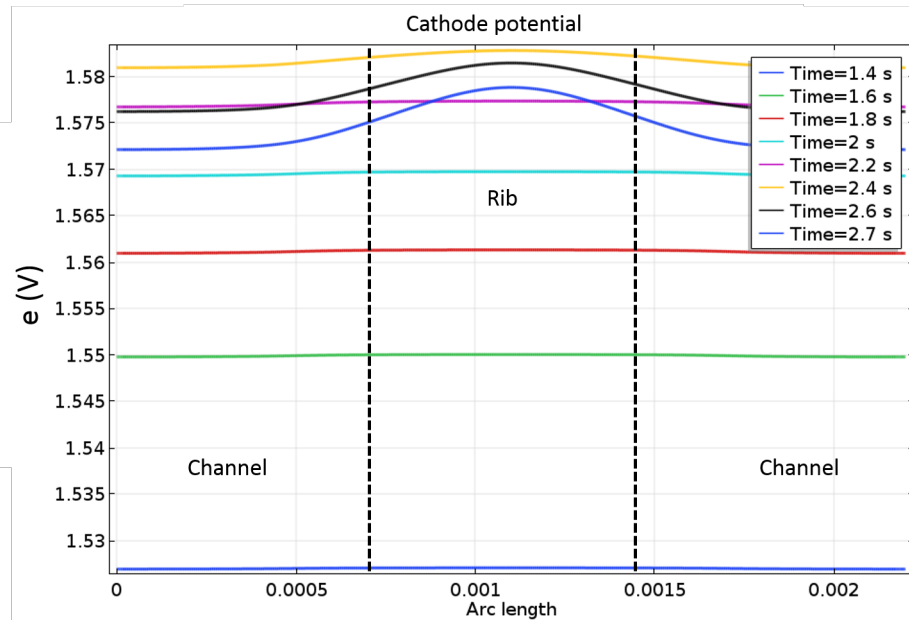


(b) Dissolved H_2 concentration in the anode catalyst layer

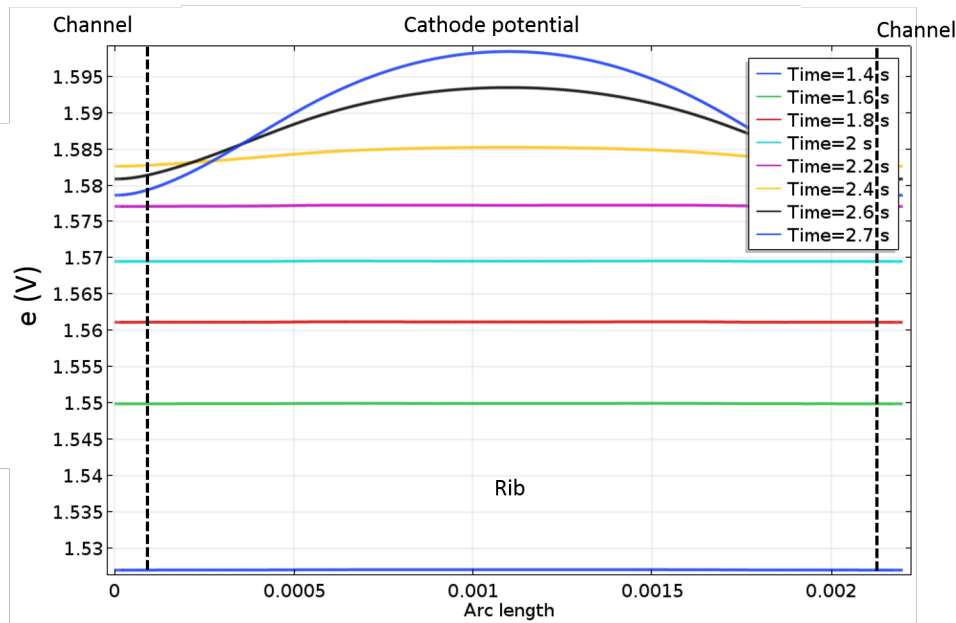
Figure 4.5: Cathodic electrode potential (a) and dissolved hydrogen concentration in the anode catalyst layer (b) at the outlet of the flow field for 90 % rib/total length ratio

Figure 4.6 shows the cathode potential for the two designs at cathode inlet (which faces the anode outlet). The hydrogen front arrives later at the end of phase 2 (around 2.4 s) as described in Figure 3.28b in chapter 3. The same heterogeneities are observed during the passage of the hydrogen front in the electrode potential in Figure 4.6. At the cathode inlet, the cathode potential heterogeneities are exacerbated even for the smaller Γ ratio (Figure 4.6a). For the

higher Γ , Figure 4.6b shows that it reaches 1.6 V under the rib whereas it is “only” 1.58 V under the channel (highest blue curve at 2.7 s).



(a) 30 % rib/total length ratio



(b) 90 % rib/total length ratio

Figure 4.6: Cathodic electrode potential at the anode outlet two design of rib/channel: 30 % (a) and 90 % (b) rib/total length ratio

In order to show the different behaviours in potential between the rib and the channel during the startup, Figure 4.7 shows the cathodic electrode potential under the middle of the channel and the rib during a startup for two designs. As shown before, the potential under the rib stays

at a higher potential when the hydrogen front goes through. As shown in Figure 4.7a, with a small rib the potential under the rib follows the same variations as the one under the channel.

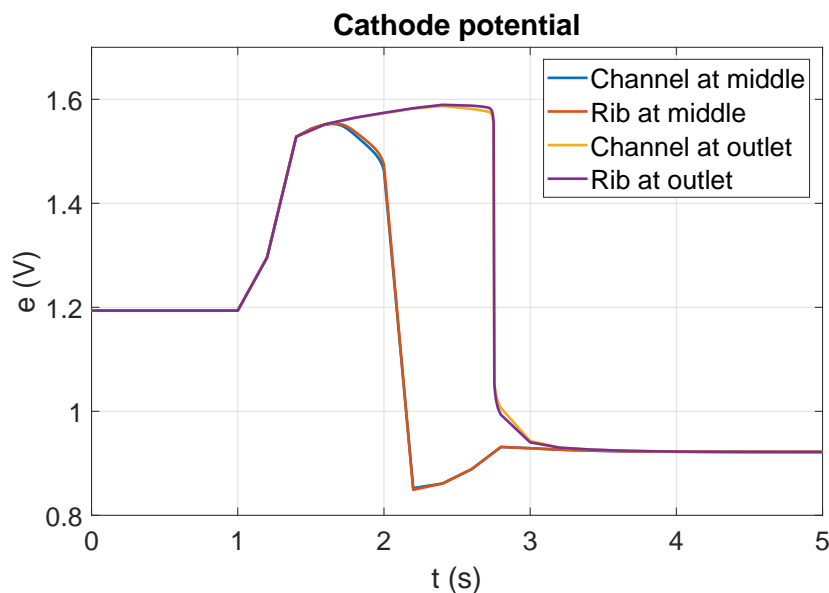
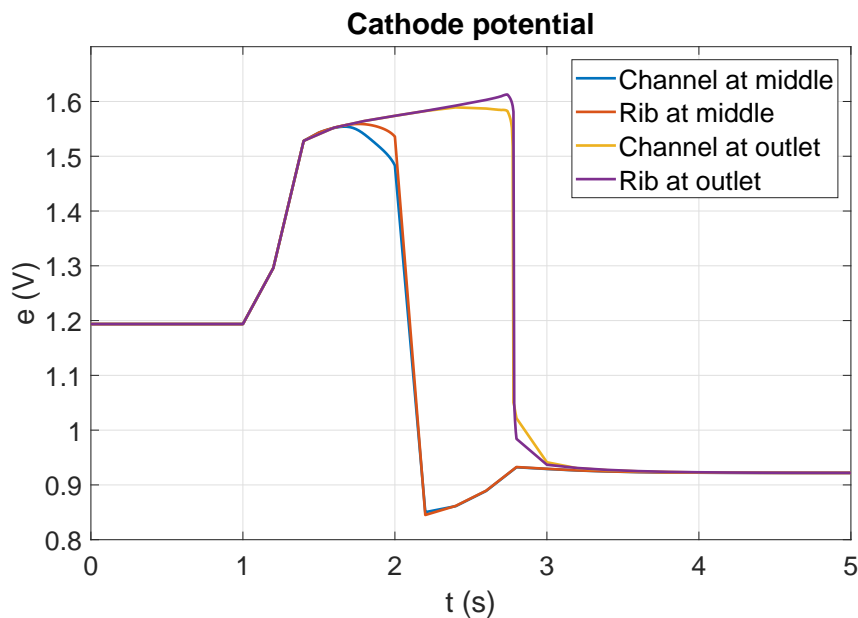
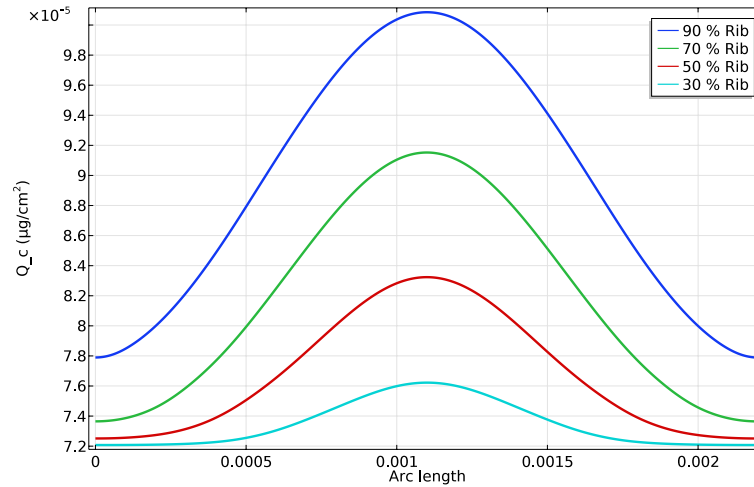
(a) $\Gamma = 30\%$ (b) $\Gamma = 90\%$

Figure 4.7: Cathode potential under the middle of the channel and the rib at the anode outlet and middle for two rib/total length ratio: 30 % (a) and 90 % (b)

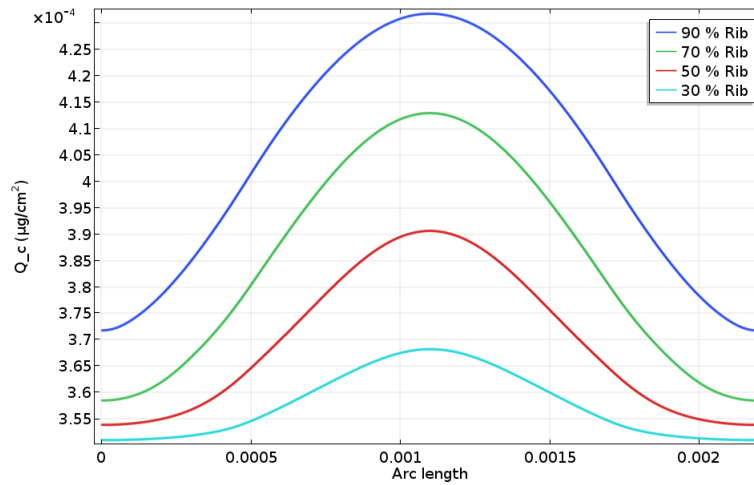
However, when the rib is larger, Figure 4.7b shows that the two potentials are more contrasted. When the hydrogen front arrives, the potential under the channel decreases (blue curve and yellow curve) whereas under the rib it stays higher for a longer period of time before it drops (red curve and purple curve). At the anode outlet, the potential is higher because of the

current distribution as explained in chapter 3.

The cathode potential heterogeneities at the rib/channel level impact the carbon corrosion. Figure 4.8 shows the carbon corrosion distribution along the cathodic catalyst layer in front of the anode middle and outlet for the different designs. Under the channel, values close to the reference case are found (Figure 3.31).



(a) Middle



(b) Outlet

Figure 4.8: Amount of oxidized carbon (in $\mu g_C/cm^2$) in the middle (a) and anode outlet (b) cathode catalyst layer for different anodic rib/total length ratio during a startup

Only the largest rib already shows around 10 % increase of corrosion under the channel. The corrosion at the cathode increases when the rib width increases. Moreover, the larger the anodic rib is, the higher the heterogeneity of the carbon corrosion distribution is. For example at the anode outlet, the corrosion is 5 % higher at the middle of the rib for the 30 % case whereas for the 90 % case it is around 16 % higher. Between the middle and outlet the heterogeneities also

varies. For the 30% case, the corrosion is only 0.6 % higher under the rib and 2.2 % higher for the 90% case. This explains why at the middle of the cell, it is difficult to observe heterogeneities in carbon corrosion at the middle of the cell whereas it appears at the anode outlet.

Table 4.1 shows the relative corrosion variation as function of the rib/total length ratio for the anode in comparison to the reference case defined as:

$$Relative\ corrosion\ (\%) = \frac{Q_c(\Gamma) - Q_c(ref)}{Q_c(ref)} \cdot 100 \quad (4.2)$$

As expected, higher corrosion happens when the rib is the largest. For a rib/total length ratio lower than 50 %, the size of the rib has a minimal impact for the corrosion. The values at the inlet are not provided because the corrosion at this location is almost non-existent (see Figure 3.31). The model shows that even if in terms of performance a larger anodic rib is preferred thanks to a fast hydrogen diffusion and a better current collection, significant corrosion appears in the cathodic catalyst layer in front of the anodic rib. In chapter 2, a varying cathode channel width along the flow is suggested to improve performance [82]. A varying anodic rib width should also be considered to mitigate the corrosion during the startup. A large anodic rib at the anode inlet may be used to favour performance and a small anodic rib at the anode outlet may be used to mitigate the carbon corrosion during startup.

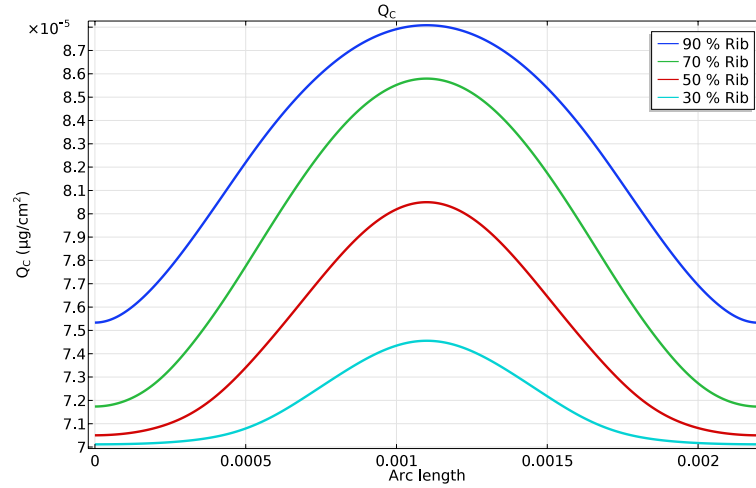
Table 4.1: Relative corrosion as function of rib-channel design and location in the flow field during a startup

Rib/Total length ratio	Middle	Outlet
90 %	20.2 %	9.5 %
70 %	10 %	5.3 %
50 %	3.1 %	1.8 %
Ref (36%)	0 %	0 %
30 %	-1.4 %	-0.94 %

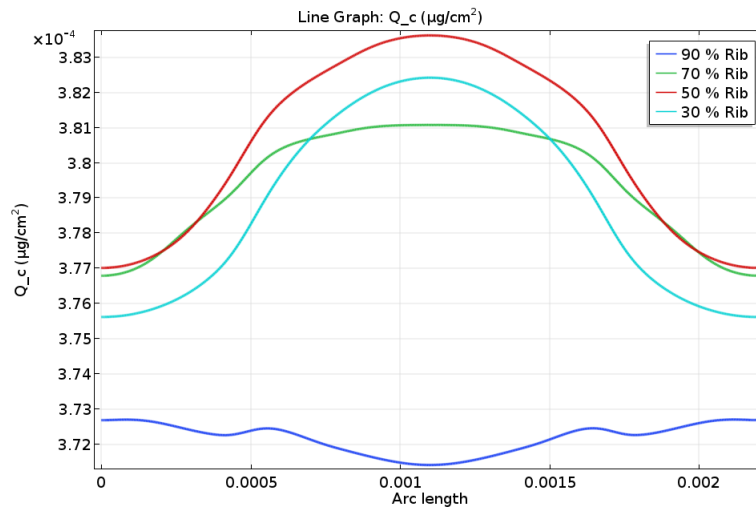
4.1.2.2 Shutdown

Figure 4.9 shows the carbon corrosion distribution along the cathodic catalyst layer at the anode middle and inlet for the different designs during a shutdown. The values under the channel are approximately the ones found for the reference case (see Figure 3.22a). At the middle, same trend is observed as during the startup for which the higher corrosion is observed for the larger rib. Except that the effect is less pronounced: relative corrosion between the reference design and $\Gamma = 90\%$ is 13.8% for a shutdown against 20.2% for the startup. Nevertheless, Figure 4.9b shows that the corrosion distribution is strongly modified by the design at the anode inlet. First, the heterogeneities are really reduced in comparison to those at the anode outlet during

the startup. Difference of corrosion between the rib and channel is at most 2%. At $\Gamma = 30\%$, the distribution looks similar as during the startup at the anode outlet. However for the three other designs the obtained profiles are totally different at the inlet. Heterogeneities are much smaller. Table 4.2 shows that in terms of total corrosion, there is more or less no difference between each designs.



(a) Middle



(b) Inlet

Figure 4.9: Amount of oxidized carbon (in $\mu\text{g}_C/\text{cm}^2$) in the middle (a) and anode inlet (b) cathode catalyst layer for different anodic rib/total length ratio during a shutdown

Table 4.2: Relative corrosion as function of rib-channel design and location in the flow field during a shutdown

Rib/Total length ratio	Middle	Inlet
90 %	13.8 %	-1.9 %
70 %	8.6 %	0.03 %
50 %	3.1 %	0.28 %
Ref (36%)	0 %	0 %
30 %	-1.2 %	-0.22 %

4.2 Operating strategies

In this section, the model is used to evaluate and comprehend mitigation strategies based on operating conditions. Two cases analysed here are:

- Using high flows in the anode compartment to flush as fast as possible the remaining oxygen. [9, 115, 109]
- Managing the cathode electrode potential by creating a current leak using a dummy load, a resistor or a capacitance in parallel. [128]

4.2.1 Gas flow velocity

Inlet flow velocity is calculated in the model as function of the stoichiometry and the current expected to be delivered by the fuel cell [82]. In the validation section of the paper, this current is adjusted to 5000 A/m^2 to match a residence time in the anode compartment of around 1.5 s as used by Gu et al [9], giving a flow velocity of 0.032 m/s . The three other cases will correspond to a velocity of 0.015 m/s (marine blue curve), 0.047 m/s (yellow curve) and 0.063 m/s (purple curve). Figure 4.10 shows the cell potential during a startup for four different anode flow velocities. For the slowest velocity, the startup lasts 3.2 s which is approximately two times longer than the reference case lasting 1.7 s . The overshoot in potential at the end of each startup is higher when the velocity increases showing the impact of the sharpness of the front on this parameter.

As shown in chapter 3, the end of phase 2 is the moment when oxygen is consumed at the anode outlet. Figure 4.11 shows the dissolved concentrations of hydrogen (green) and oxygen (blue) for the different flow velocities at the anode outlet. Concerning the dissolved oxygen concentration, when hydrogen is arriving, its concentration slightly decreases because of its consumption by the small hydrogen quantity. Then, there is an accumulation before its total consumption by the hydrogen. This accumulation decreases with the velocity which shows its impact on this phenomena.

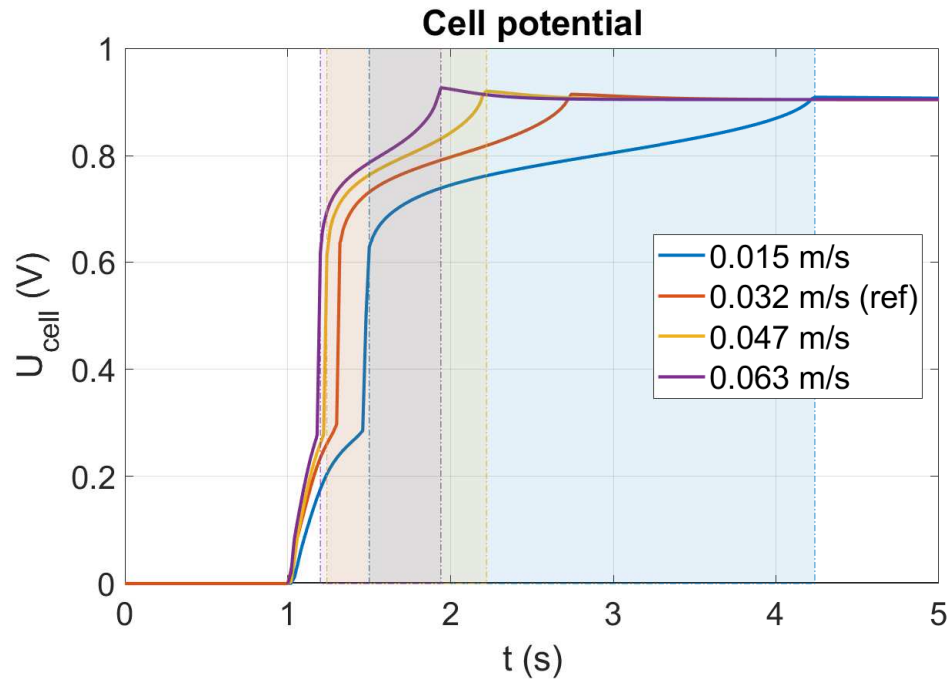


Figure 4.10: Cell potential during a startup as function of the flow velocity

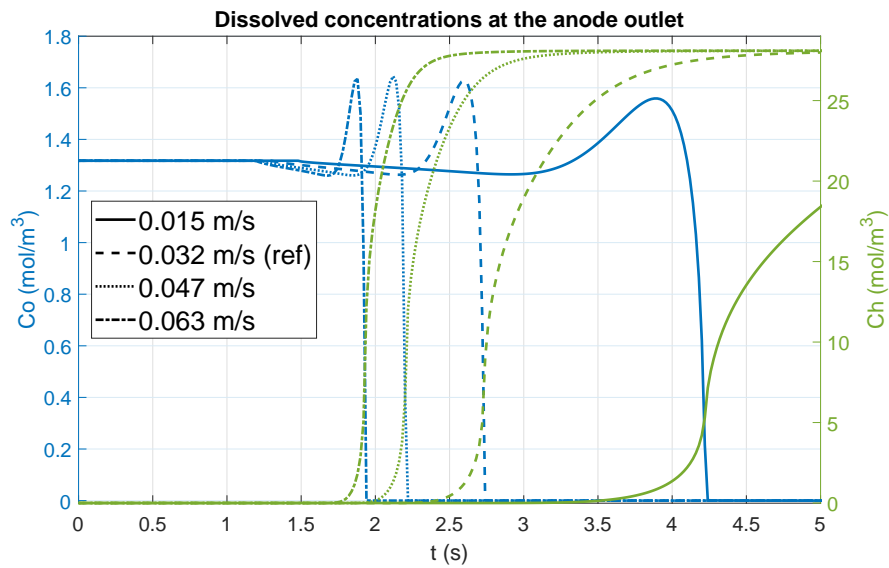


Figure 4.11: Dissolved concentration at the anode outlet during a startup for different flow velocities

Table 4.3: Elapsed time in phase 2 for the different velocities

Velocity	Elapsed time in phase 2 (s)
0.032 m/s	~ 1.4 s
0.015 m/s	~ 2.7 s
0.047 m/s	~ 0.98 s
0.063 m/s	~ 0.74 s

Looking at the cathode inlet electrode potential profile in Figure 4.12, the time elapsed in phase 2 for each case (which is shown by Table 4.3 and the coloured areas) is inversely proportional to the velocity flow. As expected, the flow velocity has a proportional effect on the time during which the fuel cell undergoes the reverse current mechanism. However the maximal potential reached in each case is also different. Indeed, the faster the front, the higher the potential reached is. Nevertheless, the difference is around 10 mV.

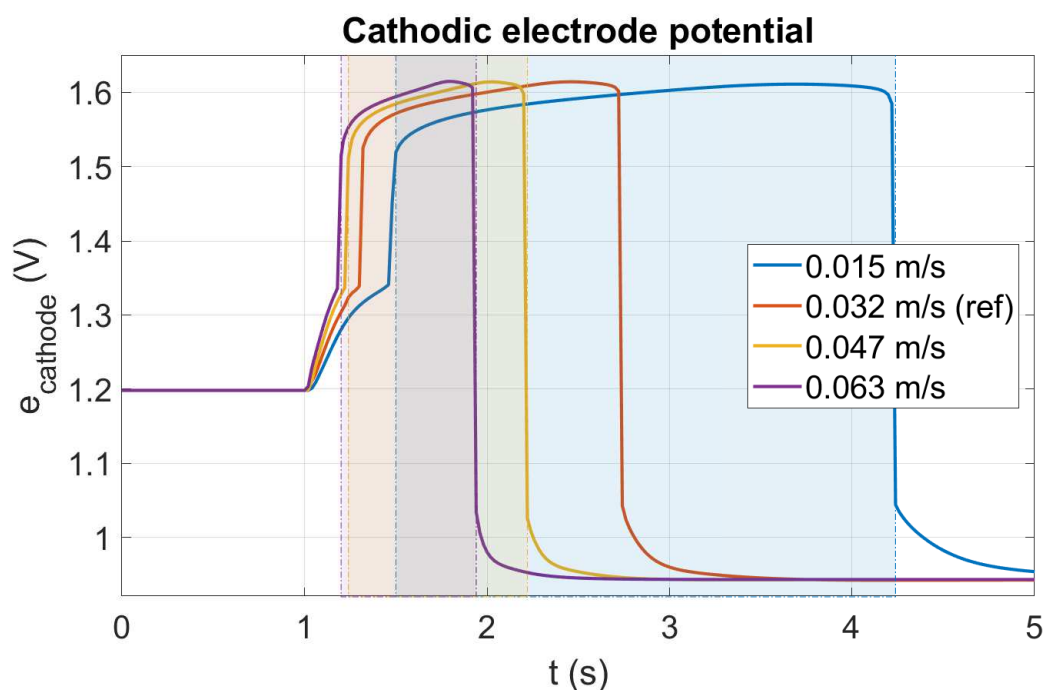


Figure 4.12: Cathodic electrode potential at the cathode inlet during a startup for different flow velocities

Figure 4.14 shows the total amount of carbon corroded as function of the anode flow velocity. As expected, the higher the velocity, the lesser the carbon is corroded (Table 4.4). Corrosion-wise, compared to the reference case, the slowest speed (twice slower than the reference case) shows an increase of corroded carbon of 76 % going from $40 \mu\text{g}_C/\text{cm}^2$ to $71 \mu\text{g}_C/\text{cm}^2$. Whereas the fastest speed (twice faster than the reference case) shows a decrease of corroded carbon around 48.5 % with $21 \mu\text{g}_C/\text{cm}^2$. The last case when the velocity is increased by 50 %, the

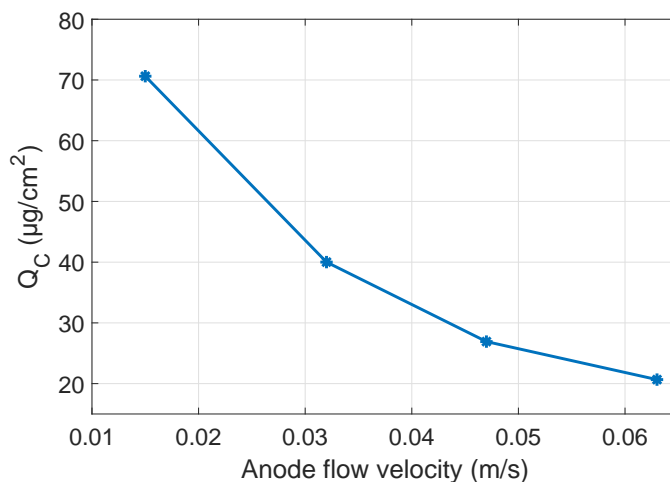


Figure 4.14: Total amount of carbon corroded as function of the anode flow velocity

total carbon degradation is 32 % lower ($27 \mu\text{g}_C/\text{cm}^2$). The mitigation obtained by the faster speed tends to slow down probably indicating a limiting value at a faster speed. Figure 4.13 shows the predicted cumulated carbon loss distribution along the cathode catalyst layer for the different flow velocities. The impact is observed mainly close to the cathode inlet (left of the image) where the carbon corrosion takes place.

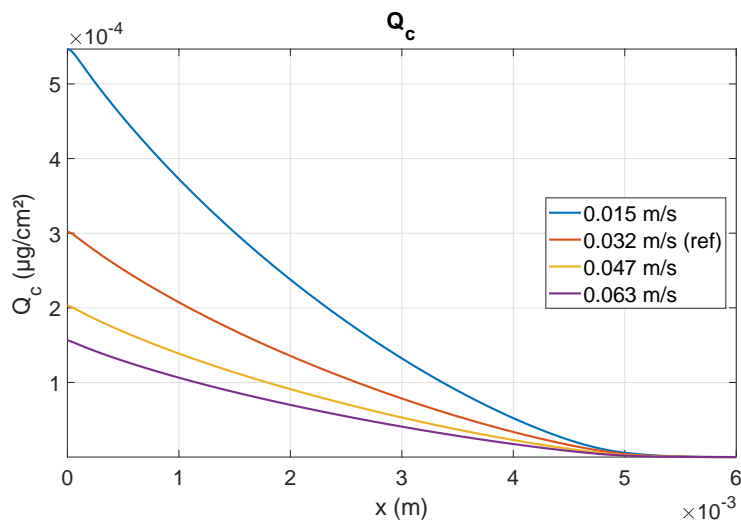


Figure 4.13: Amount of oxidized carbon predicted along the cathode flow-field for different flow velocities

4.2.2 Startup with a resistor

A mitigation strategy often evoked is a startup with a resistor creating a current leak lowering the cell and local potentials [128][109]. Figure 4.15 shows the current leak created a the resistance

of $2 \cdot 10^{-4} \Omega \cdot m^2$ during the startup. The resistance is only used when the cell potential goes over $0.5 V$ to avoid a current leak before it is actually necessary. During the phase 3, the current leak is still present in our simulation leading to lower potentials (green curve in Figure 4.17). In real situation on a system, the resistance should be disrupted when the startup is finished, but it does not affect the carbon corrosion in the simulation.

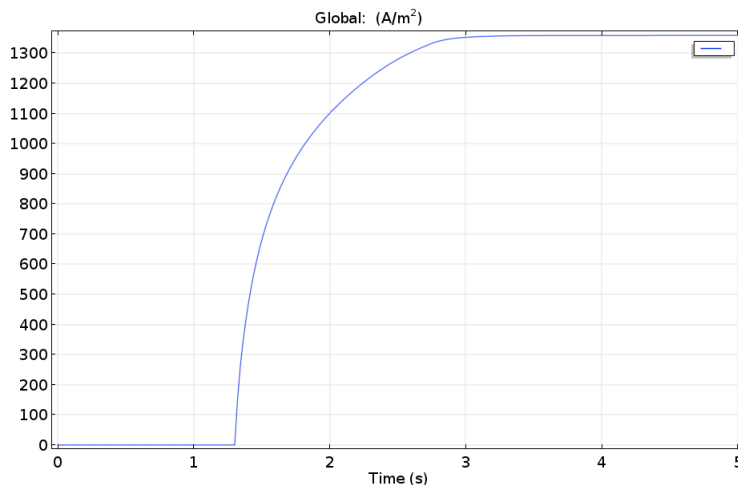


Figure 4.15: Resulting current leak during startup

Figure 4.16 shows the cell potential during a startup with and without the resistor. Until the dummy load is activated, no differences is observed between the two cases. However as soon as there current leak appears, the cell potential is lowered. Furthermore, the overshoot of potential at the end of phase 2 disappears stabilizing to the potential corresponding to the current leak. The end of phase 3 is at the same time with or without a resistor.

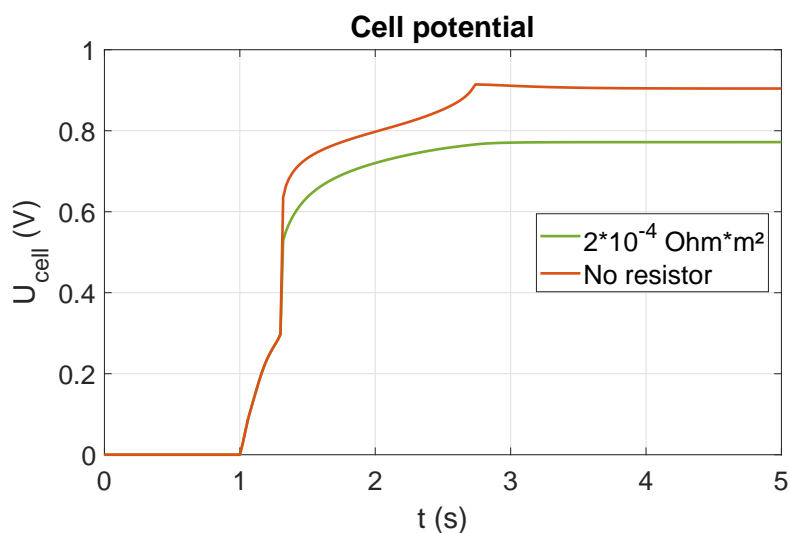


Figure 4.16: Cell potential during a startup with and without a resistor

To go further, Figure 4.17 compares the cathode potential during a startup with and without the resistor. At the beginning of the startup during phase 1, as there is no current leak, same rise of potential is observed. When phase 2 begins at 1.3 s, the cathode potential leaps to a lower value with the resistor at around 1.47 V (against 1.55 V without). Then, it slowly rises to 1.55 V at 2.3 s. Between 2.3 s and 2.72 s, the potential decreases down to 1.5 V far more faster than without the resistor. This decrease is due to the current leak facilitating the consumption of the remaining oxygen. However it does not accelerate the process as same time is elapsed in phase 2. As explained before, the electrode potential drops to a lower value during phase 3 because the current leak is not stopped after the startup in the simulation.

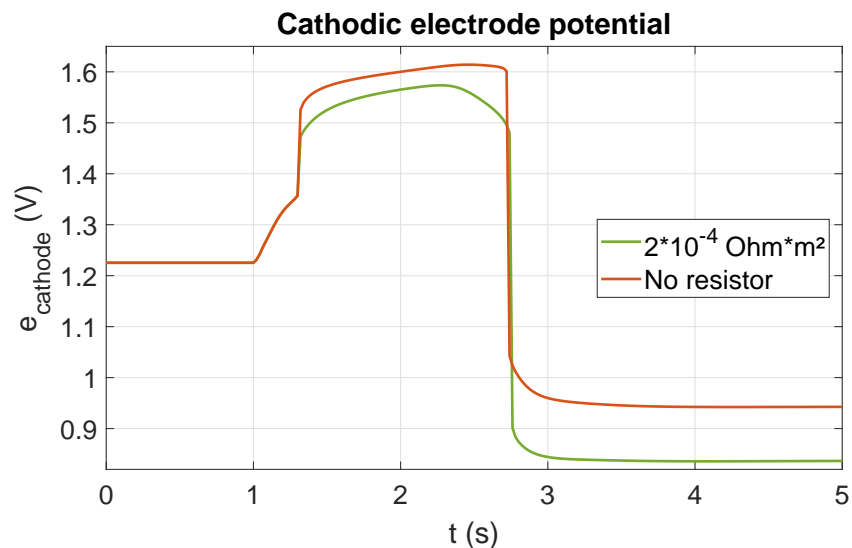


Figure 4.17: Cathodic electrode potential at the cathode inlet during a startup with and without a resistor

Figure 4.18 presents the predicted cumulated carbon loss with and without the resistor. A clear effect is observed especially at the cathode inlet (left of the figure) where the corrosion is two times lower. Looking at Table 4.4, only $15 \mu\text{g}_C/\text{cm}^2$ is corroded with the resistor compared to the $40 \mu\text{g}_C/\text{cm}^2$ meaning a decrease of around 63 % of carbon corroded.

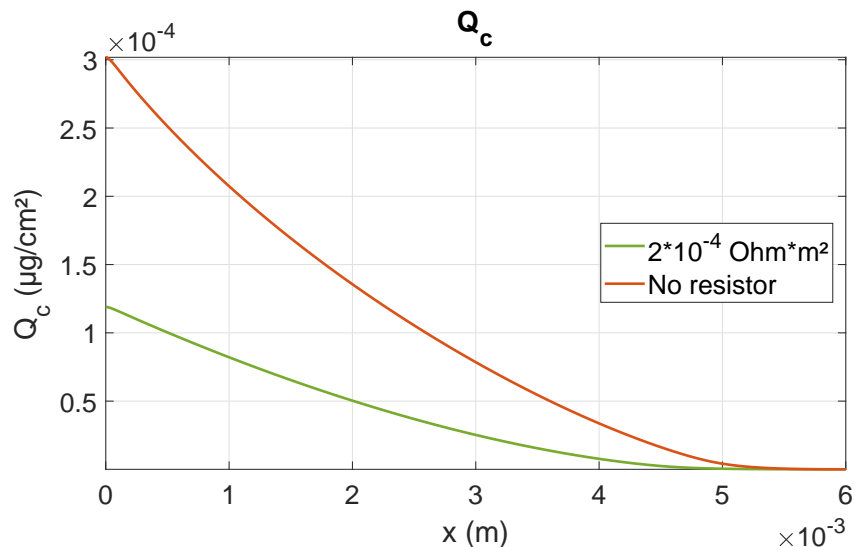


Figure 4.18: Amount of oxidized carbon predicted along the cathode flow-field with and without a resistor

4.2.3 Front dilution

As seen in chapter 3, phase 2 occurs when a hydrogen/air front moves from the anode inlet to the anode outlet during a startup. Here the anode flow velocity is set to 0.015 m/s . This phase ends when all the remaining oxygen in the catalyst layer is consumed especially at the anode outlet. In this section, the time elapsed to switch between air and hydrogen is increased to 1s, 15s and 30s. This way, hydrogen is diluted and hopefully, the oxygen is consumed more homogeneously along the anode limiting the hydrogen/air front effect. Figure 4.19 shows the molar fractions of hydrogen and oxygen fixed at the anode inlet.

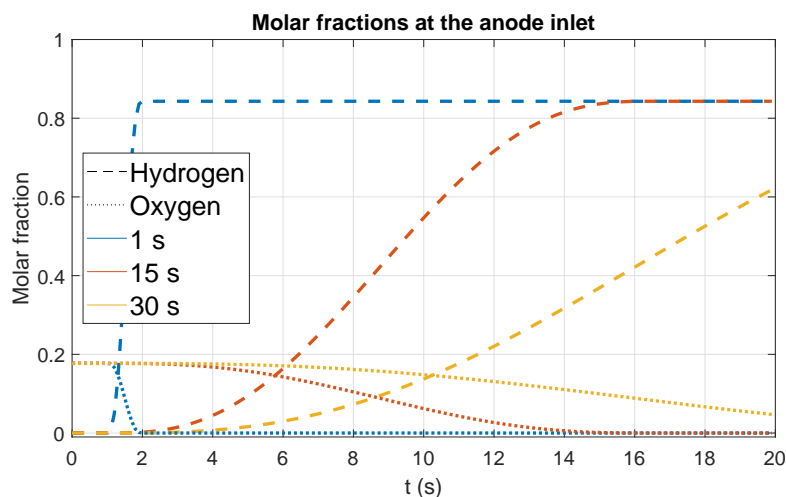


Figure 4.19: Molar fractions at the anode inlet as function of time

Figure 4.20a shows the cell potential during a startup for the different switch times. For the three cases, phase 1 ends around the same potential of 0.3 V . However for the 1 s time switch this value is reached in around 1 s whereas for the slowest switch around 12 s passed. Another effect is on the overshoot at the end of phase 2. Figure 4.20b presents a zoom on the overshoot and as higher the switch time, higher is the overshoot.

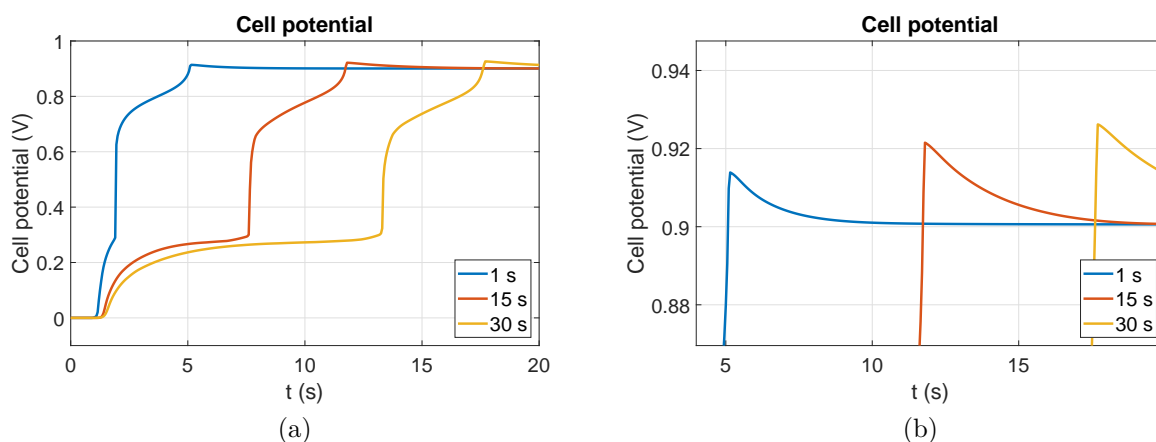


Figure 4.20: Cell potential (a) during a startup for different switch times and zoom on the overshoot (b)

Figure 4.21 shows the cathode potential at the cathode inlet during a startup for the different switch times. Looking at phase 2, small differences appear between each case. First, the elapsed time in the phase slightly increases as the switch time goes up. For a switch time of 1 s , phase 2 lasts 3 s which is slightly higher to the value found in subsection 4.2.1 of 2.7 s (see Table 4.3). For 15 s and 30 s case respectively, phase 2 lasts 4.2 s and 4.6 s . Another small effect of the dilution is the highest potential reached. Indeed, this value decreases when the switch time increases going from 1.62 V to 1.605 V . Unfortunately, quantity of corroded carbon were not integrated in this simulation.

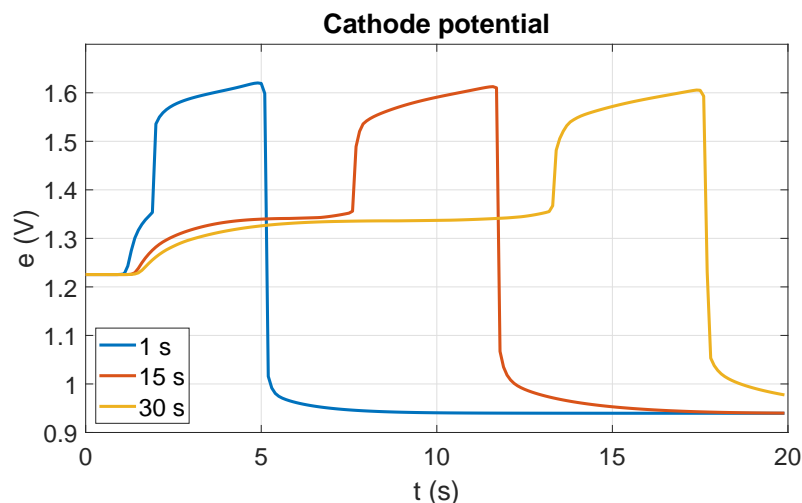


Figure 4.21: Cathode potential at the cathode inlet during a startup for different switch times

4.3 Conclusion

In this chapter several mitigation strategies are simulated and analysed. Anodic catalyst loading is first examined. Its impact on limiting carbon corrosion is confirmed through the limitation of reduction of ORR current. This reduction lowers the cathode potential which leads to a restraint corrosion. In terms of flow field design, anodic rib/channel pattern has an influence on corrosion at the cathode during startup. Model shows that during a startup, the corrosion increases with the width of the anodic rib especially beyond $\Gamma = 50\%$. Heterogeneities are also strengthened with the enlargement of the width especially the cathode section facing the anode outlet. However, results are different for shutdown. Simulations forecast that the heterogeneities are contained even face to the anode outlet. Study on anodic flow velocity shows that it influence directly the elapsed time in phase 2 as expected. By limiting the time in this phase which is when carbon corrosion occurs, the degradation are mitigated. However a limiting effect seems to appear which is due to the diffusion speed in the GDL. For the startup with a resistor, the resulting current leak has a significant effect on the corrosion. Cathode potential is restrained at lower value during all phase 2. To go further with those results, CO_2 quantity at the cathode outlet is calculated.

Figure 4.22 shows the quantity of CO_2 simulated for the startup for the different cases presents before. Depending on the mitigation strategies used, the profile of the CO_2 quantity strongly varies. For the velocity cases (marine blue, red, yellow and purple curves), the higher the speed, the lower the peak value as expected from the lower corrosion. Also, because of the change of velocity, CO_2 does not appear at the same time. Whereas for the startup with a resistor and the lower platinum loading (green and turquoise curve), CO_2 appears at the cathode outlet at the same time but the profile is modified. Table 4.4 presents a summary of

all the cases with the resulting corroded carbon. Even though the fastest case shows a lower peak in CO₂ (Figure 4.22) than the highest velocity, this latter mitigates less the corrosion.

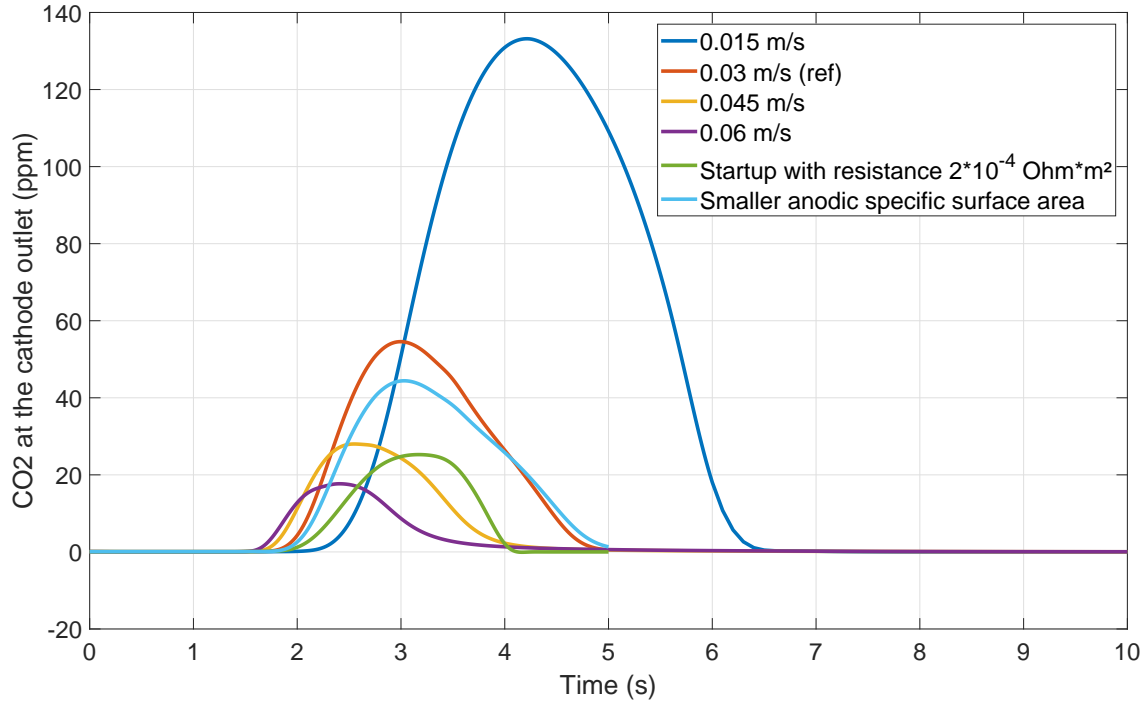


Figure 4.22: Quantity of CO₂ at the cathode outlet for several cases during a startup

Table 4.4: Summary of mitigation

Case	Carbon oxidized per startup $\mu g_C/cm^2$	Mitigation %
Ref	40	0
Anodic specific surface area divided by 2	35	- 14
Highest flow rate (0.063 m/s)	21	- 48
Higher flow rate (0.047 m/s)	27	- 33
Lowest flow rate (0.015 m/s)	71	+ 77
Leak Resistance $2 \cdot 10^{-4} \Omega \cdot m^2$	15	- 63

Conclusions and prospects

Nowadays, life expectancy of the fuel cell is one of the main hindrance of deployment in the transport field. Namely, the several thousands startups and shutdowns undergone by the fuel cell can significantly decrease its lifetime. The main degradation during these transient phases is the corrosion of the carbon support due to reverse-current decay mechanism. This phenomenon and its repercussions are still actively studied. This oxidation is liable to detachment of catalyst particles and to provoke structural collapse. In this work, a modelling approach is proposed to study the carbon corrosion during these transient phases. Two 2D models are developed inside a framework representing two cut planes of the fuel cell: along the channel and rib/channel. The goal of the framework is, through a multi-physics modeling approach, to take into account the local conditions to mechanistically analyse the operation of the fuel cell. These models are first validated and used as a performance evaluation tool in order to test the proposed approach. An optimization of rib/channel design is done taking into account the complex transport of reactive gases in the MEA. As this medium is compressed under the rib, transport is modified between the part under the rib and the channel. The simulation shows the impact of design onto performance through the competition between the transport of oxygen under the cathodic rib and the electronic current collection. Furthermore it allows to study this impact under different operating conditions.

Part of the study is then dedicated to model the startups and shutdowns of the PEMFC and their impact on the corrosion of the carbon support. As PEMFC technology is expensive through its low durability at the low platinum loading, multi-physics modeling is a cost effective tool especially for degradation analysis. Even though experiments are mandatory to have the whole impact, numerical simulations allow to isolate and discriminate mechanisms and phenomena and to extrapolate the other operating conditions. In this work, local and operating conditions enable the simulation of the reverse-current decay mechanism. Furthermore, a full transient simulation is done using high spatial resolution to finely model the local conditions taking into account operating conditions able to reproduction the reverse-current decay mechanism. This results in a spatial and temporal representation of the startup and shutdown of a fuel cell giving access to local variables that are impossible to access directly in experiments. Deep explanations about the understanding of carbon corrosion effects and the front of reverse decay mechanisms are underlined. Validations are proposed with CO_2 measurements at the cathode outlet, SAXS/WAXS experiments and in-situ/ex-situ analyses. These validations show that the simulation provides the right trends. Mitigation strategies are tested and evaluated. Simulations show that co-flow configuration presents slightly less corrosion than a counter-flow configuration. Indeed a focus on the rib/channel scale allows to explain the degradation heterogeneities during experiment and to estimate them. During a startup, the difference in the hydrogen supply to the catalyst layer under the channel and the rib is identified as the origin of these heterogeneities. However during a shutdown, the oxygen supply has less effect on the degradation heterogeneities.

Impact of gas transport in the porous media is clearly identified.

Now that the numerical tools are operational, better validation has to be done in order to identify properly the parameters of the model. For example, a fuel cell with a simpler flow field as done by Maranzana et al. [109] is a stepping stone. Furthermore, the corrosion of the carbon support implies a lot of complex mechanisms from the detachment of the catalyst nanoparticles to the micro-structure modification of the catalyst layer strengthening the need of experiments linking the corrosion with these mechanisms. Several works have shown the importance of the platinum oxides in the carbon corrosion during startup and should be added in the model. As platinum dissolution and redeposition in the membrane kinetics are already available in the framework EuROPIUM, a coupling with this work will be interesting. Study on geometry are also possible, for example an other lead is to study the impact on degradation when the anodic rib does not face a cathodic one. As suggested in chapter 4, an optimization of the anodic rib width may be done to limit degradation during startup or shutdown while maintaining good performance. Gas transport is shown to have a great impact, and channels should be discretized to study the effect of design the flow field. Finally, these models can be used to evaluate startup/shutdown strategies on an actual system.

Bibliography

- [1] Jean-Philippe Poirot-Crouvezier. *Modélisation dynamique des phénomènes hydrauliques, thermiques et électriques dans un groupe électrogène à pile à combustible destiné à l'application automobile*. PhD thesis, INPG, 2000.
- [2] Fredy Nandjou. *étude locale de la thermique dans les piles à combustible pour application automobile. Corrélation à la durée de vie*. PhD thesis, Université Grenoble Alpes, 2015.
- [3] Mathias Gerard. *Etude des interactions pile/système en vue de l'optimisation d'un générateur pile à combustible: Interactions coeur de pile/ compresseur - Interactions coeur de pile/ convertisseur*. PhD thesis, Université de Franche-Comté, 2010.
- [4] F. Micoud, S. Escribano, A. Convert, S. Rosini, and L. Guetaz. Local degradations induced in a pemfc stack by start-up/shut-down cycles: investigations coupling in-situ and ex-situ analyses. International Symposium on Electrocatalysis, 2018 August 29th - September 1st, Szczyrk, Poland, 2018.
- [5] V. Sethuraman, J. Weidner, A. Haug, A. Motupally, and L. Protsailo. Hydrogen peroxyde formation rrate in a PEMFC anode and cathode. effect of humidity and temperature. *J. Electrochem. Soc*, 155(1):B50–B57, 2008.
- [6] X. Erler. *In-situ investigation of metal nanoparticle stability during*. PhD thesis, Von der Fakultat II - Mathematik und Naturwissenschaften der Technische Universität Berlin, 2012.
- [7] Julien Durst, Adrien Lamibrac, Frederic Charlot, JÃ©rome Dillet, Luis F. Castanheira, Gael Maranzana, Laetitia Dubau, Frederic Maillard, Marian Chatenet, and Olivier Lottin.

- Degradation heterogeneities induced by repetitive start/stop events in proton exchange membrane fuel cell: Inlet vs. outlet and channel vs. land. *Applied Catalysis B: Environmental*, 138-139:416 – 426, 2013.
- [8] P. Pei, Q. Chang, and T. Tang. A quick evaluating method for automotive fuel cell lifetime. *Int. J. Hydrogen Energy*, 33:3829–3836, 2008.
- [9] Wenbin Gu, Paul T. Yu, Robert N. Carter, Rohit Makharia, and Hubert A. Gasteiger. *Modeling of Membrane-Electrode-Assembly Degradation in Proton-Exchange-Membrane Fuel Cells – Local H₂ Starvation and Start–Stop Induced Carbon-Support Corrosion*, pages 45–87. Springer New York, New York, NY, 2010.
- [10] L. Castanheira. Corrosion of high surface area carbon supports used in proton-exchange membrane fuel cell electrodes, 2014.
- [11] 2018 annual work plan and budget. Technical report, FCH2JU, 2018.
- [12] Jennifer Kurtz, Huyen Dinh, and Genevieve Saur. Doe annual report - v.f.4 fuel cell technology status: Degradation, 2016.
- [13] Jennifer Kurtz, Sam Sprik, Chris Ainscough, and Genevieve Saur. Doe annual report - vii.a.1 fuel cell electric vehicle evaluation, 2016.
- [14] Jason M. Morgan and Ravindra Datta. Understanding the gas diffusion layer in proton exchange membrane fuel cells. i. how its structural characteristics affect diffusion and performance. *Journal of Power Sources*, 251:269 – 278, 2014.
- [15] J. Healy, C. Hayden, T. Xie, K. Olson, R. Waldo, M. Brundage, H. Gasteiger, and J. Abbott. Aspects of the chemical degradation of pfsa ionomer used in pem fuel cells. *Fuel Cells*, 5(2):302–308, 2005.
- [16] Makoto Aoki, Hiroyuki Uchida, and Masahiro Watanabe. Decomposition mechanism of perfluorosulfonic acid electrolyte in polymer electrolyte fuel cells. *Electrochemistry Communications*, 8(9):1509 – 1513, 2006.
- [17] V. Sethuraman, J. Weidner, A. Haug, M. Pemberton, and L. Protsailo. Importance of catalyst stability vis-à-vis hydrogen peroxyde formation rates in pem fuel cell electrodes. *Electrochim. Acta*, 54:5571–5582, 2009.
- [18] M. Chandesris, R. Vincent, L. Guetaz, J.-S. Roch, D. Thoby, and M. Quinaud. Membrane degradation in pem fuel cells: From experimental results to semi-empirical degradation laws. *International Journal of Hydrogen Energy*, mar 2017.

-
- [19] Wolfgang Schmittinger and Ardalan Vahidi. A review of the main parameters influencing long-term performance and durability of pem fuel cells. *Journal of Power Sources*, 180:1–14, 2008.
- [20] Ahmet Kusoglu, Anette M. Karlsson, Michael H. Santare, Simon Cleghorn, and William B. Johnson. Mechanical response of fuel cell membranes subjected to a hygro-thermal cycle. *Journal of Power Sources*, 161(2):987 – 996, 2006.
- [21] Ahmet Kusoglu, Anette M. Karlsson, Michael H. Santare, Simon Cleghorn, and William B. Johnson. Mechanical behavior of fuel cell membranes under humidity cycles and effect of swelling anisotropy on the fatigue stresses. *Journal of Power Sources*, 170(2):345 – 358, 2007.
- [22] Roham Solasi, Yue Zou, Xinyu Huang, Kenneth Reifsnider, and David Condit. On mechanical behavior and in-plane modeling of constrained pem fuel cell membranes subjected to hydration and temperature cycles. *Journal of Power Sources*, 167(2):366 – 377, 2007.
- [23] K. Panha, M. Fowler, X.-Z. Yuan, and H. Wang. Accelerated durability testing via reactants relative humidity cycling on pem fuel cells. *Applied Energy*, 93:90–97, 2012.
- [24] S.F. Burlatsky, M. Gummalla, J. O’Neill, V.V. Atrazhev, A.N. Varyukhin, D.V. Dmitriev, and N.S. Erikhman. A mathematical model for predicting the life of polymer electrolyte fuel cell membranes subjected to hydration cycling. *Journal of Power Sources*, 215:135 – 144, 2012.
- [25] C. Lim, L. Ghassemzadeh, F. Van Hove, M. Lauritzen, J. Kolodziej, G.G. Wang, S. Holdcroft, and E. Kjeang. Membrane degradation during combined chemical and mechanical accelerated stress testing of polymer electrolyte fuel cells. *J. Power Sources*, 257(0):102–110, 2014.
- [26] Ramin M.H. Khorasany, Erik Kjeang, G.G. Wang, and R.K.N.D. Rajapakse. Simulation of ionomer membrane fatigue under mechanical and hygrothermal loading conditions. *Journal of Power Sources*, 279:55 – 63, 2015. 9th International Conference on Lead-Acid Batteries - LABAT 2014.
- [27] L. Dubau, Castanheira L., Maillard F., Chatenet M., Lottin O., Maranzana G., Dillet J., Lamibrac A., Perrin J.-C., Moukheiber E., ElKaddouri A., De Moor G., Bas C., Flandin L., and Caqué N. A review of pem fuel cell durability: materials degradation, local heterogeneities of aging and possible mitigation strategies. *WIREs Energy Environ.*, 3:540–560, 2014.

- [28] Shengsheng Zhang, Xiao-Zi Yuan, Jason Ng Cheng Hin, Haijiang Wang, Jinfeng Wu, K. Andreas Friedrich, and Mathias Schulze. Effects of open-circuit operation on membrane and catalyst layer degradation in proton exchange membrane fuel cells. *Journal of Power Sources*, 195(4):1142 – 1148, 2010.
- [29] S. Vengatesan, Michael W. Fowler, Xiao-Zi Yuan, and Haijiang Wang. Diagnosis of mea degradation under accelerated relative humidity cycling. *Journal of Power Sources*, 196(11):5045 – 5052, 2011.
- [30] G. DeMoor, C. Bas, E. Charvin, N. Moukheiber, F. Niepceron, N. Breilly, J. André, E. Rossinot, E. Claude, N.D. Albérola, and L. Flandin. Understanding membrane failure in pemfc: Comparison of diagnostic tools at different observation scales. *Fuel Cells*, 12(3):356–364, 2012.
- [31] E. Guilminot, A. Corcella, F. Charlot, F. Maillard, and M. Chatenet. Detection of pt^{z+} ions and pt nanoparticles inside the membrane of a used pemfc. *Journal of The Electrochemical Society*, 154(1):B96–B105, 2007.
- [32] Carolina Galeano, Josef C. Meier, Volker Peinecke, Hans Bongard, Ioannis Katsounaros, Angel A. Topalov, Anhui Lu, Karl J. J. Mayrhofer, and Ferdi SchÄEth. Toward highly stable electrocatalysts via nanoparticle pore confinement. *Journal of the American Chemical Society*, 134(50):20457–20465, 2012. PMID: 23190415.
- [33] Rod Borup and Jeremy Meyers. Scientific aspects of polymer electrolyte fuel cell durability and degradation. *Chemical Review*, 107:3904–3951, 2007.
- [34] Shao-Horn Y., Sheng W.C., Chen S., Ferreira J.P., Holby E.F., and Morgan D. Instability of supported platinum nanoparticles in low-temperature fuel cells. *Top Catal*, 2007.
- [35] Wenchao Sheng, Shuo Chen, Elio Vescovo, and Yang Shao-Horn. Size influence on the oxygen reduction reaction activity and instability of supported pt nanoparticles. *Journal of The Electrochemical Society*, 159(2):B96–B103, 2011.
- [36] Angel A. Topalov, Ioannis Katsounaros, Michael Auinger, Serhiy Cherevko, Josef C. Meier, Sebastian O. Klemm, and Karl J. J. Mayrhofer. Dissolution of platinum: Limits for the deployment of electrochemical energy conversion? *Angewandte Chemie International Edition*, 51(50):12613–12615, 2012.
- [37] B.E. Conway. Electrochemical oxide film formation at noble metals as a surface-chemical process. *Progress in Surface Science*, 49(4):331 – 452, 1995.

- [38] D.C. Johnson, D.T. Napp, and S. Bruckenstein. A ring-disk electrode study of the current/potential behaviour of platinum in 1.0 m sulphuric and 0.1 m perchloric acids. *Electrochimica Acta*, 15(9):1493 – 1509, 1970.
- [39] V.I. Birss, M. Chang, and J. Segal. Platinum oxide film formation-reduction: an in-situ mass measurement study. *Journal of Electroanalytical Chemistry*, 355(1):181 – 191, 1993. An International Journal Devoted to all Aspects of Electrode Kinetics, Interfacial Structure, Properties of Electrolytes, Colloid and Biological Electrochemistry.
- [40] Steven G. Rinaldo, Wendy Lee, JÃƒCergen Stumper, and Michael Eikerling. Model- and theory-based evaluation of pt dissolution for supported pt nanoparticle distributions under potential cycling. *Electrochemical and Solid-State Letters*, 14(5):B47–B49, 2011.
- [41] A. Baldan. Progress in ostwald ripening theories and their applications to nickel-base superalloys. *Journal of materials science*, 37:2171–2202, 2002.
- [42] Rajesh K. Ahluwalia, Srikanth Arisetty, Xiaoping Wang, Xiaohua Wang, Ram Subbaraman, Sarah C. Ball, Stacy DeCrane, and Deborah J. Myers. Thermodynamics and kinetics of platinum dissolution from carbon-supported electrocatalysts in aqueous media under potentiostatic and potentiodynamic conditions. *Journal of The Electrochemical Society*, 160(4):F447–F455, 2013.
- [43] Z. Zhao, L. Dubau, and F. Maillard. Evidences of the migration of pt crystallites on high surface area carbon supports in the presence of reducing molecules. *Journal of Power Sources*, 217:449 – 458, 2012.
- [44] H. Binder, A. Kohling, K. Richter, and G. Sandstede. Uber die anodische oxydation von aktivkohlen in wassrigen elektrolyten. *Electrochimica Acta*, 9(3):255 – 274, 1964.
- [45] K. Kinoshita, J.T. Lundquist, and P. Stonehart. Potential cycling effects on platinum electrocatalyst surfaces. *Journal of Electroanalytical Chemistry and Interfacial Electrochemistry*, 48(2):157–166, 1973.
- [46] K. Kinoshita and J.A.S. Bett. Potentiodynamic analysis of surface oxides on carbon blacks. *Carbon*, 11(4):403 – 411, 1973.
- [47] K. Kinoshita and J.A.S. Bett. Determination of carbon surface oxides on platinum-catalyzed carbon. *Carbon*, 12(5):525 – 533, 1974.
- [48] K. Kinoshita and J.A.S. Bett. Influence of electrochemical treatment in phosphoric acid on the wettability of carbons. *Carbon*, 13(5):405 – 409, 1975.

- [49] K.H. Kangasniemi, D.A. Condit, and T.D. Jarvi. Characterization of vulcan electrochemically oxidized under simulated pem fuel cell conditions. *Journal of the Electrochemical Society*, 151(4):E125–E132, 2004.
- [50] L. M. Roen, C. H. Paik, and T. D. Jarvi. Electrocatalytic corrosion of carbon support in pemfc cathodes. *Electrochemical and Solid-State Letters*, 7(1):A19–A22, 2004.
- [51] K. Kinoshita. K. kinoshita: Carbon, electrochemical and physical properties, john wiley + sons, chichester, new york, brisbane, toronto 1988. 533 seiten. *Berichte der Bunsengesellschaft für physikalische Chemie*, 92(9):1060–1060, 1988.
- [52] J. Willsau and J. Heitbaum. The influence of pt-activation on the corrosion of carbon in gas diffusion electrodes—a dems study. *Journal of Electroanalytical Chemistry and Interfacial Electrochemistry*, 161(1):93 – 101, 1984.
- [53] O.V. Cherstiouk, A.N. Simonov, N.S. Moseva, S.V. Cherepanova, P.A. Simonov, V.I. Zaikovskii, and E.R. Savinova. Microstructure effects on the electrochemical corrosion of carbon materials and carbon-supported pt catalysts. *Electrochimica Acta*, 55(28):8453 – 8460, 2010.
- [54] R. Makharia, S. Kocha, P. Yu, M.A. Sweikart, W. Gu, F. Wagner, and H.A. Gasteiger. Durable pem fuel cell electrode materials: Requirements and benchmarking methodologies. *ECS Transactions*, 1(8):3–18, 2006.
- [55] S.C. Ball, S.L. Hudson, D. Thompsett, and B. Theobald. An investigation into factors affecting the stability of carbons and carbon supported platinum and platinum/cobalt alloy catalysts during 1.2 v potentiostatic hold regimes at a range of temperatures. *Journal of Power Sources*, 171(1):18–25, 2007.
- [56] Kateryna Artyushkova, Svitlana Pylypenko, Madhu Dowlapalli, and Plamen Atanassov. Structure-to-property relationships in fuel cell catalyst supports: Correlation of surface chemistry and morphology with oxidation resistance of carbon blacks. *Journal of Power Sources*, 214:303 – 313, 2012.
- [57] Mathias M.F., Makharia R., Gasteiger H.A., Conley J.J., Fuller T.J., Gittleman C.J., Kocha S.S., Miller D.P., Mittelsteadt C.K., Xie T., Yan S.G., and Yu P.T. Two fuel cell cars in every garage? *The Electrochemical Society Interface*, 14-3:24–35, 2005.
- [58] S. Maass, F. Finsterwalder, G. Frank, R. Hartmann, and C. Merten. Carbon support oxidation in pem fuel cell cathodes. *Journal of Power Sources*, 176:444–451, 2008.

- [59] E. Passalacqua, P.L. Antonucci, M. Vivaldi, A. Patti, V. Antonucci, N. Giordano, and K. Kinoshita. The influence of pt on the electrooxidation behaviour of carbon in phosphoric acid. *Electrochimica Acta*, 37(15):2725 – 2730, 1992.
- [60] Wei Li and Alan M. Lane. Investigation of pt catalytic effects on carbon support corrosion of the cathode catalyst in pem fuel cells using dems spectra. *Electrochemistry Communications*, 11(6):1187 – 1190, 2009.
- [61] Nicolas Linse, Lorenz Gubler, Gunther G. Scherer, and Alexander Wokaun. The effect of platinum on carbon corrosion behavior in polymer electrolyte fuel cells. *Electrochimica Acta*, 56(22):7541 – 7549, 2011.
- [62] F. Maillard, A. Bonnefont, and F. Micoud. An ec-ftir study on the catalytic role of pt in carbon corrosion. *Electrochemistry Communications*, 13(10):1109 – 1111, 2011.
- [63] P.L. Antonucci, L. Pino, N. Giordano, and G. Pinna. A comparative analysis of structural and surface effects in the electrochemical corrosion of carbons. *Materials Chemistry and Physics*, 21(5):495 – 506, 1989.
- [64] Laetitia Dubau, Miguel Lopez-Haro, Luis Castanheira, Julien Durst, Marian Chatenet, Pascale Bayle-Guillemaud, Laure GuÃ©taz, Nicolas CaquÃ©, Elisabeth Rossinot, and FrÃ©dÃ©ric Maillard. Probing the structure, the composition and the orr activity of pt3co/c nanocrystallites during a 3422h pemfc ageing test. *Applied Catalysis B: Environmental*, 142-143:801 – 808, 2013.
- [65] P. J. Ferreira, G. J. la O, Y. Shao-Horn, D. Morgan, R. Makharia, S. Kocha, and H. A. Gasteiger. Instability of pt/c electrocatalysts in proton exchange membrane fuel cells. *Journal of The Electrochemical Society*, 152:A2256–A2271, 2005.
- [66] J. Xie, D. L. Wood III, , D. M. Wayne, T. A. Zawodzinski, P. Atanassov, and R. Borup. Durability of pefcs at high humidity conditions. *J. Electrochem. Soc.*, 152(1):A104–A113, 2005.
- [67] Marian Chatenet, Elodie Guilminot, Christina Iojoiu, Jean-Yves Sanchez, Elissabeth Rossinot, and FrÃ©dÃ©ric Maillard. Pt redistribution within pemfc meas and its consequence on their performances. *ECS Transactions*, 11(1):1203–1214, 2007.
- [68] Hendrik Schulenburg, Bernhard Schwanitz, Nicolas Linse, GÃ©nther G. Scherer, A. Wokaun, Julijana Krbanjevic, Roman Grothausmann, and Ingo Manke. 3d imaging of catalyst support corrosion in polymer electrolyte fuel cells. *The Journal of Physical Chemistry C*, 115(29):14236–14243, 2011.

- [69] Natalia Macauley, Dennis D. Papadias, Joseph Fairweather, Dusan Spornjak, David Langlois, Rajesh Ahluwalia, Karren L. More, Rangachary Mukundan, and Rodney L. Borup. Carbon corrosion in pem fuel cells and the development of accelerated stress tests. *Journal of The Electrochemical Society*, 165(6):F3148–F3160, 2018.
- [70] M. Secanell, A. Putz, P. Wardlaw, V. Zingan, M. Bhaiya, M. Moore, J. Zhou, C. Balen, and K. Domican. Openfcst: An open-source mathematical modelling software for polymer electrolyte fuel cells. *ECS Transactions*, 64(3):655–680, 2014.
- [71] Kenji Nagumo and Masajiro Inoue. Numerical prediction of water content distribution of catalyst coated membrane of fuel cell stack using simulation. *Honda*, 2016.
- [72] Masakazu Yoneda, Yukari Tago, Koshiro Suzuki, Masato Takimoto, and Eiji Ejiri. Macroscopic modeling and simulation for polymer electrolyte membrane fuel cells. *ECS Transactions*, 3(1):1105–1114, 2006.
- [73] Steven B. Beale, Hae-Won Choi, Jon G. Pharoah, Helmut K. Roth, Hrvoje Jasak, and Dong Hyup Jeon. Open-source computational model of a solid oxide fuel cell. *Computer Physics Communications*, 200:15 – 26, 2016.
- [74] Georg A. Futter, Pawel Gazdzicki, K. Andreas Friedrich, Arnulf Latz, and Thomas Jahnke. Physical modeling of polymer-electrolyte membrane fuel cells: Understanding water management and impedance spectra. *Journal of Power Sources*, 391:148 – 161, 2018.
- [75] P. Schott and P. Baurens. Fuel cell operation characterization using simulation. *Journal of Power Sources*, 156(1):85–91, #may# 2006.
- [76] A. A. Franco, P. Schott, C. Jallut, and B. Maschke. A multi-scale dynamic mechanistic model for the transient analysis of pefcs. *Fuel Cells*, 2:99–117, 2007.
- [77] Alejandro A. Franco, Sylvain Passot, Pascal Fugier, Christelle Anglade, Emmanuel Billy, Laure Guétaz, Nicolas Guillet, Eric De Vito, and Sophie Mailley. Ptxcoy catalysts degradation in pefc environments: Mechanistic insights. *J. Electrochem. Soc.*, 156(3):B410–B424, 2009.
- [78] Kouros Malek and Alejandro A. Franco. Microstructure-based modeling of aging mechanisms in catalyst layers of polymer electrolyte fuel cells. *The Journal of Physical Chemistry B*, 115(25):8088–8101, 2011.
- [79] A.A. Franco. Chapter 11 - modelling and analysis of degradation phenomena in polymer electrolyte membrane fuel cells. In Christoph Hartnig and Christina Roth, editors,

- Polymer Electrolyte Membrane and Direct Methanol Fuel Cell Technology*, volume 1 of *Woodhead Publishing Series in Energy*, pages 291–367. Woodhead Publishing, 2012.
- [80] C. Robin, M. Gerard, A.A. Franco, and P. Schott. Multi-scale coupling between two dynamical models for PEMFC aging prediction. *International Journal of Hydrogen Energy*, 38(11):4675–4688, 2013.
- [81] Christophe Robin, Mathias Gerard, Julien d’Arbigny, Pascal Schott, Lara Jabbour, and Yann Bultel. Development and experimental validation of a PEM fuel cell 2d-model to study heterogeneities effects along large-area cell surface. *Int. J. Hydrogen Energy*, 40(32):10211–10230, 2015.
- [82] Bolahaga Randrianarizafy, Pascal Schott, Marion Chandesris, Mathias Gerard, and Yann Bultel. Design optimization of rib/channel patterns in a pemfc through performance heterogeneities modelling. *International Journal of Hydrogen Energy*, 43(18):8907 – 8926, 2018.
- [83] Howard Brenner. Navier-stokes revisited. *Physica A: Statistical Mechanics and its Applications*, 349(1-2):60–132, 2005.
- [84] J. Clerk Maxwell. On the dynamical theory of gases. *Philosophical Transactions of the Royal Society of London*, 157:49–88, 1867.
- [85] J. Stefan. Über das Gleichgewicht und Bewegung, insbesondere die Diffusion von Gemischen. *Sitzungsberichte der Kaiserlichen Akademie der Wissenschaften Wien*, 63:63–124, 1871.
- [86] J.B. Young and B. Todd. Modelling of multi-component gas flows in capillaries and porous solids. *International Journal of Heat and Mass Transfer*, 48(25-26):5338–5353, 2005.
- [87] Henry Darcy. *Les fontaines publiques de la ville de Dijon*. Librairie des Corps Impériaux des Ponts et Chaussées et des Mines, 49, Quai des Augustins - Paris, 1856.
- [88] Martin Knudsen. Die Gesetze der Molekularströmung und der inneren Reibungsströmung der Gase durch Röhren. *Annalen der Physik*, 333(1):75–130, 1909.
- [89] W. G. Pollard and R. D. Present. On gaseous self-diffusion in long capillary tubes. *Phys. Rev.*, 73:762–774, Apr 1948.
- [90] Frank Meier and Gerhart Eigenberger. Transport parameters for the modelling of water transport in ionomer membranes for PEM-fuel cells. *Electrochimica Acta*, 49(11):1731–1742, #apr# 2004.

- [91] Alejandro A. Franco. *Un modèle physique multiéchelle de la dynamique électrochimique dans une pile à combustible à électrolyte polymère*. PhD thesis, Université Claude Bernard - Lyon 1, #nov# 2005.
- [92] S. Passot. *Etude expérimentale et par modélisation de l'impact d'impuretés de l'hydrogène sur le fonctionnement des piles à combustible à membrane échangeuse de protons (PEMFC)*. PhD thesis, Université de Grenoble, 2012.
- [93] T. E. Springer, T. A. Zawodzinski, and S. Gottesfeld. Polymer electrolyte fuel cell model. *Journal of The Electrochemical Society*, 138(8):2334–2342, 1991.
- [94] Jean Besson. *Précis de thermodynamique et cinétique électrochimiques*. Ellipses (Paris), 1984.
- [95] Markku J. Lampinen and Marina Fomino. Analysis of free energy and entropy changes for half-cell reactions. *Journal of The Electrochemical Society*, 140(12):3537–3546, 1993.
- [96] Guangyu Lin and Trung Van Nguyen. A two-dimensional two-phase model of a PEM fuel cell. *Journal of The Electrochemical Society*, 153(2):A372–A382, #feb# 2006.
- [97] R. Coulon, W. G. Bessler, and A. Franco. Modeling chemical degradation of a polymer electrolyte membrane and its impact on fuel cell performance. *ECS Trans.*, 25:259, 2010.
- [98] Thomas A. Zawodzinski, Michal Neeman, Laurel O. Sillerud, and Shimshon Gottesfeld. Determination of water diffusion coefficients in perfluorosulfonate ionomeric membranes. *J. Phys. Chem.*, 95(15):6040–6044, Jul 1991.
- [99] R. B. Bird, W. E. Stewart, and E. N. Lightfoot. *Transport Phenomena*. John John Wiley & Sons, 2007.
- [100] J.R. Davis and A.S.M.I.H. Committee. *Stainless Steels*. ASM specialty handbook. ASM International, 1994.
- [101] Steven G. Chalk and James F. Miller. Key challenges and recent progress in batteries, fuel cells, and hydrogen storage for clean energy systems. *Journal of Power Sources*, 159(1):73 – 80, 2006. Special issue including selected papers from the 3rd International Conference on Materials for Advanced Technologies (ICMAT 2005, Singapore, Malaysia) and the Summer School on Synthesis of Nanostructured Materials for Polymer Batteries (Augustow, Poland) together with regular papers.
- [102] Maxime Piffard, Mathias Gerard, Ramon Da Fonseca, Paolo Massioni, and Eric Bideaux. Sliding mode observer for proton exchange membrane fuel cell: automotive application. *Journal of Power Sources*, 388:71 – 77, 2018.

-
- [103] N. Yousfi-Steiner, Ph. Mocoteguy, D. Candusso, and D. Hissel. A review on polymer electrolyte membrane fuel cell catalyst degradation and starvation issues: Causes, consequences and diagnostic for mitigation. *Journal of Power Sources*, 194:130–145, 2009.
- [104] Pucheng Pei and Huicui Chen. Main factors affecting the lifetime of proton exchange membrane fuel cells in vehicle applications: A review. *Applied Energy*, 125:60–75, 2014.
- [105] Carl A. Reiser, Lawrence Bregoli, Timothy W. Patterson, Jung S. Yi, J. Deliang Yang, Mike L. Perry, and Thomas D. Jarvi. A reverse-current decay mechanism for fuel cells. *Electrochemical and Solid-State Letters*, 8(6):A273–A276, 2005.
- [106] Qiang Shen, Ming Hou, Dong Liang, Zhimin Zhou, Xiaojin Li, Zhigang Shao, and Baolian Yi. Study on the processes of start-up and shutdown in proton exchange membrane fuel cells. *Journal of Power Sources*, 189(2):1114–1119, 2009.
- [107] Jeremy P. Meyers and Robert M. Darling. Model of carbon corrosion in PEM fuel cells. *J. Electrochem. Soc.*, 153(8):A1432–A1442, 2006.
- [108] Jan Hendrik Ohs, Ulrich Sauter, Sebastian Maass, and Detlef Stolten. Modeling hydrogen starvation conditions in proton-exchange membrane fuel cells. *Journal of Power Sources*, 196(1):255–263, 2011.
- [109] G. Maranzana, A. Lamibrac, J. Dillet, S. Abbou, S. Didierjean, and O. Lottin. Startup (and shutdown) model for polymer electrolyte membrane fuel cells. *Journal of The Electrochemical Society*, 162(7):F694–F706, 2015.
- [110] A. Lamibrac, G. Maranzana, O. Lottin, J. Dillet, J. Mainka, S. Didierjean, A. Thomas, and C. Moyne. Experimental characterization of internal currents during the start-up of a proton exchange membrane fuel cell. *Journal of Power Sources*, 196(22):9451 – 9458, 2011.
- [111] I. A. Schneider and S. von Dahlen. Start-stop phenomena in channel and land areas of a polymer electrolyte fuel cell. *Electrochemical and Solid-State Letters*, 14(2):B30–B33, 2011.
- [112] Stefan Kreitmeier, Alexander Wokaun, and F. N. Buchi. Local catalyst support degradation during polymer electrolyte fuel cell start-up and shutdown. *Journal of The Electrochemical Society*, 159(11):F787–F793, 2012.
- [113] Sofyane Abbou, Jerome Dillet, Dusan Spornjak, Rangachary Mukundan, Joseph D. Fairweather, Rod L Borup, Gael Maranzana, Sophie Didierjean, and Olivier Lottin. Time

- evolution of local potentials during pem fuel cell operation with dead-ended anode. *ECS Transactions*, 58(1):1631–1642, 2013.
- [114] J. Dillet, D. Spornjak, A. Lamibrac, G. Maranzana, R. Mukundan, J. Fairweather, S. Didierjean, R.L. Borup, and O. Lottin. Impact of flow rates and electrode specifications on degradations during repeated startups and shutdowns in polymer-electrolyte membrane fuel cells. *Journal of Power Sources*, 250:68–79, 2014.
- [115] E. Brightman and G. Hinds. In situ mapping of potential transients during start-up and shut-down of a polymer electrolyte membrane fuel cell. *Journal of Power Sources*, 267:160 – 170, 2014.
- [116] T. F. Fuller and Gary Gray. Carbon corrosion induced by partial hydrogen coverage. *ECS Transactions*, 8(1):345–353, 2006.
- [117] Wenbin Gu, Robert N. Carter, Paul T. Yu, and Hubert A. Gasteiger. Start/stop and local h₂ starvation mechanisms of carbon corrosion: Model vs. experiment. *ECS Transactions*, 11(1):963–973, 2007.
- [118] Kunal Jain, Ashok Gidwani, Sanjiv Kumar, and James Vernon Cole. Cfd study of carbon corrosion in pem fuel cells. *ECS Transactions*, 16(2):1323–1333, 2008.
- [119] Alejandro A. Franco, Mathias Gerard, Magalie Guinard, Benoit Barthe, and Olivier Lemaire. Carbon catalyst-support corrosion in polymer electrolyte fuel cells: Mechanistic insights. *ECS Transactions*, 13(15):35, 2008.
- [120] Gael Maranzana, Christian Moyne, Jerome Dillet, Sophie Didierjean, and Olivier Lottin. About internal currents during start-up in proton exchange membrane fuel cell. *Journal of Power Sources*, 195(18):5990 – 5995, 2010. Selected Papers Presented at 4th International Conference on Polymer Batteries and Fuel Cells.
- [121] Hideto Imai, Koichi Izumi, Masashi Matsumoto, Yoshimi Kubo, Kazuo Kato, and Yasuhiko Imai. In situ and real-time monitoring of oxide growth in a few monolayers at surfaces of platinum nanoparticles in aqueous media. *Journal of the American Chemical Society*, 131(17):6293–6300, 2009. PMID: 19358577.
- [122] Kotaro Sasaki, Nebojsa Marinkovic, Hugh S. Isaacs, and Radoslav R. Adzic. Synchrotron-based in situ characterization of carbon-supported platinum and platinum monolayer electrocatalysts. *ACS Catalysis*, 6(1):69–76, 2016.

-
- [123] Tong Zhang, Peiqi Wang, Huicui Chen, and Pucheng Pei. A review of automotive proton exchange membrane fuel cell degradation under start-stop operating condition. *Applied Energy*, 223:249 – 262, 2018.
- [124] Yi Yu, Zhengkai Tu, Haining Zhang, Zhigang Zhan, and Mu Pan. Comparison of degradation behaviors for open-ended and closed proton exchange membrane fuel cells during startup and shutdown cycles. *Journal of Power Sources*, 196(11):5077 – 5083, 2011.
- [125] Hiroshi Yano, Tomohiro Akiyama, Petra Bele, Hiroyuki Uchida, and Masahiro Watanabe. Durability of pt/graphitized carbon catalysts for the oxygen reduction reaction prepared by the nanocapsule method. *Phys. Chem. Chem. Phys.*, 12:3806–3814, 2010.
- [126] Carl Reiser, Deliang Yang, and Richard Sawyer. Procedure for starting up a fuel cell system using a fuel purge, 2008.
- [127] Axel Ofstad, John Davey, Svein Sunde, and Rodney L. Borup. Carbon corrosion of a pemfc during shut-down/start-up when using an air purge procedure. *ECS Transactions*, 16(2):1301–1311, 2008.
- [128] Jae Hong Kim, Eun Ae Cho, Jong Hyun Jang, Hyoung Juhn Kim, Tae-Hoon Lim, In-Hwan Oh, Jae Jun Ko, and Seung Chan Oh. Development of a durable pemfc startup process by applying a dummy load: I. electrochemical study. *Journal of The Electrochemical Society*, 156(8):B955–B961, 2009.
- [129] Yoo Yeon Jo, Eun Ae Cho, Jung Hyeun Kim, Tae-Hoon Lim, In-Hwan Oh, Jong H. Jang, and Hyoung-Juhn Kim. Effects of a hydrogen and air supply procedure on the performance degradation of pemfcs. *International Journal of Hydrogen Energy*, 35(23):13118 – 13124, 2010. Asian Hydrogen Energy Conference 2009.
- [130] KwangSup Eom, GyeongHee Kim, EunAe Cho, Jong Hyun Jang, Hyoung-Juhn Kim, Sung Jong Yoo, Soo-Kil Kim, and Bo Ki Hong. Effects of pt loading in the anode on the durability of a membrane electrode assembly for polymer electrolyte membrane fuel cells during startup/shutdown cycling. *International Journal of Hydrogen Energy*, 37(23):18455 – 18462, 2012.
- [131] Tristan Asset, Raphael Chattot, Jakub Drnec, Pierre Bordet, Nathalie Job, Frederic Mailard, and Laetitia Dubau. Elucidating the mechanisms driving the aging of porous hollow pt_{ni}/c nanoparticles by means of coads stripping. *ACS Applied Materials & Interfaces*, 9(30):25298–25307, 2017. PMID: 28649841.

- [132] Henrike Schmies, Arno Bergmann, Jakub Drnec, Guanxiong Wang, Detre Teschner, Stefanie Kühl, Daniel J. S. Sandbeck, Serhiy Cherevko, Martin Gocyla, Meital Shviro, Marc Heggen, Vijay Ramani, Rafal E. Dunin-Borkowski, Karl J. J. Mayrhofer, and Peter Strasser. Unravelling degradation pathways of oxide-supported pt fuel cell nanocatalysts under in situ operating conditions. *Advanced Energy Materials*, 8(4):1701663.

SAXS/WAXS Description

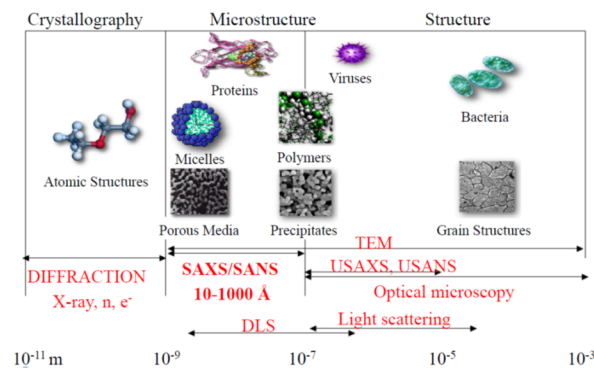


Figure A.1: Scale of different scattering methods

Why operando Small Angle X-ray Scattering and Wide Angle X-ray Scattering (SAXS/WAXS)

:

- Quantify water distribution, especially in the catalyst layers and in the membrane
- Determine catalyst structure:
 - can Pt oxidation be evidenced
 - can size of particles be evidenced
- Possibility of the evaluation of carbon structure: carbon corrosion evidence ?

To reconstruct a 3D information of the fuel cell, tomography is used with the use of these X-ray. High-energy X-rays have their energy ranges from 80 to 1000 keV which is one order of magnitude higher than conventional X-rays. It allows deep penetration into matter allowing probing of thick samples and permits an in-air sample environment and operation.

The experiments were performed at the beamline ID31 at ESRF in Grenoble. Figure A.2 is scheme of the beamline experiment. Thanks to this setup, it is possible to conduct SAXS and WAXS on the same time. Figure A.3 shows a picture of the design of the cell. A single cell is used with an active area of 25 cm² and a single serpentine flow field. Two different MEA are used: one made by the CEA with N117 or NRE212 + GDE (Pt/C) on SGL 24 BC and a commercial one Solvicore H600E.

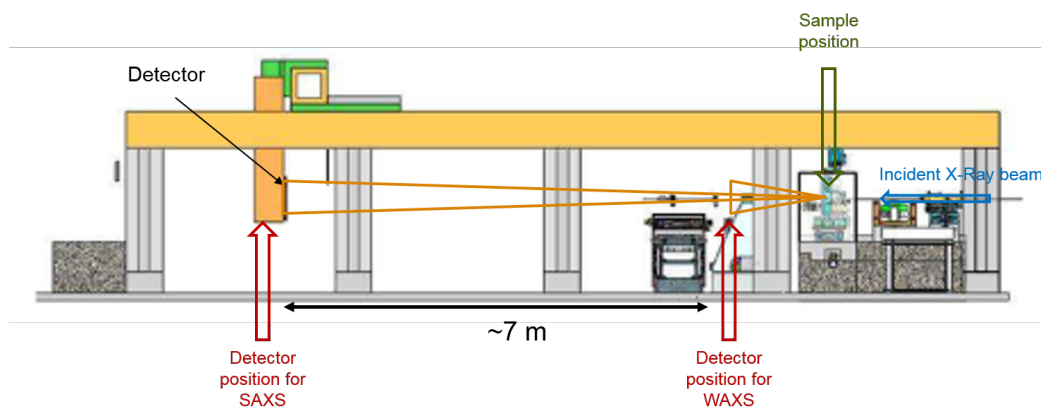


Figure A.2: Scheme of beamline experiment

Figure A.4 describes how the sample can move in space and the direction of the incident X-ray beam. Thanks to an expected spatial resolution of few microns, description of layers are expected. This beamline is very active in the electrochemistry field especially on studies of electrocatalysts for ORR by WAXS [131, 132]. This non-intrusive technique has a very high time resolution of about 0.01 s allowing a 2D tomography in about 45 min. Multiple motors enable moves in different axis and different rotations. After verifying the good alignment and the planeness of the sample, full plane scan can be done. Figure A.5 shows results of a scan along the thickness of the cell (z-axis). Each curves correspond a full spectre at a certain z. By sweeping the thickness, spectres at different layers are obtain as shown in the right image. The left image present spectres at 2.3 μm of space of the MEA that should correspond to a location in the MEA.

Figure A.6 shows examples of spectra obtained which are supposed for the first to be in the membrane and the second in the catalyst layer. The peaks searched are for Nafion at 1.2 \AA^{-1} and 2.78 \AA^{-1} , graphite at 1.8 \AA^{-1} and 2.9 \AA^{-1} and platinum (111) at 2.8 \AA^{-1} . In the left spectrum, a high spike around 1.2 \AA^{-1} suggests high proportion of Nafion. A stretched peak is also observed around 2.8 \AA^{-1} which can correspond to platinum but certainly contain also a bit

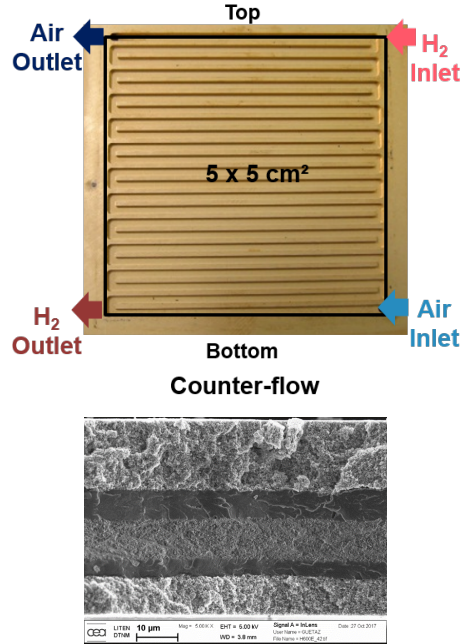


Figure A.3: Design of the cell and MEA used

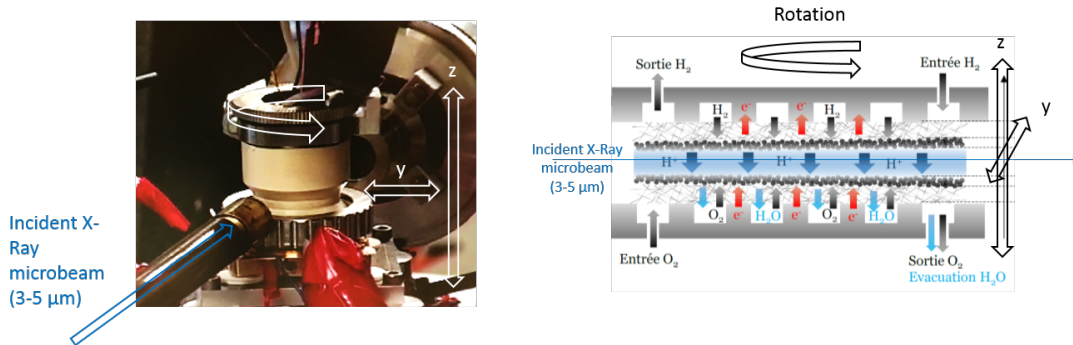


Figure A.4: Movement description of the sample

of Nafion peak hence the spread out peak. Comparing to the right spectrum, the first Nafion peak is significant less marked. However the platinum peak is more defined which suggests high concentration. A peak around 1.8 \AA^{-1} is attributed to the graphite which highlights the presence of these three components characteristic of the catalyst layer.

Another type of exploitation possible is to follow spatially the evolution of intensity of certain peaks: for example the graphite, platinum 111 and Nafion. Figure A.7 shows these intensity as function of the position in the z-axis. Looking at the intensity of the graphite, there are spikes at each extremity of the spectrum which is the signal of the rib which is in graphite here. At the middle, three zones are distinguished: from the left is the anode where the signal of the graphite starts to decrease and a peak for the platinum is observed. At the same time the signal for the Nafion also increases giving the sign of the presence of the three-phase. Then a

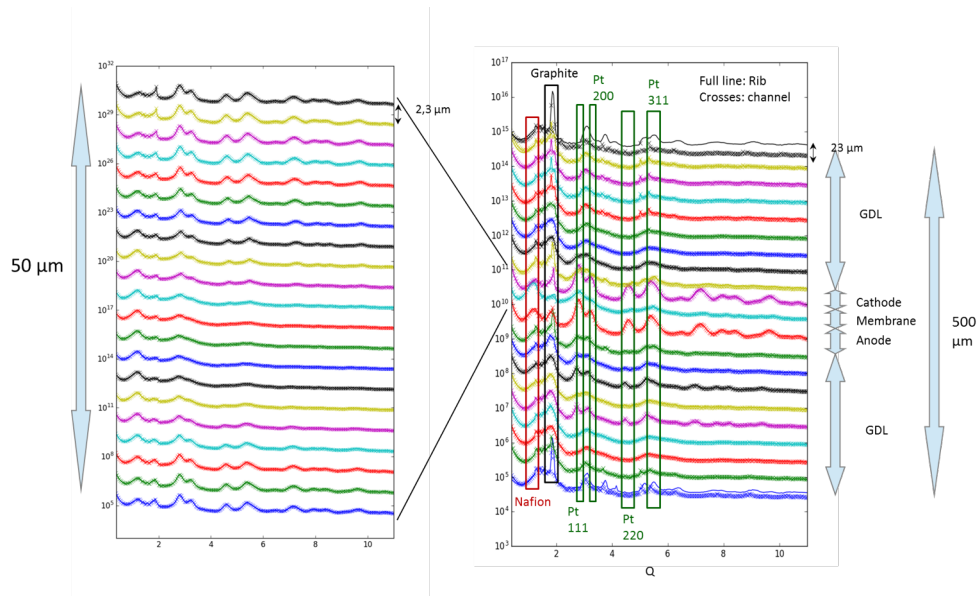


Figure A.5: Example of a full scan in the thickness (z-axis) in N_2/N_2 at 65% RH

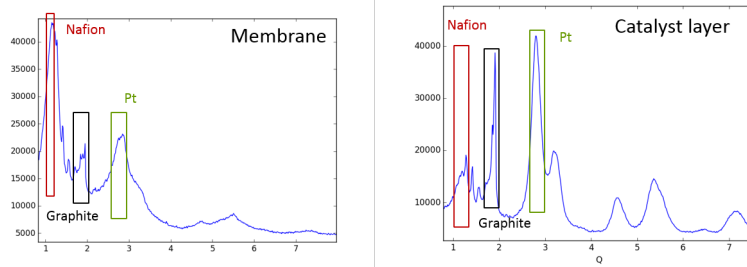


Figure A.6: Examples of isolated spectra expected to be in the membrane and in a catalyst layer

spike of intensity for Nafion signal is observed where platinum and graphite signal are low. This is characteristic of the membrane which is mainly ionomer. And then at the right side of the membrane, same trends as the anode with higher and larger spike for the platinum which is the signature of the cathode.

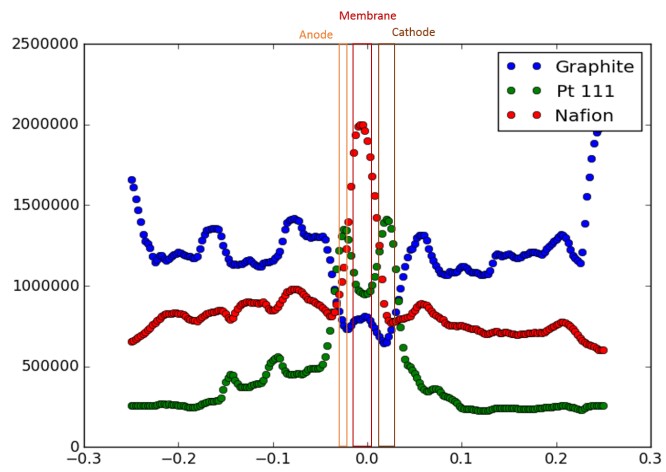


Figure A.7: Intensity of the graphite, Pt 111 and Nafion peak along the thickness

Résumé

Afin de rendre les piles à combustible à membrane échangeuse de protons viables économiquement dans le domaine automobile, des problèmes de durabilité et de coût sont à résoudre. La compréhension et le contrôle des dégradations à l'intérieur de la cellule et surtout de l'AME sont toujours le centre d'intérêt de nombreux laboratoires mais aussi d'industriels. Les milliers d'arrêt-démarrages subis par la pile provoquent une importante corrosion du support carbone. Le platine utilisé étant un catalyseur onéreux, la modélisation numérique permet l'analyse de phénomènes à moindre coût.

Dans ces travaux, deux modèles ont été développés afin de modéliser les phases transitoires que sont les arrêt-démarrages. Tout d'abord, une étude sur les performances de la pile a été effectuée en utilisant le modèle. Le couplage entre les modèles le long du canal et dent/canal est introduit. Ensuite, une analyse des phénomènes se déroulant durant les arrêt-démarrages est effectuée. Des phases temporelles sont proposées afin de découper ces différents phénomènes. Le mécanisme des courants inverses (durant lequel la corrosion du carbone apparaît) est minutieusement détaillé avec l'aide du modèle. L'accent est porté sur les hétérogénéités de dégradations apparaissant en entrée ou en sortie et même sous la dent. Enfin, le modèle est utilisé afin de simuler et proposer des stratégies d'atténuation. Les tendances attendues par la littérature sont confirmées mais aussi évaluées. Parmi les idées suggérées, l'optimisation du design dent/canal tout au long du canal est proposée afin de limiter les dégradations.

Abstract

In order to make Proton Exchange Membrane Fuel Cells economically viable for an automotive application, durability and cost problems have to be addressed. Understanding and mitigating degradations inside the cell especially in the MEA are still the focus of several laboratories and also industrials. The several thousands startups and shutdowns that the fuel cell underwent induce severe corrosion of the carbon support. As the catalyst used is expensive, namely platinum, modeling is a great asset to comprehend and analyze this phenomenon.

In this work, two models were developed for modeling the transient phases that are the startup and shutdown. First a performance study is presented to validate the use of the model and to introduce the coupling between the along the channel model and the rib/channel model. Then an analysis of the phenomena occurring during the startup (and shutdown) is carried out. Phases are suggested to break down the different phenomena. The reverse-current decay mechanism, when carbon corrosion occurs, is thoroughly detailed using the model. Degradation heterogeneities are highlighted whether they are at the inlet inlet or at the outlet or even under the rib. Finally the model is used to emulate and suggest mitigation strategies. Degradation trends are confirmed and evaluated. New ideas like an original flow field design are tested to mitigate degradation.

